Multidimensional and Temporal SAR Data Representation and Processing based on Binary Partition Trees

A DISSERTATION PRESENTED
BY
ALBERTO ALONSO-GONZÁLEZ
TO
THE SIGNAL THEORY AND COMMUNICATIONS DEPARTMENT (TSC)

IN PARTIAL FULFILLMENT OF THE REQUIREMENTS
FOR THE DEGREE OF
DOCTOR OF PHILOSOPHY
IN THE SUBJECT OF
SIGNAL THEORY AND COMMUNICATIONS

UNIVERSITAT POLITÈCNICA DE CATALUNYA (UPC)
BARCELONA, SPAIN
APRIL 2014

DISSERTATION ADVISOR
CARLOS LÓPEZ-MARTÍNEZ

UPC
UNIVERSITAT POLITÈCNICA DE CATALUNYA
BARCELONATECH
Department of Signal Theory
and Communications

Multidimensional and Temporal SAR Data Representation and Processing based on Binary Partition Trees

ABSTRACT

This thesis deals with the processing of different types of multidimensional SAR data for distinct applications. Instead of handling the original pixels of the image, which correspond to very local information and are strongly contaminated by speckle noise, a region-based and multiscale data abstraction is defined, the Binary Partition Tree (BPT). In this representation, each region stands for an homogeneous area of the data, grouping pixels with similar properties and making easier its interpretation and processing. The work presented in this thesis concerns the definition of the BPT structures for Polarimetric SAR (PolSAR) images and also for temporal series of SAR acquisitions. It covers the description of the corresponding data models and the algorithms for BPT construction and its exploitation.

Particular attention has been paid to the speckle filtering application. The proposed technique has proven to achieve arbitrarily large regions over homogeneous areas while also preserving the spatial resolution and the small details of the original data. As a consequence, this approach has demonstrated an improvement in the performance of the target response estimation with respect to other speckle filtering techniques. Moreover, due to the flexibility and convenience of this representation, it has been employed for other applications as scene segmentation and classification.

The processing of SAR time series has also been addressed, proposing different approaches for dealing with the temporal information of the data, resulting into distinct BPT abstractions. These representations have allowed the development of speckle filtering techniques in the spatial and temporal domains and also the improvement and the definition of additional methods for classification and temporal change detection and characterization.

To my beloved Alba.

To my father Fernando and my mother Carmen.

Preface

I would like to express my gratitude to my thesis advisor Carlos López-Martínez for providing me the great opportunity to carry out this project. During all this time, he has turned the course of this thesis into an exciting venture, providing both valuable technical challenge and support. He has allowed and motivated me to the development of my own ideas and interests, while also providing helpful guidance when needed. Through all this time he has been a pleasant colleague rather than a boss.

Thanks must also go to Philippe Salembier, for the valuable support provided along the development of this thesis. Moreover, I have to admit that he awakened my interest in signal and image processing during the studies and, consequently, this thesis could not be possible without his engaging lectures. Additionally, I would like also to thank Jordi Mallorqui, for his support at the beginning of this project, and Juan M. Lopez-Sanchez and Florence Tupin for their review of the document.

During this time some people have contributed to make all the work more bearable and pleasant. In this regard, I really appreciate the company of the *SAR coffee group* and I am very grateful for having colleagues and friends like Alberto, Dani, Giuseppe, Rubén and Alba. I would also like to thank Eduard and Marc for the many enjoyable Thursday *tapas route* that we have shared all together.

Special thanks to my loved Alba, for being by my side during all this journey and supporting me, for her endless patience whenever I started to speak in math or other strange languages and for all the moments we have shared together, that have enabled me to complete this work. I have to mention also the warmth company provided by Zener, which has been able to draw a smile in our faces at any time.

Finally, I want to thank my beloved family, Fernando, Carmen and Carlos for always being there and providing unconditional support during all this period of time.

Alberto Alonso-González
Barcelona, April 2014

Acknowledgments

I would like to acknowledge the following institutions

- Agència de Gestió d'Ajuts Universitaris i de Recerca (AGAUR) and the CUR of the DIUE of the Autonomous Government of Catalonia and the European Social Fund for providing financial support through the FI-DGR pre-doctoral fellowship program for the development of this thesis.
- CICYT (Comisión Interministerial de Ciencia y Tecnología) for providing support to part of the research performed in the frame of this thesis, under the MICINN TEC project MUSEO (TEC2011-28201-C02-01).
- DLR (Deutsches Zentrum für Luft- und Raumfahrt) for providing the ESAR and FSAR data, the European Space Agency (ESA) for the Flevoland data, through the AgriSAR 2009 campaign, and the MDA through the project SOAR-EU 6779 for providing the Barcelona dataset.

Contents

List of Figures

List of Tables

If you knew what you are doing, it wouldn't be called research.

Albert Einstein

1

Introduction

REMOTE SENSING allows the extraction of information about a distant object or phenomenon without having direct contact with it. This may be achieved thanks to the interaction with the matter of some type of propagated signal as, for instance, electromagnetic waves or also sonic waves. Human beings and many other types of animals may achieve this aim though their senses of sight, hearing or smell. However, they provide a limited amount of information that rapidly became insufficient to our natural human curiosity, resulting in the emergence of a large number of technologies devoted to gather additional data from our environment. Nowadays, the term remote sensing generally refers to a wide set of techniques dedicated to collect information about different Earth features and their dynamics. This concept comprises the whole process of acquisition, processing and interpretation of the data.

The visibility and attraction of remote sensing technologies has experienced an exponential growth in the latest years, specially through its ability to gather information about the Earth from the space at global scales employing sensors on board satellites or spaceships. Remote sensing can be very helpful to many fields of great interest today as, for instance, map generation, cartography and digital terrain models generation, but the amount of information that can be extracted does not end here and constantly new applications are appearing. Currently, remote sensing techniques are employed to perform weather and ocean forecasting, to predict natural disasters, for biological and biophysical monitoring, etc. Moreover, it is also possible to monitor the environmental effects produced by the human beings as the evolution of the urban areas, forest inventory information and biomass measures, desertification control, climate change, etc. The global concern about this matter is illustrated by the Kyoto Protocol to the United Nations Framework Convention on Climate Change, intended to prevent dangerous human-induced interferences to the climate system [107].

Different criteria may be employed to classify the distinct technologies employed in Earth remote sensing. On the one hand, they may be categorized depending on the electromagnetic source employed for illumination. Accordingly, those systems having their own illumination source are also called *active systems*, while others systems that just measure the radiation emitted or reflected by the target from an external source, are called *passive systems*. On the other hand, another classification may be performed according to the electromagnetic spectrum range employed as, for instance, microwave, infrared or optical systems. According to this categorization, this thesis deals with Synthetic Aperture Radar (SAR) systems or imaging radars, which may be classified as active systems working at microwave frequencies.

The origin of the SAR technology dates from the beginning of the '50s, when an important improvement in the spatial resolution of the radars was achieved in the flight direction through a coherent registration and processing of the returned radar echoes [111]. SAR systems, thus, employ the relative motion of the platform on which they are mounted on in order to regularly record a set of observations of the scene at different positions. These measurements are coherently processed together in order to simulate the acquisition of a larger virtual antenna array, the *synthetic aperture*, resulting into a substantial increase in the radar resolution in the azimuth direction. The SAR sensors have become more popular over the years since they can produce reflectivity images of the scene, which may attain up to planetary coverage when mounted on board a satellite platform, while presenting a high spatial resolution. Moreover, the data acquired by SAR systems are almost independent of most of the weather conditions and the night and day cycles, thanks to the fact that they are active sensors operating at the microwave frequencies, for which the atmosphere is almost transparent. Formerly, SAR systems only operated at one frequency and polarization but, since then, the technology has evolved greatly with the introduction of multidimensional sensors. These sensors are capable of acquiring simultaneously different images of the scene by changing some parameter (frequency, polarization, spatial position, etc), which has empowered the emergence of the SAR polarimetry and interferometry technologies.

The electromagnetic waves polarization makes reference to the vectorial nature of the electric and magnetic fields [21]. This nature allows the generation of waves having the electric field moving over different planes and, consequently, presenting a different interaction with the targets depending in their physical structure [123]. Polarimetric SAR systems (PolSAR) obtain multidimensional images by combining different polarizations of the incident and reflected waves [33]. PolSAR has demonstrated, specially during the last decade, its usefulness for the study and characterization of the Earth surface, due to its ability to retrieve biophysical and geophysical information from the scene [76][49]. This thesis has been developed in the context of polarimetric SAR data processing, analysis and characterization. Indeed, nowadays there is a great interest on PolSAR technology, which may be deduced by the large number of future space-borne polarimetric SAR missions planed, like SENTINEL-1 (C-band), BIOMASS (P-band), ALOS 2 (L-band), RADARSAT Constellation Mission (RCM) (C-band), NOVASAR-S (S-band), SAOCOM (L-band) and the PAZ together with TerraSAR-X and TanDEM-X (X-band).

In most of the cases in SAR systems, the size of the resolution cell is much larger than the wavelength and, thus, the measured echo is, under the Born approximation [58], a coherent combination of all the individual target echoes within that cell. This coherent combination may be constructive or destructive, and it appears over the SAR images with a characteristic granularity known as *speckle* [40][102]. Although the speckle is real electromagnetic measure, from the point of view of the acquisition system it is considered as noise, since it can not be predicted accurately and is contaminating the measure of the reflectivity of the resolution cell. The useful information, then, must be extracted from the statistics of the data [73].

There are a wide number of techniques to extract these statistics and eliminate, as far as possible, the contaminant effect of the speckle term in SAR images. The most basic technique is to average the image values over the image using a particular window, usually a rectangular window, which is also known as the multilook filter [119]. In fact, this estimation corresponds to the Maximum Likelihood Estimator (MLE) of the reflectivity [56]. Then, by applying the multilook, the reduction factor of the speckle is proportional to the number of samples averaged and inversely proportional to the resulting resolution. In this sense, this filter poses a significant inconvenience, since it implies a spatial resolution loss which is one of the most valuable advantages of the SAR systems.

Newer speckle filtering techniques are focused towards a different direction. Statistically it makes only sense to consider pixels over the image belonging to the same statistical distribution, that is, over homogeneous areas. Some speckle filtering techniques, as the adaptive Lee filter [74][80], proposed the adaptation of the averaging window to the morphology of the image. To do so, a set of predefined windows are defined and the one containing the more homogeneous sample set is selected for filtering. The Intensity Driven Adaptive Neighborhood (IDAN) filter [125] improves the adaptation capability by defining an arbitrary homogeneous neighborhood around each pixel. However they have some limitations in the amount of possible spatial structure adaptation, resulting into some degree of spatial resolution loss, or they introduce some distortion or bias over the estimated data. In order to overcome these limitations, some newer techniques have proposed breaking away with the idea of spatial locality, as the Non-Local means [28][42], in order to further increase the available samples for estimation.

If it were possible to delimit correctly the homogeneous areas over the image, then it would be possible to average only the samples within them, obtaining results with higher quality and also preserving the spatial resolution. Nevertheless, this work may be complex since arbitrary structures of different sizes may be found over the image, as they reflect the complexity of the scene. Different strategies have been developed to tackle with this issue from different points of view. Some examples are the multiresolution representations, such as wavelets [88][115]. However, this approach has clear limitations as it is a linear processing technique, resulting into a limited resolution preservation. On the other hand, non-linear processing techniques may be employed for data segmentation and denoising, as the Markov Random Fields (MRF) models, employed to represent the sample contextual information [85]. The main difficulty of MRF is that its computational complexity rapidly becomes intractable for most models, requiring some approximation techniques.

Moreover, remote sensing techniques are continuously evolving, increasing in terms of data quality and quantity. Very high spatial resolution SAR systems are every day more precise and even they can operate at different frequency bands and/or spatial baselines simultaneously. This fact increases the amount of potential information that may be extracted from the observed scene, but it also involves a dramatic increment in terms of data volume and, consequently, in computational demands for processing it.

There are, however, other implications not so obvious for the exploitation of these large datasets. As the number of collected samples gets increased, the amount of information obtained may not grow in the same proportion, resulting into that neighboring samples may not be considered as independent, as their scale of representation is far too low with respect to the content scale [14]. The classical pixel-based approaches, based on the assumption that each pixel may be processed independently, are becoming less efficient in this scenario, as they are unable to exploit this interrelationship properly.

In this thesis, a different non-linear approach is proposed for data processing, based on the assumption that neighboring samples having similar properties may be modeled and grouped together into an entity named *region*. The pixel-based signal representation is replaced by a region-based representation, composed of a set of regions with lower cardinality. Then, under this assumption, instead of processing each of the original pixels of the data, these obtained regions are processed individually. This concept automatically encompasses the sample interrelationship within these entities and scales naturally to high resolution sensors.

With this idea in mind, the Binary Partition Tree (BPT) [109] image representation was defined with the intention of being generic enough to support a wide range of applications. The BPT is a region-based and multi-scale data abstraction that has been employed for image processing [109], achieving good results, but it needs an adaptation to be able to process and model PolSAR data.

Then, the objectives for this thesis are the design, the implementation and the evaluation of the BPT representation for processing different types of multidimensional SAR data, encompassing PolSAR images and temporal series. This involves the adaptation of the BPT concepts and algorithms for multidimensional SAR data modeling, in order to be able to generate properly their corresponding BPT representation and to perform the consequent BPT exploitation for different applications. In this work, a particular focus is devoted to the speckle filtering and, consequently, this application will be analyzed with a great level of detail. However, other applications are also considered as, for instance, scene segmentation and data classification. The exploitation of the temporal dimension of the data in SAR polarimetry is a difficult task that is now starting to be studied and developed, and this thesis sheds some light in this direction, analyzing the target modeling in the temporal dimension for PolSAR time series. Some approaches are proposed to study the temporal evolution of the data and the scene dynamics. When these approaches are employed in combination with the BPT, the time information allows the improvement of some previously defined methods, as the polarimetric estimation or the classification techniques. Moreover, this supplementary information allows the development of additional applications, such as the detection and characterization of the scene changes.

Structure of the Thesis

This manuscript has been divided into eight different chapters that are described briefly in the following.

The first chapter, as an introduction, puts the reader in position to the scope of this work and its objectives. The second chapter makes a brief description of the basic concepts behind the SAR systems, on which this work is focused on. The wave polarimetry notion is presented and the most relevant concepts of SAR polarimetry (PolSAR) are introduced. In this chapter, special attention is paid to the statistics of SAR and PolSAR data, particularly the polarimetric Gaussian model to describe the distributed scattering mechanism. The Entropy (H), Anisotropy (A) and averaged Alpha angle ($\bar{\alpha}$) polarimetric decomposition is also described as a tool for the interpretation of the polarimetric information. The central application of this thesis is speckle filtering and, consequently, this chapter also describes and briefly analyzes some relevant multidimensional speckle filtering techniques, as the adaptive Lee [74][80] or the IDAN [125] filters. Finally, some polarimetric classification techniques are also described, as it composes other of the applications developed during the course of this thesis.

Chapter 3 describes the Binary Partition Tree (BPT), which is the data abstraction employed in this work for data processing. Its structure is defined in detail, including the rationale and the motivation for this representation, and a generic BPT based processing scheme is proposed. The algorithms for its construction and exploitation are defined and analyzed in this chapter. For the generation of the BPT structure an efficient iterative method in a bottom-up approach has been proposed, based on the divide and conquer strategy. Once it has been constructed, a tree pruning mechanism is performed for its exploitation, which may be interpreted as the extraction of the useful or interesting regions for a particular application. Finally, an analysis of the processing complexity is briefly described and some additional thoughts are provided on the BPT limitations as a data abstraction.

The generic BPT processing scheme previously depicted is adapted to process PolSAR data in Chapter 4. A statistical region model is proposed for this data, based on the sample covariance matrix. For the BPT construction algorithm, some dissimilarity measures are defined in this region model space, some of them being capable of exploiting the whole polarimetric information under the Gaussian hypothesis. Distinct BPT pruning strategies are defined to exploit this structure for the speckle filtering application. As it corresponds to the central application of this thesis, an extensive analysis of this application may be found in this chapter, including studies with real and simulated PolSAR data. Additionally, the coastline detection application based on the BPT is briefly described and analyzed, in order to give a wider idea of the usefulness of this representation for PolSAR data processing.

This thesis also deals with another type of multidimensional data: temporal series. The BPT based processing approach is extended to process PolSAR time series in Chapter 5. The processing of these datasets is still a challenge that is now starting to be developed. Then, this chapter describes two different approaches for dealing with the temporal dimension of the data. These approaches differ in the way a target is characterized among this additional dimension. Two distinct BPT representations are obtained according to these two concepts which are studied in this chapter. The exploitation of these two structures is also defined by an extension of the same techniques employed for PolSAR data in the context of the speckle filtering application.

Additionally, an additional application is developed specifically to exploit the temporal information and describe the dynamics of the scene: change detection and characterization. These applications are analyzed and evaluated with real PolSAR datasets over urban and agricultural areas.

Some of the previously detected limitations in various aspects of the proposed BPT based processing scheme are addressed in Chapter 6. To overcome these drawbacks, a technique is proposed for filtering and matrix regularization and some concepts are defined for the polarimetric change analysis and interpretation. Additionally, a new region model is proposed in order to improve the characterization of heterogeneous regions, including a mixture of different targets or texture. Moreover, all these proposed improvements are defined in terms of the same concepts on which the BPT is based, contributing to the completeness of this approach.

Chapter 7 is devoted to the BPT based classification application. Supervised and unsupervised classification methods over PolSAR images and polarimetric time series are proposed, employing the same models and dissimilarity measures previously mentioned in Chapters 4 to 6. Consequently, this chapter also contributes to the analysis and evaluation of the these concepts, from a different point of view. The performance of the proposed classification techniques is evaluated with real PolSAR time series data for which some ground truth information is available, in order to verify the ability of these approaches to identify and separate the distinct areas of the scene.

Finally, Chapter 8 presents the most relevant conclusions after the research work performed during the course of this thesis and some possible future research lines are outlined.

Additionally, in the Appendix A, a complementary analysis of the stability in front of the speckle noise of the sample covariance matrix eigenvectors, eigenvalues, and the Entropy (H), Anisotropy (A) and averaged Alpha angle ($\bar{\alpha}$) parameters may be found. This analysis is based on the employment of the matrix perturbation theory [129] in order to model the estimation errors due to speckle [91]. Appendix B presents some additional results that have not been analyzed in as much detail as the other results in the previous chapters, but they may serve to demonstrate the usefulness of the BPT to process other types of data as L-band ALOS data, very high resolution X-band FSAR data or dual-polarimetric TerraSAR-X time series. Finally, a compilation of all the publications carried out during the course of this thesis may be found in Appendix C.

If you can't explain it to a six years old, you don't understand it yourself.

Albert Einstein

2

Multidimensional Synthetic Aperture Radar

This chapter is intended to give a general introduction of the Synthetic Aperture Radar (SAR) framework on which this PhD thesis is developed. It does not aim to be an exhaustive review of SAR state-of-the-art, but a brief review of the general concepts involved in this work, in order to produce a self-contained manuscript.

First, in Section 2.1, the basic concepts of SAR are introduced, devoting special attention to data description and statistics. On Section 2.2 electromagnetic wave polarimetry is introduced and its application to radar and SAR is described. The statistical analysis of the previous section is also extended to the multidimensional systems. Additionally, some additional information is included on the interpretation of the polarimetric SAR radar response.

Finally, Sections 2.3 and 2.4 are devoted to describe some state-of-the-art techniques for two particular applications that are strongly related with this work: speckle filtering and data classification.

2.1 SYNTHETIC APERTURE RADAR

A SAR system is a type of remote sensing imaging sensor capable of obtaining high resolution information about the scene. Specifically, SAR measures the complex reflectivity of the scene at the microwave region of the spectrum. The most salient feature of SAR, with respect to other remote sensing sensors, as optical imaging, is that it is an *active sensor*, in the sense that it produces its own source of illumination. This, in combination with the fact that the atmosphere may be considered almost transparent at microwave frequencies, makes SAR independent of most of the atmospheric effects, as the night and day cycles and the weather conditions. Moreover, since they are working at microwave frequencies, they are sensitive to different target properties than other techniques, working at distinct frequencies. As a consequence, SAR is a valuable complement to other remote sensing methods.

2.1.1 BASIC CONCEPTS

Typically, on a radar system, a pulse is transmitted as an electromagnetic wave by means of an antenna. When this pulse hits a target, a fraction of the power associated with the pulse is reradiated towards the receiver, which is also known as *radar echo*. This echo may be captured by the receiver antenna, where it may be detected and processed.

On SAR systems, a high resolution reflectivity image of the scene is obtained by means of a coherent processing of different radar echoes obtained at distinct positions. Consequently, SAR systems are typically on board a moving platform, usually an airplane or a satellite. In this context, the *azimuth* direction is defined as the flight direction, which defines the movement of the radar. The radar beam is slanted from the nadir direction to a direction perpendicular to the flight direction, known as *range* direction. The thickness of the strip generated by the footprint of antenna beam due to the radar movement is referred to as *swath*, as represented on Fig. 2.1

In an imaging system, the resolution δ may be seen as the minimum separation of two targets to be detected and distinguished as two different targets at different positions. SAR systems, as two dimensional imaging systems, may present different resolution values for the range δ_r and the azimuth δ_a dimensions. In the range dimension the resolution is closely related with the pulse duration τ_p, requiring a shorter pulse in order to obtain a better resolution

$$\delta_r = c\frac{\tau_p}{2} \tag{2.1}$$

where c stands for the propagation speed of the electromagnetic waves in vacuum.

However, to attain both a good level of Signal to Noise Ratio (SNR) and a good resolution,

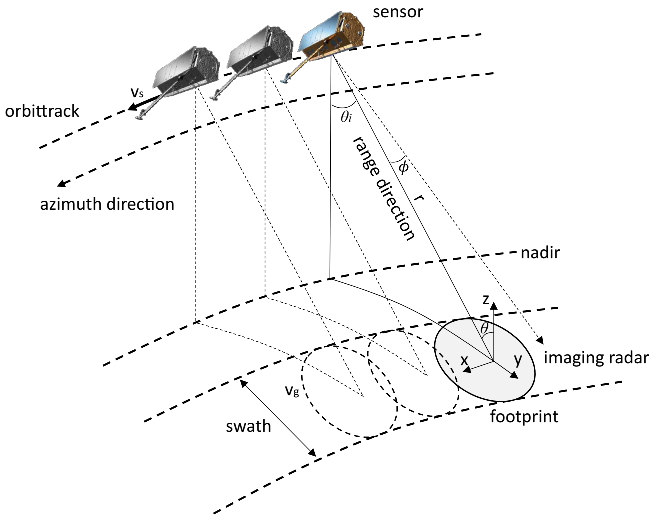

Figure 2.1: Synthetic aperture radar acquisition geometry.

a large amount of energy has to be transmitted in a short period of time. This approximation is not practical as real transmitters are not able to produce short pulses having high energy at the same time. Alternatively, a *pulse compression* technique may be applied to solve this problem. It is based on transmitting a long modulated pulse and processing it afterwards by a matched filter [31][122]. With this technique, the large pulse may be compressed to a duration equivalent to $1/B$

$$\delta_r = \frac{c}{2B} \tag{2.2}$$

where B represents the bandwidth of the transmitted pulse.

In the azimuth direction, the radar resolution depends on the antenna angular beam width θ_a, which is proportional to

$$\theta_a \propto \frac{\lambda}{D_a} \tag{2.3}$$

where λ refers to wavelength and D_a is the antenna length in the azimuth direction. As a consequence, the resolution in the azimuth direction δ_a will be

$$\delta_a = r_0 \frac{\lambda}{2D_a} \tag{2.4}$$

where r_0 represents the range distance between the antenna and the target. Note that for radars on board a satellite platform, good azimuth resolution, in the order of meters, can only be obtained with very large antennas, in the order of kilometers length in the azimuth direction, which is completely unfeasible.

In order to increase the resolution in the azimuth direction, the concept of *synthetic aperture* may be applied [40][27][48]. Not surprisingly, this concept is applied in SAR to exploit the movement of the platform in order to synthesize an antenna array with an effective length much larger than the physical length of the receiver antenna. The synthetic antenna is conformed by a linear array, following the path of the moving platform, where each element of this array is the original antenna.

Consequently, when employing the synthetic aperture concept, the angular beam width θ_{sa} of the corresponding synthetic antenna will be proportional to the length of this antenna L_e. Then, the obtained azimuth resolution with synthetic aperture radar δ_{sa} will be

$$\delta_{sa} = r_0 \frac{\lambda}{2L_e}. \tag{2.5}$$

Note that the maximum length of the synthetic aperture L_e is bounded by the set of positions on which the same target gets illuminated by the antenna beam. Therefore, it depends on the beam width of the original antenna θ_a, which depends on its azimuth dimension D_a, and on the distance to the target r_0

$$L_e < \frac{\lambda r_o}{D_a}. \tag{2.6}$$

This bound on the maximum length of the synthetic aperture also defines a limit on the azimuth resolution $\delta_{sa_{max}}$ that may be achieved with this technique

$$\delta_{sa_{max}} = \frac{D_a}{2}. \tag{2.7}$$

It is worth noticing that, for a SAR system, the attainable azimuth resolution δ_a does not depend neither on the distance to the target r_0 nor the wavelength λ. This maximum azimuth resolution only depends on the antenna size in the azimuth dimension D_a and, as a consequence, the smaller the antenna the higher the resolution. This surprising result is caused by the fact that, the smaller the antenna, the larger is the angular beam width θ_a, and also the time on which the target is illuminated by the antenna is enlarged, making possible a larger synthetic aperture. The same idea can be applied to the distance to the target r_0, having larger synthetic apertures for further targets. In practice, some limitations apply, specially those related to the achieved SNR, since a smaller antenna implies a smaller received pulse energy. However, spatial resolutions in the order of meters or even smaller have been achieved from space-borne SAR systems.

2.1.2 SAR System Impulse Response

During the data acquisition process of a SAR system, the received echo for each transmitted radar pulse at each position is recorded. This data are referred to as *raw data* and can not be directly related with the reflectivity of the scene. On raw data, the information of each scene target is spread among all the echoes that conform the synthetic aperture. In order to obtain the radar reflectivity of the scene, the information of each target may be effectively combined in the so-called *focusing* process, resulting in a reflectivity image of the scene.

For a good understanding and characterization of the SAR imaging system, the impulse response of the system must be known, that is, the response of the system to a single point target, including both processes: the data acquisition and the image focusing process. On this simplified scenario, having only one target at a given location, is assumed to be present on the scene, which will produce only one radar echo. Once this impulse response has been characterized, the complete image of the scene may be understood as a combination of the contributions of an arbitrary number of single targets, considering the superposition theorem.

The complex SAR image obtained after the acquisition and focusing processes for a point target at coordinates (x_0, r_0) is [40]

$$S(x,r) = \sigma_s(x_0, r_0) \cdot \exp\left(j\frac{4\pi}{\lambda}(r - r_0)\right) \cdot \operatorname{sinc}\left(\frac{\pi(r - r_0)}{\delta_r}\right) \cdot \operatorname{sinc}\left(\frac{\pi(x - x_0)}{\delta_a}\right) \tag{2.8}$$

where $\sigma_s(x_0, r_0)$ refers to the complex Radar Cross Section (RCS) of the target [112][30][124] and δ_r and δ_a represent the range and azimuth resolution, respectively. From (2.8), it can be seen that the SAR system impulse response, including the acquisition and focusing stages, is proportional to a phase term multiplied by two sinc functions

$$h(x,r) \propto \exp\left(j\frac{4\pi}{\lambda}r\right) \cdot \operatorname{sinc}\left(\frac{\pi r}{\delta_r}\right) \cdot \operatorname{sinc}\left(\frac{\pi x}{\delta_a}\right). \tag{2.9}$$

Then, from (2.9), the impulse response of the SAR system can be seen as a rectangular filter with a bandwidth in the range dimension equal to $2B/c$ and $2/D_a$ in the azimuth direction [40][52][84]. Additionally, from (2.9) the phase term associated with the range delay can be related to the scene, instead of to the SAR system, resulting in an impulse response proportional to

$$h(x,r) \propto \operatorname{sinc}\left(\frac{\pi r}{\delta_r}\right) \cdot \operatorname{sinc}\left(\frac{\pi x}{\delta_a}\right). \tag{2.10}$$

2.1.3 SAR Image Statistics

Once the SAR system impulse response has been described, as stated in (2.10), it may be seen as a low pass filter over the scene radar reflectivity. However, in the previous section only one point target has been assumed. Nevertheless, in a real situation, many targets may be found over the scene. Then, the concept of *resolution cell* may be introduced tightly related with this interpretation of the impulse response. It may be seen as the area within a cell of size δ_r by δ_r in range and azimuth dimensions, respectively. Note that, according to the previous definition of the resolution notion, all the targets within this area may not be distinguished by the radar. Typically, the azimuth and range resolution are significantly larger than the wavelength λ and, as a consequence, many individual or point targets may be present within the resolution cell, as represented on Fig. 2.2.

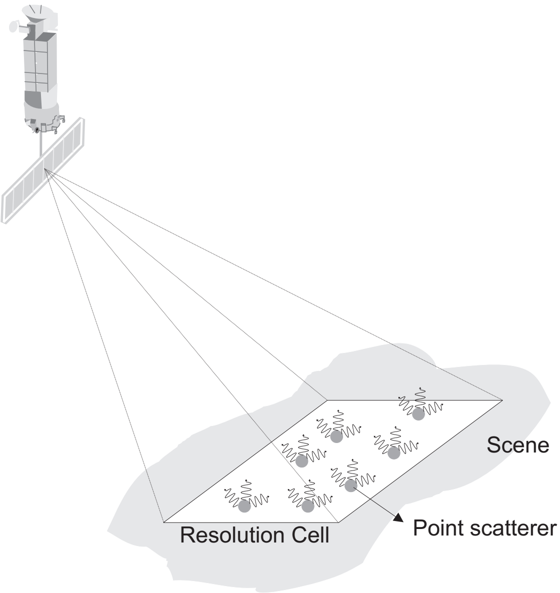

Figure 2.2: Resolution cell representation having multiple individual targets within.

In this scenario, the retrieved signal is the coherent combination of all the echoes of the individual targets within the resolution cell, which has been represented on Fig. 2.3. The amplitude and phase of each target may depend on the targets themselves and also on their orientation and distribution within the resolution cell. This complex coherent sum for a given resolution cell, represented as $r\exp(j\theta)$ is also known as the random walk, and may be expressed as [95][44]

$$r\exp(j\theta) = \sum_{k=1}^{N} A_k \exp(j\theta_k) \tag{2.11}$$

$$\Re\{S\} = \sum_{k=1}^{N} A_k \cos(j\theta_k) \tag{2.12}$$

$$\Im\{S\} = \sum_{k=1}^{N} A_k \sin(j\theta_k) \tag{2.13}$$

where N represents the number of targets within the resolution cell and $\Re\{\cdot\}$ and $\Im\{\cdot\}$ represent the real and imaginary part, respectively.

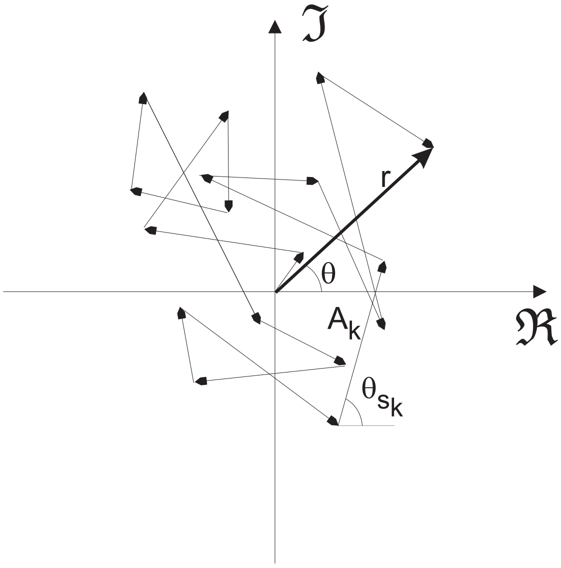

Figure 2.3: The received echo for a resolution cell is the coherent combination of the echoes of the individual targets within this cell.

Unfortunately, most of geophysical terrains as, for instance, rough surfaces, vegetation, ice, snow, etc... have a very complicated structure and composition. In such cases, the complete knowledge of the scattered electromagnetic field, when illuminated by an incident wave, is only possible with a complete description of the terrain geometry and composition. In practical situations, this type of information is completely unattainable for obvious reasons. Then, the characterization of this reflection processes may only be performed through a statistical analysis [124] [93][101]. Since these targets are composed by a large number of individual targets distributed around the resolution cell, they are called *distributed targets*, as opposite to point targets, as suggested in Section 2.1.2.

For the statistical characterization of the complex SAR image $S(x, r)$, some considerations are taken into account related to the elementary targets $A_k \exp(j\theta_k)$ [23][59]:

- The amplitude A_k and phase θ_k of the k-th phasor are statistically independent from each other and from the other phasors. This means that the scattering center of the elemental targets are uncorrelated and that the amplitude is not dependent on the phase.

- The phase of each one of the individual targets are uniformly distributed in the interval $(-\pi, \pi]$. This may also be interpreted as having all the individual targets uniformly distributed within the resolution cell.

Additionally, if the resolution is much larger than the wavelength, that is, $\delta_r \gg \lambda$ and $\delta_a \gg \lambda$, then the Central Limit Theorem [104] may be assumed as $N \to \infty$. Under this assumption $\Re\{S\}$ and $\Im\{S\}$ are following a zero-mean Gaussian distribution [23][59][104][58].

$$E\{\Re\{S\}\} = \sum_{k=1}^{N} E\{A_k \cos(\theta_k)\} = \sum_{k=1}^{N} E\{A_k\}E\{\cos(\theta_k)\} = 0 \tag{2.14}$$

$$E\{\Im\{S\}\} = \sum_{k=1}^{N} E\{A_k \sin(\theta_k)\} = \sum_{k=1}^{N} E\{A_k\}E\{\sin(\theta_k)\} = 0 \tag{2.15}$$

where $E\{\cdot\}$ refers to the statistical expectation operator. Similarly, the variance of $\Re\{S\}$ and $\Im\{S\}$ may also be computed

$$E\{\Re^2\{S\}\} = \sum_{k=1}^{N} E\{A_k^2\}E\{\cos^2(\theta_k)\} = \frac{N}{2}E\{A_k^2\} \tag{2.16}$$

$$E\{\Im^2\{S\}\} = \sum_{k=1}^{N} E\{A_k^2\}E\{\sin^2(\theta_k)\} = \frac{N}{2}E\{A_k^2\}. \tag{2.17}$$

The real and imaginary parts of S are uncorrelated

$$E\{\Re\{S\}\Im\{S\}\} = \sum_{k=1}^{N}\sum_{l=1}^{N} E\{A_k A_l\}E\{\cos(\theta_k)\sin(\theta_l)\} = 0. \tag{2.18}$$

To simplify the notation, $\Re\{S\}$ may be renamed to x and $\Im\{S\}$ to y; then, their probability density functions can be expressed as

$$p_x(x) = \frac{1}{\sqrt{\pi\sigma^2}} \exp\left(-\left(\frac{x}{\sigma}\right)^2\right) \qquad x \in (-\infty, \infty) \tag{2.19}$$

$$p_y(y) = \frac{1}{\sqrt{\pi\sigma^2}} \exp\left(-\left(\frac{y}{\sigma}\right)^2\right) \qquad y \in (-\infty, \infty) \tag{2.20}$$

where $\sigma^2/2 = (N/2)E\{A_k^2\}$. As it may be seen, $p(x)$ and $p(y)$ are following a zero-mean Gaussian distribution, also expressed as $\mathcal{N}(0, \sigma^2/2)$.

The probability density function of the amplitude $p_r(r)$ and phase $p_\theta(\theta)$, considering $r = \sqrt{x^2 + y^2}$ and $\theta = \arctan(y/x)$, can also be obtained

$$p_{r,\theta}(r, \theta) = \frac{2r}{2\pi\sigma^2} \exp\left(\frac{-r^2}{\sigma^2}\right) \tag{2.21}$$

$$p_r(r) = \frac{2r}{\sigma^2} \exp\left(\frac{-r^2}{\sigma^2}\right) \qquad r \in [0, \infty) \tag{2.22}$$

$$p_\theta(\theta) = \frac{1}{2\pi} \qquad \theta \in (-\pi, \pi]. \tag{2.23}$$

As it can be seen, the amplitude and phase distribution are separable. The distribution $p_r(r)$ is also referred to as a Rayleigh distribution, whereas $p_\theta(\theta)$ is a uniform distribution in $(-\pi, \pi]$. This means that the phase θ of a distributed target has no information about the target itself. For a Rayleigh distribution, like $p_r(r)$, the mean value and its variance are

$$E\{r\} = \frac{\sqrt{\pi\sigma^2}}{2} \tag{2.24}$$

$$\sigma_r^2 = \left(1 - \frac{\pi}{4}\right)\sigma^2. \tag{2.25}$$

Another statistical parameter usually employed in SAR is the coefficient of variation (CV), defined as the relation between the standard deviation and the mean [102]. From the previously defined expressions, it can be derived as $\sqrt{\frac{4}{\pi} - 1}$ for r.

Generally, the study of SAR data is interested in the intensity I, rather than the amplitude r, defined as $I = r^2$, which pdf can be expressed as

$$p_I(I) = \frac{1}{\sigma^2} \exp\left(\frac{-I}{\sigma^2}\right) \qquad I \in [0, \infty) \tag{2.26}$$

and consequently, I is following an exponential distribution. Therefore, its mean value will be $E\{I\} = \sigma^2$ and its variance $\sigma_I^2 = \sigma^4$. It is worth to mention that the CV of the intensity for a SAR image, then, will be equal to 1.

2.1.4 MULTIPLICATIVE MODEL FOR SAR SPECKLE NOISE

As indicated in (2.26), the probability density function of the SAR image intensity has been identified as an exponential distribution. For simplicity, the identity

$$I = \sigma^2 z \tag{2.27}$$

may be introduced on (2.26) and, then, the distribution of $p_z(z)$ may be expressed as

$$p_z(z) = \exp(-z) \qquad z \in [0, \infty). \tag{2.28}$$

Equation (2.27) shows that the intensity of a SAR image pixel can be considered as a deterministic value, containing information about the incoherent reflected power (σ^2), multiplied by the *speckle noise* (z), having an exponential distribution, as expressed in (2.28), with mean and variance values equal to one. This is one of the main reasons why the speckle noise is usually considered as a multiplicative noise respect to the SAR image intensity [58][73][87][40]. It should be noted however that the speckle noise is not a random process, as it is an electromagnetic measure of the interactions of all the individual targets. Nevertheless, due to the complexity of the reflection process, it can not be predicted for a given pixel and then, it is interpreted as a random process corrupting the deterministic component σ^2.

With the previous assumptions, all the useful information about the scene reflectivity is contained within the term σ^2, and the phase has no information, as stated before. Then, the SAR image $S(x, r)$ can be described over an homogeneous area as

$$S(x, r) = \sigma n \exp(j\theta) \tag{2.29}$$

where n denotes the multiplicative component of the speckle noise in amplitude, following an exponential distribution and characterized by $E\{n\} = 1$ and $\mathrm{var}\{n\} = 1$. On the other hand, the phase θ is following a uniform distribution, as mentioned before. Then the useful information about the scene is contained in σ, independently of the speckle noise term $n \exp(j\theta)$.

2.2 SAR POLARIMETRY

Polarimetric SAR (PolSAR) systems are multidimensional SAR systems that may obtain additional information about the scene by exploiting the vectorial nature of the electromagnetic waves. This vectorial nature may be employed to imbue different polarizations on the transmitted and received echoes that interact in a different manner with the targets on the scene. As a consequence PolSAR sensors will acquire different SAR images or channels according to the different polarization states of transmitted and received radar echoes. Moreover, if two orthogonal polarization states are employed for transmission and reception, the *polarization synthesis* [24] may be applied in order to explore the target response at any other polarizations state, conforming a valuable source of information.

2.2.1 WAVE POLARIMETRY

Electromagnetic waves were firstly postulated by James Clerck Maxwell as a solution to the Maxwell equations, and subsequently confirmed by Heinrich Hertz. This solution may be extracted from the electric and magnetic equations, representing the energy transportation from one plane to another [21]. Employing the classical Cartesian coordinates $[\hat{\mathbf{x}}, \hat{\mathbf{y}}, \hat{\mathbf{z}}]$ to describe the electric field of a wave propagating on the $\hat{\mathbf{z}}$ direction, it can be obtained as

$$\vec{E}(\vec{z}, t) = E_x(\vec{z}, t)\hat{\mathbf{x}} + E_y(\vec{z}, t)\hat{\mathbf{y}} = E_{0x}\cos(wt - kz - \delta_x)\hat{\mathbf{x}} + E_{0y}\cos(wt - kz - \delta_y)\hat{\mathbf{y}} \quad (2.30)$$

where δ_x and δ_y are two constant phase terms, E_{0x} and E_{0y} represent the electric field amplitude at directions $\hat{\mathbf{x}}$ and $\hat{\mathbf{y}}$ and k is defined as

$$k = 2\frac{\pi}{\lambda} = \frac{w}{c}. \quad (2.31)$$

For compactness, the expression in (2.30) may also be expressed in the vectorial form

$$\vec{E}(\vec{z}, t) = \begin{bmatrix} E_x \\ E_y \end{bmatrix} = \begin{bmatrix} E_{0x}\cos(wt - kz - \delta_x) \\ E_{0y}\cos(wt - kz - \delta_y) \end{bmatrix}. \quad (2.32)$$

The components E_x and E_y are related through the expression

$$\left(\frac{E_x}{E_{0x}}\right)^2 + \left(\frac{E_y}{E_{0y}}\right)^2 - 2\frac{E_x E_y}{E_{0x}E_{0y}} = \sin^2(\delta) \quad (2.33)$$

where $\delta = \delta_x - \delta_y$.

The previous expression (2.33) defines the geometric figure described by the electric field vector $\vec{E}(\vec{z}, t)$ along the temporal dimension for any value of z. As it may be seen, this figure, in the most general case, is following the shape of an ellipse, also known as the polarization ellipse. Note that the aspect of this ellipse does not depend neither the space nor the time and, consequently, it is characteristic of the electromagnetic wave. The polarization ellipse and its

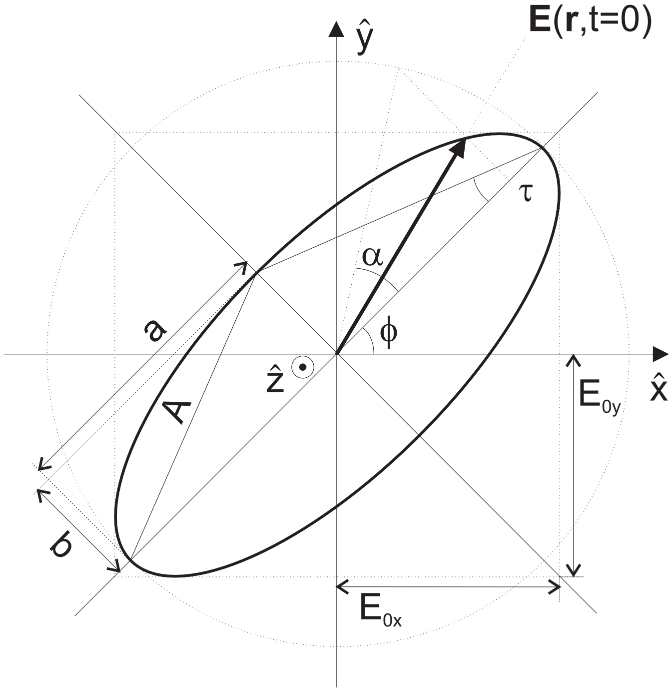

Figure 2.4: Generic polarization ellipse for an electromagnetic wave propagating on $\hat{\mathbf{z}}$ direction.

parameters are represented in Fig. 2.4.

Consequently, the polarization state of an electromagnetic wave can be defined by the following parameters describing its direction of propagation and the polarization ellipse

- Orientation in the space of the plane containing the polarization ellipse. It is determined by its normal vector, which is the propagation direction of the electromagnetic wave. On Fig. 2.4 it has been assumed as $\hat{\mathbf{z}}$.
- Orientation angle ϕ of the major axis of the ellipse with respect to the $\hat{\mathbf{x}}$ direction. The values for this parameters are in the interval $\left[\frac{-\pi}{2}, \frac{\pi}{2}\right]$.
- Ellipticity angle τ, representing the aperture of the ellipse and having values in the interval $\left[\frac{-\pi}{4}, \frac{\pi}{4}\right]$.
- Polarization direction, indicating the turning direction of the polarization ellipse. It is expressed by the sign of the ellipticity τ. It is determined by the IEEE convention; when looking to the wave towards the propagation direction, if the electric field vector is rotating in clockwise direction then $\tau < 0$, if it is rotating counter-clockwise then $\tau > 0$.
- The amplitude of the polarization ellipse A, defined as $A = \sqrt{a^2 + b^2}$, where a and b are the amplitude of the major and minor axis of the ellipse, respectively.

	Linear horizontal	Linear vertical	Circular clockwise	Circular counter-clockwise
ϕ	0	$\frac{\pi}{2}$	$\left[\frac{-\pi}{2}, \frac{\pi}{2}\right]$	$\left[\frac{-\pi}{2}, \frac{\pi}{2}\right]$
τ	0	0	$\frac{-\pi}{4}$	$\frac{\pi}{4}$

Table 2.1: Some typical polarization states and its associated parameters

- The initial phase α with respect to the phase origin for $t = 0$, defined in the interval $(-\pi, \pi]$.

As an example, Table 2.1 shows the values of ϕ and τ defining the polarization ellipse for some typical polarization states.

2.2.2 Scattering Polarimetry

As mentioned before, when an electromagnetic wave encounters an object, part of its energy gets re-radiated towards the radar receiver. The polarization state of the scattered wave would depend on the target and its geometry and, consequently, polarimetry may contribute to the characterization of the target.

In the more general scenario, the SAR system may be considered as a system having two antennas, the transmitting antenna and the receiving antenna, that may be located at different positions. When this is the case, the scattering process is called *bistatic*, whereas when both antennas are placed in the same position, as when the same antenna is employed for transmission and reception, it is called *monostatic*. Additionally, in a bistatic scenario, when the receiver antenna is located behind the target in the same line defined by the transmitter antenna and the target, a particular configuration process is obtained called *forward scattering*.

Consequently, a convention has to be defined for the Cartesian coordinate system $[\hat{\mathbf{x}}, \hat{\mathbf{y}}, \hat{\mathbf{z}}]$ that will be assumed for transmitted and received waves. Generally, the transmitted wave coordinates are defined with respect to the transmitting antenna, whereas the received wave may be expressed in the same coordinates or in those defined by the receiving antenna.

The electric field vector can be completely described by two orthogonal polarization states [103]. In the following, these two orthogonal polarization states will be assumed as the linear horizontal $\hat{\mathbf{h}}$ and linear vertical $\hat{\mathbf{v}}$ polarization states, conforming the polarization basis $\{\hat{\mathbf{h}}, \hat{\mathbf{v}}\}$. Following this notation, the incident electric field may be expressed in terms of two components E_h^i and E_v^i over this basis, and its coordinate system is centered on the transmitting antenna $[\hat{\mathbf{h}}_i, \hat{\mathbf{v}}_i, \hat{\mathbf{k}}_i]$. On the other hand, for the scattered electric field, expressed in terms of the coordinates $[\hat{\mathbf{h}}_s, \hat{\mathbf{v}}_s, \hat{\mathbf{k}}_s]$, there are different conventions depending on the SAR system type. One convention may be the Forward Scattering Alignment (FSA), which employs the same coordinate system than the incident wave for the scattered wave. Another convention, called Backward Scattering Alignment (BSA), defines the scattered wave in terms of the coordinates of the receiving antenna. Fig. 2.5 shows both conventions for the incident and scattered electric waves.

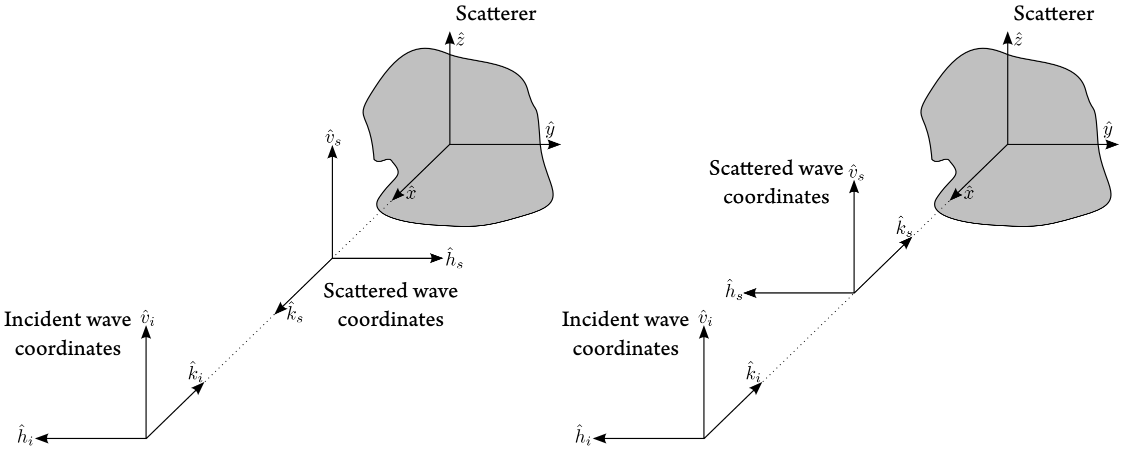

(a) FSA **(b)** BSA

Figure 2.5: Incident and scattered electric field coordinate reference conventions.

As it may be seen, the equivalence of the different conventions can be extracted easily for the incident and scattered electric waves. In the case of the BSA convention $\hat{\mathbf{h}}_s = \hat{\mathbf{h}}_i$, $\hat{\mathbf{v}}_s = \hat{\mathbf{v}}_i$ and $\hat{\mathbf{k}}_s = \hat{\mathbf{k}}_i$, whereas for the FSA convention $\hat{\mathbf{h}}_s = -\hat{\mathbf{h}}_i$, $\hat{\mathbf{v}}_s = \hat{\mathbf{v}}_i$ and $\hat{\mathbf{k}}_s = -\hat{\mathbf{k}}_i$. In the following, the BSA convention will be employed, since the monostatic case is the most common for SAR systems. Employing the selected polarization basis $\{\hat{\mathbf{h}}, \hat{\mathbf{v}}\}$, the incident and scattered waves can be expressed as

$$E^i = E^i_h \hat{\mathbf{h}}_i + E^i_v \hat{\mathbf{v}}_i \tag{2.34}$$

$$E^s = E^s_h \hat{\mathbf{h}}_s + E^s_v \hat{\mathbf{v}}_s. \tag{2.35}$$

The relation between the incident and the scattered waves, assuming the far field hypothesis, may be expressed by the 2 by 2 scattering matrix $\mathbf{S}$. As it is a relation between the two electric fields, $\mathbf{S}$ is a complex dimensionless matrix, which is characteristic of the target [76]

$$\begin{bmatrix} E^s_h \\ E^s_v \end{bmatrix} = \frac{\exp(-jkr)}{r} \begin{bmatrix} S_{hh} & S_{hv} \\ S_{vh} & S_{vv} \end{bmatrix} \begin{bmatrix} E^i_h \\ E^i_v \end{bmatrix} \tag{2.36}$$

or, equivalently, in matrix notation

$$\mathbf{E}^{\mathbf{s}} = \frac{\exp(-jkr)}{r}\mathbf{S}\mathbf{E}^{\mathbf{i}} \tag{2.37}$$

where r represents the distance between the receiver antenna and the target.

In the monostatic case, applying the reciprocity theorem [123][121], the following identity applies

$$S_{vh} = S_{hv} \tag{2.38}$$

for the BSA convention and, consequently, for the FSA convention

$$S_{vh} = -S_{hv}. \tag{2.39}$$

2.2.3 DISTRIBUTED SCATTERING

The scattering matrix **S** defined in (2.36) characterizes the scattering process for the employed acquisition geometry and frequency. However, this information is only useful for point scatterers, as described in Section 2.1.3, having only one dominant scatterer within the resolution cell and, thus, a deterministic response. In general, since the spatial resolution is usually considerably larger than the wavelength, a wide number of targets are present within each resolution cell and the retrieved scattering echo is the coherent combination of their individual responses.

In this case, in the presence of speckle noise, the scattering matrix **S** is a random variable and the target information should be extracted from its statistics. To simplify its manipulation and statistical characterization, usually the matrix **S** is vectorized to form the *scattering vector*, usually denoted as **k**. It may be expressed through a vectorization operator $V(\mathbf{S})$ [26][32]

$$\mathbf{k}_4 = V(\mathbf{S}) = \frac{1}{2}\mathrm{tr}(\mathbf{S}H) = [k_1, k_2, k_3, k_4]^T \tag{2.40}$$

where tr() denotes the matrix trace, ^{T} is the vector transpose and H is a complex 2 by 2 orthogonal matrix base. The simplest matrix base may be the lexicographic base H_L

$$H_L = \left\{ \begin{bmatrix} 2 & 0 \\ 0 & 0 \end{bmatrix}, \begin{bmatrix} 0 & 2 \\ 0 & 0 \end{bmatrix}, \begin{bmatrix} 0 & 0 \\ 2 & 0 \end{bmatrix}, \begin{bmatrix} 0 & 0 \\ 0 & 2 \end{bmatrix} \right\}, \tag{2.41}$$

which ends up with the lexicographic scattering vector $\mathbf{k}_{4L}$

$$\mathbf{k}_{4L} = [S_{hh}, S_{hv}, S_{vh}, S_{vv}]^T. \tag{2.42}$$

Another typical matrix base for the scattering vector is the Pauli base

$$H_P = \left\{ \sqrt{2} \begin{bmatrix} 1 & 0 \\ 0 & 1 \end{bmatrix}, \sqrt{2} \begin{bmatrix} 1 & 0 \\ 0 & -1 \end{bmatrix}, \sqrt{2} \begin{bmatrix} 0 & 1 \\ 1 & 0 \end{bmatrix}, \sqrt{2} \begin{bmatrix} 0 & -j \\ j & 0 \end{bmatrix} \right\}, \tag{2.43}$$

which generates the Pauli scattering vector $\mathbf{k}_{4P}$

$$\mathbf{k}_{4P} = \frac{1}{\sqrt{2}} \left[S_{hh} + S_{vv}, S_{hh} - S_{vv}, S_{hv} + S_{vh}, j(S_{hv} - S_{vh}) \right]^T . \tag{2.44}$$

The advantage of the Pauli scattering vector is that its components may be easily related with the elementary or canonical physical scattering mechanisms. The first component may be related with surface scattering, the second component may be associated with double bounce scattering whereas the third and fourth correspond to volume scattering.

An important property of the scattering process is the total amount of reflected energy in relation with the incident one, expressed as $||\mathbf{S}||$, also known as the *Span*. Note that this is an important attribute for target characterization and, therefore, it should be maintained in the scattering vector as $||\mathbf{k}||$. This is the reason why the constant factors are included in (2.41) and (2.43).

For the monostatic case, the previous scattering vectors may be simplified according to (2.38) or (2.39), depending on the convention employed. In this situation, the scattering vectors contain only three complex components and, then, it will be denoted as $\mathbf{k}_3$. Assuming the BSA convention, these two simplified scattering vectors may be expressed as

$$\mathbf{k}_{3L} = \left[S_{hh}, \sqrt{2} S_{hv}, S_{vv} \right]^T \tag{2.45}$$

$$\mathbf{k}_{3P} = \frac{1}{\sqrt{2}} \left[S_{hh} + S_{vv}, S_{hh} - S_{vv}, 2S_{hv}) \right]^T . \tag{2.46}$$

As mentioned in Section 2.2.3, the scattering matrix is only useful to characterize point scatterers that have a deterministic response. For distributed scattering, the target information has to be extracted from the statistics of this matrix. Then, the scattering vector $\mathbf{k}$, defined as a vectorization of the scattering matrix, may help to simplify this statistical characterization.

A polarimetric SAR system measures all the elements of the scattering matrix for each resolution cell. The $\mathbf{S}$ matrix, then, may be considered as 4 individual SAR images, corresponding to the scattering measurement at each combination of polarization states. As mentioned in Section 2.1.3, for a distributed scattering scenario, each one of these images will be following a zero-mean complex Gaussian distribution. However, the ability of a PolSAR system to measure all this information simultaneously and coherently allows the exploitation of an additional source of information: the correlation between the different SAR images.

Then, for distributed targets the scattering vector $\mathbf{k}$ may be defined by a multidimensional zero mean complex Gaussian distribution. This distribution is characterized by its covariance matrix $\mathbf{C}$ [77][117][66]

$$p_{\mathbf{k}}(\mathbf{k}) = \frac{1}{\pi^p |\mathbf{C}|} \exp(-\mathbf{k}^H \mathbf{C}^{-1} \mathbf{k}) \tag{2.47}$$

where p corresponds to the dimension of the scattering vector and ^{H} denotes hermitian transpose of complex vectors and matrices. This distribution may be denoted as $\mathcal{N}(0, \mathbf{C})$ and it is completely characterized by its covariance matrix, as all of its higher statistical moments may be derived from $\mathbf{C}$ [100] [106]. Moreover, this matrix is Hermitian and positive semi-definite [104], and it may be defined as

$$\mathbf{C} = E\{\mathbf{k}_{4L}\mathbf{k}_{4L}^H\} = \begin{bmatrix} E\{S_{hh}S_{hh}^*\} & E\{S_{hh}S_{hv}^*\} & E\{S_{hh}S_{vh}^*\} & E\{S_{hh}S_{vv}^*\} \\ E\{S_{hv}S_{hh}^*\} & E\{S_{hv}S_{hv}^*\} & E\{S_{hv}S_{vh}^*\} & E\{S_{hv}S_{vv}^*\} \\ E\{S_{vh}S_{hh}^*\} & E\{S_{vh}S_{hv}^*\} & E\{S_{vh}S_{vh}^*\} & E\{S_{vh}S_{vv}^*\} \\ E\{S_{vv}S_{hh}^*\} & E\{S_{vv}S_{hv}^*\} & E\{S_{vv}S_{vh}^*\} & E\{S_{vv}S_{vv}^*\} \end{bmatrix} \tag{2.48}$$

$$\mathbf{C} = E\{\mathbf{k}_{3L}\mathbf{k}_{3L}^H\} = \begin{bmatrix} E\{S_{hh}S_{hh}^*\} & \sqrt{2}E\{S_{hh}S_{hv}^*\} & E\{S_{hh}S_{vv}^*\} \\ \sqrt{2}E\{S_{hv}S_{hh}^*\} & E\{S_{hv}S_{hv}^*\} & \sqrt{2}E\{S_{hv}S_{vv}^*\} \\ E\{S_{vv}S_{hh}^*\} & \sqrt{2}E\{S_{vv}S_{hv}^*\} & E\{S_{vv}S_{vv}^*\} \end{bmatrix} \tag{2.49}$$

for the bistatic and for the monostatic cases, respectively.

Similarly, the coherence matrix $\mathbf{T}$ may be defined as the covariance matrix of the Pauli scattering vector

$$\mathbf{T} = E\{\mathbf{k}_{4P}\mathbf{k}_{4P}^H\} \tag{2.50}$$

$$\mathbf{T} = E\{\mathbf{k}_{3P}\mathbf{k}_{3P}^H\} \tag{2.51}$$

respectively. Again, the advantage of this coherence matrix is that its values may be related with canonical scattering mechanisms easily. Nevertheless, since the lexicographic scattering vector $\mathbf{k}_{3L}$ and the Pauli vector $\mathbf{k}_{3P}$ represent the same information, expressed in a different polarization basis, the covariance and coherence matrices also contain the same information. In fact, they are related by the following expression [35]

$$\mathbf{T} = \frac{1}{2}\begin{bmatrix} 1 & 0 & 0 & 1 \\ 1 & 0 & 0 & -1 \\ 0 & 1 & 1 & 0 \\ 0 & j & -j & 0 \end{bmatrix} \mathbf{C} \begin{bmatrix} 1 & 1 & 0 & 0 \\ 0 & 0 & 1 & j \\ 0 & 0 & 1 & -j \\ 1 & -1 & 0 & 0 \end{bmatrix}. \tag{2.52}$$

$$\mathbf{T} = \frac{1}{2}\begin{bmatrix} 1 & 0 & 1 \\ 1 & 0 & -1 \\ 0 & \sqrt{2} & 0 \end{bmatrix} \mathbf{C} \begin{bmatrix} 1 & 1 & 0 \\ 0 & 0 & \sqrt{2} \\ 1 & -1 & 0 \end{bmatrix}. \tag{2.53}$$

These matrices contain, in the diagonal elements, the RCS value of the distributed target in the different channels, that is, the retrieved power at each combination of polarization states, but, additionally, in the off-diagonal elements they contain information about the correlation between the different elements of the scattering matrix, that are very useful for the PolSAR data interpretation.

2.2.4 POLSAR DATA STATISTICS

In a distributed target scenario, as stated in the previous section, the useful information of the target scattering process has to be extracted from its statistical characterization. The covariance and coherence matrices have been defined in order to perform this characterization but, in a real situation, these matrices have to be estimated from the data. Usually, the estimation of the covariance matrix is performed by spatial averaging the matrices of n pixels, and is called *multilook*. In the following, the estimated covariance matrix, also known as sample covariance matrix, will be denoted as $\mathbf{Z}$, and can be expressed as [102][77][117][60]

$$\mathbf{Z} = \langle \mathbf{k}\mathbf{k}^H \rangle_n = \frac{1}{n}\sum_{i=1}^{n} \mathbf{k}_i \mathbf{k}_i^H. \tag{2.54}$$

This matrix $\mathbf{Z}$ estimated over n samples is also referred to as *n-look* PolSAR data. Due to the presence of speckle noise in the data, the sample covariance matrix $\mathbf{Z}$ will differ from the ideal covariance matrix $\mathbf{C}$, as defined in (2.48) or (2.49). It is worth to mention that the multilook estimator corresponds to the Maximum Likelihood Estimator (MLE) of the covariance matrix. The number of averaged pixels n also plays an important role here, as a large n value will produce a better estimation of the ideal covariance matrix that characterizes the target [119]. On the other hand, this spatial averaging may also be seen as a low-pass filtering in the spatial dimension resulting, thus, in a spatial resolution loss. More specifically, this averaging only makes sense, from a statistical point of view, over homogeneous samples since spatial stationarity is assumed. When it is performed over non stationary areas, a spatial resolution loss is obtained, as may happen near contours or point scatters. Unfortunately, real data is strongly inhomogeneous, as it reflects the complexity of the scene under observation and, then, a compromise between speckle filtering and spatial resolution loss has to be made when applying the multilook.

Assuming that the scattering vector $\mathbf{k}$ is following a zero-mean complex Gaussian distribution, the probability distribution of the sample covariance matrix $\mathbf{Z}$ can be expressed as a complex Wishart distribution. This distribution is characterized by the true covariance matrix $\mathbf{C}$ and the number of samples averaged n, and may be expressed as $\mathcal{W}(\mathbf{C}, n)$ [60]

$$p_{\mathbf{Z}}(\mathbf{Z}) = \frac{n^{pn}|\mathbf{Z}|^{n-p}}{|\mathbf{C}|^{n}\widetilde{\Gamma}_p(n)} \operatorname{etr}(-n\mathbf{C}^{-1}\mathbf{Z}) \tag{2.55}$$

where $\operatorname{etr}(\mathbf{X})$ is the exponential of the matrix trace and

$$\widetilde{\Gamma}_p(n) = \pi^{\frac{1}{2}p(p-1)} \prod_{i=1}^{p} \Gamma(n-i+1). \tag{2.56}$$

where p is the dimension of the $\mathbf{k}$ vector and Γ is the gamma function.

It is worth noticing that this distribution is only valid for full-rank $\mathbf{Z}$ matrices, as its determinant $|\mathbf{Z}|$ appears on the numerator, which is zero for any degenerate matrix. As a consequence, the Wishart distribution is only valid for $n \geq p$, requiring, thus, an averaging of, at least, p different samples.

In Section 2.1.4, the speckle noise has been described as a multiplicative noise over the single channel SAR intensity image. The same concept may be extended to each element of the sample covariance matrix $\mathbf{Z}$. Following the same notation, each element of the scattering matrix S_m, or equivalently, of the scattering vector $\mathbf{k}$ may be expressed as

$$S_l = \sqrt{\sigma_l} N_l \exp(j\theta_m) \tag{2.57}$$

where N refers to the speckle noise, σ_l is the local RCS and l refer to the polarization state index of the scattering vector $\mathbf{k}$. Then, for the estimated covariance matrix elements $\langle S_l S_q^* \rangle$

$$\langle S_l S_q^* \rangle = \langle \sqrt{\sigma_l \sigma_q} \exp(j(\theta_l - \theta_q)) \rangle \langle N_l N_q^* \rangle. \tag{2.58}$$

According to the multiplicative speckle noise model previously stated for single channel SAR image in Section 2.1.4, the component $\langle N_l N_q^* \rangle$ must have an expectation $E\{N_l N_q^*\} = 1$ when

$l = q$. If it is assumed that this expectation is equal to zero for all other pairs $l \neq q$, then it will result in a diagonal covariance matrix, which is generally not true [102].

This observation reveals that this expectation may not be considered as zero. In fact, this information is what allows a polarimetric interpretation of the covariance matrix by extracting the different scattering mechanisms present in a distributed target, as it will be seen in the following sections. An extension of SAR multiplicative speckle noise may be found in [88] for the polarimetric case, based on the study of the complex hermitian product of a pair of SAR images. With the same notation, each element of the single-look covariance matrix $\mathbf{Z}$ may be defined as

$$S_l S_q^* = |S_l S_q^*| \exp\left(j(\theta_l - \theta_q)\right) = z \exp(j\varphi) \tag{2.59}$$

which amplitude z and phase φ are following the probability distributions [117]

$$p_z(z) = \frac{4z}{\phi^2(1-|\rho|^2)} I_0\left(\frac{2|\rho|z}{\phi(1-|\rho|^2)}\right) K_0\left(\frac{2z}{\phi^2(1-|\rho|^2)}\right) \tag{2.60}$$

$$p_\varphi(\varphi) = \frac{1-|\rho|^2}{2\pi}\left(\frac{\beta\left(\frac{1}{2}\pi + \arcsin(\beta)\right)}{(1-\beta^2)^{3/2}} + \frac{1}{1-\beta^2}\right) \tag{2.61}$$

where ρ is the complex correlation coefficient between the pair of images, ϕ represents the average power from both channels, calculated as $\phi = \sqrt{\sigma_l \sigma_q}$, being σ_l and σ_q the backscattering coefficients of the images S_l and S_q, β is defined as $\beta = |\rho| \cos(\varphi - \varphi_x)$ with φ_x as the effective phase difference between the image pair, I_0 is the modified Bessel function of the first kind whereas K_0 is the modified Bessel function of the third kind.

Analyzing the speckle noise model for the difference phasor [79][77] it may be observed that real and imaginary parts of the hermitian product of a pair of SAR images can be divided into three additive terms

$$z \exp(j\varphi) = [zN_c + (zv_1' + jzv_2')] \exp(j\varphi_x). \tag{2.62}$$

Considering separately the contribution to the global noise of each one of the terms, a more detailed speckle noise model can be derived for the hermitian product of a pair of SAR images, as proposed in [88]

$$S_l S_q^* = \phi N_c \bar{z}_n n_m \exp(j\varphi_x) + \phi(|\rho| - N_c \bar{z}_n) \exp(j\varphi_x) + \phi(n_{ar} + jn_{ai}) \tag{2.63}$$

where n_m is a multiplicative noise component associated with the first term, n_{ar} and n_{ai} are additive noise components associated with the real and imaginary parts of the hermitian product,

$\bar{z}_n$ is the expected value of amplitude normalized of the hermitian product, obtained for the case $\phi = 1$, and N_c contains approximately the same information as the coherence $|\rho|$. Note that the terms of (2.63) may be classified as

$$S_l S_q^* = \underbrace{\phi N_c \bar{z}_n n_m \exp(j\varphi_x)}_{\text{Multiplicative term}} + \underbrace{\phi(|\rho| - N_c \bar{z}_n)\exp(j\varphi_x) + \phi(n_{ar} + jn_{ai})}_{\text{Additive term}}. \tag{2.64}$$

Consequently, the first term of (2.63) is called multiplicative term, since the useful signal is multiplied by a multiplicative speckle term n_m. The second and third terms are contaminated by the additive components of the speckle noise n_{ar} and n_{ai}.

Finally, note that (2.63) may be considered as a generalization of the speckle noise model obtained in Section 2.1.4, by making $l = q$, and, consequently, $|\rho| = 1$ and $\varphi_x = 0$ radians. Then (2.63) is simplified to

$$S_l S_l^* = |S_l|^2 = \phi n_m \tag{2.65}$$

where $\phi = E\{|S_l|^2\}$. As it can be seen, this result is consistent with the multiplicative speckle noise model defined in Section 2.1.4.

2.2.5 The Product Model

The Wishart distribution, described in (2.55), characterizes the variability of the samples due to the speckle term. However, more complex models have been defined in the literature in order to take into account the effect of the *texture*, which represents the spatial variation of the scattering parameters of the targets that are not perfectly homogeneous [16]. The most widely used model for characterizing this additional variability is the *product model* [120][55]. This model assumes that the obtained matrix **Z** may be expressed as a product of two independent random variables

$$\mathbf{Z} = T\mathbf{W} \tag{2.66}$$

where **W** is following a Wishart distribution $\mathbf{W} \sim \mathcal{W}(\mathbf{C}, n)$, as described in (2.55), representing the variability due to the speckle noise, and T stands for the texture, being independent of the polarization state and common for all the channels.

Note that the probability distribution of **Z** depends on the distribution of the texture T. Different families of distribution may be employed for T, resulting into different types of distributions [16]. In [55], the generalized inverse gamma distribution is proposed for T, resulting into the $\mathcal{G}^\circ$ distribution. Other authors have proposed the employment of the gamma distribution [78] or the Fisher-Snedecor [25], defining the $\mathcal{K}$ and the $\mathcal{U}$ distributions, respectively. Nevertheless, although these distributions may represent more accurately textured areas, they are more difficult to estimate than the Wishart, as they are more complex and have a larger amount of parameters, requiring more samples for a proper initialization and characterization.

2.2.6 H/A/$\bar{\alpha}$ Polarimetric Decomposition

As mentioned in Section 2.2.3, the covariance matrix $\mathbf{C}$ or, in practice, its estimation, the sample covariance matrix $\mathbf{Z}$, characterizes the distributed targets scattering process under the Gaussian hypothesis. However, these matrices may be difficult to interpret directly in order to relate their information with physical target properties. Different polarimetric decomposition techniques may be found on the literature for this purpose as, for instance, the Huynen [65], the Krogager [72], the Cameron [29], the Freeman-Durden [54] or the TSVM [118] decompositions.

Another polarimetric decomposition, proposed by Cloude and Pottier [36], is based on the projection of the coherence matrix $\mathbf{T}$ into the polarimetric base generated by its eigenvalues

$$\mathbf{T} = \sum_{i=1}^{p} \lambda_i \mathbf{v}_i \mathbf{v}_i^H = \sum_{i=1}^{p} \lambda_i \mathbf{T}^i \qquad (2.67)$$

where $\lambda_1 > \lambda_2 > \ldots > \lambda_p$ are the ordered eigenvalues and $\mathbf{v}_i$ are the corresponding eigenvectors.

According to (2.67), the 3 by 3 coherence matrix, in the monostatic case, may be expressed as a sum of three rank-one matrices formed by its unitary eigenvectors $\mathbf{v}_1, \mathbf{v}_2, \mathbf{v}_3$. Note that these eigenvectors are expressed in the Pauli basis and, according to the eigendecomposition theorem, the polarimetric basis they conform diagonalizes the covariance matrix. Consequently, they correspond to the three statistically independent scattering mechanisms that may be found within the distributed target and the eigenvalues correspond to their backscattering power.

Then, the Entropy H and Anisotropy A parameters can be defined as

$$H = \sum_{i=1}^{3} -P_i \log_3 P_i \qquad (2.68)$$

$$A = \frac{\lambda_2 - \lambda_3}{\lambda_2 + \lambda_3} \qquad (2.69)$$

where the pseudo-probabilities P_i are defined as

$$P_i = \frac{\lambda_i}{\sum_{j=1}^{3} \lambda_j}. \qquad (2.70)$$

Therefore, the Entropy H parameter indicates the degree of randomness of the scattering process, being equal to 1 when all the mechanisms are equally probable, that is, all of them have the same reflected power, and equal to 0 when only one mechanism is present. On the other hand, Anisotropy A gives an idea of the dominance of the second eigenvalue versus the third one, in terms of the reflected power, as shown in (2.69). It ranges from $A = 1$ when there is no reflected power for the third mechanism to $A = 0$ when the second and the third polarimetric mechanisms have the same power.

The third parameter of the decomposition, the mean Alpha angle $\bar{\alpha}$ refers to the weighted average of the three different pure scattering mechanism angles α_i. These angles come from the first component of the eigenvectors, as expressed in

$$\mathbf{v}_i = e^{j\varphi_i} \begin{bmatrix} \cos\alpha_i & \sin\alpha_i \sin\beta_i e^{j\delta_i} & \sin\alpha_i \cos\beta_i e^{j\gamma_i} \end{bmatrix}^T \tag{2.71}$$

for $i = 1, 2, 3$.

Then, the mean Alpha angle $\bar{\alpha}$ is defined as

$$\bar{\alpha} = \sum_{i=1}^{3} P_i \alpha_i \tag{2.72}$$

where the angle α_i refers to the type of reflection, from surface scattering $\alpha_i = 0^\circ$ to volume scattering $\alpha_i = 45^\circ$ and double bounds in conductive surfaces $\alpha_i = 90^\circ$. Here α_i refers to the angle of the i-th eigenvector $\mathbf{v}_i$ with the first component of the Pauli basis, as expressed in (2.71), corresponding to surface scattering [36].

2.3 A REVIEW OF POLSAR SPECKLE FILTERING TECHNIQUES

As described in previous sections, for distributed targets, the sample covariance matrix $\mathbf{Z}$ has to be employed to describe the polarimetric behavior of the targets of the scene. However, in order to obtain a well defined (full rank) and reliable estimation of this matrix some degree filtering is required. This estimation process is also known as speckle filtering, as it reduces the effect of the speckle noise and provides a better estimation of the polarimetric information related with these targets.

In this section some of the most well-known state-of-the-art speckle filtering techniques are presented.

2.3.1 BOXCAR / MULTILOOK FILTERING

The multilook filtering has been presented in Section 2.2.4 in the context of the sample covariance matrix estimation process from the data employing n different pixels, as described in (2.54). Since it employs a rectangular window it is also called Boxcar filter. It is based on assuming local stationarity around the given pixel in order to average n pixels in the neighboring window [119].

Boxcar filter is the fastest and the simplest speckle filter and, additionally, since it correspond to the MLE of the covariance matrix, it does not introduce neither bias nor distortion over homogeneous areas. However, as it may be expected, the local stationarity hypothesis may not hold over some areas. This is specially the case near contours or point scatterers, where the multilook results may not be valid due to the mixture of different samples following distinct statistical distributions. In these situations, the Boxcar filter may also be seen as a low pass filter, reducing, thus, the spatial resolution of these details and blurring these image features that are not produced just by speckle noise. This effect is particularly apparent on strong point scatterers, as they appear enlarged according to the window size. Then, as stated in Section 2.2.4, the amount of speckle filtering achieved by the multilook is in compromise with the amount of spatial resolution loss obtained. One example of the results obtained with this filter may be found later on this chapter, on Fig. 2.7b, where it is compared with other filtering techniques.

2.3.2 LEE ADAPTIVE FILTERING

The mentioned problems of the multilook filter are produced when the local stationarity hypothesis is not valid, resulting in a mixture of not homogeneous samples. To overcome these problems, the Lee filter [74][80] was proposed as an adaptive filter to improve the precision of the estimated coherence. It tries to adapt to the morphology of the scene by choosing one averaging window from a set of eight predefined directional windows. These windows are represented in Fig. 2.6.

The window containing the set of most homogeneous samples is selected, according to the sample dispersion among the average of the total power received, that is, the Span of the sample covariance matrix $\mathbf{Z}$. Then, the pixels within the most homogeneous directional window are employed for the estimation of the covariance matrix $\tilde{\mathbf{Z}}$ employing the Local Linear Minimum Mean Squared Error (LLMMSE)

$$\tilde{\mathbf{Z}} = \bar{\mathbf{Z}} + b(\mathbf{Z} - \bar{\mathbf{Z}}) \tag{2.73}$$

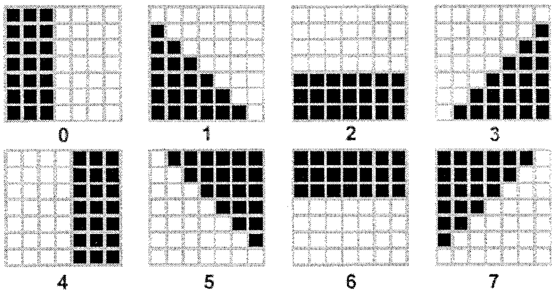

Figure 2.6: The eight predefined directional windows in the Lee adaptive filter [80]. The selected pixels are represented in white color.

where $\bar{\mathbf{Z}}$ refers to the sample covariance matrix averaged over the selected directional window, $\mathbf{Z}$ refers to the value of the sample covariance matrix for the central pixel and $b \in [0,1]$ is a weighting factor calculated with the degree of local stationarity.

For the computation of the b factor, a multiplicative noise is assumed in the received power, in the form

$$y = xn \tag{2.74}$$

where y is the value of the central pixel, x is the value we want to estimate and n represents the multiplicative noise, with an expectation equal to one and variance σ_n^2. Then, the weighting factor b can be calculated as

$$b = \frac{\mathrm{var}(x)}{\mathrm{var}(y)} \tag{2.75}$$

and

$$\mathrm{var}(x) = \frac{\mathrm{var}(y) - \bar{y}^2\sigma_n^2}{1 - \sigma_n^2} \tag{2.76}$$

where $\bar{y} = E\{y\}$.

The idea is that over homogeneous areas $\mathrm{var}(x) = 0$, then $b = 0$ and $\tilde{\mathbf{Z}} = \bar{\mathbf{Z}}$, resulting in the multilook filter over the selected window. On the other hand, over a point scatter or very heterogeneous areas, when $b = 1$ then the estimated sample covariance matrix corresponds to the central pixel value $\tilde{\mathbf{Z}} = \mathbf{Z}$, resulting in preserving the original value and no filtering at all.

The set of directional windows are intended to preserve the edges of the image, whereas the LLMMSE tends to preserve point scatters. However, the set of predefined windows allow a very limited adaptation to the morphology of the scene. An example of the filtering results obtained with the Lee adaptive filter may be seen in Fig. 2.7c. It is worth mentioning that, since it just employs the span of the sample covariance matrix for window selection, only a small fraction of the polarimetric information is employed.

2.3.3 IDAN FILTER

The Intensity Driven Adaptive Neighborhood (IDAN) [125] represents a step forward respect to the Lee filter in terms of adaptation to the image morphology. It is based on the concept of removing the limitation of the predefined windows by defining an arbitrary set of homogeneous adjacent samples for each pixel of the image. This set of samples is called the Adaptive Neighborhood (AN) of the pixel under study and it is constructed employing the Region Growing technique [4].

The adaptive neighborhood notion was firstly employed for processing medical images, as introduced in [61]. A seed is generated for each pixel and, then, a neighborhood is constructed employing the region growing process. This AN may have a variable shape and size and, ideally, it contains only pixels with the same distribution than the seed. In the IDAN filter, the seed is calculated by applying a median filter to the adjacent pixels to the pixel of interest, as described in [125]. Note that the median filter is employed to avoid as much as possible the spatial resolution loss.

Compared to the Lee filter, the IDAN has the advantage of being able to achieve a stronger filtering and a better adaptation to the image structure. However, since intensity SAR images are not following a symmetric distribution, as stated in Section 2.1.3, it introduces an important bias over the estimated values due to the median filter [57]. This bias makes impossible employing the IDAN filter for SAR applications employing quantitatively the estimated information. The presence of this bias has been discussed in [127] and compensated up to a certain point by the authors in [126].

To construct the AN for each pixel, the IDAN employs the region growing technique taking into account the elements of the main diagonal of the sample covariance matrix, generating the vector of power measurements p

$$p(m,n) = \begin{bmatrix} T_{11}(m,n) \\ T_{22}(m,n) \\ T_{33}(m,n) \end{bmatrix} = \begin{bmatrix} p_1(m,n) \\ p_2(m,n) \\ p_3(m,n) \end{bmatrix} \tag{2.77}$$

where m and n are the coordinates of the image pixels.

The set of adjacent pixels are analyzed in order to retain within the AN only those pixels that are within the interval of 2 times the CV around the seed

$$\frac{\|p_i(k,l) - \hat{p}_i(m,n)\|}{\|\hat{p}_i(m,n)\|} \leq 2\frac{\sigma}{\mu} \tag{2.78}$$

where $p_i(k,l)$ represents the pixel to add to the AN, $\hat{p}_i(m,n)$ refers to the seed value and the subindex i refers to each one of the three SAR intensity images, as defined in (2.77). The CV is expressed as σ/μ, which is a standard parameter in intensity SAR images, as described in Section 2.1.3, having a value equal to $1/\sqrt{L_{eq}}$ for homogeneous areas contaminated by speckle noise, where L_{eq} represents the number of independent samples averaged.

A similar concept is applied in the Lee sigma filter [75] since, according to the multiplicative noise model for intensity SAR images, the 95% of the samples are expected to be in this interval of values. Then, this process is iterated for each component of the p vector until no more pixels can be added to the AN or a limit number of pixels is achieved.

However, when computing the AN with this threshold, there is a high risk of generating neighborhoods containing non-homogeneous pixels, as the established limit of 2 times the CV may be too permissive. A refinement of this region growing process is proposed in [125], by applying it in two stages with different thresholds. In the first step, the AN is computed by adding the pixels within the interval of 2/3 times the CV, corresponding to the interval where the 50% of the samples are expected to lie

$$\frac{\|p_i(k,l) - \hat{p}_i(m,n)\|}{\|\hat{p}_i(m,n)\|} \leq \frac{2}{3}\frac{\sigma}{\mu}. \tag{2.79}$$

With this first step, the estimation of the seed is refined and then, a second step of region growing is performed, according to the previous limit, as expressed in (2.78). Finally, once the neighborhood is defined for each pixel, the estimated sample covariance matrix $\mathbf{Z}$ may be obtained by applying the multilook filtering or the LLMMSE within the AN, as described in Section 2.3.2.

To illustrate the effect of the different speckle filtering techniques presented in this section, Fig. 2.7 shows an example of an area of a PolSAR image and the results obtained with them [1]. Fig. 2.7a represents the original PolSAR image represented in the Pauli composition assigned to RGB channels. The effect of the speckle noise can be seen as a granular texture over the image. On Fig. 2.7b the 7x7 Boxcar multilook filter has been applied and an important reduction of the speckle noise may be observed. However, all the contours and small details of the image appear blurred, resulting a spatial resolution loss. Figs. 2.7c and 2.7d show results after applying the adaptive Lee filter, defined in Section 2.3.2, and the IDAN filter, defined in this section. These filters achieve a relatively good speckle reduction while also maintaining the spatial resolution much better than the multilook filter. However, as it will be seen, they may introduce some bias

---

[1] The PolSARPro software [3] has been employed to process this data and for Pauli image generation. For the IDAN filtering, a maximum AN size parameter of 100 pixels has been employed.

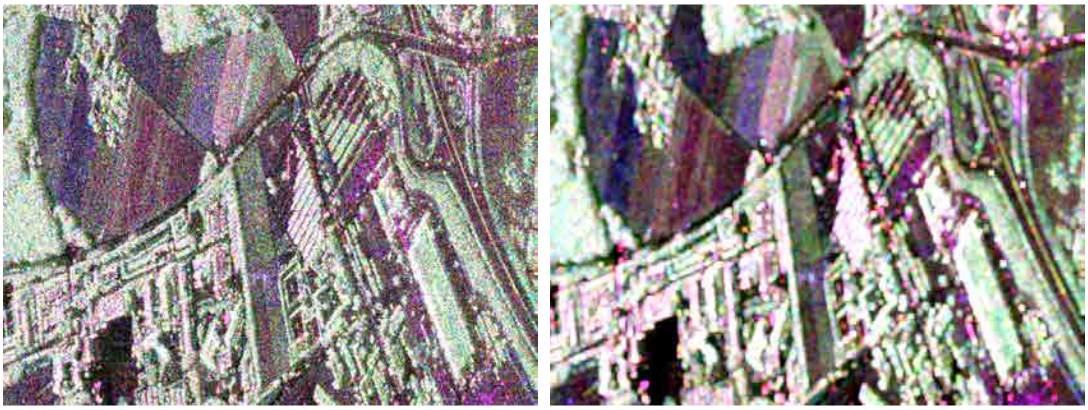

(a) Original **(b)** Boxcar 7x7

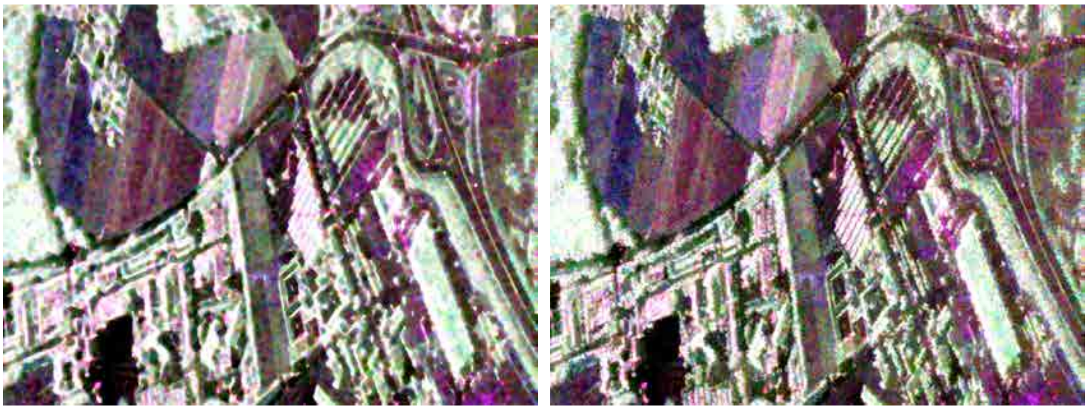

(c) Lee filter **(d)** IDAN filter

Figure 2.7: PolSAR images filtered employing different speckle filters. The Pauli vector $\mathbf{k}_{3P}$ is represented, assigning its components to the RGB channels ($|S_{hh}+S_{vv}|$, $|S_{hv}+S_{vh}|$, $|S_{hh}-S_{vv}|$).

or distortion over the filtered images.

2.3.4 NON-LOCAL MEANS FILTERING

As highlighted in the previous sections, the multilook filter, the adaptive Lee filter and the IDAN filter are based on the spatial locality of the data. That is, they are assuming similar values may be found in a close area around the given pixel. The adaptive Lee filter and the IDAN have defined some mechanisms to refine this local area to adapt to the morphology of the scene but they still rely on looking for them in a neighboring area.

The non-local means filter (NL-means) [28] is following a completely different approach, by breaking with the idea of local stationarity, as its name suggests. It is based on a non-local weighted average of pixels but, in contrast with the adaptive Lee or IDAN filters, these pixels are not required to be in a neighborhood of the given pixel, and they may be located at any position of the image.

Given a discrete image $v = \{v(i) | i \in I\}$, where I represents the set of pixel positions, the NL-means filter for pixel at position i may be computed as the weighted average of all the image pixels

$$NL(i) = \sum_{j \in I} w(i,j) v(j) \tag{2.80}$$

where the set of weights $w(i,j)$ are selected based on the similarity between pixel at positions i and j and satisfy the conditions

$$0 \leq w(i,j) \leq 1 \qquad \forall i,j \in I \tag{2.81}$$

$$\sum_{j \in I} w(i,j) = 1 \qquad \forall i \in I. \tag{2.82}$$

Moreover, to compute the similarity between the pixels i and j, instead of employing their values, the set of values around a patch or neighborhood of each pixel is employed. Then, this similarity comparison does not only require two similar pixel values but also a similar context around them. Mathematically, this may be expressed as

$$w(i,j) = \frac{1}{Z(i)} \exp\left(- \frac{\|v(N_i) - v(N_j)\|^2}{h^2} \right) \tag{2.83}$$

where N_i represents the set of neighboring pixels around the i pixel, $Z(i)$ is the normalizing constant, defined as

$$Z(i) = \sum_j \exp\left(- \frac{\|v(N_i) - v(N_j)\|^2}{h^2} \right) \tag{2.84}$$

where h is a factor controlling the amount of filtering.

A representation of this patch based comparison may be seen on Fig. 2.8, where three pixels at positions $q1$, $q2$ and $q3$ are compared with the pixel at position p. The neighborhood area is represented as a square around each pixel position.

The NL-means filter has also been extended to process PolSAR data, as described in [42]. In this case, the similarity between each pixel of a patch is computed based on the scattering vector absolute value relations, being proportional to

$$\ln\left(\frac{|k_{1,1}|}{|k_{2,1}|} + \frac{|k_{2,1}|}{|k_{1,1}|} \right) + \ln\left(\frac{|k_{1,2}|}{|k_{2,2}|} + \frac{|k_{2,2}|}{|k_{1,2}|} \right) + \ln\left(\frac{|k_{1,3}|}{|k_{2,3}|} + \frac{|k_{2,3}|}{|k_{1,3}|} \right) \tag{2.85}$$

where $\mathbf{k}_1$ and $\mathbf{k}_2$ refers to the scattering vectors of each one of the two pixels being compared

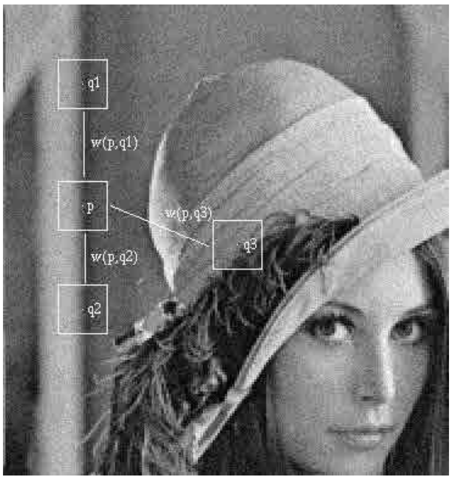

Figure 2.8: NL-means similarity comparison. $q1$ and $q2$ obtain large weights w whereas $q3$ gets a smaller weight, as it is surrounded by a different neighborhood [28].

on the patch, $k_{i,j}$ refers to the j-th component of i scattering vector and ln refers to the natural logarithm.

Note that, similarly to the IDAN filter, it only exploits the information related to each channel power information, and not the correlation between them, that is contained in the off-diagonal elements of the covariance matrix. However, on [41] an iterative refinement of the filter is proposed, which is also extended in [42] to take into account all the polarimetric information contained in the coherence matrix $\mathbf{T}$, based on the symmetric Kullback Leibler divergence

$$SD_{KL}(\hat{\mathbf{T}}_1, \hat{\mathbf{T}}_2) \propto \mathrm{tr}(\hat{\mathbf{T}}_1^{-1}\hat{\mathbf{T}}_2) + \mathrm{tr}(\hat{\mathbf{T}}_2^{-1}\hat{\mathbf{T}}_1) - 6. \tag{2.86}$$

The NL-mean filter employs a neighborhood in order to compare the similarity between pixels and this effectively reduces the effect of the speckle noise in terms of the similarity comparison. However, two similar pixels require also to be located in a comparable context in order to be considered similar, resulting into sub-optimality in terms of filtering, as studied in [94].

2.4 A Review of PolSAR Classification Techniques

As mentioned in Section 2.2, SAR polarimetry enlarges significantly the amount of information that can be extracted from the scatterer. Not surprisingly, terrain identification or classification is, thus, an important application for PolSAR.

Classification techniques are usually divided into two main types: supervised and unsupervised methods. In a supervised approach, a set of examples are manually provided for each class and the most similar areas to these ones are obtained. On the other hand, unsupervised techniques are not provided with any kind of input data and, consequently, they try to extract the most differentiated areas that may be found on the scene.

In this section, two of the most well-known and widely employed unsupervised PolSAR classification techniques are described.

2.4.1 H/A/$\bar{\alpha}$ POLARIMETRIC CLASSIFICATION

In Section 2.2.6, the $H/A/\bar{\alpha}$ polarimetric decomposition has been described. Moreover, its interpretation shows that it is able to distinguish between some different physical targets. Then, an unsupervised classification may be obtained by simply defining ranges of values for the $H/A/\bar{\alpha}$ decomposition parameters.

According to [36], the most distinctive traits are found in the Entropy (H) and the averaged Alpha angle ($\bar{\alpha}$), then, nine different regions are defined according to these value ranges, as represented on Fig. 2.9.

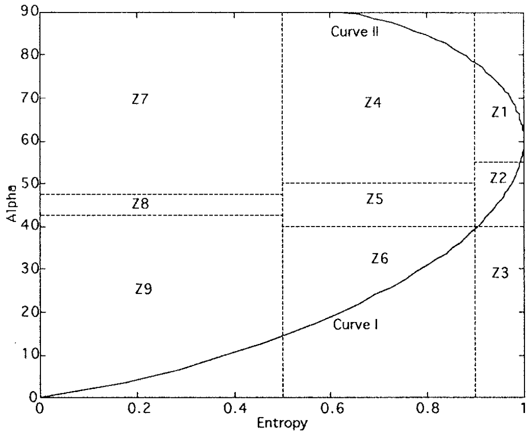

Figure 2.9: Feasible set of values for H and $\bar{\alpha}$ polarimetric decomposition parameters and the corresponding scattering classification regions [36].

The physical interpretation of the meaning of these zones and the main scattering mechanisms that they represent may be described briefly as [36]

- **Zone 9: Low Entropy Surface Scatter:** this area is characterized by $H < 0.5$ and $\bar{\alpha} < 42.5^\circ$. Typically, Bragg surface scattering and specular scattering are included in this class. This is the case for water surfaces at L and P-Bands, for example.

- **Zone 8: Low Entropy Dipole Scattering:** having $H < 0.5$ and $42.5^\circ < \bar{\alpha} < 47.5^\circ$. This region represents isolated dipole scattering, having a large imbalance between *hh* and *vv* polarizations states in amplitude.

- **Zone 7: Low Entropy Multiple Scattering:** when $H < 0.5$ and $\bar{\alpha} > 47.5^\circ$. Corresponds to low Entropy double or even bounce scattering occurrence, usually produced by isolated dielectric and metallic dihedral scatters.

- **Zone 6: Medium Entropy Surface Scatter:** defined by $0.5 < H < 0.9$ and $\bar{\alpha} < 40^\circ$. This class also represents surface scattering, as the class defined by Zone 9, but with an increased level of roughness.

- **Zone 5: Medium Entropy Vegetation Scattering:** represented by $0.5 < H < 0.9$ and $40^\circ < \bar{\alpha} < 50^\circ$. Areas including vegetation scattering with anisotropic scatterers will lie within this region.

- **Zone 4: Medium Entropy Multiple Scattering:** in the case of $0.5 < H < 0.9$ and $\bar{\alpha} > 50^\circ$. These parameters indicate dihedral scattering with moderate Entropy. This situation may happen, for instance, when having dihedral scattering behind a canopy, which increases the Entropy of the mechanism.

- **Zone 3: High Entropy Surface Scatter:** for $H > 0.9$ and $\bar{\alpha} < 40^\circ$. Note that this area is not feasible, since it is outside the posible area, represented by the curve in Fig. 2.9. This fact is a consequence of the disability of the radar to detect the different scattering mechanisms when the Entropy increases.

- **Zone 2: High Entropy Vegetation Scattering:** described by $H > 0.9$ and $40^\circ < \bar{\alpha} < 55^\circ$. Typically high Entropy volume scattering is produced at $\bar{\alpha} = 45^\circ$ and $H = 0.95$. In the case of forest canopies these type of scattering is obtained.

- **Zone 1: High Entropy Multiple Scattering:** distinguished by by $H > 0.9$ and $\bar{\alpha} > 55^\circ$. Even in the case of high Entropy, double bounce scattering may be distinguished, which are represented by this class.

As it may be seen, the previous $H/\bar{\alpha}$ polarimetric classification yields to eight different classes. The boundaries of these regions are not completely fixed and they will depend on the parameters of the radar and the amount of filtering employed, as described in [36]. Moreover, an additional distinction may be performed by taking into account the Anisotropy A parameter. In this case, called $H/A/\bar{\alpha}$ polarimetric classification, each of the previously defined classes may be separated in two different groups, having $A < 0.5$ and $A > 0.5$, resulting in a total of 16 different classes.

2.4.2 WISHART CLASSIFIER

The $H/\bar{\alpha}$ and $H/A/\bar{\alpha}$ classifiers are useful to make a polarimetric classification of the scatterers of a scene. However, this segmentation is completely pre-defined and, as stated before, it may depend on the data and the amount of speckle filtering. Moreover, depending on the scene, this type of pre-defined classification may not make sense, as some type of targets may not be present on the scene.

The Wishart classifier tends to adapt the classification scheme to the given scene, solving the previously mentioned disadvantages of the direct $H/\bar{\alpha}$ and $H/A/\bar{\alpha}$ classifiers. As its name suggests, it is based on the Wishart distribution, defined in (2.55). Assuming that we have a set of N classes, identified by their mean covariance matrices $\mathbf{C}_i$, for $i \in [1, N]$, then the probability of the sample covariance matrix $\mathbf{Z}$ of belonging to the class defined by $\mathbf{C}_i$ may be obtained as

$$p_{\mathbf{C}_i}(\mathbf{Z}) = \frac{n^{pn}|\mathbf{Z}|^{n-p}}{|\mathbf{C}_i|^n \widetilde{\Gamma}_p(n)} \mathrm{etr}(-n\mathbf{C}_i^{-1}\mathbf{Z})p(i). \tag{2.87}$$

where $p(i)$ refers to the a priori probability of belonging to the class i.

The Wishart classifier, then, will assign the sample covariance matrix $\mathbf{Z}$ to class i having the largest $p_{\mathbf{C}_i}(\mathbf{Z})$. In order to simplify the computations, the logarithm of (2.87) may be applied before maximization, as the logarithm is an increasing function

$$\ln\left(p_{\mathbf{C}_i}(\mathbf{Z})\right) = pn\ln(n) + (n-p)\ln|\mathbf{Z}| - n\ln|\mathbf{C}_i| - \ln(\widetilde{\Gamma}_p(n)) + \mathrm{tr}(-n\mathbf{C}_i^{-1}\mathbf{Z}) + \ln\left(p(i)\right). \tag{2.88}$$

Additionally, if we assume that all the samples have an uniform filtering, that is, the equivalent number of looks parameter n of the distribution is the same for all the samples, then the factors depending only on n may be taken out from (2.88), as they are constant factors and do not play any role in the maximization process. This is also the case for the term depending on the $\mathbf{Z}$ determinant, being constant for all i class. Moreover, the a priori probabilities of belonging to each class $p(i)$ may be considered equal for each class, resulting into

$$\ln\left(p_{\mathbf{C}_i}(\mathbf{Z})\right) \propto -\ln|\mathbf{C}_i| - \mathrm{tr}(\mathbf{C}_i^{-1}\mathbf{Z}). \tag{2.89}$$

Usually, the process of maximizing $\ln\left(p_{\mathbf{C}_i}(\mathbf{Z})\right)$ is transformed into the minimization of its negative $-\ln\left(p_{\mathbf{C}_i}(\mathbf{Z})\right)$, as all the probabilities are smaller than 1, resulting into negative log-values. Then, the process of assigning the sample $\mathbf{Z}$ to the class i may be expressed as [81]

$$i = \underset{j\in[1,N]}{\arg\min}\ \ln|\mathbf{C}_j| + \mathrm{tr}(\mathbf{C}_j^{-1}\mathbf{Z}). \tag{2.90}$$

The Wishart classifier, as defined in [81], is a combination of the $H/\bar{\alpha}$ classifier with an iterative adaptation employing the Wishart cluster assignation as expressed in (2.90). The process performed by the Wishart classification is described by the following steps:

1. Perform the $H/\bar{\alpha}$ classification of the data as an initial step, to initialize the 8 clusters.
2. Compute the covariance matrix $\mathbf{C}_i$ of each cluster i by averaging all the samples in each region of the $H/\bar{\alpha}$ classification.
3. Assign each sample covariance matrix $\mathbf{Z}$ of the image to the most probable cluster, according to (2.90).
4. Re-compute each cluster covariance matrix $\mathbf{C}_i$ according to the previous assignation.
5. Repeat steps 3 to 5 until a convergence criterion is fulfilled.

The convergence criterion employed in step 5 may be, for instance, to limit the number of iterations that the algorithm may perform or to stop it when the number of samples that have changed its cluster assignment is below a given percentage. Note that, since the algorithm requires a robust initialization, the $H/\bar{\alpha}$ classification is applied, which results into 8 different clusters. Alternatively, the $H/A/\bar{\alpha}$ classification may be applied, resulting into 16 classes. However, no technique is described in [81] for an appropriate initialization with an arbitrary number of classes.

To show the results obtained by the $H/\bar{\alpha}$ classification and the Wishart classification techniques, an example is included with ESAR system, at L-band, over the Oberpfaffenhofen testsite, southern Germany. After applying some speckle filtering, employing the 9 by 9 multilook filter, the Entropy (H) and the averaged Alpha angle $(\bar{\alpha})$ has been obtained and its values are shown on Figs. 2.10a and 2.10b, respectively.

With the Entropy and the averaged Alpha angle presented in Fig. 2.10, the $H/\bar{\alpha}$ classification has been applied, described in Section 2.4.1, and the results may be seen in Fig. 2.11a. The $H/\bar{\alpha}$ plane of all the values of the image may be seen on Fig. 2.11b, where the color code employed in Fig. 2.11a is also represented.

For comparison purposes, Fig. 2.12a shows the result of applying the Wishart classification to the same dataset. In this case, a different color map than in Fig. 2.11a has been employed, as the obtained classes do not correspond to the initial assignment in the $H/\bar{\alpha}$ plane due to the adaptation of the Wishart classifier.

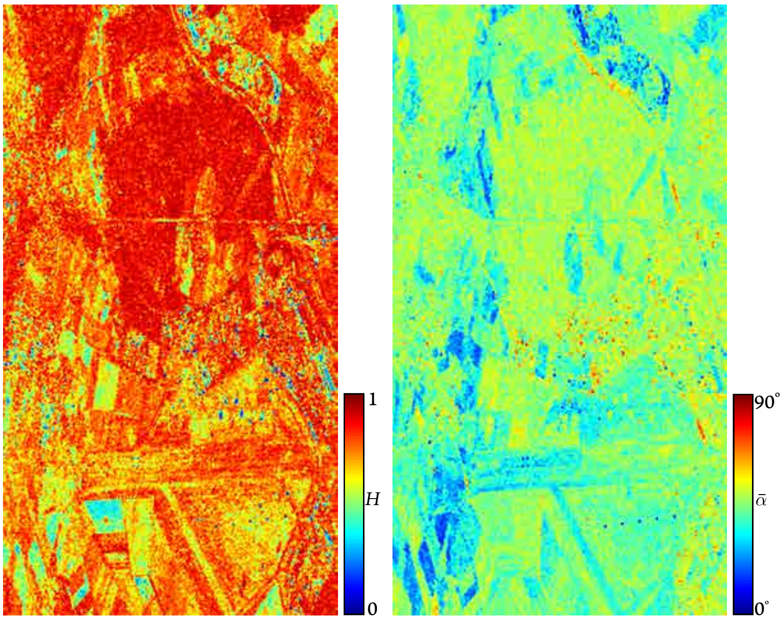

(a) H **(b)** $\bar{a}$

Figure 2.10: Entropy (a) and averaged alpha angle (b) for the Oberpfaffenhofen dataset.

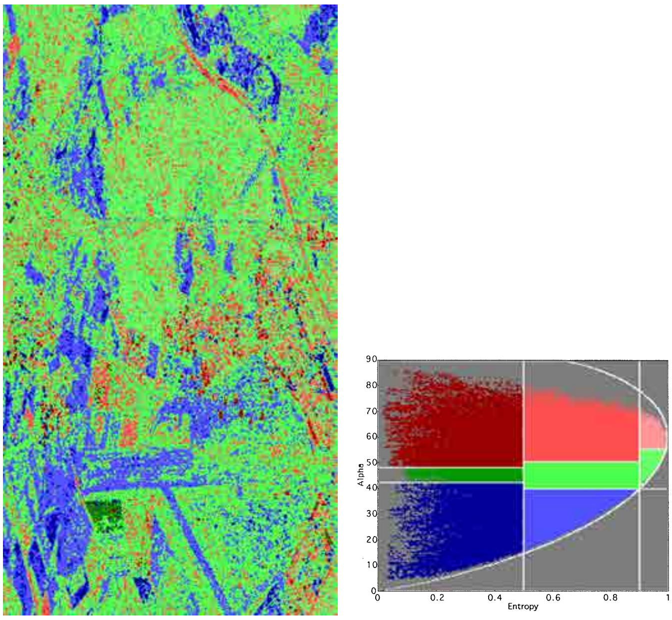

(a) $H/\bar{a}$ classification **(b)** $H/\bar{a}$ plane

Figure 2.11: $H/\bar{a}$ classification (a) and $H/\bar{a}$ plane and color code (b) of the Oberpfaffenhofen image.

As it may be seen, some areas are more clearly separated on Fig. 2.12a than on Fig. 2.11a, where the amount of noise observed over the classification results is larger. This noise is ob-

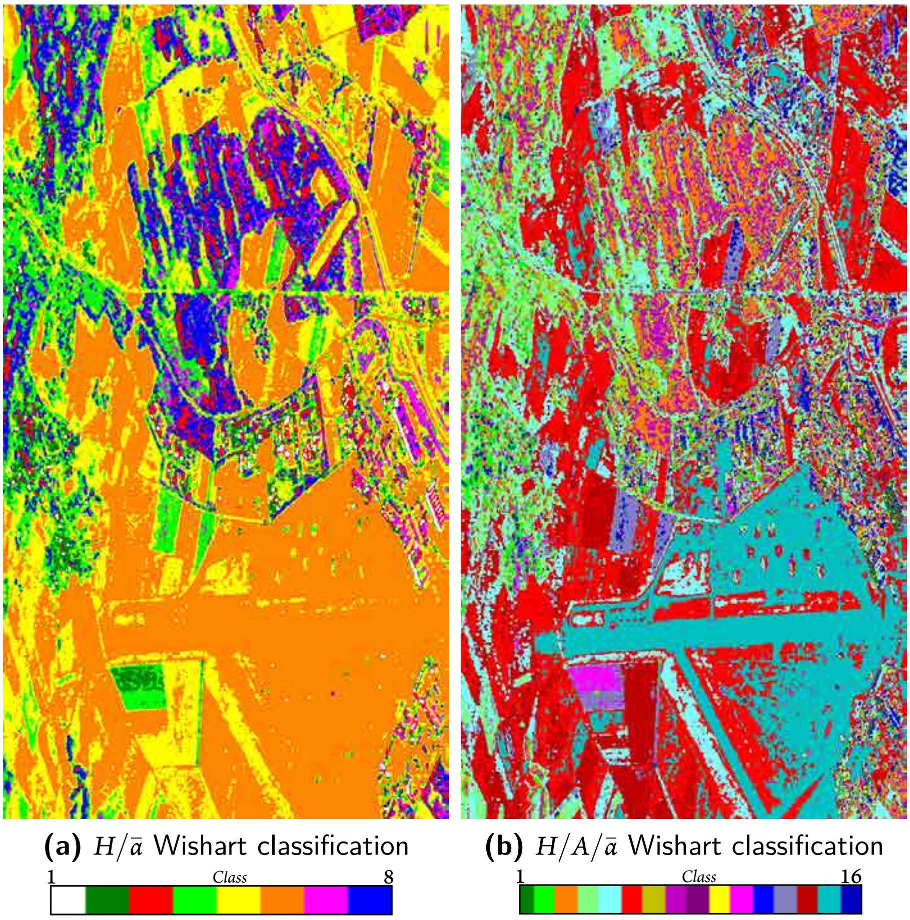

(a) $H/\bar{\alpha}$ Wishart classification

(b) $H/A/\bar{\alpha}$ Wishart classification

Figure 2.12: $H/\bar{\alpha}$ Wishart classification (a) and $H/A/\bar{\alpha}$ Wishart classification (b) of the Oberpfaffenhofen image.

served due to some areas of the image presenting a polarimetric response in between two of the $H/\bar{\alpha}$ classes. When applying the Wishart classifier to the data, since it is able to adapt to the content of the image, this boundary effect is reduced. Additionally, Fig. 2.12b presents the results after applying the $H/A/\bar{\alpha}$ Wishart classification, resulting into 16 classes. In this case, further details of the image are observed, specially on the bottom part of the image, as a larger number of classes are available.

All fixed set patterns are incapable of adaptability or pliability. The truth is outside of all fixed patterns.

Bruce Lee

3

Binary Partition Tree

The Binary Partition Tree (BPT) data abstraction is presented in this chapter. At this point, this structure is described from a generic point of view, without entering into the details of the underlying data. On the following chapters, the BPT will be particularized to represent and process PolSAR images and temporal series.

First of all, the basic concepts of the BPT and the motivation for its adoption are discussed. A general BPT based processing scheme is proposed based on two main steps: the BPT construction from the original data and its exploitation for different applications. Secondly, the algorithms for performing these processing steps are described, performing a brief analysis of the computational complexity of these methods. Finally, a few thoughts are commented regarding the limitations of the BPT for data representation.

3.1 The BPT as a Data Abstraction

The Binary Partition Tree (BPT) may be considered as a region-based and multi-scale data representation [109]. Hence, in contrast with a pixel-based approach, where a rectangular array of pixels is assumed, the basic entity of this data abstraction is a connected area of the data, grouping adjacent pixels or elements with similar properties. Additionally, it is a hierarchical structure being able to describe the data at multiple scales and also to provide ordered access to subsets of regions. In the following sections, the BPT structure and the different concepts related with this abstraction will be presented.

3.1.1 Region-based Approach

The BPT, as mentioned before, is a region-based data representation. As opposite to a pixel-based method, where a rectangular array of pixels is assumed, on a region-based approach the data is represented by a set of connected regions, and each region is processed independently, being the basic entity of the processing paradigm.

A region may be seen as a set of *connected* elements of the data that may be considered similar under some criterion. Note that this definition implies the selection of a connectivity scheme for the dataset. In image processing, for instance, when dealing with 2-dimensional data, the 4-connectivity or 8-connectivity are the typical choices. Under this assumption, a connected region is a region on which any pair of data elements contained are connected through a path that lies completely within the region itself.

On a pixel-based processing approach, the assumption that is usually performed behind is the *local stationarity*. That is, it is presumed that pixels that are close in the spatial domain will also present similar values. Then, the data portion within a local window around a given pixel may be considered as stationary and, as a consequence, the samples within this window may be processed jointly. This approach usually fails near contours or for small details of the scene, where the local stationarity approach may not hold. On the other hand, the region-based approach is based on the idea that, although data are not stationary, they may be decomposed into stationary connected components or regions, which may be processed individually and independently. As it may be seen, this assumption is more general and flexible, being able to adapt to regions of different sizes, taking profit of large amount of data for a reliable estimation of data parameters on large regions, while also preserving the small details or the contours within the data. In fact, the decomposition of the data into connected components or regions conforms a data segmentation itself, being very useful for data processing and interpretation.

The difficulty derived on the region-based processing paradigm is that it has to rely on a trustworthy division into stationary connected components. The construction of this division may be a very complex task, requiring a large amount of computational resources and a complicated data modeling. In this scenario, the BPT simplifies this task by performing this division automatically, in terms of a metric measure, while also being efficient, by applying a divide and conquer algorithm strategy.

3.1.2 Hierarchical Multi-scale Approach

As mentioned before, the BPT data representation has an inherent multi-scale nature. It contains all the information in the original data plus additional information related to its structure at different detail levels. The BPT is intended to be a generic data representation, being useful for different applications. To achieve this goal, a data separation into stationary connected components may not be enough, as distinct applications will require a completely different region-based decomposition. As a consequence, in order to produce a generic structure, it must contain the decomposition into stationary connected components at different scales.

However, if the division of a dataset into its connected components is a difficult task, the need of performing it in a multi-scale basis may turn the problem intractable. Fortunately, this is not the case for the BPT construction process, where its multi-scale essence comes out naturally. As indicated before, the BPT may be constructed in an efficient manner by a divide and conquer strategy, by recursively breaking the complex problem into smaller parts until they become tractable. Consequently, during the construction process the algorithm traverses over a wide range of region sizes, covering from the individual elements to very large areas of the dataset. The BPT, then, is constructed by keeping track of all this intermediate results, arranging all this information hierarchically conforming a binary tree, which describes connected regions of the data with similar properties at different scales.

3.1.3 The BPT Structure

To enter into details on this binary tree structure, some basic notions about graphs and graph theory will be presented in the following. Graphs are a representation of a set of objects having some relations between pairs of them. From a formal point of view, a graph G may be seen as a mathematical structure consisting of a set V of *vertices* or *nodes* and a set E of *edges* or *lines*, and it is denoted as $G = (V, E)$ [63]. The set of edges E contains 2-element subsets of V, since an edge is related with two nodes. In this work only *undirected* graphs will be considered, which means that the edges of the graph do not have a particular direction and then, the set E can be defined as an unordered pair of vertices. Fig. 3.1 shows a representation of a simple graph with 4 vertices and 4 edges.

A *weighted graph* is a graph on which each edge has a value, i.e., a weight, associated. A sample representation of a weighted graph is presented in Fig. 3.2.

In this context, a *tree* is a special case of graph, in which every two nodes are connected by *exactly one* path. This means that there are no cycles inside a tree, also known as closed paths,

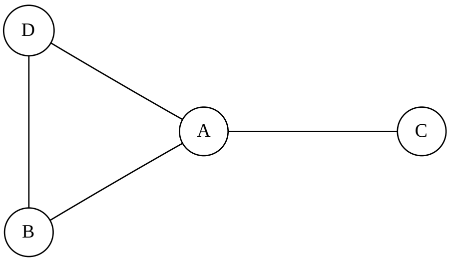

Figure 3.1: A graph $G = (V, E)$ representation with $V = \{A, B, C, D\}$ and $E = \{\{A, B\}, \{A, C\}, \{A, D\}, \{B, D\}\}$.

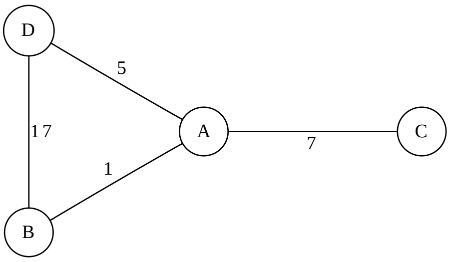

Figure 3.2: A weighted graph $G = (V, E)$ representation, having $V = \{A, B, C, D\}$ and $E = \{\{A, B, 1\}, \{A, C, 7\}, \{A, D, 5\}, \{B, D, 17\}\}$.

and that a tree is a connected graph, having a path that connects any pair of nodes. Typically, trees are employed to model hierarchies and, consequently, they are represented in a top-down scheme. Then, a *root* node has to be defined, which is the highest level of the hierarchy, usually represented on top of the drawing. The other nodes connected to each node are represented in a level below it and, according to the hierarchy simile, they are called its *sons*. The nodes of the tree having no sons are called *leaves*. Fig. 3.3 shows a representation of a tree with 4 leaves and 6 nodes.

Assuming the previous definition of a tree, Property 3.1 may be deduced [63].

Property 3.1 *A tree with n nodes has always* $n - 1$ *edges.*

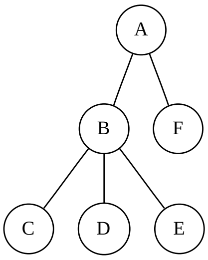

Figure 3.3: A tree representation having 4 leaves $\{C, D, E, F\}$. The root node A has 2 sons $\{B, F\}$ whereas the node B has 3 sons $\{C, D, E\}$.

A *binary tree* is a special case of tree having exactly 2 sons per node except for the tree leaves. In this case, the two sons can be named left and right sons. Fig. 3.4 represents a binary tree with 4 leaves $\{A, B, C, D\}$.

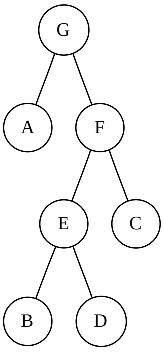

Figure 3.4: A binary tree representation.

Due to the mentioned restrictions that apply to binary trees, Property 3.2 may be employed to relate the number of nodes and edges on a binary tree with the number of leaves.

Property 3.2 *A binary tree with n leaves has* $2n - 1$ *nodes and, applying Property 3.1,* $2n - 2$ *edges.*

As stated before, the BPT is a hierarchical data representation structured in form of a binary tree. As a region-based approach, each node of the tree represents a connected region of the original data. The leaves of the tree represent each one of the original data elements whereas other nodes represent the merging of its two child nodes. Consequently, by applying this definition recursively, the root node of the tree represents the whole dataset. Between the leaves and the root nodes there are a wide number of regions representing the data structure at different detail levels that can be exploited for different applications. Fig. 3.5 represents a BPT generated from a 4-element $\{A, B, C, D\}$ dataset, corresponding to the tree leaves.

Note that the BPT is not a balanced tree, and then regions with arbitrary sizes in terms of the original dataset elements contained may be merged to generate the parent node. For instance, in the BPT representation presented in Fig. 3.5 this effect can be clearly seen by the fact that the leaves $\{A, B, C, D\}$ appear at different levels of the tree.

3.1.4 BPT BASED PROCESSING SCHEME

Once the BPT data abstraction has been constructed, it may be employed for different applications, as described before. However, the extraction of useful information from the BPT re-

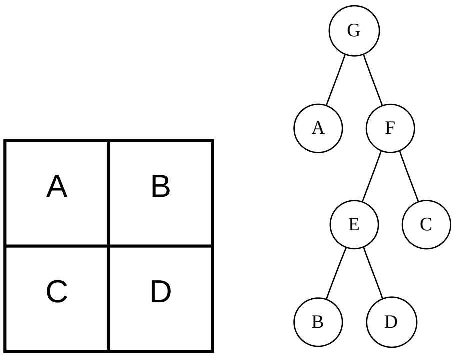

(a) Original data elements **(b)** BPT representation

Figure 3.5: BPT representation of a dataset containing 4 elements $\{A, B, C, D\}$.

quires a completely different approach than processing the original data in terms of pixels since, instead of them, a binary tree has to be exploited. Usually we are interested in obtaining a result in the same domain than the original data. In this case, the BPT exploitation may be seen as the *selection* or *extraction* from the tree of the most *useful* or *interesting* regions for a particular application. Then, the BPT exploitation may be performed by a tree pruning algorithm, as proposed on [109], considering the leaves of the pruned tree as the selected regions.

Consequently, the data processing scheme based on the BPT representation may be decomposed into two main steps: the BPT construction and the BPT exploitation. Fig. 3.6 represents this two main steps of the mentioned processing scheme.

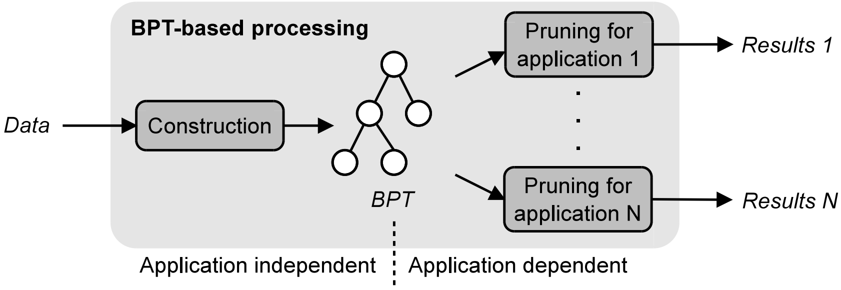

Figure 3.6: BPT-based processing scheme.

It is worth noticing that the BPT construction process may be seen as *application independent*, in the sense that it does not depend on the final application on which it will be employed. The idea of the BPT, as presented before, is to be a generic data representation. The BPT construction process, which is presented in detail in the following section, only exploits the internal relationships within the data being, consequently, independent of the final application. Hence, the BPT has to be constructed only once per dataset which is also an advantage since it is the step that has a larger computational complexity of the processing chain.

On the other hand, the BPT exploitation or pruning, as presented before, may be seen as *application dependent* since it looks for useful regions for a particular application. Then, once the BPT has been constructed for a specific dataset, it may be employed for different applications through different pruning processes. This is an important fact about the proposed processing scheme since usually the BPT pruning is the fastest step of the presented chain.

This separation of the processing procedure into two parts has some other attractive implications. Note that this scheme decouples the application independent and the application dependent part of the processing chain. As a consequence, if each application is defined in terms of a BPT pruning pruning process, it allows the generalization of the application rationale from the original data space. Therefore, the same pruning process may be exported to a completely different data domain for which the BPT structure has been constructed and is available. In other words, the application rationale is defined and generalized in terms of the BPT abstraction being, then, independent of the data. Some examples of this generalization capability will be seen on Chapters 4 and 5.

3.2 BPT Construction

The previous sections have described the BPT structure and how it may be interpreted. Additionally, a basic processing scheme has been outlined on Fig. 3.6 which is based on two main steps: the BPT construction and its exploitation through a tree pruning. In this section, the BPT construction process will be described in detail, that is, the procedure to generate the structure presented on Fig. 3.5b from the original dataset, shown on Fig. 3.5a.

A direct approach to face this process will be to start from the root node of the tree, the whole dataset, and start to divide it recursively into two smaller regions up to the single data elements, conforming the leaves of the tree. This approach may be seen as a *top-down* approach, since it starts from the root node, represented at the top of the drawing, to the leaves of the tree, at the bottom. Note that, in this case, the two smaller regions must be connected regions and mutually disjoint in order to preserve the BPT structure as defined before.

However, this top-down approach may present some difficulties to be implemented. Given a region, the number of possible divisions may become extremely high even for small regions and, moreover, there is not a clear way to define or perform the *optimal division* at each step. Instead of this approach, a divide and conquer strategy is proposed, splitting this large problem into smaller ones until they become tractable. Divide and conquer is a well-known paradigm in algorithm design[1], and merge sort [56] or Fast Fourier Transform (FFT) [38] are two common examples. When pushing this idea to the limit we arrive to the individual data elements and, then, the construction may be proposed from a *bottom-up* approach. In this approach, starting from the individual data elements, two adjacent regions are merged to generate a larger one at each construction step until the root node is generated. This approach is more feasible computationally, since the number of adjacent regions is smaller than the number of possible divisions for a given region.

Consequently, an iterative BPT construction algorithm was defined in [109], based on the aforementioned bottom-up approach. Note that, in this algorithm, the sequence of regions that are merged during the construction process completely defines the final BPT obtained. This sequence is called the *merging sequence*. On the example presented in Fig. 3.5, for instance, the merging sequence will contain the original leaf nodes and the sequence of pairs of adjacent regions that are merged: $(\{A, B, C, D\}, (B, D)|(E, C)|(A, F))$.

In order to obtain a meaningful BPT abstraction, some criterion has to be employed to decide which pair of regions should be merged at each construction step. If we want a data representation containing regions representing areas with similar values, a *similarity criterion* may be employed. With this in mind, a BPT construction algorithm was proposed in [109], based on merging at each iteration the two *most similar* neighboring regions. This involves the evaluation of the *similarity* between regions, which is conceptualized as a *similarity measure*.

3.2.1 Region Model

Since each node of the tree represents a region of the original data, a region model is introduced into every node, to describe the useful information contained within and to characterize the region. From a computational point of view, this region model is a descriptor of the region, avoiding the need to visit all the single elements of the region in order to characterize it, which would be very inefficient.

This region model should ideally be complete enough to be able to represent properly all the regions within the tree, ranging from single element regions, the tree leaves, to the whole dataset, the root node. The definition of this region model can be an arduous task but, in fact, a good region model is essential to obtain a good BPT data representation, as it will be seen on the following sections.

---

[1] The first known divide and conquer algorithm is considered to be the Euclidean algorithm, to compute the greatest common divisor of two numbers, which is dated about 375 BC.

3.2.2 DISSIMILARITY MEASURE

The similarity measure conceptualizes the amount of similarity between two adjacent regions. Since each region is described by a region model, the similarity measure d is defined on the region model domain space $d : X \times X \mapsto \Re$, where X represents the region model domain.

As mentioned before, the role of this similarity measure d is to guide the BPT construction algorithm to obtain a meaningful representation, by defining the merging order. Mathematically, a *metric* or *distance* measure are typical choices for this purpose in similar applications. However, for the BPT construction process, we are interested only on the ordering they define over the possible merging choices, not on their current values. Taking this into account, this measure may be considered to be more similar to an *heuristic function*, typically used in mathematical optimization or search algorithms. As a consequence, the mathematical properties of d may be relaxed with respect to a distance measure and, henceforth, it will be called *dissimilarity measure* [17]. Then, the following properties are assumed for a dissimilarity measure

1. $d(A, B) \geq d_0$ (generalized non-negativity)
2. $d(A, B) = d_0 \Leftrightarrow A = B$ (identity of indiscernibles)
3. $d(A, B) = d(B, A)$ (symmetry)

3.2.3 CONSTRUCTION ALGORITHM

As mentioned before, the BPT construction algorithm is based on merging at each iteration the two most similar adjacent regions. To model the concept of adjacency or neighborhood between the different regions, a Region Adjacency Graph (RAG) is employed [108]. On a RAG each node represents a connected region and each edge represents the neighborhood relation between two regions. Additionally, the edges are weighted employing the dissimilarity measure d described before, to indicate the similarity between the regions. Then, for each pair of adjacent regions A and B an edge is added to the RAG $\mathbf{W}$ having as weight $d(A, B)$, as shown on Fig. 3.7.

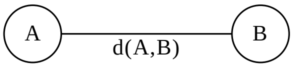

Figure 3.7: Weighted Region Adjacency Graph. An edge is added for every neighboring relation weighted by the dissimilarity measure.

In order to construct the BPT, as an initialization step, the RAG $\mathbf{W}$ has to be constructed from the original data. Algorithm 3.1 describes the algorithm for the construction of $\mathbf{W}$ from the original dataset **D** employing the dissimilarity measure d. The first loop of the algorithm initializes the RAG by inserting all the nodes whereas the second loop introduces all the edges between them.

Algorithm 3.1 RAG generation algorithm

```
Require: dataset $\mathbf{D}$, dissimilarity measure $d$
Ensure: RAG $\mathbf{W}$ is generated
for each element $i \in \text{data\_elements}(\mathbf{D})$ do
    $I \leftarrow \text{create\_node}(i)$
    $\text{add\_node}(\mathbf{W}, I)$
end for
for each node $I \in \text{nodes}(\mathbf{W})$ do
    for each node $K \in \text{neighborhood}(I)$ do
        $e \leftarrow \text{create\_weighted\_edge}(I, K, d(I, K))$
        $\text{add\_edge}(\mathbf{W}, e)$
    end for
end for
```

Once the RAG **W** has been constructed, the BPT construction algorithm, as described before, may be performed. This process is detailed on Algorithm 3.2, where **B** represents the BPT structure. The first loop initializes the BPT with all the nodes of **W** that will become the leaves of the final BPT generated. Then, at each iteration the edge e having the smallest weight is selected and the two corresponding regions A and B are merged to generate a larger node F, that will become their father node on **B**. Accordingly, the RAG **W** gets updated to represent this new state by removing A and B and inserting F. All the other edges involving A or B have to be updated to point to the father node F, indicating that F is a neighbor of all the adjacent nodes of A and B. Finally, this process is repeated until no adjacent regions are found on **W**, that is, there are no more possible region merges.

Fig. 3.8 represents all the states of **W** and **B** during the described BPT construction as described in Algorithm 3.2 for the example represented on Fig. 3.5. At each state, the edge from **W** with the smaller weight has been colored in blue, to represent the edge e that is selected and whose nodes are merged by the algorithm at each step.

The complexity [5] of Algorithm 3.1, induced by the second loop, may be considered to be $O(k_n n) = O(n)$, where n represents the number of elements in the dataset **D** and k_n is a constant indicating the number of neighbors per element. This k_n is defined by the connectivity scheme which, in most cases, may be considered to be a constant number for each element.

Algorithm 3.2 BPT construction algorithm

```
Require: RAG $\mathbf{W}$, dissimilarity measure $d$
Ensure: BPT $\mathbf{B}$ is constructed
$\mathbf{B} \leftarrow \emptyset$
for each node $K \in$ nodes($\mathbf{W}$) do                                   ▷ Initialize $\mathbf{B}$
    add_node($\mathbf{B}$, $K$)
end for
while edges($\mathbf{W}$) $\neq \emptyset$ do                                        ▷ BPT construction
    $e \leftarrow$ min(edges($\mathbf{W}$))
    $A, B \leftarrow$ nodes($e$)
    $F \leftarrow$ merge($A, B$)
    add_node($\mathbf{W}$, $F$)
    for each node $K \in$ (neighbors($\mathbf{W}$, $A$) $\cup$ neighbors($\mathbf{W}$, $B$)) $\setminus \{A, B\}$ do
        $n \leftarrow$ create_weighted_edge($F, K, d(F, K)$)
        add_edge($\mathbf{W}$, $n$)
    end for
    remove_edges($\mathbf{W}$, edges_from($A$) $\cup$ edges_from($B$))
    remove_nodes($\mathbf{W}$, $\{A, B\}$)
    add_node($\mathbf{B}$, $F$)
    $l \leftarrow$ create_edge($F, A$)
    $r \leftarrow$ create_edge($F, B$)
    add_edge($\mathbf{B}$, $l$)
    add_edge($\mathbf{B}$, $r$)
end while
```

According to Property 3.2, a BPT with n leaves will have $2n - 1$ nodes in total. Consequently, $n - 1$ nodes have to be generated during the construction algorithm. Then, the second loop of the Algorithm 3.2 will last for $n - 1$ iterations, since one node is generated at each iteration, being the father node of the two selected regions. However, note that on this loop the search for the minimum edge and the update of $\mathbf{W}$ is performed. This task may require an inspection of all the edges, having a complexity $O(n)$, raising the total complexity of the algorithm to $O(n^2)$. Alternatively, a search structure may be employed in order to sort and find arbitrary edges more efficiently, having $O(\log n)$ computational cost. It is worth noticing that, when employing this search structure, the complexity of Algorithm 3.1 raises to $O(n \log n)$. Nevertheless, in this situation, the complexity of the BPT construction algorithm is reduced to $O(k_n n \log n)$ which may be considered to be $O(n \log n)$ if the amount of neighboring regions per regions may be considered bounded by a constant factor k_n along the whole construction process. In fact, this is the case if the BPT construction is constructed properly, since regions of similar detail scale are present among the whole process. In order to achieve this goal, the region size is a term that has to be taken into account when defining similarity measures, as it will be described in the

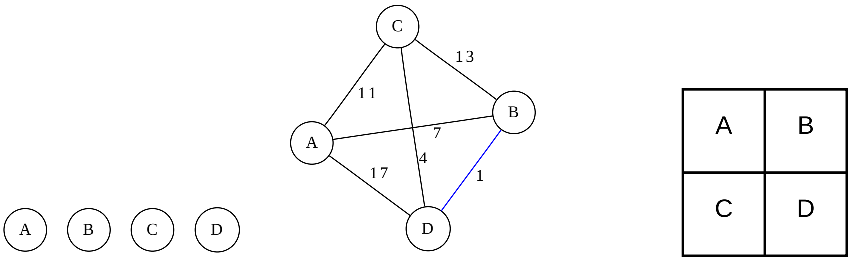

(a) **B** at first step **(b)** **W** at first step **(c)** Regions at first step

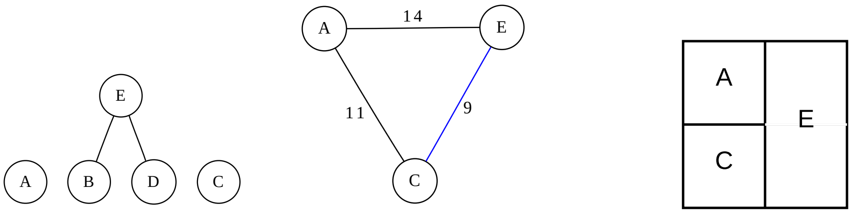

(d) **B** at second step **(e)** **W** at second step **(f)** Regions at second step

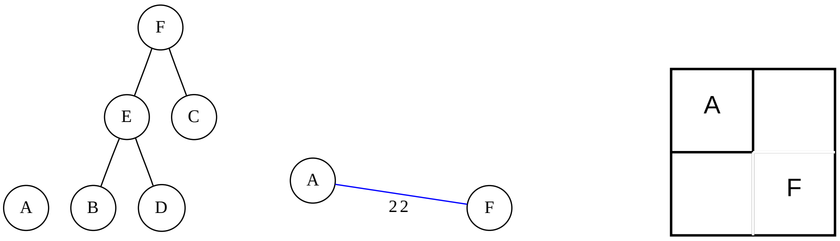

(g) **B** at third step **(h)** **W** at third step **(i)** Regions at third step

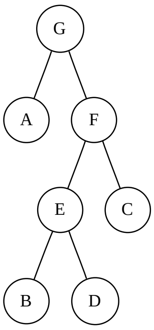

(j) Final BPT **B** generated

Figure 3.8: BPT construction process step-by-step. RAG and regions for each step is also represented. The edge for the two most similar regions is colored in blue.

following chapter.

It is worth to mention that the $O(n \log n)$ complexity is attained assuming that all the operations performed during the BPT construction presented in Algorithm 3.2 are executed in constant time, including the *merge* operation. That is, the region model of the generated node may be computed in constant time taking into account the region model of its two son nodes. In the event that the region model computation of the merged region could not be calculated efficiently this way, the total cost may raise to $O(n^2)$, increasing considerably the complexity of the algorithm, probably resulting in being intractable for large images. This may happen, for instance, if the region model computation requires the inspection of all the individual elements of each region. Thus, the region model computation *efficiency* is something to be taken into account. The region models that will be employed in this work are considered efficient in the sense that they produce a global $O(n \log n)$ complexity.

3.3 BPT Exploitation

The previous sections have described the process of generating the BPT structure from the original data. This structure is intended to be an abstract representation of the dataset, containing also additional information related to its structure at different detail levels. Once it has been constructed, the ultimate objective is to employ it to extract useful results for different applications. As mentioned before, this BPT exploitation process is completely application dependent, since it looks for meaningful regions for a particular purpose. This process may present some difficulties, as the BPT is larger and more complex than the original data. However, its hierarchical structure encourages an agile navigation within it and the definition of efficient algorithms for this purpose. In the following section, a generic algorithm will be described intended to extract from the BPT the most useful or interesting regions for a particular application.

3.3.1 Tree Pruning Process

As mentioned previously, a tree pruning process will be considered for BPT exploitation. Computationally, it may be seen as a tree simplification in order to remove some branches representing small details of the data that are not relevant for the application. From a practical point of view, this process may also be seen as a node selection from the tree, that is, the extraction of the most useful or interesting regions from the BPT structure [109]. It is worth to mention that the BPT structure is not modified during this tree pruning process, as we are just interested in the leaves of the pruned tree, which are obtained from the BPT with this process. Then, the same BPT may be employed for many different prunes for distinct applications.

In this context, a pruning criterion Υ has to be defined to conceptualize this notion of usefulness. A region X, then, may be considered as useful if $\Upsilon(X)$ evaluates to true. The BPT pruning process will look for regions that fulfill Υ within the tree. However, in order to construct a valid tree pruning, the following conditions should be considered:

1. Each element of the original data has to be assigned to a pruned region. This condition may also be seen as that the set of pruned regions must cover the whole dataset.

2. All the pruned regions must be mutually disjoint, that is, each element only corresponds to a single pruned region.

In practice, it may happen that within the same tree branch different subnodes have distinct behavior in terms of Υ, as it may be seen on Fig. 3.9a. In Fig. 3.9 the nodes that fulfill Υ are colored in blue, whereas the nodes that not fulfill it are represented in red. As it may be seen, the L node, for instance, fulfills $\Upsilon(L)$ whereas its son node K does not. Some criterion has to be defined, according to the pruning conditions previously stated, in order to determine the tree pruning for these situations. This selection problem will be called the *pruning decision problem*. Two main possible solutions are considered:

- On the one hand, the larger regions from the tree may be pruned that fulfill the criterion Υ. Note that this process is equivalent to start from the root node and, navigating to the leaves, prune the first nodes found that fulfill Υ. Accordingly, this process may be called *top-down* tree pruning, and it is represented on Fig. 3.9b. As a consequence, the larger regions from the dataset fulfilling Υ will be obtained with this pruning.

- On the other hand, a region may be selected for pruning if and only if it and all of its subnodes fulfill Υ. This process may also be seen as, starting from the leaves of the tree and navigating to the root node, prune the first nodes those father nodes do not fulfill Υ. Therefore, this process will be called *bottom-up* tree pruning, and it is represented on Fig. 3.9c.

In general, the top-down tree pruning may seen as the pruning process that produces more filtering, as larger regions from the tree are obtained, whereas the bottom-up pruning may be seen as the one that preserves more details, as its pruning requirements are stricter, resulting in smaller pruned regions. This effect may be clearly observed when comparing Figs. 3.9b and 3.9c. As it may be seen, on the top-down BPT pruning the node L gets pruned as it fulfills $\Upsilon(L)$ whereas on the bottom-up pruning it cannot be pruned as one of its sons, the K node, does not fulfill it. On the other hand, the I node may be pruned as all of its subnodes fulfill Υ.

It is worth to mention that the region-based processing of the BPT is related with connected operators and morphological image processing techniques [110]. In fact, the pruning decision problem is produced when the pruning criterion Υ is *non-increasing*. A criterion may be math-

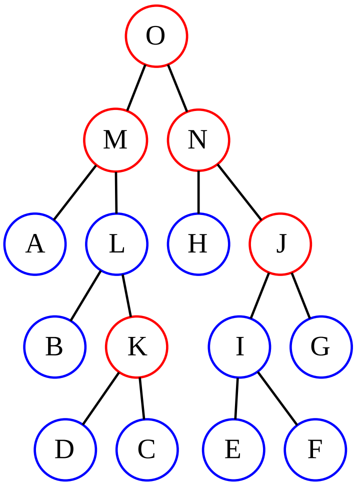

(a) Original BPT

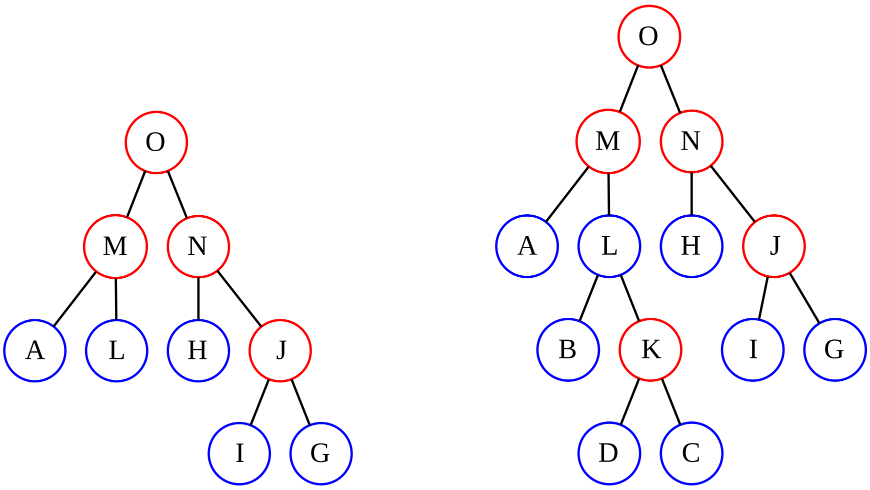

(b) Top-down pruned BPT **(c)** Bottom-up pruned BPT

Figure 3.9: BPT pruning processes. Nodes that fulfill Υ are colored in blue, whereas nodes that not fulfill it are colored in red.

ematically considered increasing if

$$\forall R_1 \in R_2 : \Upsilon(R_1) \Rightarrow \Upsilon(R_2). \tag{3.1}$$

Additionally, the top-down and the bottom-up pruning strategies correspond to the *Min-rule* and *Max-rule*, respectively, as defined in [14].

The top-down BPT pruning process may be implemented in an efficient manner, as described in Algorithm 3.3. In this algorithm, the BPT **B** is traversed in a depth-first search. Starting from the root node R, each node A of the tree is checked for the pruning criterion $\Upsilon(A)$. If the node

A fulfills Υ, it is included into the set of pruned nodes Θ, otherwise the two child nodes of A are checked. This process is repeated until a node fulfilling Υ or a tree leaf is found. Note that the need to include a tree leaf even in the case it does not fulfills Υ is mandatory to guarantee that each element of the dataset is assigned to a pruned region (pruning condition 1, defined before in page 58). For instance, on the example presented in Fig. 3.9b, the set of pruned regions will be $\Theta = \{A, L, H, I, G\}$.

Algorithm 3.3 Top-down BPT pruning algorithm

```
Require: BPT $\mathbf{B}$ completely generated with root node $R$, pruning criterion $\Upsilon$
Ensure: The set $\Theta$ contains the pruned regions
$\Theta \leftarrow \emptyset$
$\mathbf{Q} \leftarrow \{R\}$                                    ▷ Initialize queue $\mathbf{Q}$ with root node $R$
while $\mathbf{Q} \neq \emptyset$ do
    $K \leftarrow$ extract_first_node($\mathbf{Q}$)
    if $\Upsilon(K)$ or is_leaf($K$) then
        $\Theta \leftarrow \Theta \cup \{K\}$
    else
        $A, B \leftarrow$ sons($\mathbf{B}, K$)
        $\mathbf{Q} \leftarrow \mathbf{Q} \cup \{A, B\}$
    end if
end while
```

The bottom-up pruning process may be performed in a similar manner, starting from the leaves of the tree and navigating upwards to the root node R. For each leave node A it will navigate through the ancestor nodes until a node J not fulfilling the pruning criterion $\Upsilon(J)$ is found. The pruned node, then, will be the ancestor just before J. In this case, as the pruning process starts from all the leaves of the tree, the first pruning condition stated before is automatically achieved. However, the bottom-up approach requires a more complicated mechanism in order to ensure that the set of pruned regions corresponds to a disjoint segmentation of the original dataset. It is possible that different nodes get selected for pruning, coming from the bottom-up traversal starting at different leaves, over the same branch, resulting in the undesirable situation that one pruned region contains the other, as represented in Fig. 3.10.

As it may be seen in Fig. 3.10, when starting the bottom-up pruning process from leaf node L_1, the first region selected for pruning is node B, as all the ancestor nodes from L_1 to B fulfill Υ. Note that, since father nodes are generated by the merging of its two child nodes, all the ancestors of a given node contain the region represented by this node. More formally, for each node K of the BPT $\forall F \in \text{ancestors(K)} : K \subset F$. When starting the pruning process from L_2

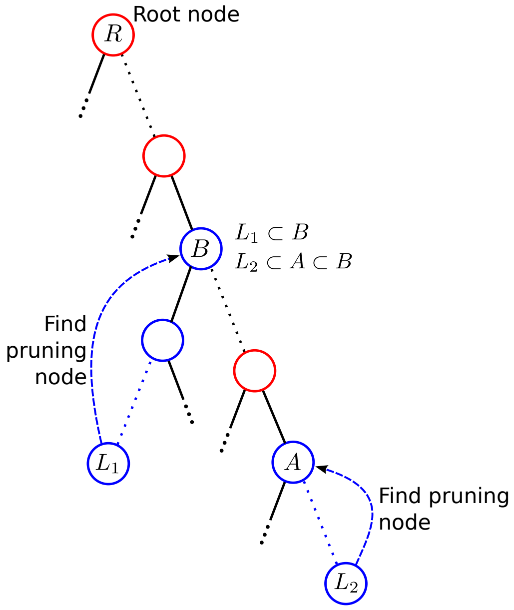

Figure 3.10: Situation when bottom-up BPT pruning may select two non disjoint regions. Nodes that fulfill Υ are colored in blue, whereas nodes that not fulfill it are colored in red.

a node is found not fulfilling Υ before arriving to B and, then, node A is selected for pruning. However, since the B node is a common ancestor with A, two regions A and B have been selected for pruning having $A \subset B$ which do not fulfill the second pruning condition, as they are not mutually disjoint.

On the situation presented in Fig. 3.10, the node B may not be pruned, as it contains nodes not fulfilling the Υ pruning criterion. Nonetheless, this situation may not be observed until the pruning process has been started from all of its leaves, in order to inspect all of its subnodes. To circumvent these situations, an additional verification step in the pruning algorithm is proposed in order to verify that the selected pruning region is disjoint (pruning condition 2, defined before in page 58). First, when a node A is pruned all of its ancestors are marked as non-eligible, as they represent regions containing some of the already pruned ones. Secondly, if during this step a node B is found which has been previously selected for pruning, it is replaced by the set of sibling nodes $\mathbf{S}$ of all the ancestors from A to B. Note that $\mathbf{S}$ are the larger possible nodes that cover the B region without including the A region, that is, the region represented by $\mathbf{S} \cup \{A\}$ is covering the same area than B. Fig. 3.11 shows the proposed verification process when applied to the previous situation and Algorithm 3.4 describes the proposed bottom-up pruning process that ensures mutually disjoint pruned regions.

The complexity of the top-down BPT pruning algorithm is $O(n)$ at most, where n repre-

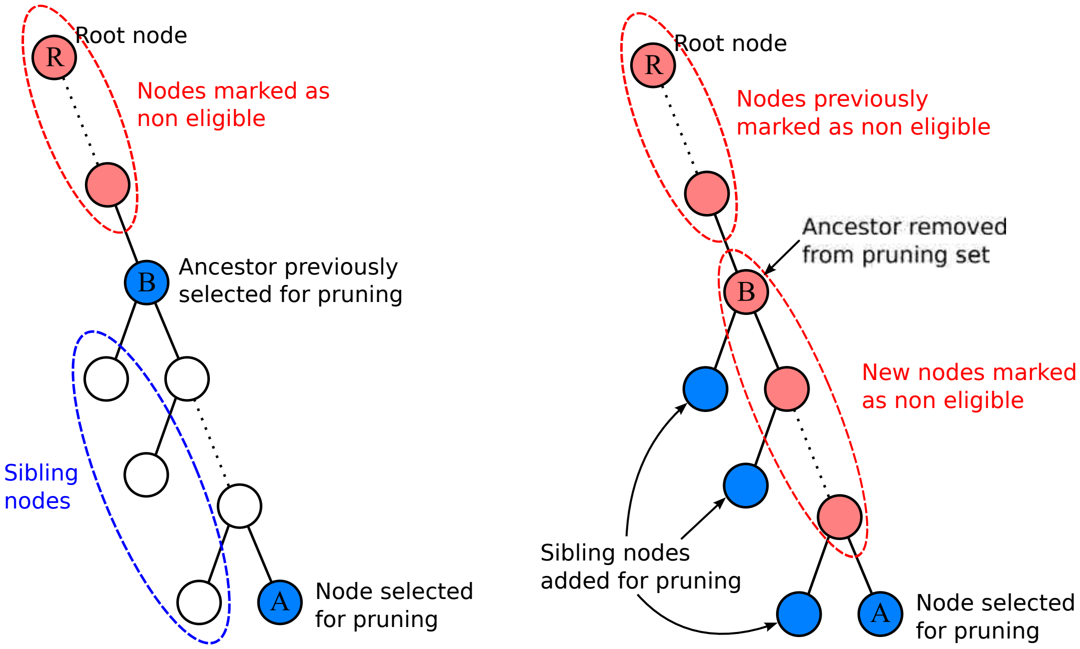

(a) Before disjoint verification **(b)** After disjoint verification

Figure 3.11: BPT disjoint verification process performed during bottom-up pruning after node A gets selected for pruning. Nodes selected for pruning set are filled with blue, whereas nodes marked as non-eligible are filled with red.

sents the number of nodes in the BPT, as it is traversing through the BPT nodes only once. On the other hand, the bottom-up tree pruning algorithm has a complexity that is not so obvious to compute, due to the disjoint verification process. Note that all the nodes above the final pruned set Θ get traversed only once, as they are properly marked as non eligible by the first node pruned within, and subsequent verification processes stop when a non eligible node is found. However, the nodes below the pruned ones may be traversed more than once, resulting in computational cost of $O(n \log n)$, assuming that the tree is not unbalanced, or $O(n^2)$ in the extreme case of an unbalanced tree. This increased computational cost is produced due to the fact that the process is initiated on each leaf of the tree, resulting in repeated navigation over some paths. To make it more efficient, it may be implemented in a top-down fashion, employing a recursive Depth First Search (DFS) [50] over the tree, in order to avoid path repetition [2]. This concept is employed in Algorithm 3.5, which, in fact, produces exactly the same results than Algorithm 3.4. In this case, the complexity is reduced to $O(n)$ as each node is traversed only once thanks to the recursive scheme of the DFS. However, this algorithm is more complex

---

[2] The first known version of DFS was developed during the 19th century as an strategy to solve mazes [43] by French mathematician Charles Pierre Trémaux.

Algorithm 3.4 Bottom-up BPT pruning algorithm

```
Require: BPT $\mathbf{B}$ completely generated with root node $R$, pruning criterion $\Upsilon$
Ensure: The set $\Theta$ contains the pruned regions
$\Theta \leftarrow \emptyset$
$\mathbf{N_e} \leftarrow \emptyset$                                          ▷ Set of not eligible nodes
for each node $K \in$ leaves($\mathbf{B}$) do
    while $K \neq R$ and $\Upsilon$(father($\mathbf{B}, K$)) and father($\mathbf{B}, K$) $\notin \mathbf{N_e}$ do    ▷ Find pruning node
        $K \leftarrow$ father($\mathbf{B}, K$)
    end while
    $\Theta \leftarrow \Theta \cup \{K\}$
    $\mathbf{S} \leftarrow \emptyset$                                          ▷ Set of sibling nodes
    while $K \neq R$ and father($\mathbf{B}, K$) $\notin \mathbf{N_e}$ do           ▷ Disjoint verification process
        $\mathbf{S} \leftarrow \mathbf{S} \cup$ sibling($R$)
        $K \leftarrow$ father($\mathbf{B}, K$)
        $\mathbf{N_e} \leftarrow \mathbf{N_e} \cup K$
        if $K \in \Theta$ then
            $\Theta \leftarrow (\Theta \setminus \{R\}) \cup \mathbf{S}$    ▷ Replace previously selected node for pruning by $\mathbf{S}$
        end if
    end while
end for
```

to understand since it follows a different approach than the intuitive idea behind a bottom-up approach and, consequently, the previous algorithms and examples are provided in order to better understand the rationale of the bottom-up pruning concept.

3.4 BPT Limitations

As mentioned in previous sections, the BPT is intended to be a generic region-based and multi-scale data abstraction. In section 3.2.3 an algorithm has been defined for BPT construction from the original data. This algorithm is based on the merging at each iteration of the two most similar neighboring regions. Note that this scheme corresponds to the selection at each step of the locally optimal decision. Then, this algorithm may be considered as a *greedy algorithm* [39]. However, it is worth to mention that the selection of the locally optimal decision at each step does not necessarily produce a global optimum solution. This strategy is usually performed in order to produce an approximation of the global optimum solution for complex problems at a reasonable time. Nevertheless, a greedy algorithm only found the global optimum solution if the problem has *optimal substructure*, that is, an optimal solution can be constructed efficiently

Algorithm 3.5 Bottom-up BPT pruning algorithm implemented as a top-down Depth First Search

```
procedure BOTTOM_UP_PRUNE($\mathbf{B}, \Upsilon, R$)
Require: BPT $\mathbf{B}$ completely generated with root node $R$, pruning criterion $\Upsilon$
Ensure: The set $\Theta$ contains the pruned regions
    $\Theta \leftarrow \emptyset$
    $N_e \leftarrow \emptyset$
    DFS_RECURSIVE_PRUNE($\mathbf{B}, \Upsilon, \Theta, \mathbf{N_e}, R$)
end procedure

procedure DFS_RECURSIVE_PRUNE($\mathbf{B}, \Upsilon, \Theta, \mathbf{N_e}, K$)
Require: BPT $\mathbf{B}$ completely generated, pruning criterion $\Upsilon$
Ensure: Pruned nodes within $K$ are added into $\Theta$ set and $\mathbf{N_e}$ gets updated accordingly
    if is_leaf($K$) then                                          ▷ Base case
        if not $\Upsilon(K)$ then
            $\Theta \leftarrow \Theta \cup \{K\}$
        end if
    else
        $A, B \leftarrow$ sons($\mathbf{B}, K$)
        DFS_RECURSIVE_PRUNE($\mathbf{B}, \Upsilon, \Theta, \mathbf{N_e}, A$)             ▷ DFS recursive calls
        DFS_RECURSIVE_PRUNE($\mathbf{B}, \Upsilon, \Theta, \mathbf{N_e}, B$)
        if $A \in \mathbf{N_e}$ or $A \in \Theta$ then        ▷ If $A$ or one of its subnodes has been pruned
            $\mathbf{N_e} \leftarrow \mathbf{N_e} \cup \{K\}$                       ▷ Mark $K$ as non eligible
            if $B \notin \mathbf{N_e}$ and $B \notin \Theta$ then
                $\Theta \leftarrow \Theta \cup \{B\}$             ▷ Prune $B$ as its father is non eligible
            end if
        else if $B \in \mathbf{N_e}$ or $B \in \Theta$ then   ▷ If $B$ or one of its subnodes has been pruned
            $\mathbf{N_e} \leftarrow \mathbf{N_e} \cup \{K\}$                       ▷ Mark $K$ as non eligible
            $\Theta \leftarrow \Theta \cup \{A\}$                 ▷ Prune $A$ as its father is non eligible
        else if not $\Upsilon(K)$ then
            $\Theta \leftarrow \Theta \cup \{A, B\}$
        end if
    end if
end procedure
```

from optimal solutions of its subproblems[3] [39]. In the general case, this property does not necessarily holds and, consequently, the BPT construction may lead to sub-optimal representations, although there is not a clear way to define the optimality of a BPT.

Another intrinsic limitation of the BPT is that each region is produced by the merging of its

---

[3] A typical example of optimal substructure is the change-making problem. Most currencies have a set of coin values presenting this property in order to facilitate the computation of the change.

two child nodes. As a consequence, new nodes represent regions of the data having as contours a combination of the previous ones. Equivalently, no new contours are generated during the BPT construction process. This may be a problem for some datasets, where *optimal regions*, under some criterion, may have different contours for different detail levels. Fig. 3.12 represents this scenario. Over the original data, on Fig. 3.12a, the optimal segmentation into 2 and 3 regions are represented in Figs. 3.12c and 3.12b, respectively. Note that the contour of the 2 optimal regions in Fig. 3.12c is completely different to the contours of the 3 optimal regions, in Fig. 3.12b. In this case, there is no possible merging of the 3 optimal regions in order to obtain the regions corresponding to Fig. 3.12c. The possible regions obtained with the BPT are represented in Figs. 3.12d and 3.12e, corresponding to the merging of $A \cup B$ or $B \cup C$ regions. As a consequence, in this scenario the BPT structure may not contain the optimal regions at all detail levels since no new contours are generated when producing larger regions of the tree structure.

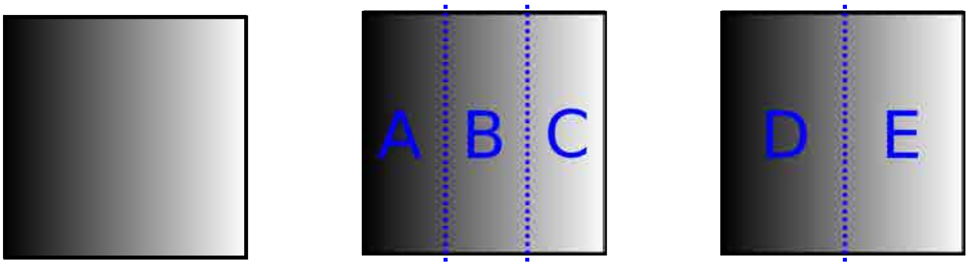

(a) Original

(b) Optimal segmentation into 3 regions

(c) Optimal segmentation into 2 regions

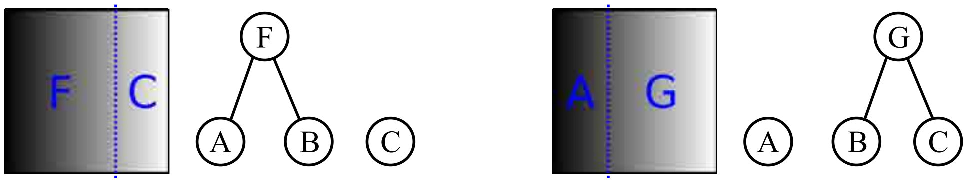

(d) BPT regions after merging A and B

(e) BPT regions after merging B and C

Figure 3.12: Since on BPT new regions are formed by merging of existing ones, no new contours may appear on new regions.

It always seems impossible until it's done.

Nelson Mandela

4

Polarimetric SAR Image BPT based Processing

PolSAR data have to be described statistically for distributed targets and, in order to attain a proper estimation, a sample averaging has to be performed, as mentioned in Chapter 2. However, this estimation has to be performed only over homogeneous areas and, in practice, SAR data are strongly heterogeneous as it reflects the complexity of the scene. Then, the motivation to employ the BPT in this scenario is to be able to adapt to the spatial structure and to extract the homogeneous areas of the image.

The Chapter 3 has introduced the key theoretical concepts involving the BPT and its processing. The present chapter is devoted to describe its employment to process PolSAR image data for the speckle filtering and coastline segmentation applications [8][9][11]. It will describe all the details involving its adaptation to represent and process this type of data.

As mentioned in Chapter 3, the BPT based processing scheme may be decomposed into two main steps: the BPT construction and its exploitation for different applications. Consequently, this chapter is divided into these main parts.

4.1 PolSAR Image BPT Construction

This section describes all the concepts required to apply the BPT construction process that has been generically defined in Section 3.2 for PolSAR data. The objective is to be able to apply the BPT construction algorithm, as described in Algorithm 3.2, for a single PolSAR image.

4.1.1 PolSAR Image Connectivity Scheme

The BPT is a region-based data representation, where the region concept stands for a connected data segment of the data, as described in Section 3.1.1. As a consequence, the data connectivity has to be defined for every pixel of the PolSAR image. From a computational point of view, this is the set of neighboring pixels for a given one, which is employed in the step prior to the BPT construction, the RAG generation, described in Algorithm 3.1.

The pixel connectivity is a common concept in image processing techniques, being the *4-connectivity* and the *8-connectivity* the most typical choices, as it has been highlighted in Section 3.1.1. A representation of these connectivity schemes has been depicted in Fig. 4.1.

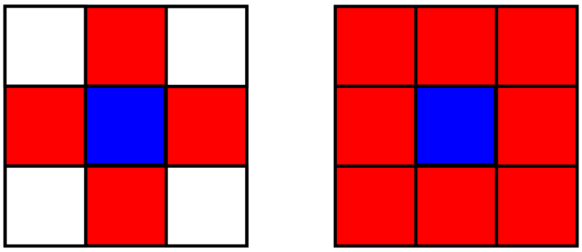

(a) 4-connectivity **(b)** 8-connectivity

Figure 4.1: Pixel connectivity schemes. Every image pixel, in blue, has 4 or 8 neighbors, represented in red.

Reducing the number of neighbors per pixel, as in the case of the 4-connectivity, represented in Fig. 4.1a, has a positive impact in the computational cost, reducing the number of similarity measures computation in the RAG generation and also during the BPT construction. However, this connectivity scheme do not consider diagonal pixels as adjacent, being unable to represent thin diagonal structures of the image as a single region. In this work, the 8-connectivity scheme shown on fig. 4.1b will be employed to avoid this limitation, as it is assumed that physical structures may be present on any orientation of the image.

4.1.2 PolSAR Data Region Model

As mentioned in Section 3.2.1, each node of the BPT represents a connected region of the data through a region model. This region model should be complete enough to describe all the relevant information of the region at all the scales of the tree. Then, in order to apply the BPT structure to PolSAR images, a region model has to be defined to describe the different spatial regions of PolSAR data.

Section 2.2.4 has described the Gaussian polarimetric model for distributed scattering mechanisms. According to this model, the covariance matrix **C** of the distribution completely characterizes the target. Consequently, the sample covariance matrix **Z** has been proposed as an estimator of **C**, which corresponds to its MLE. Therefore, the region A may be represented by its sample covariance matrix $\mathbf{Z}_A$ [8][11]

$$\mathbf{Z}_A = \langle \mathbf{k}\mathbf{k}^H \rangle_{n_A} = \frac{1}{n_A} \sum_{i \in A} \mathbf{k}_i \mathbf{k}_i^H \tag{4.1}$$

where n_A represents the number of pixels within the region A.

In fact, equation (4.1) is very similar to the multilook defined in (2.54), except that the average is computed over the pixels within the region A instead of a fixed window around the central pixel. Using this model is highly convenient as most of the polarimetric inversion and information extraction models are based on the covariance matrix [76][33].

Under the Gaussian hypothesis, the sample covariance matrix **Z** is a good region model to represent homogeneous areas of the image, as described in Section 2.2.4. However, this is not the case for heterogeneous areas, when estimated employing samples following a different statistical distribution. In the BPT, as a multi-scale data representation, regions of very different sizes will be found and some of them, specially the larger regions, may not be considered as homogeneous. This is especially the case for the root node, for instance, covering the whole image. In most of the cases, the whole image is not homogeneous and, consequently, it can not be properly represented by its sample covariance matrix **Z**.

Thus, employing the region model defined in (4.1) will have a negative impact on the larger regions of the BPT, corresponding to the nodes closer to the root, since they may be heterogeneous. In the following sections, the sample covariance matrix **Z** will be employed as a region model for convenience, resulting into the aforementioned limitations for inhomogeneous regions. However, if the final applications for which the BPT is intended to be used are interested only in homogeneous regions of the image, this effect may not be a drawback, as it will be seen.

Another limitation of the sample covariance matrix is that it results into singular matrices when directly calculated over the single pixels of the original image, when $\mathbf{Z} = \mathbf{k}\mathbf{k}^H$. Actually, this is a limitation of the multilook estimator, as described in Section 2.2.4. In practice, this limitation will affect all the regions of the BPT containing a number of pixels n_A smaller than the sample covariance size, that is, $n_A < p$. This fact might constitute a problem for some applications or even for some similarity measures employed for BPT construction. As a consequence, an initial filtering or regularization of the data may be needed for some applications, in order to obtain full-rank matrices for each pixel of the image.

Nonetheless, a more detailed discussion about the limitations on matrix regularization and on representing inhomogeneous regions may be found on Chapter 6, including some improved models and techniques in order to reduce the impact of these restrictions on the BPT and on the final applications.

4.1.3 Dissimilarity Measures for PolSAR Data

The dissimilarity measure defines the merging sequence during the BPT construction process and, consequently, it defines completely the final tree that will be obtained, as explained in Section 3.2.2. It is established in the region model space and, therefore, for PolSAR data it has to be defined over the sample covariance matrix **Z**, as expressed in (4.1).

It is worth to mention that, since the dissimilarity measure is tied to the region model space, all the limitations of the chosen region model will become also limitations on this measure. As mentioned in the previous section, since the sample covariance matrix is not able to represent properly inhomogeneous regions, the dissimilarity measures defined on this space will also fail to evaluate the similarity between these regions, as they are not accurately characterized.

Moreover, as mentioned before, the **Z** matrices may be rank-deficient which may pose a problem for some measures. This limitation may be overcome by employing only the diagonal elements of the covariance matrix, corresponding to the retrieved power for each polarization state. Alternatively, an initial filtering may be applied to obtain full-rank matrices. However, this is normally a small filtering, focused on matrix regularization instead of speckle filtering. Usually a 3 by 3 multilook filter is applied for this purpose, resulting into a very small spatial resolution loss. In this regard, the similarity measures have been classified into full-matrix measures and diagonal measures [8][9]:

- Full-matrix measures employ all the information contained within the sample covariance matrix **Z** and, therefore, they are sensitive to the fully polarimetric information under the Gaussian hypothesis. As a consequence, they are able to achieve better adaptation to the changes at any polarimetric feature. However, they need full-rank sample covariance matrices in order to properly exploit the complete polarimetric space. This fact implies the need of a prior filtering of the data for matrix regularization, as stated before.

- Diagonal measures are focused only on the diagonal elements of the covariance matrix, corresponding to the backscattered power. Mathematically, they are assuming that all the off-diagonal elements are equal to zero. This results automatically in a full-rank matrix, avoiding the problem of having singular matrices and also the need for the initial filtering. However, this assumption is arbitrary and it may not be true and, in fact, the correlation between the different polarimetric channels contains useful information that is ignored by these measures. It is worth noticing that the adaptive Lee and IDAN filters, described in Sections 2.3.2 and 2.3.3, have also this limitation, as they are not exploiting the complete polarimetric information under the Gaussian hypothesis.

FULL-MATRIX DISSIMILARITY MEASURES

On this section, full-matrix dissimilarity measures for PolSAR data are going to be presented. In the following, it is assumed that two adjacent regions, denoted by A and B, having covariance matrices $\mathbf{Z}_A$ and $\mathbf{Z}_B$, respectively, and region sizes of n_A and n_B pixels, are evaluated by the dissimilarity measure d, which is expressed as $d(A, B)$.

- **Symmetric revised Wishart dissimilarity**, denoted by d_{sw}. This measure assumes that the sample covariance matrices $\mathbf{Z}_A$ and $\mathbf{Z}_B$ are following a Wishart distribution and performs a statistical hypothesis test to evaluate if they are following the same distribution [68]. To do so, one of the two sample covariance matrices is assumed to be known, that is, it is assumed that the real covariance matrix $\mathbf{C}$ that defines the distribution is equal to $\mathbf{Z}$. Aside from being false, this assumption involves the inconvenience that the measure depends on which of the two sample covariance matrices is assumed to be known. Therefore, this statistical test is not symmetric, i.e. $d_w(A, B) \neq d_w(B, A)$. A modification is proposed in [68] to generate a symmetric measure d_s as $d_s = d_w(A, B) + d_w(B, A)$. Then, the symmetric revised Wishart measure, defined in [8], is obtained based on this concept and adding a term depending on the region size, as it will be detailed in the following

$$d_{sw}(A, B) = \left(\mathrm{tr}(\mathbf{Z}_A^{-1}\mathbf{Z}_B) + \mathrm{tr}(\mathbf{Z}_B^{-1}\mathbf{Z}_A)\right)(n_A + n_B) \tag{4.2}$$

  where $\mathrm{tr}(.)$ denotes the matrix trace and n_A denotes the number of pixels within the region A.

- The **Geodesic dissimilarity**, designated as d_{sg}, is defined in [9] according to a completely different approach. It considers the positive definite matrix cone geometry [22], that is, the geometry of the sample covariance matrix space. Accordingly, it measures the distance over the geodesic path, instead of the euclidean path, that follows the curvature of the matrix cone space. The geodesic path concept is based on differential geometry [22] and additional details about this concept will be found later in this section. In this case, since it is a measure defined through the matrix logarithm, a modified version is generated by adding a logarithmic term depending on the region size

$$d_{sg}(A,B) = \| \log\left(\mathbf{Z}_A^{-1/2}\mathbf{Z}_B\mathbf{Z}_A^{-1/2}\right) \|_F + \ln\left(\frac{2n_A n_B}{n_A + n_B}\right) \tag{4.3}$$

where $\|.\|_F$ represents the Frobenius matrix norm, $\log(.)$ represents the matrix logarithm and $\ln(.)$ represents the natural logarithm.

- The **Ward relative dissimilarity**, denoted by d_{wr}, is based on a measure from Ward hierarchical clustering [128]. In this clustering technique, an error measure based on the Error Sum-of-Squares (ESS) was introduced to quantify the amount of information loss when two clusters are merged. This measure can also be applied to measure the information loss when merging two neighboring regions. In order to employ it for PolSAR data, a normalization matrix is introduced to tackle the multiplicative nature of the speckle noise. Then, the Ward relative dissimilarity measure may be defined as

  $$d_{wr}(A,B) = n_A \cdot \|\mathbf{N}_{AB}^H(\mathbf{Z}_A - \mathbf{Z}_{AB})\mathbf{N}_{AB}\|_F^2 + n_B \cdot \|\mathbf{N}_{AB}^H(\mathbf{Z}_B - \mathbf{Z}_{AB})\mathbf{N}_{AB}\|_F^2 \tag{4.4}$$

  where $\mathbf{Z}_{AB}$ denotes the covariance matrix of the region $A \cup B$ and $\mathbf{N}_A$ denotes the normalization matrix of $\mathbf{Z}_A$, defined as

  $$\mathbf{N}_A = \begin{pmatrix} \sqrt{Z_{A_{11}}} & 0 & 0 \\ 0 & \sqrt{Z_{A_{22}}} & 0 \\ 0 & 0 & \sqrt{Z_{A_{33}}} \end{pmatrix} \tag{4.5}$$

  where $Z_{A_{ij}}$ refers to the (i,j)-th element of the sample covariance matrix $\mathbf{Z}_A$.

Note that there is a term depending on the region sizes n_A and n_B on all the dissimilarity measures. It is required since, during the BPT construction, regions of different sizes will be compared. The concept represented by this term is that it may be assumed that larger regions will have less noisy estimations of the region model and, then, the dissimilarity over them may be more restrictive than with smaller regions. This idea is in accordance with the Wishart distribution, defined in (2.55), as it depends on the equivalent number of looks n. In addition, this term or similar ones also appear when employing other rationales to define distance or statistical measures over PolSAR data, as it may be seen on [98].

In order to get a better idea of the rationale on which is based the geodesic dissimilarity measure d_{sg}, an example within a simplified space is presented in the following to show the adaptation to the space geometry. Since the 3 by 3 complex covariance matrix space is too complicated to represent graphically, a real symmetric 2 by 2 covariance matrix space will be employed

$$\mathbf{C} = \begin{bmatrix} C_{11} & C_{12} \\ C_{12} & C_{22} \end{bmatrix} = \begin{bmatrix} C_{11} & \sqrt{C_{11}C_{22}}\rho \\ \sqrt{C_{11}C_{22}}\rho & C_{22} \end{bmatrix} \tag{4.6}$$

where $-1 \leq \rho \leq 1$ represents the correlation coefficient.

It may be seen from (4.6) that the 2 by 2 real covariance matrices have three independent components, C_{11}, C_{12}, C_{22}, where the set of possible values for C_{12} depends on the other two. As this space has only three real components, it can be represented graphically in a tree-dimensional plot, as it is shown on Fig. 4.2, where the limits of the space are represented. These boundary surfaces are obtained for the extreme cases $\rho = -1$ and $\rho = 1$. As it can be seen, the space is confined within a cone, which is called the positive definite matrix cone.

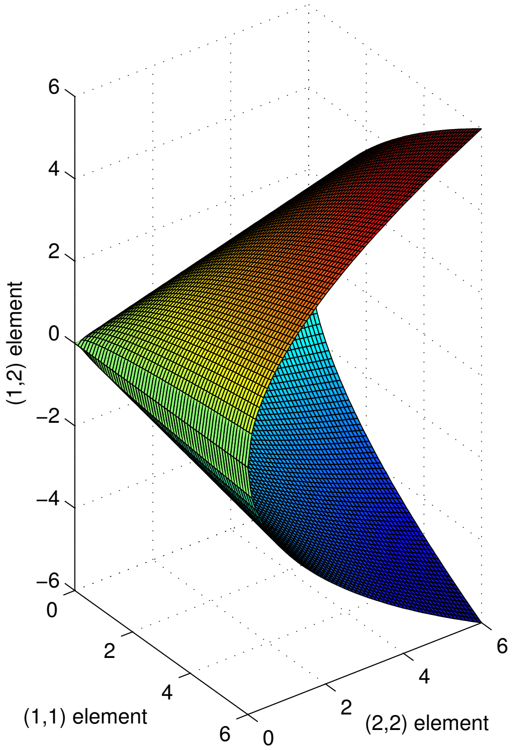

Figure 4.2: The 2 by 2 real symmetric covariance matrix space cone.

In this space, the euclidean distance may be defined as $\|\mathbf{Z}_A - \mathbf{Z}_B\|_F$, whereas the geodesic distance is $\|\log\left(\mathbf{Z}_A^{-1/2}\mathbf{Z}_B\mathbf{Z}_A^{-1/2}\right)\|_F$ [22]. Note that it corresponds to the first term of the geodesic dissimilarity d_{sg}, the term depending on the region sample covariance matrices. The rationale behind that measure is that it is based on the *geodesic path* instead of the euclidean path, which is following the curvature of the positive definite matrix cone space.

Then, the euclidean path γ_e, which length is measured by the euclidean distance, can be defined as

$$\gamma_e(t) = \mathbf{Z}_A + t(\mathbf{Z}_B - \mathbf{Z}_A) \tag{4.7}$$

with $0 \leq t \leq 1$. As it may be seen, $\gamma_e(0) = \mathbf{Z}_A$ whereas $\gamma_e(1) = \mathbf{Z}_B$.

On the other hand, according to [22], the geodesic path γ_g is defined by

$$\gamma_g(t) = \mathbf{Z}_A^{\frac{1}{2}}\left(\mathbf{Z}_A^{-\frac{1}{2}}\mathbf{Z}_B\mathbf{Z}_A^{-\frac{1}{2}}\right)^t\mathbf{Z}_A^{\frac{1}{2}} \tag{4.8}$$

for $0 \leq t \leq 1$.

For this example, the following values for $\mathbf{Z}_A$ and $\mathbf{Z}_B$ are assumed

$$\mathbf{Z}_A = \begin{bmatrix} 2 & -1 \\ -1 & 1 \end{bmatrix}, \quad \mathbf{Z}_B = \begin{bmatrix} 1 & 1 \\ 1 & 2 \end{bmatrix}. \tag{4.9}$$

With these values, the euclidean path γ_e and geodesic path γ_g are represented in Fig. 4.3, in black and magenta colors, respectively. These paths are obtained by changing the t parameter from 0 to 1. The plot over the original space is presented in Fig. 4.3a, where the bounds of the positive definite matrix cone have been also represented. As it may be expected, the euclidean path γ_e follows a straight line from $\mathbf{Z}_A$ to $\mathbf{Z}_B$. On the other hand, the geodesic path γ_g is following a curved line which is adapted to the positive definite matrix cone geometry.

Considering that the geodesic dissimilarity d_{sg} is based on the Frobenius norm in the matrix logarithmic space, the euclidean γ_e and geodesic γ_g paths have been represented also in this space in Fig. 4.3b. It is worth noticing that, as mentioned before, the logarithm applied is the matrix logarithm, not the logarithm to each element of the matrix individually. In this space, the bounds of the positive definite matrix cone can not be represented since when an eigenvalue tends to 0 the matrix logarithm tend its elements to infinity. Therefore, the positive definite matrix cone is unbounded in the logarithmic space. As it can be seen in Fig. 4.3b, in the matrix logarithmic space the euclidean path γ_e appears as a curved line whereas the geodesic path develops a straight line behavior.

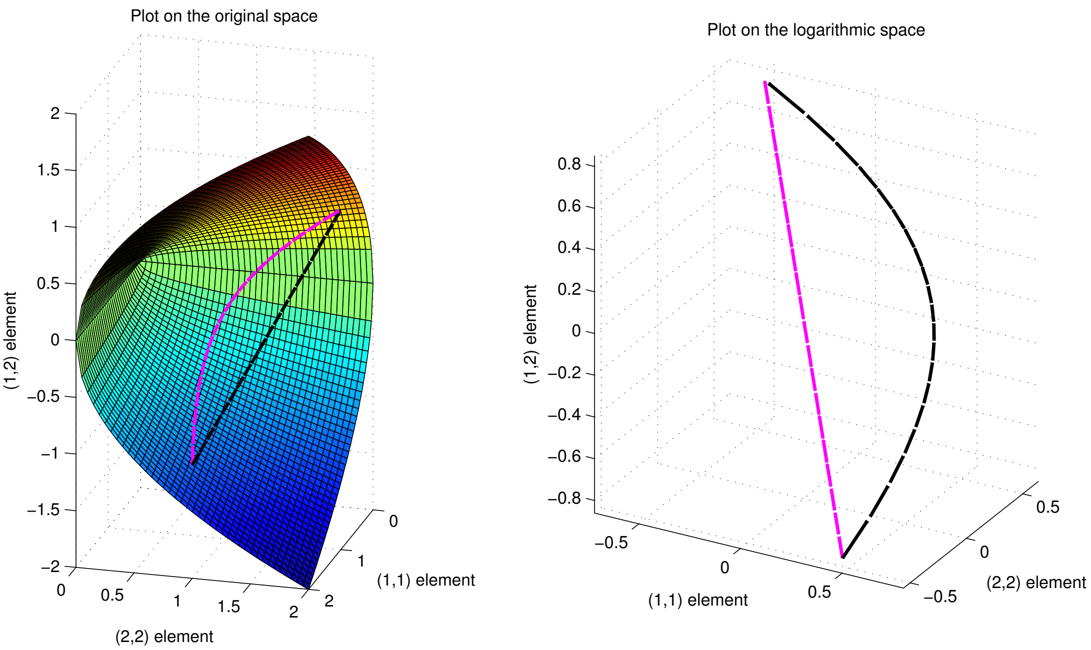

(a) Original space

(b) Matrix logarithmic space

Figure 4.3: Euclidean (black) and geodesic (magenta) paths over the original and logarithmic spaces.

Diagonal Dissimilarity Measures

These measures, as mentioned before, take only into account the diagonal elements of the covariance matrix, that is, the backscattered power for each polarization state. This automatically ensures a full-rank matrix, avoiding the need for an initial filtering for matrix regularization. Assuming that the off-diagonal elements are equal to zero, a diagonal variant of the previous dissimilarity measures may be defined.

- The **Diagonal revised Wishart dissimilarity**, referred to as d_{dw}, is obtained with (4.2) when assuming that $\mathbf{Z}_A$ and $\mathbf{Z}_B$ are diagonal p by p matrices, as mentioned before,

$$d_{dw}(A,B) = \left(\sum_{i=1}^{p} \left(\frac{Z_{A_{ii}}^2 + Z_{B_{ii}}^2}{Z_{A_{ii}} Z_{B_{ii}}} \right) \right) \cdot (n_A + n_B) \tag{4.10}$$

  where $Z_{A_{ij}}$ and $Z_{B_{ij}}$ represent the (i,j)-th element of the estimated covariance matrices $\mathbf{Z}_A$ and $\mathbf{Z}_B$, respectively.

- The **Diagonal geodesic dissimilarity**, designated as d_{dg}, similarly to the previous case

case, is based on (4.3) but assuming that $\mathbf{Z}_A$ and $\mathbf{Z}_B$ are diagonal p by p matrices

$$d_{dg}(A,B) = \sqrt{\sum_{i=1}^{p} ln^2\left(\frac{Z_{Aii}}{Z_{Bii}}\right) + ln\left(\frac{2n_A n_B}{n_A + n_B}\right)} \tag{4.11}$$

Considering that full matrix and diagonal dissimilarity measures are based on the same principles, a comparison between them may be useful to compare the advantages and disadvantages of employing the full matrix information in front of employing only the diagonal information, while assuming that all off-diagonal elements equal to 0.

Furthermore, some additional diagonal dissimilarities have been defined, based on the relative comparison of the matrix diagonal elements.

- **Diagonal relative normalized dissimilarity**, labeled d_{dn}, is based on the euclidean norm of the normalized difference of the matrix diagonal vector. Firstly, the difference of the diagonal vectors is normalized by their sum for each component, which produces a result bounded in the interval $[-1,1]$ for each diagonal element. Secondly, the euclidean norm of the resulting vector is applied and, finally, the d_{dn} dissimilarity measure is obtained after multiplying it by a term depending on the region size

$$d_{dn}(A,B) = \left(\sum_{i=1}^{p}\left(\frac{Z_{Aii} - Z_{Bii}}{Z_{Aii} + Z_{Bii}}\right)^2\right)^{1/2} \cdot (n_A + n_B). \tag{4.12}$$

- The **Diagonal relative dissimilarity**, denoted as d_{dr}, is computed as the euclidean norm of the sum of relative errors of both diagonal elements. Note that this comparison, as opposite to d_{dn}, is not bounded, taking values on the interval $[0,\infty)$. Again, a term depending on the region size is also included to take into account this information

$$\begin{aligned} d_{dr}(A,B) &= \left(\sum_{i=1}^{p}\left(\frac{Z_{Aii} - Z_{Bii}}{Z_{Bii}} + \frac{Z_{Bii} - Z_{Aii}}{Z_{Aii}}\right)^2\right)^{1/2} \cdot (n_A + n_B) \\ &= \left(\sum_{i=1}^{p}\left(\frac{(Z_{Aii} - Z_{Bii})^2}{Z_{Aii}Z_{Bii}}\right)^2\right)^{1/2} \cdot (n_A + n_B). \end{aligned} \tag{4.13}$$

4.2 POLARIMETRIC SAR BPT BASED APPLICATIONS

Once all the components mentioned in Section 4.1 have been defined, it is possible to construct the BPT representation of a PolSAR image, employing the process described in Section 3.2.3.

At this point, some methods have to be defined for the exploitation of this data abstraction for different applications.

It is worth noticing that, as stated in Chapter 3, the whole BPT construction process is application independent and, thus, the same applies for all the concepts defined in the previous section. Then, according to the region model and dissimilarity measures defined in the previous sections, the obtained BPT structure will represent regions of the image having similar polarimetric characteristics, in terms of its sample covariance matrix **Z**. Conversely, the concepts introduced in the following sections are focused on some particular applications and then, two different sections may be found according to distinct applications. Two applications that exploit the PolSAR BPT will be described: speckle filtering and coastline segmentation. Special attention will be paid to the speckle filtering application, that will be analyzed in detail, defining different pruning methods and criteria. Moreover, its results will be evaluated with real and simulated data. Finally, the coastline segmentation application will be described briefly. As it will be seen, the two mentioned applications are completely different and they will exploit distinct information contained within the BPT.

4.3 BPT BASED ESTIMATION OR SPECKLE FILTERING

As mentioned in Chapter 2, SAR images are contaminated by speckle noise, which is a handicap for their further use or interpretation. Most applications require a speckle filtering as a preprocessing step in order to reduce the effect of the speckle and to a achieve a proper estimation of the target polarimetric response. Additionally, as described in Section 2.3, there is a tendency in the recent state-of-the-art speckle filtering techniques to adapt to the spatial content of the image to avoid the mixture of inhomogeneous samples during the speckle filtering process. Therefore, the motivation here is to apply the BPT data abstraction for this purpose.

One of the most important applications of this thesis is the speckle filtering or polarimetric information estimation. In the context of a region-based processing scheme, this is equivalent to the delimitation of the homogeneous areas of the scene, according to the selected region model, the sample covariance matrix **Z**. Once this delimitation of the scene has been performed, the speckle filtering application comes out automatically, since the region model of an homogeneous area may be employed to describe its polarimetric response accurately, under the Gaussian hypothesis.

As outlined in Section 3.3, the BPT exploitation may be performed by a tree pruning process, which extracts the most useful or interesting regions for a particular application. Thus, this section describes two different pruning strategies for the BPT-based estimation or speckle filtering.

Additionally, results will be analyzed in detail both with synthetic and real PolSAR data.

4.3.1 Pruning based on the Number of Regions

One possible BPT pruning mechanism is to define the number of regions N to extract of the image and, in accordance, extract the *N most different* regions from the tree. Note that this pruning strategy requires the definition of a measure to quantify the difference of the regions. However, as described in Section 4.1.3, this is exactly the role of the previously defined dissimilarity measures. Then, the same dissimilarity measure employed for BPT construction may also be also applied for its pruning based on the number of the regions.

Note that, when the same dissimilarity measure is employed for BPT construction and pruning, this pruning strategy is equivalent to stop the BPT construction process when the number of regions N has been achieved. The remaining regions may be considered as the N most different regions according to the dissimilarity measure. This pruning strategy has the advantages of being simple, while also not requiring the definition of any additional criterion for pruning. Moreover, due to its simplicity, it does not require the application of the pruning processes defined in Section 3.3.1, as this pruning is completely defined by the merging order. On the other hand, it has the disadvantage of having to decide the number of regions N parameter, which may be really difficult to figure out a priori.

To see the results obtained by this pruning strategy, Fig. 4.4 and Fig. 4.5 show examples of two 256 by 256 pixel PolSAR image crops, corresponding to some agricultural fields and an urban area, respectively. Data, acquired by the DLR's ESAR system at L-band, will be presented in detail in the following sections devoted to analyze the obtained results in detail. Results are shown for the 9x9 multilook filter, as a reference, and for the mentioned BPT pruning based on the number of regions. Fig. 4.4a and Fig. 4.5a present the original data crop whereas Fig. 4.4c to Fig. 4.4e and Fig. 4.5c to Fig. 4.5e show the results for different number of regions N parameter values.

On these results, as mentioned before, each region has been represented with its estimated sample covariance matrix averaged within the region, and employing a Pauli RGB color composition. For the BPT construction process and, hence, for the pruning process, the geodesic dissimilarity measure d_{sg} described in (4.3) has been employed. Note that, since the d_{sg} measure is employing the full covariance matrix information, an initial filtering is needed for matrix regularization. In this case, an initial 3 by 3 multilook filtering has been employed.

The difference between a region-based and a pixel-based processing is clear when comparing results with the multilook and with the BPT in Fig. 4.4 and Fig. 4.5. The edges on the multilook

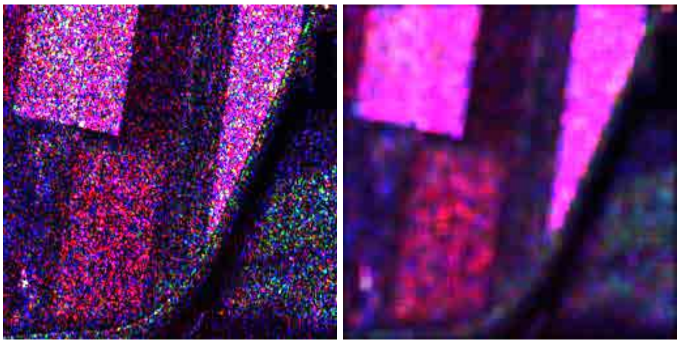

(a) Original **(b)** 9x9 multilook

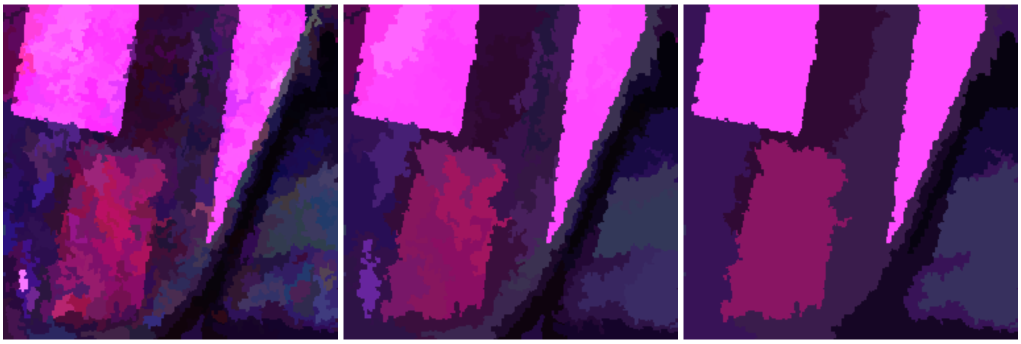

(c) $N = 250$ **(d)** $N = 50$ **(e)** $N = 10$

Figure 4.4: Results after applying the 9x9 multilook and the BPT pruning based on the number of regions of an agricultural fields area for different values of N. The BPT has been constructed employing the geodesic d_{sg} dissimilarity. Images are represented using Pauli RGB composition $(|S_{hh} + S_{vv}|, |S_{hv} + S_{vh}|, |S_{hh} - S_{vv}|)$.

appear blurred, due to the spatial resolution loss produced by this low-pass filtering. On the other hand, the edges of the BPT region appear perfectly clear, as filtering is performed independently within each pruned region, which is the processing element of the BPT and, consequently, since all the pixels of a given region have the same region model, they appear with a constant color over the results. Moreover, it may be seen that the BPT-based region contours are following the contours of the scene, except when the number of regions N is too small to represent properly the complexity of the scene, resulting into large regions mixing different areas of the image.

The multi-scale nature of the BPT may also be seen on Figs. 4.4 and 4.5, when changing the number of regions parameter N. Reducing the N parameter results into larger regions, pruning nodes of the tree closer to the root. Increasing N has the opposite effect, obtaining regions farther from the root and closer to the leaves of the tree. It is worth noticing that all the regions obtained for the different parameters, in this case $N = \{250, 50, 10\}$, correspond to the same

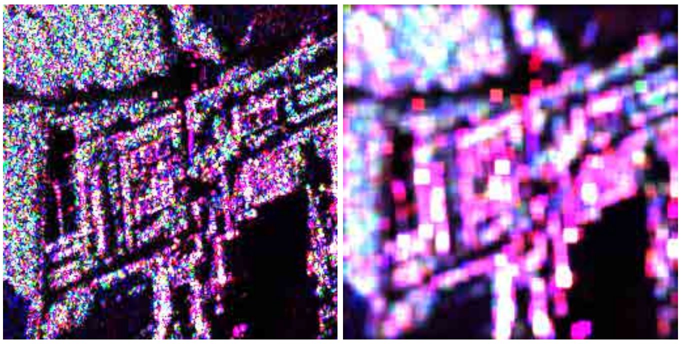

(a) Original **(b)** 9x9 multilook

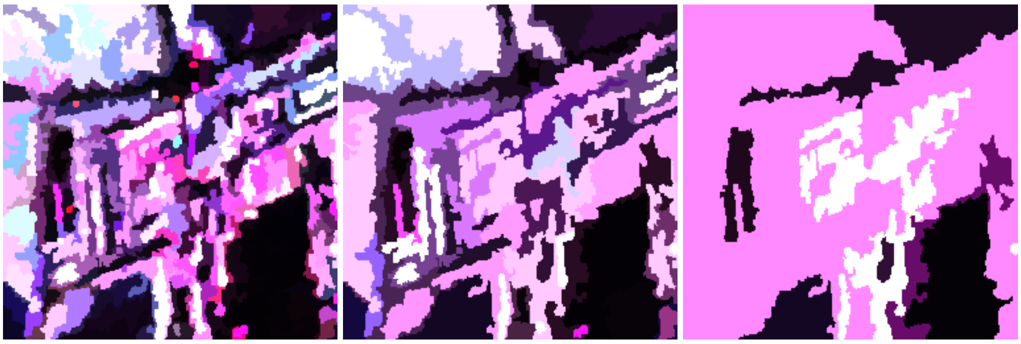

(c) $N = 250$ **(d)** $N = 50$ **(e)** $N = 10$

Figure 4.5: Results after applying the 9x9 multilook and the BPT pruning based on the number of regions of an urban area for different values of N. The BPT has been constructed employing the geodesic d_{sg} dissimilarity. Images are represented using Pauli RGB composition $(|S_{hh} + S_{vv}|, |S_{hv} + S_{vh}|, |S_{hh} - S_{vv}|)$.

BPT, but pruned at different detail levels, clearly showing the multi-scale nature of this data representation.

Another consideration when analyzing results obtained in Figs. 4.4 and 4.5 is that there is no clear way to define the optimum number of regions N. Furthermore, it strongly depends on the scene complexity. On the agricultural area, for instance, where large homogeneous regions may be found, a small value of N, even $N = 10$, may be enough to properly represent all the regions of the scene, as it may be seen in Fig. 4.4e, whereas on urban areas, having a much more complex spatial structure, this value is totally inadequate, as seen in Fig. 4.5e, requiring a larger value, in the order of $N = 250$ or even larger, as shown on Fig. 4.5c.

In order to perform a more detailed analysis of the region sizes, Table 4.1 shows the minimum and the maximum size, in pixels, of all the pruned regions for each case of the results shown on Figs. 4.4 and 4.5. Additionally, Fig. 4.6 shows the histograms of the pruned region sizes for the

	Agricultural zone			Urban zone		
Number of regions N	250	50	10	250	50	10
Minimum region size	44	157	1693	1	45	45
Maximum region size	570	2539	12094	918	4948	40430

Table 4.1: Pruned regions and region sizes in pixels over urban and agricultural areas for BPT pruning based on the number of regions with different N.

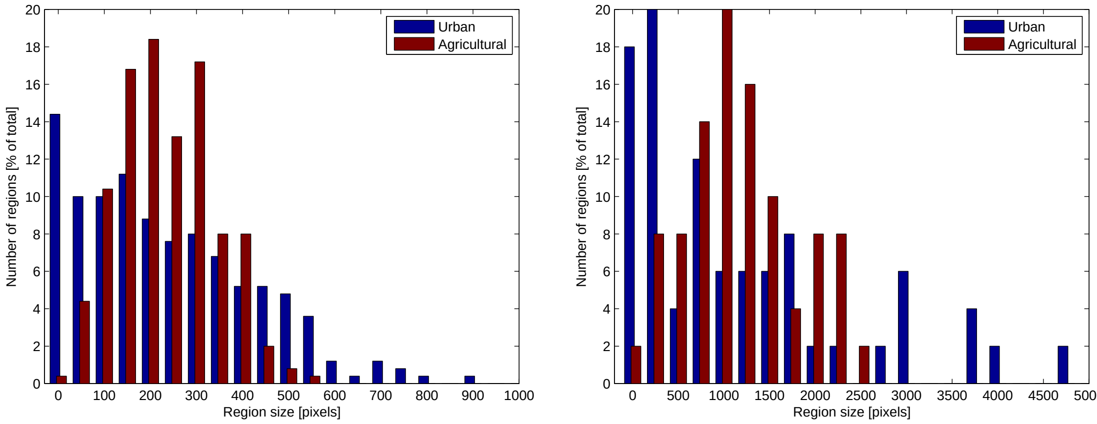

(a) $N = 250$ **(b)** $N = 50$

Figure 4.6: Region size histograms for $N = 250$ and $N = 50$ over agricultural and urban area images presented in Fig. 4.4 and Fig. 4.5.

previous pruning results obtained at $N = 250$ and $N = 50$ values.

Analyzing the differences between the region size histograms of the two environments, it can be seen that the dynamic range of the pruned region sizes is much more narrow in the agricultural area than in the urban area, mainly because the difference in complexity of both scenes. Moreover, it can be seen that the region sizes obtained are very dependent on the pruning parameter N, as it may be expected, as the average region size is fixed by N according to the total number of pixels over N. Also, for $N = 250$ the maximum region size density for agricultural area is between 150-400 pixels, with around 80% of total regions, whereas for $N = 50$ only 8% of regions are within these values. One would expect that, since the structure of the image is the same, those values should be more similar for both cases.

In conclusion, although the BPT pruning based on the number of regions may be simpler, as it does not require the introduction of any new concept or measure, it has the disadvantage of having to choose the number of regions N parameter a priori. This is a difficult task, as it strongly depends on the image structure, being not easy to figure out a priori. Additionally, the obtained region sizes have a strong dependence with the N parameter, when in fact they should depend more on the image structure. This is consistent with the fact that dissimilarity measures have a strong dependence with the region size, as stated on Section 4.1.3. Indeed, the underlying problem is that the number of regions is highly dependent on the image structure and, then, it can not be employed as a pruning parameter when we want to obtain a segmentation that adapts to this image structure.

Another limitation of this pruning strategy is that it is based only on the region model to define the pruned regions, as it is based on the dissimilarity measure. Then, as stated in Section 4.1.2, all the limitations of this model for representing an heterogeneous region are also transfered to this pruning approach. As a consequence, this method may not obtain proper results for relatively small values of N, depending on the scene spatial complexity.

4.3.2 HOMOGENEITY BASED PRUNING

The BPT pruning based on the number of regions, described in the previous section, has shown the ability of the BPT to adapt to the spatial structure of the image. Additionally, its region-based and multi-scale nature have been shown through different examples. However, some important drawbacks have been detected, specially regarding to the definition of the N pruning parameter and its dependence with the image structure. In order to overcome all these limitations, the following guidelines need to be taken into account:

1. Ideally, the pruning parameter should be completely independent of the image structure, to avoid the trouble of defining a different value for each image.

2. The dependence of the pruned region sizes with the pruning criterion should be avoided as much as possible, allowing that regions with completely different sizes appear at the same tree pruning.

3. To avoid the propagation of the region model limitations, the pruning criterion should depend on all the pixel values contained within the region, not only on the region model, to mitigate the problems when dealing with heterogeneous regions, for instance.

With all these guidelines in mind, a new BPT pruning strategy is defined. Ultimately, the main goal of the PolSAR information estimation or speckle filtering process is to extract the largest homogeneous areas of the scene. Accordingly, an homogeneity measure Φ is defined, in order to estimate the region homogeneity. The pruning process, then, is performed by applying a pruning threshold δ_p over this measure, by marking a region A for pruning if $\Phi(A) < \delta_p$. Note that, in this case, the pruning algorithms defined in Section 3.3.1 have to be applied.

Note that, for each region A, the homogeneity measure $\Phi(A)$ should be independent of its size, in order to fulfill the second guideline, and it should depend not only on its region model, according to the third guideline. With this in view, the first point is automatically fulfilled since Φ is a measure of the homogeneity of the given region, which is assumed to be dependent only on the spatial content within it. Accordingly, the following homogeneity measure Φ is defined

$$\Phi(A) = \frac{1}{n_A} \sum_{i \in A} \frac{\|\mathbf{Z}^i - \mathbf{Z}_A\|_F^2}{\|\mathbf{Z}_A\|_F^2} \tag{4.14}$$

where $\mathbf{Z}^i$ represents the covariance matrix of pixel i within region A, $\mathbf{Z}_A$ represent its estimated covariance matrix and n_A its total number of pixels.

It is worth to mention that (4.14) may also be seen as the relative Mean Squared Error (MSE) that is committed when representing all the pixels of the region $\mathbf{Z}_i$ by its sample covariance matrix $\mathbf{Z}_A$. In contrast to the classical MSE, the Φ region homogeneity (4.14) is a relative error measure, as it is divided by the squared norm of the region model $\|\mathbf{Z}_A\|_F^2$ in order to cancel out the multiplicative nature of the speckle noise.

With the proposed region homogeneity measure Φ, a pruning criterion Υ_h may be defined in order to select from the tree only homogeneous regions. Accordingly, a region A may be defined as homogeneous if it has a relative MSE below a pruning threshold δ_p value

$$\Upsilon_h(A): \quad \Phi(A) < \delta_p. \tag{4.15}$$

In the following, for convenience, the pruning factor δ_p will be expressed in dB, corresponding to the following expression

$$\Upsilon_h(A): \quad 10 \cdot log_{10}\left(\Phi(A)\right) < \delta_p(dB). \tag{4.16}$$

With the proposed Υ_h pruning criterion, in contrast to the pruning based on the number of regions defined in Section 4.3.1, the number of regions obtained is automatically defined by the image content. The pruned regions will be as large as possible while maintaining a relative MSE below the threshold. As a consequence, for a given δ_p value, a large number of small regions will be obtained naturally in images having complex structures, whereas large regions will be obtained in images having large homogeneous areas. And, what is even more important, the appropriate region size may be obtained in all cases when having an image with a combination of large and small structures.

For comparison purposes, the same PolSAR images than on Figs. 4.4 and 4.5 have been processed with the homogeneity based region pruning. Fig. 4.7 and Fig. 4.8 show the images presented in Fig. 4.4a and Fig. 4.5a, corresponding to an agricultural and a urban area, respectively, filtered employing the defined region homogeneity based pruning Υ_h for different pruning factor δ_p values.

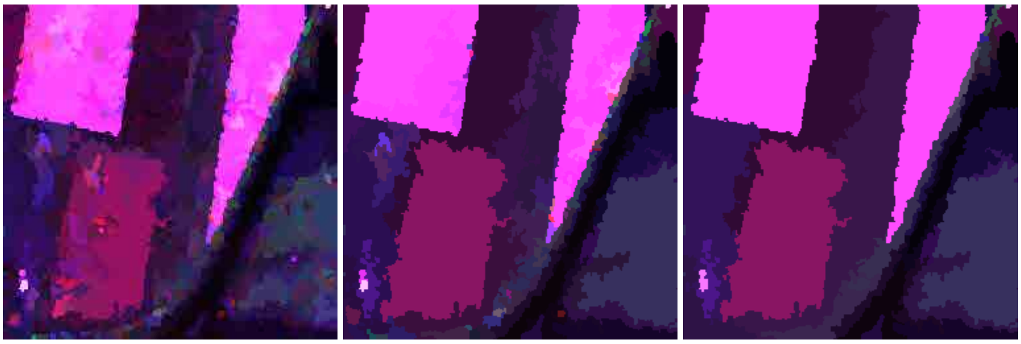
(a) $\delta_p = -2dB$ **(b)** $\delta_p = -1dB$ **(c)** $\delta_p = 0dB$

Figure 4.7: BPT homogeneity based pruning of an agricultural fields image for different values of δ_p. The BPT has been constructed employing the geodesic d_{sg} dissimilarity. Images are represented using Pauli RGB composition ($|S_{hh} + S_{vv}|$, $|S_{hv} + S_{vh}|$, $|S_{hh} - S_{vv}|$).


(a) $\delta_p = -2dB$ **(b)** $\delta_p = -1dB$ **(c)** $\delta_p = 0dB$

Figure 4.8: BPT homogeneity based pruning of an urban area image for different values of δ_p. The BPT has been constructed employing the geodesic d_{sg} dissimilarity. Images are represented using Pauli RGB composition ($|S_{hh} + S_{vv}|$, $|S_{hv} + S_{vh}|$, $|S_{hh} - S_{vv}|$).

When comparing Fig. 4.7 with Fig. 4.4, roughly similar results may be seen for pruning thresholds $\delta_p = -2, -1, 0\ dB$ than for $N = 250, 50, 10$. The contours of the fields are closely obtained in both cases and large regions may be retrieved corresponding to them. However, when analyzing in detail the results of the region based homogeneity pruning, important differences are observed. Even for a large pruning threshold, in the case of $\delta_p = 0dB$, small details are preserved in the image, as it may be seen on the down-left part of Fig. 4.7c, that is, a larger range of values is observed for the obtained region sizes. This fact is produced thanks to the independence of the pruning criterion from the region size, which was, indeed, one of the premises of the pruning strategy. Nonetheless, the benefits of this pruning mechanism become much more evident in the results presented in Fig. 4.8 in comparison with Fig. 4.5. In this scenario, the spatial complexity of the image is significantly higher, presenting a large number of small regions and, in fact, the region homogeneity based pruning adapts to this scenario producing a much larger number of regions than for the agricultural area, even when employing the same pruning threshold parameters. This adaptation was, in fact, another of the proposed guidelines for this pruning strategy.

In order to assess this adaptation numerically, Table 4.2 shows the achieved number of regions and the maximum and minimum region size for each pruning process of Figs. 4.7 and 4.8.

	Agricultural zone			Urban zone		
δ_p	$-2dB$	$-1dB$	$0dB$	$-2dB$	$-1dB$	$0dB$
Number of regions	502	116	32	2652	1696	1043
Minimum region size	2	4	11	1	1	1
Maximum region size	3602	8697	8698	898	1403	3052

Table 4.2: Pruned regions and region sizes in pixels over urban and agricultural areas for homogeneity based pruning with different pruning threshold δ_p values.

The adaptation of the region based homogeneity pruning to the image structure is clear from the number of pruned regions, corresponding to the second row of Table 4.2. As observed on the results, over urban area a large number of smaller regions are obtained, as they correspond to the small structures that are present on the scene. On the other hand, for the same pruning threshold δ_p values, larger regions are obtained in the agricultural area than on urban area. The ability to preserve small details while also having large regions for homogeneous areas may also be seen when comparing the minimum and maximum region sizes, which is an improvement compared with the pruning based on the number of regions, as previously shown on Table 4.1.

To analyze the region size distribution closely, Fig. 4.9 presents the region size histograms for different pruning thresholds δ_p over the agricultural and the urban area. It is worth mentioning that for the urban area, shown on Fig. 4.9a, the maximum density of region sizes is around 20 pixels for all the pruning factor values whereas for the agricultural area, depicted in Fig. 4.9b, this value is around 100 pixels, but it is also maintained for different δ_p values.

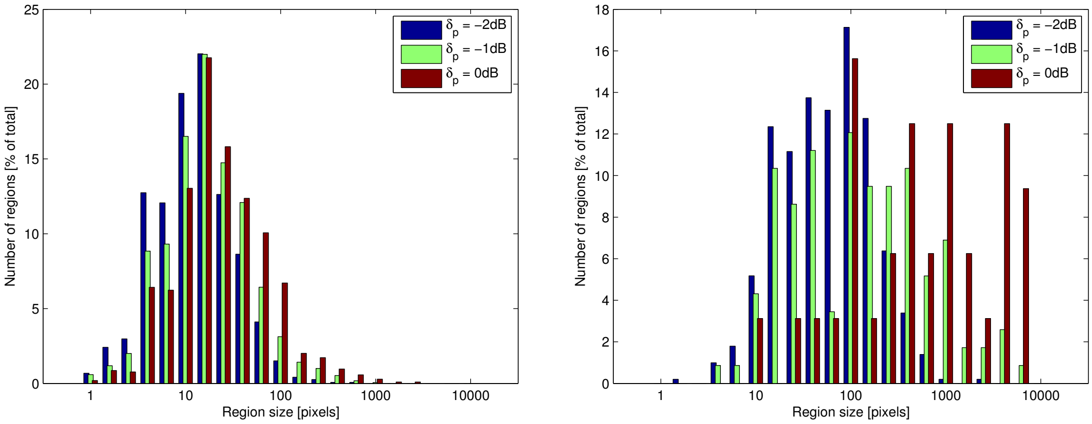

(a) Urban area **(b)** Agricultural area

Figure 4.9: Logarithmic region size histograms for different pruning factor δ_p values over agricultural and urban area images presented in Fig. 4.4 and Fig. 4.5.

All in all, the homogeneity based pruning is able to obtain a wider range of region size values than the pruning based on the number of regions, since it is independent of the region size. Additionally, it does not depend on image size or complexity, resulting into similar filtering values for a given δ_p in any type of image or scenario. The number of regions is automatically obtained by the pruning criterion Υ_h in order to fulfill the relative MSE on all the pruned regions, extracting as large regions as possible from the BPT. This pruning strategy, then, overcomes all the major drawbacks of the pruning based on the number of regions, as described in Section 4.3.1. On the other hand, it is more complex than the pruning based on the number of regions, as it requires the definition and the computation of the region homogeneity measure $\Phi(A)$ for each region A of the tree and, additionally, it requires to apply the pruning algorithm to the tree. However, when comparing this increase in complexity with the BPT construction process, it is negligible, as the pruning procedure is much faster. Furthermore, the region homogeneity measure $\Phi(A)$ may be computed efficiently in a bottom-up approach in linear time respect to the number of nodes.

It is worth noticing that all the results shown in Figs. 4.4 and 4.7 and in Figs. 4.5 and 4.8 correspond to different pruning processes over the same BPT structures. This fact may give an idea of the large amount of information that may be extracted from the BPT data abstraction of a PolSAR image.

4.3.3 RESULTS WITH REAL DATA

This section is devoted to a more detailed analysis of the previously described pruning mechanisms with real PolSAR data. In particular, they will be compared with some state-of-the-art speckle filtering techniques described in Section 2.3. Moreover, their ability to estimate the covariance matrix without introducing any bias or distortion will be also analyzed.

In the previous sections some examples have been presented to illustrate the effects of the pruning strategies defined. These examples are small crops of a full dataset having different areas that will be processed and studied in this section. This full dataset corresponds to a measuring campaign conducted by DLR in 1999 with its experimental ESAR system over the Oberpfaffenhofen test-site, southern Germany. Data were collected at L-band, with a spatial resolution of 1.5m x 1.5m in fully polarimetric mode. The whole PolSAR image has 2816 rows by 1540 columns and its Pauli RGB representation is shown in Fig. 4.10a. The scene contains some urban areas, having different buildings and human made structures, in the central part of the image, a forest area in the top part and an agricultural area, with large fields and grass areas, in the bottom area.

Fig. 4.10b shows the result obtained after applying the BPT homogeneity based pruning with a pruning threshold $\delta_p = -2dB$. In this case, the BPT has been constructed employing the symmetric revised Wishart d_{sw} dissimilarity measure, as defined in (4.2). When comparing it with the original image, qualitatively the same colors are observed but it appear much less noisy. The contours of the filtered image seem to correspond to the structure of the original image and the small details are also preserved.

In order to compare the BPT-based estimation approach with other speckle filtering techniques, the dataset presented in Fig. 4.10a has been processed with a 7x7 multilook as a reference, the IDAN[1] filter [125], and the two proposed BPT pruning approaches: pruning based on the number of regions and region homogeneity based pruning. Although the whole dataset has been processed, to perform a more detailed analysis of the filtering techniques, results will be studied over a 512 by 512 pixel crop of the full dataset, presented in Fig. 4.11a. The area of the scene within this crop contains large agricultural fields at the bottom part of the image and a urban area with small details in the center and right parts. A forest area can also be found at the top part of the image. This crop area of the results after applying the 7x7 multilook and the IDAN filtering are shown on Fig. 4.11b and Fig. 4.11c, respectively.

---

[1] The PolSARPro [3] IDAN implementation has been employed for this work, with a maximum AN size parameter of 100 pixels.

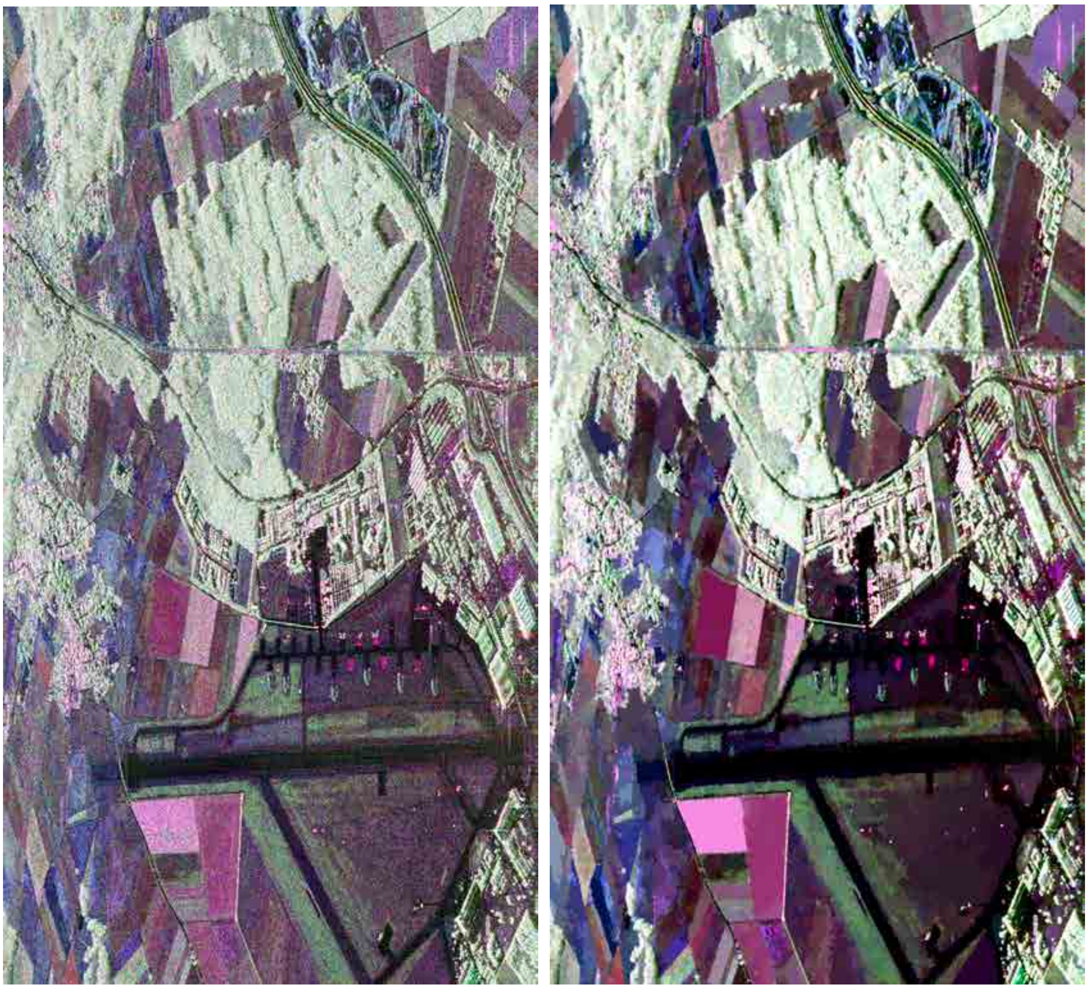

(a) Original **(b)** $d_{sw}, \delta_p = -2dB$

Figure 4.10: Pauli representation of the original and BPT-based filtered images of Oberpfaffenhofen. The revised Wishart dissimilarity measure d_{sw} has been employed for BPT construction and region homogeneity based pruning with $\delta_p = -2dB$ ($|S_{hh} + S_{vv}|$, $|S_{hv} + S_{vh}|$, $|S_{hh} - S_{vv}|$).

As mentioned previously, the multilook, shown in Fig. 4.11b, is able to achieve a relatively good amount of speckle filtering but it results into a spatial resolution loss, blurring all the contours and small details of the image. On the other hand, the IDAN, shown in Fig. 4.11c, has a better spatial resolution preservation, as it maintains the contours and details. However, the amount of speckle reduction achieved by the IDAN is smaller than in the multilook case.

Results after applying the proposed BPT-based approach over the same area are represented in Fig. 4.12. The figures on the left column (Figs. 4.12a, 4.12c, 4.12e) correspond to BPT prun-


(a) Original **(b)** 7x7 multilook **(c)** IDAN

Figure 4.11: Detail Pauli RGB images. (a) Original, (b) filtered with 7x7 multilook and (c) filtered with IDAN ($|S_{hh}+S_{vv}|$, $|S_{hv}+S_{vh}|$, $|S_{hh}-S_{vv}|$).

ing based on the number of regions[2] whereas the right column (Figs. 4.12b, 4.12d, 4.12f) show the results of region homogeneity based pruning. Note that all the results in Fig. 4.12 have been generated by pruning over the same BPT, constructed with the symmetric revised Wishart d_{sw} dissimilarity over the entire image, presented in Fig. 4.10a.

Analyzing the BPT-based estimation results in Fig. 4.12, the differences previously mentioned between the two defined pruning mechanisms may be seen. Moreover, when processing a large dataset, the inconveniences of the BPT pruning based on the number of regions are even more evident. In the examples processed in Sections 4.3.1 and 4.3.2, two small crops of this dataset have been processed. These crops, however, contained only one type of scenario: a agricultural area or a urban area. In a large PolSAR image, as the one represented in Fig. 4.10a, having a mixture of different types of areas, it is not possible to define a number of regions parameter N suitable for all the areas. A large value, such as $N = 50000$, shown in Fig. 4.12a, may be required for a proper representation of the urban area. Nevertheless, over the agricultural area a smaller value of N will be required, in the order of $N = 2000$, as shown in Fig. 4.12e. As a consequence, there is no possible value of N suitable to obtain a good detail representation over all the areas of the image.

On the other hand, the region homogeneity based pruning results, shown in the right column of Fig. 4.12, do not present these issues. In this case, the pruning threshold parameter δ_p acts like an indicator of the degree of filtering, showing more details for smaller values $\delta_p = -2dB$ than for larger ones $\delta_p = 0dB$, as shown in Figs. 4.12b to 4.12f. However, the region size adapts

---

[2] Note that the results are shown over a detailed area of 512 by 512 pixel, but the whole image, presented in Fig. 4.10a is processed. Then, the number of regions N refers to the regions in the whole image and, thus, only a small subset of regions appear over the crop area shown.

(a) $d_{sw}, N = 50000$ **(b)** $d_{sw}, \delta_p = -2dB$

(c) $d_{sw}, N = 10000$ **(d)** $d_{sw}, \delta_p = -1dB$

(e) $d_{sw}, N = 2000$ **(f)** $d_{sw}, \delta_p = 0dB$

Figure 4.12: Detail Pauli RGB images. (a), (c), (e) filtered with pruning based on the number of regions and (b), (d), (f) filtered with region homogeneity based pruning ($|S_{hh} + S_{vv}|$, $|S_{hv} + S_{vh}|$, $|S_{hh} - S_{vv}|$).

better to the content of the scene, as larger regions are observed in the agricultural areas than in the urban zone for all the pruning threshold δ_p values, being able to properly represent all the regions of the image with a given pruning threshold.

Another characteristic of the BPT-based pruning is that when the pruning threshold δ_p or N parameters gets increased or decreased, respectively, resulting into larger regions, some region contours of the image disappear, but no new contours appear, as it may be seen on the image sequence from Figs. 4.12a, 4.12c, 4.12e and Figs. 4.12b, 4.12d, 4.12f. This is a consequence of the way in which new regions are generated on the BPT. Since larger regions are always constructed as the merging of two smaller ones, only the contours between them are not present in the father region, while the rest of them are preserved.

In order to show more clearly this ability of the region homogeneity based pruning to preserve small details of the original image and, at the same time, perform strong filtering over large homogeneous areas, a crop of the original image containing five corner reflectors over an homogeneous field, near to the main runway of the airport, in the bottom part of the original image, shown in Fig. 4.10a, has been processed. The results are shown in Fig. 4.13 for the multilook, the IDAN and the region homogeneity based pruning techniques for different δ_p values.

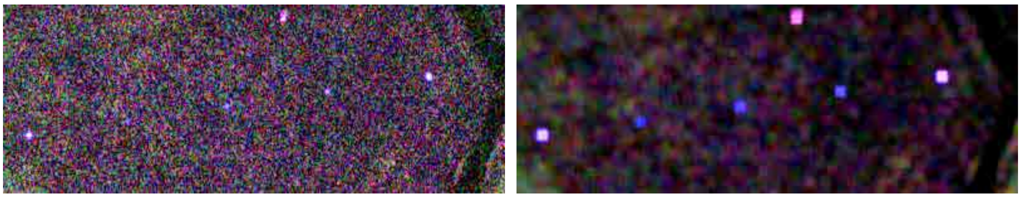

(a) Original

(b) 7x7 multilook

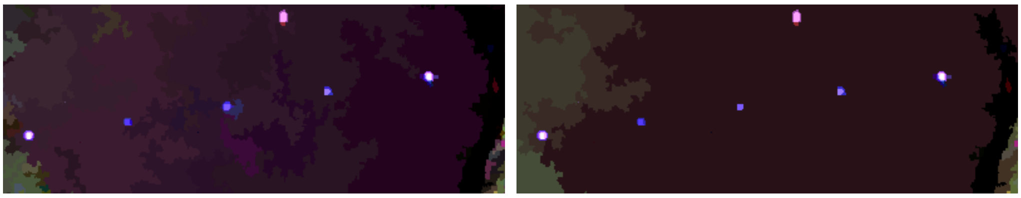

(c) $d_{sw}, \delta_p = -2dB$

(d) $d_{sw}, \delta_p = -1dB$

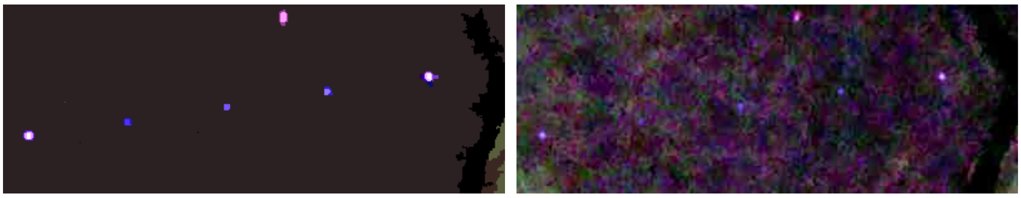

(e) $d_{sw}, \delta_p = 0dB$

(f) IDAN

Figure 4.13: Detail Pauli RGB images of corner reflectors preservation with the multilook, the IDAN and the BPT based filtering ($|S_{hh} + S_{vv}|$, $|S_{hv} + S_{vh}|$, $|S_{hh} - S_{vv}|$).

The original image crop containing the corner reflectors is represented on Fig. 4.13a. As it may be seen, they are difficult to identify due to their small size and the high level of speckle noise in the area. The 7x7 multilook filter, whose results are shown on Fig. 4.13b, reduces significantly the speckle over the field and the corner reflectors appear highly contrasted but, since they have much more reflectivity than the surrounding area, they appear enlarged according to the filter window. The IDAN filter, depicted in Fig. 4.13f, has a good detail preservation, preserving the corner reflectors, but the amount of speckle reduction is much smaller than the multilook. Results for the BPT-based speckle filtering are shown on Figs. 4.13c to 4.13e for different δ_p values. It may be seen that for all the pruning threshold values shown the corner reflectors are preserved as small points while large regions appear over the field. Over the field large regions appear, even for $\delta_p = -2dB$, where some details are observed within the field, showing its internal structure. In the case of $\delta_p = 0dB$, all the underlying field is merged into just one region while all the corner reflectors and details are preserved. The amount of speckle reduction achieved by the BPT-based pruning is much more visible over the field than in the IDAN and 7x7 multilook filtering, specially for $\delta_p = 0dB$, as all the pixels of the field are averaged together, resulting into a better estimation of the polarimetric response.

In Section 4.1.3 different dissimilarity measures for PolSAR data have been defined. All the previous examples correspond to different pruning strategies over the same BPT constructed employing the symmetric revised Wishart d_{sw} dissimilarity measure, as defined in (4.2). To show the effect of this function in the final results, different BPTs of Fig. 4.10a have been constructed employing the distinct dissimilarity measures defined and the same region homogeneity based pruning has been applied to them, employing $\delta_p = 0dB$. These results are shown on Fig. 4.14 over the same crop area presented in Fig. 4.11a. In order to apply the full matrix measures, an initial 3x3 multilook filter has been applied for matrix regularization, as in the previous case.

When considering the results shown on Fig. 4.14 it may be surprising that most of them obtain very similar results. Although the distinct dissimilarity measures defined in Section 4.1.3 are based on completely different approaches, all of the results roughly identify the main contours of the agricultural fields and also preserve the details of the urban area. This may give an idea of the robustness of the proposed BPT-based processing scheme in terms of the dissimilarity measure employed for BPT construction. However, an in-depth analysis shows some differences, specially when considering the *noise* over the straight contours of the fields or the ability to distinguish between all the different agricultural fields. In general, the full matrix measures, shown in Figs. 4.14b and 4.14d, have a better ability to distinguish the different fields. Additionally, from all the different dissimilarity measures it seems that the geodesic measure

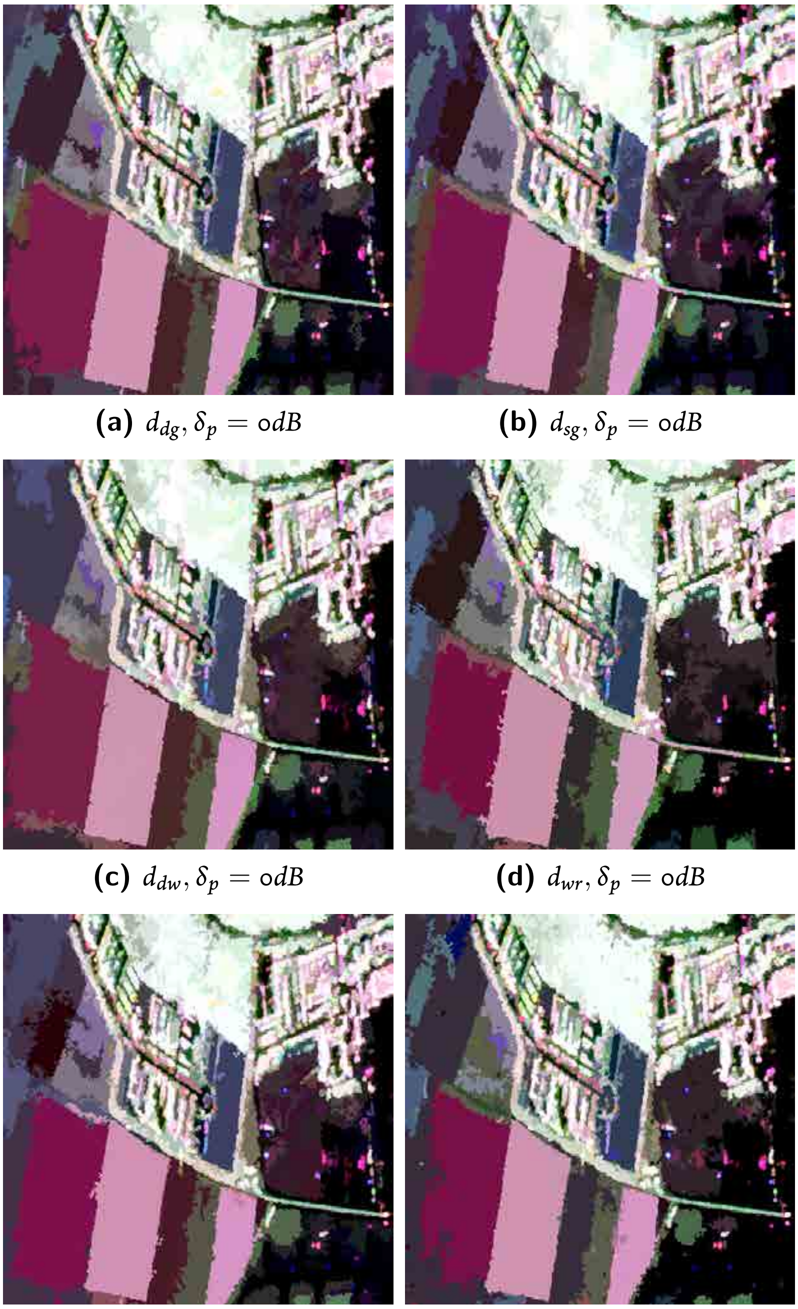

(a) $d_{dg}, \delta_p = 0dB$ **(b)** $d_{sg}, \delta_p = 0dB$

(c) $d_{dw}, \delta_p = 0dB$ **(d)** $d_{wr}, \delta_p = 0dB$

(e) $d_{dn}, \delta_p = 0dB$ **(f)** $d_{dr}, \delta_p = 0dB$

Figure 4.14: Detail Pauli RGB images processed using region homogeneity based pruning with $\delta_p = 0dB$ over different trees constructed employing various dissimilarity functions $(|S_{hh} + S_{vv}|, |S_{hv} + S_{vh}|, |S_{hh} - S_{vv}|)$.

d_{sg}, defined in (4.3), presents the better results in terms of contour noise and region distinction. Note that a more detailed analysis of the results is complex by the absence of ground truth, but in Section 4.3.4 a more detailed analysis will be performed with simulated data to overcome this limitation.

Fig. 4.15 shows the morphology of the pruned trees constructed with different dissimilarity measures. In this case, in order order to obtain a small enough tree to be able to represent it graphically, instead of the full image, a small crop has been processed corresponding to an area of agricultural fields, presented in Fig. 4.4a. All the presented pruned trees have been pruned with the region homogeneity based pruning employing $\delta_p = 0 dB$. Finally, the leaves of the pruned tree have been colored in green if they correspond to single pixels, that is, leaves of the original BPT, and in red otherwise.

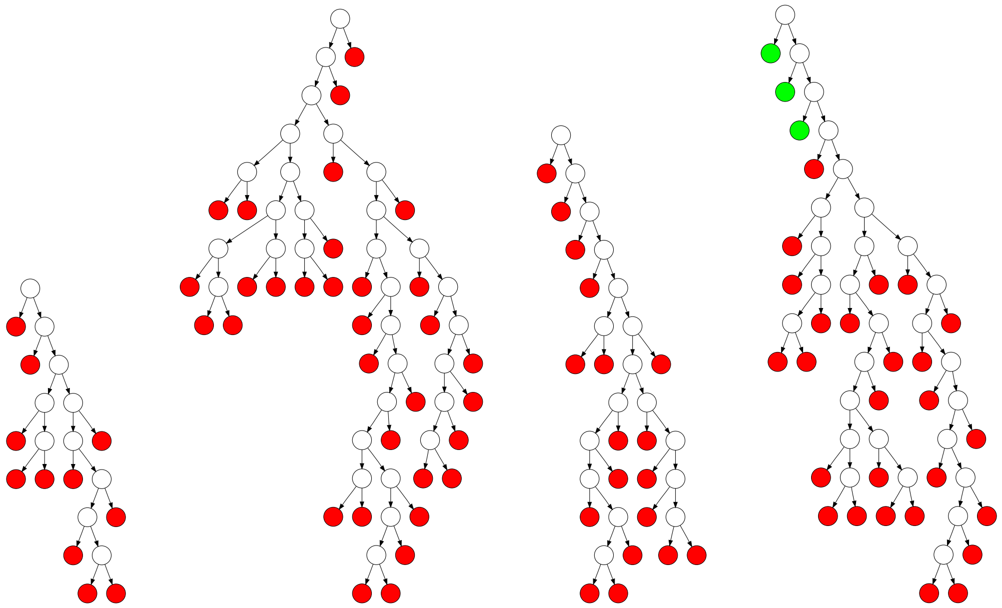

(a) d_{dg} **(b)** d_{sg} **(c)** d_{dw} **(d)** d_{sw}

Figure 4.15: Pruned BPTs using region homogeneity based pruning with $\delta_p = 0dB$ over different trees constructed employing various dissimilarity functions. Pruned nodes are colored in green if they are leaves or in red otherwise.

The analysis of the BPT morphology is a very difficult task, as it depends on the structure of the PolSAR image itself, and it will not be addressed in this work. By the way, some general differences may be observed when comparing the pruned BPTs obtained after its construction employing diagonal or full matrix dissimilarity measures. It may be seen that the trees obtained with diagonal measures, shown in Figs. 4.15a and 4.15c, are less balanced than those obtained with full matrix measures, represented in Figs. 4.15b and 4.15d. As a consequence, the pruned BPTs obtained with diagonal measures appear thiner. Moreover, the pruned tree obtained with the d_{sw} dissimilarity measure contains single pixels near to the root node. Note that this is not the desired structure for a BPT, as it is expected to find large regions close to the root. However, in this case a small piece of data has been processed, having only 256 by 256 pixels and, thus, these results are not very representative. Unfortunately, the pruned BPT of the whole image has thousand of nodes making very difficult its representation and analysis, which is out of the scope of this work.

In the previous examples a qualitative comparison of the BPT pruning results has been performed in terms of the obtained Pauli images. Note, then, that only the information corresponding to the retrieved power in the Pauli basis of the estimated covariance $\mathbf{Z}$ is represented. In order to do a broader analysis of the preservation of the polarimetric information, an additional study is performed. The Entropy (H), Anisotropy (A) and averaged Alpha angle ($\bar{\alpha}$) decomposition, as described in Section 2.2.6, will be employed in the following analysis to do a more comprehensive assessment of the polarimetric information preservation. Fig. 4.16 shows these parameters for the 7x7 multilook, the IDAN filtering and the proposed region homogeneity based pruning for $\delta_p = -2dB$ and $\delta_p = 0dB$. The Entropy and Anisotropy are represented from 0, in blue, to 1, in red color; the averaged Alpha angle is represented from 0°, in blue, to 90°, in red. In this case, the symmetric revised Wishart d_{sw} has been employed for BPT construction, corresponding, thus, to the same Pauli results shown in Figs. 4.12b and 4.12f.

A qualitative evaluation of the polarimetric decomposition parameters presented in Fig. 4.16 reveals that the same colors may be seen on all the filtering processes, indicating that the polarimetric information is roughly maintained. Nevertheless, the BPT is able to perform an stronger averaging over large homogeneous areas, as in the agricultural fields or in the forest, reducing considerably the noise over these parameters. For $\delta_p = 0dB$, over the forest area in the top of the image, the Entropy H tends to 1 whereas the Anisotropy A tends to 0, which fits with the theoretical response for a random volume scattering, as it is supposed to occur over forest [36]. Additionally, the ability of the BPT to preserve small details may also be seen, specially over the urban area in the center of the image. Some small spots may be seen on this area for the multilook, specially on H and $\bar{\alpha}$, corresponding to point scatterers. These details also appear on the BPT results but without the characteristic enlargement of the multilook. The proposed filtering scheme, then, improves the estimation of the polarimetric information both, in point as well as in distributed scatterers, with respect to the multilook filter.

The comparison of these results is not clear due to the absence of ground truth. In order to overcome this limitation when dealing with real data, some visually homogeneous areas from the data may be selected in order to do a statistical analysis of the results obtained over these areas. This analysis has been performed in this dataset over the three areas shown on Fig. 4.17.

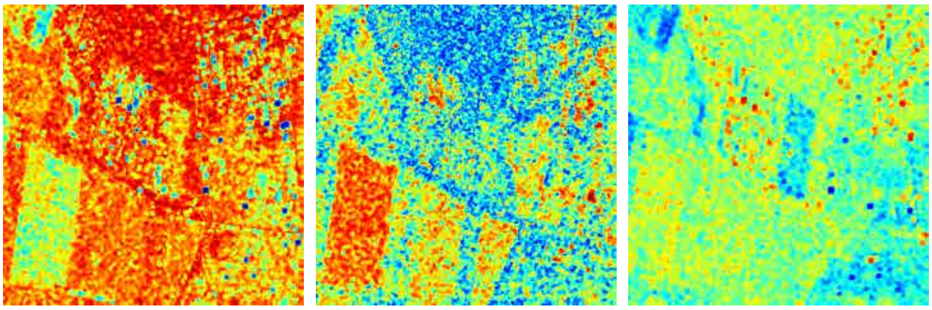

(a) H, 7x7 multilook **(b)** A, 7x7 multilook **(c)** $\bar{\alpha}$, 7x7 multilook

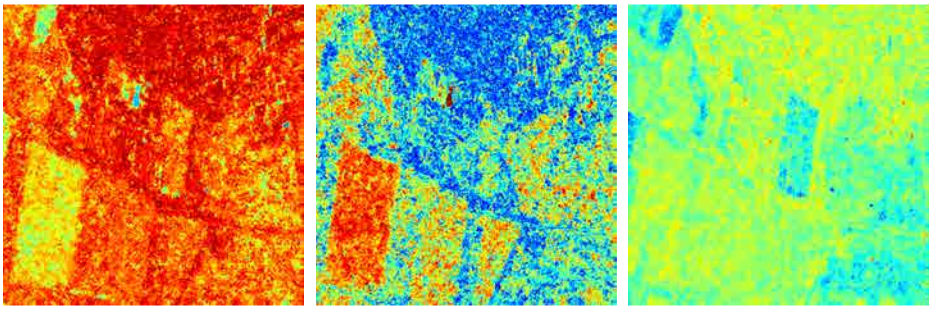

(d) H, IDAN **(e)** A, IDAN **(f)** $\bar{\alpha}$, IDAN

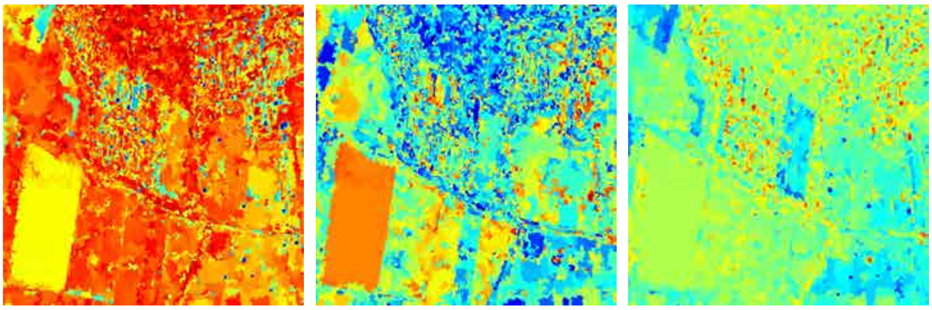

(g) H,d_{sw}, $\delta_p = -2dB$ **(h)** A,d_{sw}, $\delta_p = -2dB$ **(i)** $\bar{\alpha}$, d_{sw}, $\delta_p = -2dB$

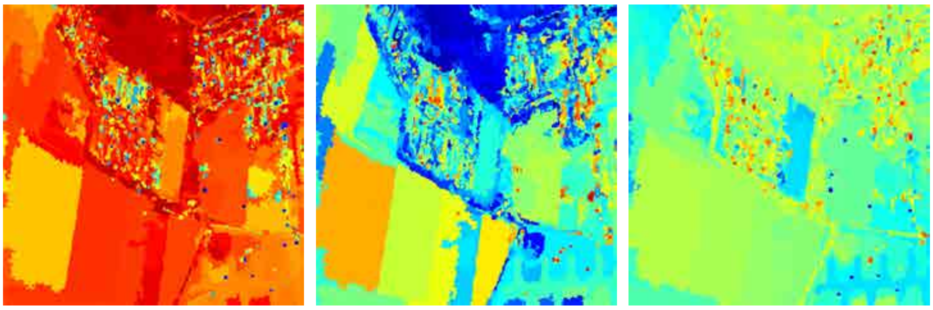

(j) H,d_{sw}, $\delta_p = 0dB$ **(k)** A,d_{sw}, $\delta_p = 0dB$ **(l)** $\bar{\alpha}$, d_{sw}, $\delta_p = 0dB$

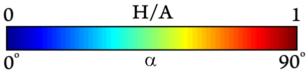

Figure 4.16: $H/A/\bar{\alpha}$ of processed images with 7x7 multilook, IDAN and using region homogeneity based pruning.

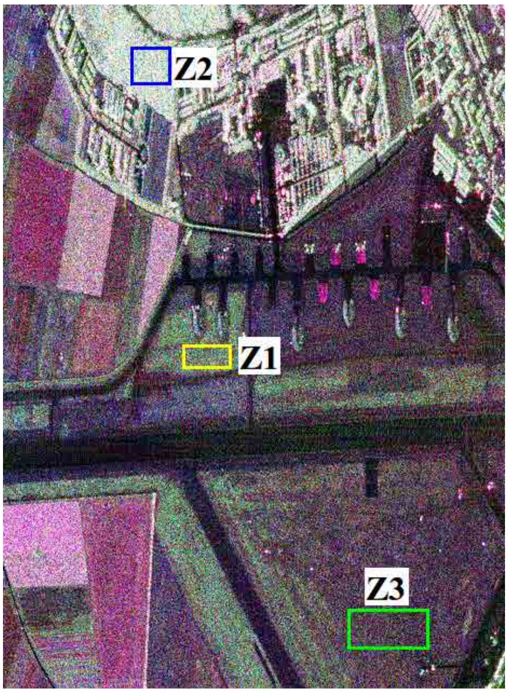

Figure 4.17: Homogeneous zones manually selected over the original image for the quantitative analysis ($|S_{hh}+S_{vv}|$, $|S_{hv}+S_{vh}|$, $|S_{hh}-S_{vv}|$).

The average results obtained over these areas for different filtering mechanisms are shown on Table 4.3. In this analysis, the original data is compared with the results of the 7x7 multilook, the IDAN filter and the BPT region homogeneity based pruning strategy for $\delta_p = -2dB, -1dB$ and $0dB$ values. To show the ability to preserve the elements of the covariance matrix elements, the averaged value of the diagonal elements is displayed in the C_{11} to C_{33} columns. Additionally, the real and imaginary parts of C_{13} element is also presented. Finally, the last three columns show the averaged values obtained for the Entropy (H), Anisotropy (A) and averaged Alpha angle $(\bar{\alpha})$ polarimetric decomposition parameters. As mentioned in Section 2.2.6, these parameters require a full-rank matrix and, thus, they cannot be computed for the original image.

In order to compare the results obtained by the different techniques, the 7x7 multilook may be used as a reference, as it corresponds to the MLE. In fact, it may be seen that it obtains values close to the original data for all the covariance matrix elements. The BPT-based processing also obtains similar values for all the different values of δ_p. However, for higher values of the pruning threshold, when $\delta_p = 0dB$, some values start to diverge from the original ones due to the mixture of different regions that may not be so homogeneous. On the other hand, the IDAN filter has a noticeable bias on the obtained values, tending to underestimate all the covariance matrix elements. The presence of this bias has been mentioned in Section 2.3.3 and it is dis-

Region	Filtering	C_{11}	C_{22}	C_{33}	$\Re(C_{13})$	$\Im(C_{13})$	H	A	$\bar{\alpha}$
Z1 5000 px	Original	28.27	16.06	18.34	5.242	5.504	-	-	-
	ML 7x7	28.21	15.97	18.36	5.321	5.465	0.8012	0.3543	48.29
	IDAN	18.73	9.661	12.03	2.471	2.595	0.8558	0.3050	49.48
	BPT -2dB	28.15	16.10	18.17	5.466	5.605	0.8271	0.2873	48.27
	BPT -1dB	28.20	15.20	18.08	5.558	5.612	0.8618	0.2036	47.91
	BPT 0dB	27.76	14.47	16.96	5.813	5.211	0.8694	0.1630	47.74
Z2 5950 px	Original	279.3	159.1	172.8	49.80	-14.37	-	-	-
	ML 7x7	280.8	159.3	172.9	49.18	-15.27	0.8598	0.2907	49.06
	IDAN	173.0	102.4	105.8	20.59	-7.978	0.9003	0.2501	51.29
	BPT -2dB	278.1	158.4	171.5	48.05	-16.12	0.8475	0.2984	49.50
	BPT -1dB	280.4	157.7	172.4	50.24	-15.42	0.8925	0.2269	49.41
	BPT 0dB	292.2	160.8	177.0	50.74	-13.42	0.9305	0.1307	49.61
Z3 18000 px	Original	10.70	2.782	13.13	2.644	5.599	-	-	-
	ML 7x7	10.70	2.789	13.14	2.662	5.593	0.6781	0.4248	42.62
	IDAN	7.123	1.864	8.678	1.433	2.896	0.7438	0.4505	44.39
	BPT -2dB	10.33	2.713	12.94	2.498	5.255	0.7370	0.3755	43.32
	BPT -1dB	10.36	2.799	13.23	2.434	5.136	0.7445	0.3881	43.60
	BPT 0dB	11.76	3.405	13.59	2.556	5.351	0.7852	0.3471	44.34

Table 4.3: Mean estimated values over homogeneous areas for different speckle filtering strategies.

cussed in [127]. The authors have compensated up to a certain point this bias in [126], but, unfortunately, there is no free implementation of this filter in order to compare the results.

For the $H/A/\bar{\alpha}$ parameters, represented in the last three columns of Table 4.3, all the filters obtain similar values, including the IDAN. It may seem odd that the bias in the covariance matrix elements is not reflected into these parameters which, in fact, are extracted from the estimated covariance matrix. This effect is caused by the relative nature of these elements, which do not depend on the absolute power reflected by the target. Since the bias factor is roughly similar for all the covariance matrix elements, it does not affect significantly the $H/A/\bar{\alpha}$ parameters. The comparison of the obtained values for these elements is not as straightforward as in the other elements, since they may not be computed for original data. The multilook may be employed as a reference but, although it is an unbiased estimator of the covariance matrix, it does have a bias over the $H/A/\bar{\alpha}$ parameters estimated indirectly from the obtained $\mathbf{Z}$ matrices, as shown on [90][91]. According to this work, the Entropy H and Anisotropy A are always underestimated and overestimated, respectively, and increasing the number of looks reduces the bias. A similar trend may be seen in Table 4.3 when increasing the pruning threshold δ_p which, in fact, increases the obtained region sizes and accordingly the number of averaged samples, the obtained values for H and A slightly increase and decrease, respectively, as the estimation bias is reduced. A detailed mathematical characterization of the estimated $H/A/\bar{\alpha}$ parameters and its bias may be found in Appendix A, while modeling the effect of the speckle noise with matrix perturbation theory [91]. Finally, some additional results with different SAR sensors may be found in the Appendix B.

4.3.4 ANALYSIS WITH SIMULATED DATA

A more detailed analysis of the obtained results may not be performed with real data as we have no knowledge of the ground truth. In order to conduct a thorough analysis, the true statistics of the data must be known and also its detailed spatial distribution. This kind of information is unknown for a real scenario as it is almost impossible to acquire.

To overcome these limitations, a synthetic dataset may be generated according to a given artificial ground truth in order to perform an in deep analysis of the obtained results. In this section two different synthetic datasets will be employed to do a more detailed analysis of the BPT-based PolSAR estimation techniques defined in sections 4.3.1 and 4.3.2.

Fig. 4.18 shows an example of the first dataset employed. It corresponds to a 128 by 128 pixels image having 4 equal size zones, as represented in Fig. 4.18a. The simulated data have been generated employing the complex Gaussian polarimetric model, as described in [99], assuming a reflection symmetric target, since most of natural targets are assumed to follow this model, having a covariance matrix **C** of the form

$$\mathbf{C} = \sigma_{HH} \begin{pmatrix} 1 & 0 & \rho\sqrt{\gamma} \\ 0 & \varepsilon & 0 \\ \rho^* \sqrt{\gamma} & 0 & \gamma \end{pmatrix} \tag{4.17}$$

where * denotes the complex conjugate.

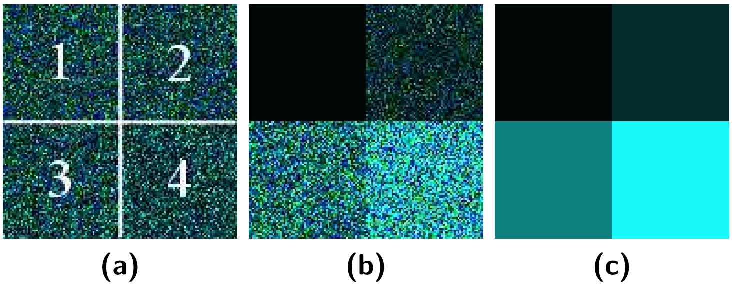

(a) (b) (c)

Figure 4.18: Simulated PolSAR dataset with 4 equal size zones. Z_{11}, Z_{22} and Z_{33} are assigned to blue, red and green channels, respectively. (a) Zones shape and numeration, (b) and (c) one realization of the image with intensity variations and image ground-truth, respectively.

According to the model presented in (4.17), three different datasets have been simulated, employing $\gamma_i = 1$ and $\varepsilon_i = 0.1$ and variations for σ_{HHi} and ρ_i in the different regions $i = 1 \ldots 4$ numbered as denoted in Fig. 4.18a:

1. Variations in intensity: $\rho_i = 0.5;\ \ \sigma_{HH} = \{1,\ 9,\ 25,\ 49\}$
2. Variations in correlation: $\rho = \{0,\ 0.25e^{j\pi},\ -0.5,\ 0.75e^{-j\pi}\};\ \sigma_{HHi} = 1$
3. Variations both in correlation and in intensity: $\rho = \{0,\ 0.25e^{j\pi},\ -0.5,\ 0.75e^{-j\pi}\};$ $\sigma_{HH} = \{1,\ 9,\ 25,\ 49\}$

The idea behind these datasets is to generate simple images in order to make the interpretation of the obtained results as easy as possible. Moreover, the contrast between the different regions varies in terms of the retrieved power or channel correlation, in order to compare the sensitivity of the obtained BPTs to these traits of the data separately. Figs. 4.18b and 4.18c, for instance, show one realization and the simulated ground truth for the first dataset, having variations in intensity.

To assess the obtained results X in comparison with the simulated ground truth Y, an error measure is proposed E_R, based on the averaged relative error measure per pixel [8]

$$E_R(X, Y) = \frac{1}{n_h \cdot n_w} \sum_{i=1}^{n_h} \sum_{j=1}^{n_w} \frac{\|\mathbf{X}^{ij} - \mathbf{Y}^{ij}\|_F}{\|\mathbf{Y}^{ij}\|_F} \tag{4.18}$$

where n_h and n_w are the image height and width in pixels, respectively, $\mathbf{X}^{ij}$ represents the (i, j)th pixel value of image X, that is, its estimated sample covariance matrix $\mathbf{Z}$, and $\|\cdot\|_F$ denotes Frobenius matrix norm. It is worth noting that the relative error measure defined in (4.18) is based on the inverse signal to noise ratio (SNR^{-1}) averaged for all the pixels in the image.

The filtering error E_R figures obtained over these three datasets employing the BPT pruning based on the number of regions, as described in Section 4.3.1, may be seen on Fig. 4.19. Each chart shows the E_R measure on the vertical axis, in dB, in terms of the number of regions N, in the top horizontal axis, for different BPTs constructed employing most of the dissimilarity measures defined in Section 4.1.3, including diagonal and full-matrix measures. Additionally, in the bottom horizontal axis the average region size is represented, corresponding to the total number of pixels of the image divided by the number of regions, calculated as $(n_h \cdot n_w)/N$. Both the horizontal axes are shown in logarithmic scale. These plots have been obtained after averaging the outcome of 25 different realizations of each dataset. These results are also compared with those of the multilook or Boxcar filter, for different window sizes. Note that for the Boxcar filter, the bottom horizontal axis represents the total size, in pixels, of its averaging window, i.e. the n in (2.54). In order to be able to apply the full-matrix d_{sw} (4.2) and d_{wr} (4.4) dissimilarity measures an initial 3x3 multilook filtering has been applied to get full-rank matrices. The standard deviation values over the 25 realizations have also been represented for the multilook and for the d_{sw} case. The rest of the BPT based curves present similar standard deviation values to the d_{sw}, but they have not been represented to make the plots more readable.

When analyzing the E_R relative error results obtained in Fig. 4.19 two completely different behaviors may be observed. Figs. 4.19a and 4.19c present very similar trends whereas Fig. 4.19b shows a distinct evolution. In fact, when there are variations in intensity, those dominate among the variations in correlation, as they are much more important in terms of the E_R measure than the variations in correlation. In Figs. 4.19a and 4.19c, for small values of the region size, the results from the BPT and the multilook present similar values, as the effect of the region mixture in the multilook is negligible. However, when the region size increases, while reducing the number of regions N, the curve of the multilook starts to increase in terms of relative error. This is produced by the fact that the error committed by the region mixture is larger than the reduction in speckle when increasing its window size. Then, according to the E_R measure, the optimum multilook window size will be 7 by 7 pixels, corresponding to a region size of 49 in Fig. 4.19. The plots of the BPT based filtering continue its trend, decreasing when the region sizes increases. Here, the spatial adaptation of the BPT avoids the region mixture over the region contours, allowing the increase of the number of pixels averaged, resulting in an additional reduction of the error due to the speckle noise reduction over the data. Theoretically, the best results may be obtained for 4 regions, when pruning the BPT at $N = 4$, as the simulated ground truth has exactly 4 regions. As it may be seen, most of the BPT based plots achieve its optimum near 4 regions, except when employing the d_{dr} measure. If the number of regions N is reduced below 4 regions, the region mixture is unavoidable, resulting into large values of E_R.

On the other hand, when only variations on correlation are present, as shown in Fig. 4.19b, results are completely different. Note that the correlation between channels is contained in the off-diagonal elements of the covariance matrix and, then, only the full-matrix measures d_{sw} and d_{wr} are sensitive to them. Then, the regions generated when employing d_{dn} (4.12), d_{dr} (4.13) and d_{dw} (4.10) dissimilarity measures rapidly start mixing non-homogeneous regions, since they can not adapt to the spatial morphology, and never improve the multilook filter performance. Conversely, full matrix measures d_{sw} (4.2) and d_{wr} (4.4) can adapt to the image spatial morphology, avoiding the region mixture effect, and achieving better results than the multilook filter. It is worth noticing that, in Fig. 4.19b, the intensity is constant over the entire image. Then, the mixture of different regions do not have such a dramatic impact in E_R as in Fig. 4.19a and 4.19c. This also explains why the minimum of the Boxcar relative error occurs at region

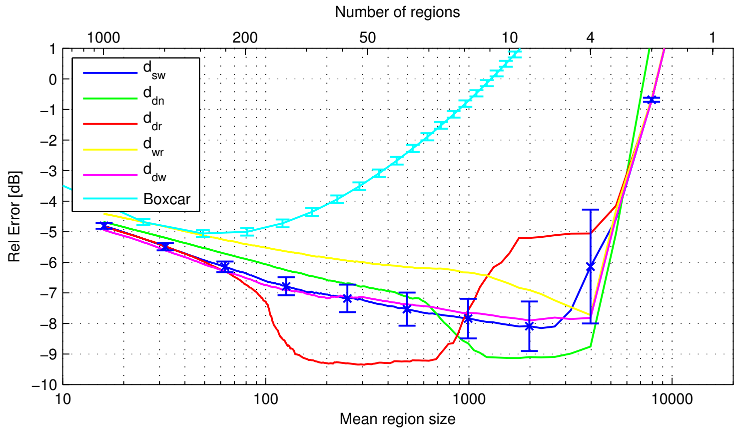

(a) Variation in intensity

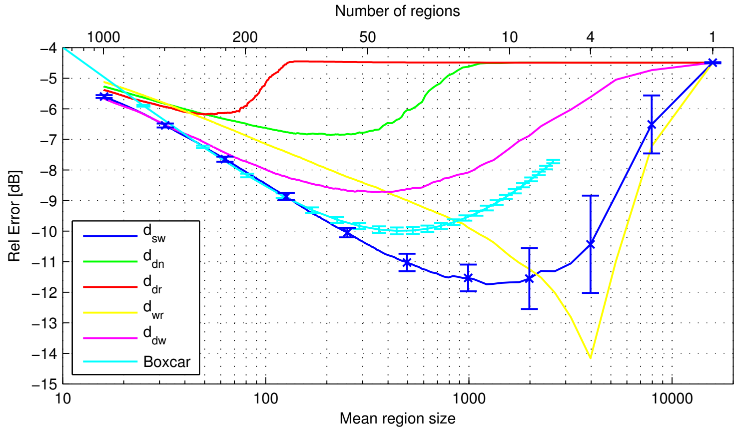

(b) Variation in correlation

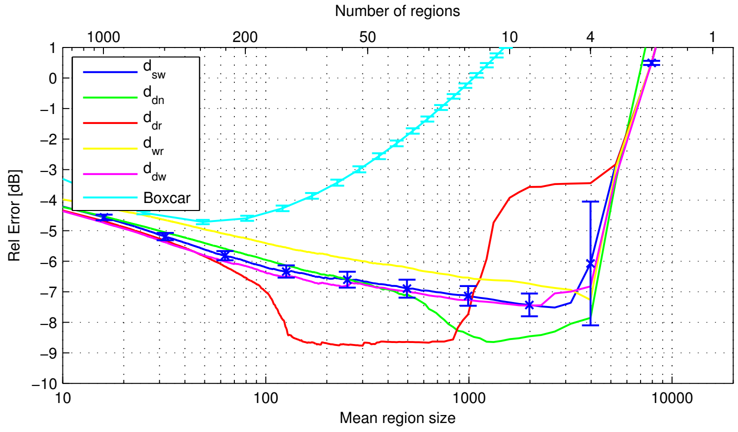

(c) Variations both in correlation and in intensity

Figure 4.19: Relative error measure for simulated images with 4 equal size zones filtered with a BPT pruning based on the number of regions. The lines have been obtained averaging the results of 25 simulated realizations.

sizes about 400-500 pixels, equivalent to a 21x21 multilook filtering.

When comparing the results obtained for all the dissimilarity measures in the three cases, it may be seen that they present different behaviors also in terms of the number of regions N. The Wishart based dissimilarity measures d_{sw} and d_{dw} present the most stable behavior, having a constant decrease in terms of E_R when decreasing the number of regions N. The d_{dn} and d_{dr} measures may present better values of relative error than the other measures at some N, but they do not have a constant behavior and are only sensitive to diagonal elements of the covariance matrix. The Ward relative dissimilarity measure d_{wr} presents more error than the other measures but it is the only one that has a clear minimum in $N = 4$ for all cases. However, when there are no variations in intensity, the full matrix measures are the only ones that can adapt to the spatial contours and improve the Boxcar filter performance, as shown on Fig. 4.19b.

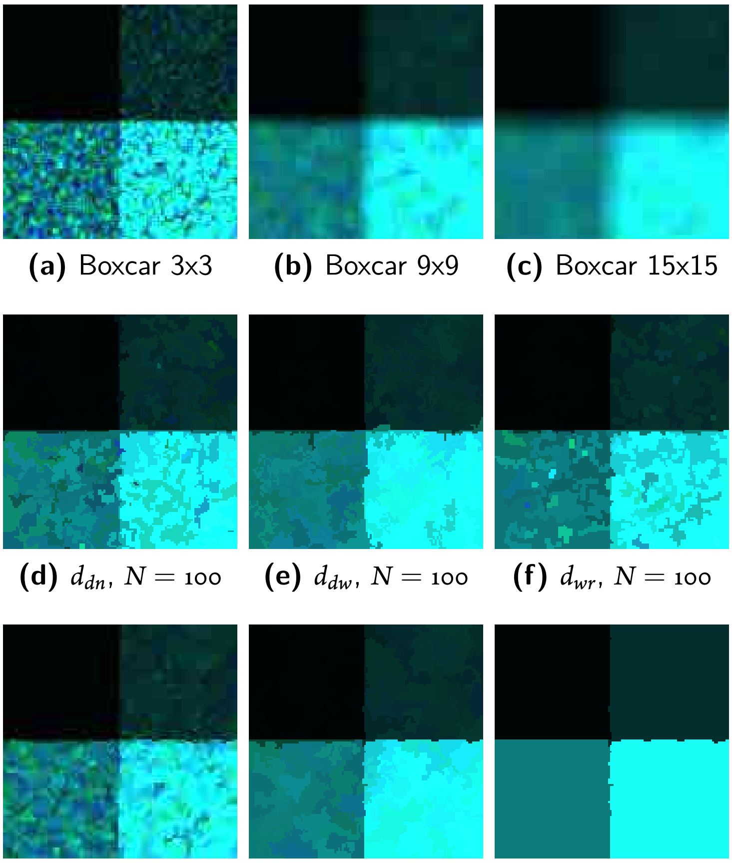

(a) Boxcar 3x3 **(b)** Boxcar 9x9 **(c)** Boxcar 15x15

(d) d_{dn}, $N = 100$ **(e)** d_{dw}, $N = 100$ **(f)** d_{wr}, $N = 100$

(g) d_{sw}, $N = 1000$ **(h)** d_{sw}, $N = 100$ **(i)** d_{sw}, $N = 4$

Figure 4.20: Boxcar and BPT pruning based on the number of regions results for one of the simulated PolSAR images with variations in both correlation and intensity employing different dissimilarity measures. Z_{11}, Z_{22} and Z_{33} are assigned to blue, red and green channels, respectively.

For the visual inspection of the obtained results, Fig. 4.20 shows the outcome of the multilook filtering and the BPT pruning based on the number of regions when employing different dissimilarity measures and N parameter values.

The first row, Figs. 4.20a to 4.20c, shows the Boxcar filter results for window sizes from 3x3 to 15x15. As it may be seen, when increasing the size the effect of the speckle gets also reduced. However, the impact of the region mixture near contours gets also increased, resulting into blurred transitions between regions. On the second row, Figs. 4.20d to 4.20f, the number of regions N parameter is set to 100 and results are shown for different dissimilarity measures: d_{dn}, d_{dw} and d_{wr}. All of them are able to detect the main contours of the image avoiding the region mixture, for this value of N. Note that the contours within each of the four regions may be considered as random, as there are no contours in the simulated ground truth and, consequently, these contours are produced by the effect of the speckle noise. The third row, composed by Figs. 4.20g to 4.20i, shows the obtained results over the BPT constructed employing the symmetric Wishart d_{sw} measure for different values of N. Fig. 4.20i depicts the obtained result for $N = 4$, corresponding to the real number of regions in the simulated ground truth. As it may be seen, the obtained regions are very close to this ground truth, shown in Fig. 4.18c, with small differences on the region contours. This similarity is also confirmed by the small values observed in terms of the relative error measure E_R.

The same analysis have been performed with the region homogeneity based pruning, as described in Section 4.3.2. Fig. 4.21 shows the results after applying this pruning strategy to the different BPTs constructed employing all the dissimilarity measures defined in Section 4.1.3. These plots show the relative error measure E_R, defined in (4.18), in the vertical axis in terms of the pruning threshold δ_p in the horizontal axis. In these plots both axes expressed in dB. As in Fig. 4.19, the results have been obtained after averaging the outcome of 25 different realizations of each simulated image. Again, the values of the standard deviation are shown for the symmetric revised Wishart dissimilarity d_{sw}.

When comparing Figs. 4.21a to 4.21c it may be seen that all of them present a similar trend, as opposed to Figs. 4.19a to 4.19c. For all the plots, there is a clear minimum for all the dissimilarity measures, that may be located around $\delta_p = -6dB$. Moreover, when there are variations on intensity, as in Figs. 4.21a and 4.21c, a wide range of values for δ_p may be chosen having a near-optimum behavior. This is produced by the fact that the region mixture on these cases produces a strong increase in the region homogeneity measure and then, the pruning factor has to be substantially increased in order to prune this non-homogeneous regions. On the other hand, when there are only variations in correlation the effect of the region mixture is much more subtle

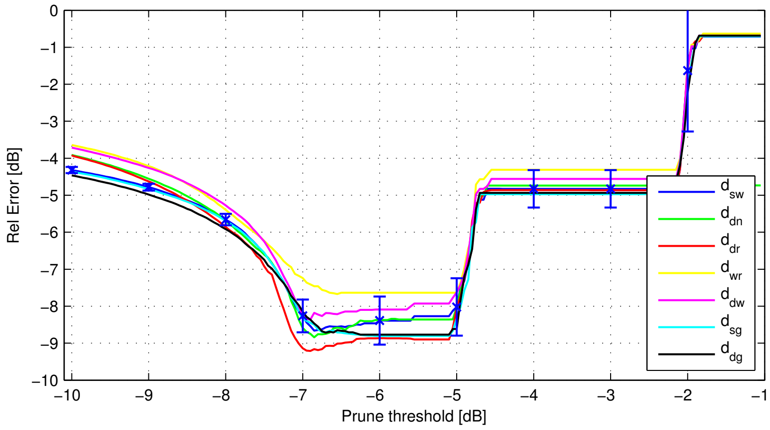

(a) Variation in intensity

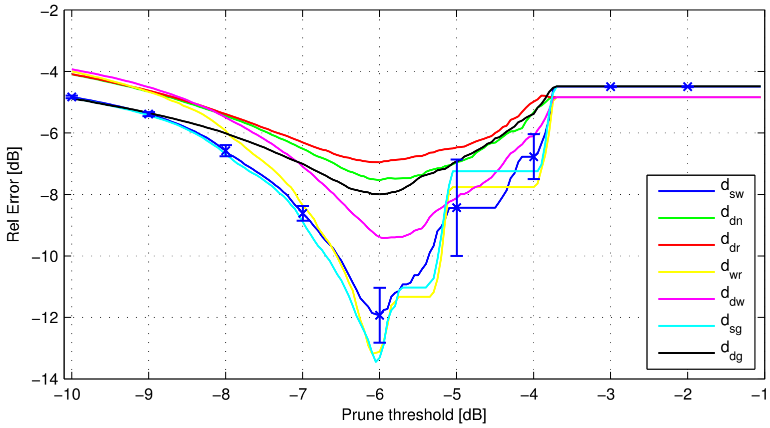

(b) Variation in correlation

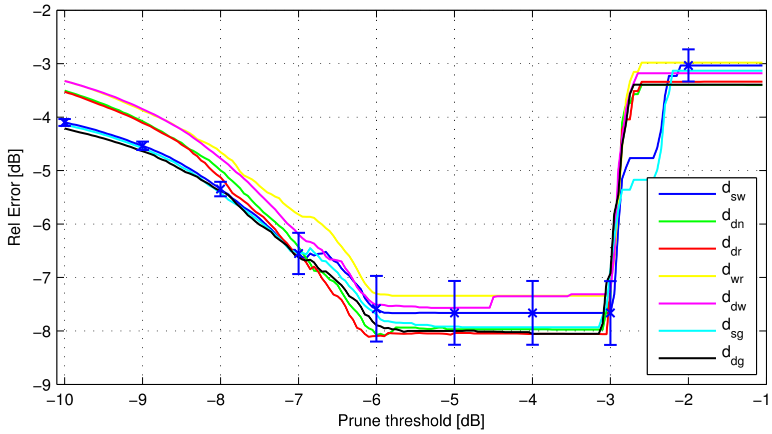

(c) Variations both in correlation and in intensity

Figure 4.21: Relative error for simulated images with 4 equal size zones filtered with the region homogeneity based pruning. Results have been obtained averaging 25 realizations.

in terms of the homogeneity measure, but there is also a minimum at the same pruning threshold value $\delta_p = -6dB$.

The minimum values, in terms of the relative error measure, obtained by the region homogeneity based pruning, represented in Fig. 4.21, are roughly the same than in the pruning based on the number of regions, as shown in Fig. 4.19, as the same regions may be obtained from the corresponding BPTs. However, the region homogeneity based pruning has the advantage of having a predictable behavior and the same optimum pruning threshold value, independently of the image content or dissimilarity measure employed for BPT construction. Additionally, when there are only variations in correlation, as represented in Fig. 4.21b, it may improve somewhat the results obtained by the pruning based on the number of regions for diagonal measures, as the homogeneity measure is sensitive to the full covariance matrix information, mitigating slightly the limitations of these measures.

Fig. 4.22 shows the results obtained after applying the region homogeneity based pruning to one realization of the dataset having variations in both correlation and intensity. Figs. 4.22a to 4.22f show the results of the region homogeneity based pruning with a threshold value of $\delta_p = -6dB$, which produces the optimum E_R value in all the datasets, for the different BPTs constructed employing various dissimilarities measures. As it may be seen, on all of them the 4 regions of the image are clearly obtained. The main variations among them lies in the precision of the contours retrieved and the presence of some small regions within the 4 squares that only correspond to speckle features. The best results seem to be obtained by the full-matrix measures d_{sw}, d_{wr} and d_{sg}. Additionally, in order to show the obtained results evolution when varying the pruning threshold δ_p value, Figs. 4.22g to 4.22l depict the obtained results for the homogeneity based pruning pruning with threshold values from $\delta_p = -9dB$ to $\delta_p = -4dB$. For these results the geodesic dissimilarity measure d_{sg} has been employed in all cases. As mentioned before, there are a wide range of values for the pruning threshold δ_p that produce the optimum result, as it may be seen from Fig. 4.22j to 4.22l.

When comparing both BPT pruning strategies, represented in Figs. 4.19 and 4.21, it is worth to mention that the simulated image having 4 equal size regions is not complex enough to be representative. In fact, one of the most remarkable benefits of the region homogeneity BPT based pruning is its ability to extract homogeneous regions of different sizes, as stated in Section 4.3.2. These advantages have been clearly seen when processing real data, as it may be observed on the results presented in Section 4.3.3. The simulated datasets employed in the previous analysis do not present this level of structural complexity, as they only have 4 equal size regions. Although they may be useful to understand and interpret the obtained results, they may not be realistic.

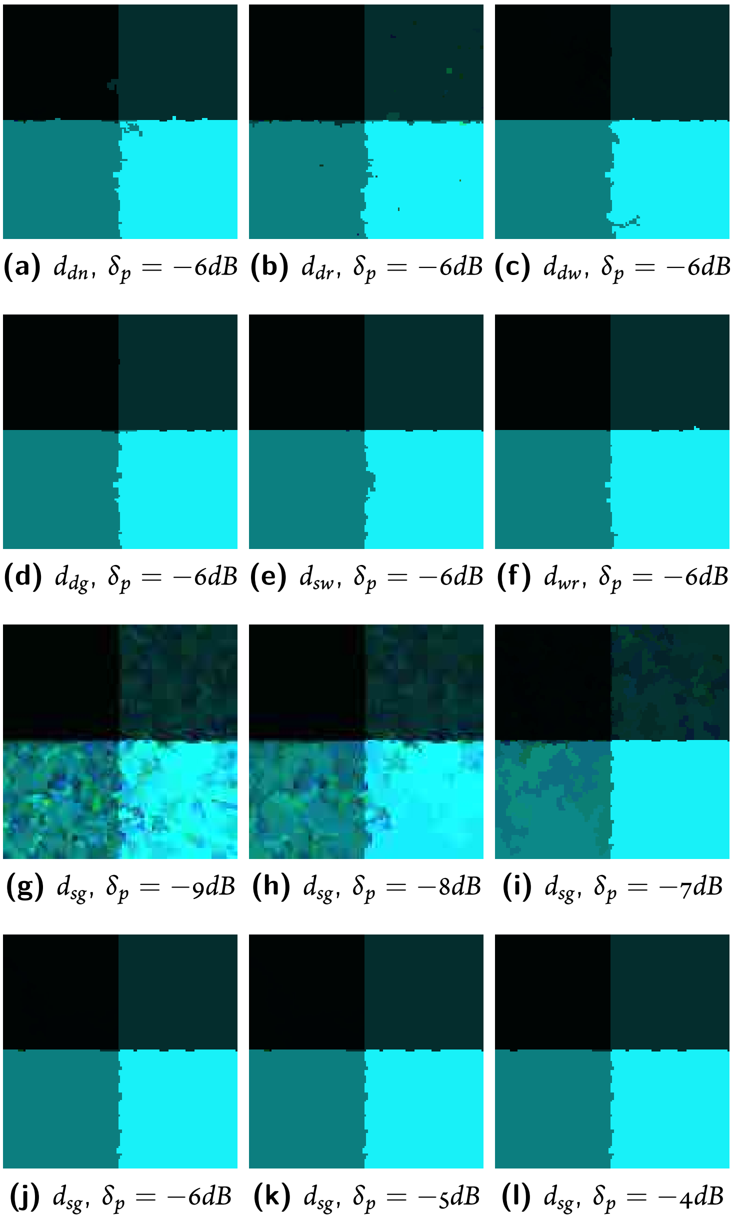

(a) d_{dn}, $\delta_p = -6dB$ **(b)** d_{dr}, $\delta_p = -6dB$ **(c)** d_{dw}, $\delta_p = -6dB$

(d) d_{dg}, $\delta_p = -6dB$ **(e)** d_{sw}, $\delta_p = -6dB$ **(f)** d_{wr}, $\delta_p = -6dB$

(g) d_{sg}, $\delta_p = -9dB$ **(h)** d_{sg}, $\delta_p = -8dB$ **(i)** d_{sg}, $\delta_p = -7dB$

(j) d_{sg}, $\delta_p = -6dB$ **(k)** d_{sg}, $\delta_p = -5dB$ **(l)** d_{sg}, $\delta_p = -4dB$

Figure 4.22: BPT homogeneity based pruning results for one of the simulated PolSAR images with variations in both correlation and intensity employing different dissimilarity measures and prune thresholds. Z_{11}, Z_{22} and Z_{33} are assigned to blue, red and green channels, respectively.

Then, in order to obtain a more representative results, the simulated ground truth may describe a more realistic complex scenario, similar to a real PolSAR image. Ideally, it should contain large homogeneous areas, like agricultural fields, and also small details, like the corner reflectors or the urban area, as seen before. Moreover, it would be desirable that the covariance matrix $\mathbf{C}$ for every region represents realistic values that can be found in real data. Therefore, in order to accomplish the previously mentioned requirements, a ground truth may be generated by a segmentation of a real image. Since a manual segmentation is not affordable, due to the large number of small regions and details of a real image, a segmentation technique may be employed. To generate this realistic ground truth, the BPT region homogeneity based pruning with a pruning factor $\delta_p = -1dB$ has been employed over the tree constructed with the geodesic dissimilarity d_{sg} presented in (4.3). Figs. 4.23a and 4.24a present the 512 by 512 pixel crops of the Oberpfaffenhofen dataset and Figs. 4.23b and 4.24b represent the obtained regions after applying the previously mentioned BPT pruning strategy.

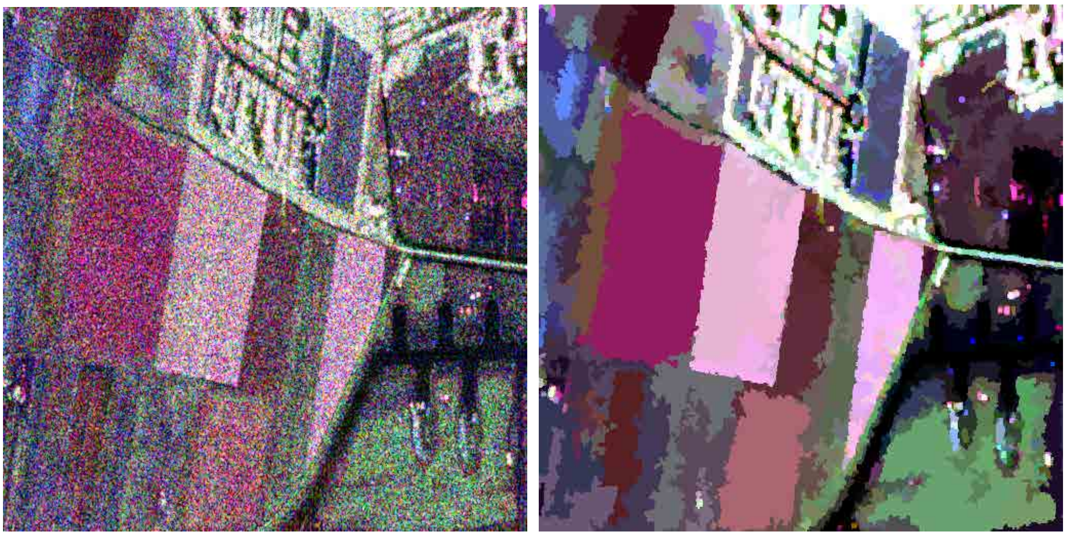

(a) Original crop **(b)** Filtered ($d_{sg}, \delta_p = -1dB$)

Figure 4.23: Pauli representation of the original and filtered images of an agricultural area ($|S_{hh} + S_{vv}|$, $|S_{hv} + S_{vh}|$, $|S_{hh} - S_{vv}|$).

As it may be seen on Figs. 4.23 and 4.24, both images have large and small homogeneous regions but they correspond mainly to an agricultural area and a urban area, respectively. Consequently, Fig. 4.23a is dominated by large regions whereas on Fig. 4.24a a much higher number of small details may be observed. Indeed, the number of regions of the ground truth images are 1939 for the agricultural zone and 6869 for the urban zone.

Then, in order to simulate a realistic ground truth, the images represented in Figs 4.23b and 4.24b may be employed as a ground truth for the simulation process. Note, however, that these results may not correspond to the real ground truth of the Oberpfaffenhofen dataset, due to segmentation and modeling errors of the region homogeneity based pruning employed for their generation. Nonetheless, they are good choices for an analysis with simulated data as they have

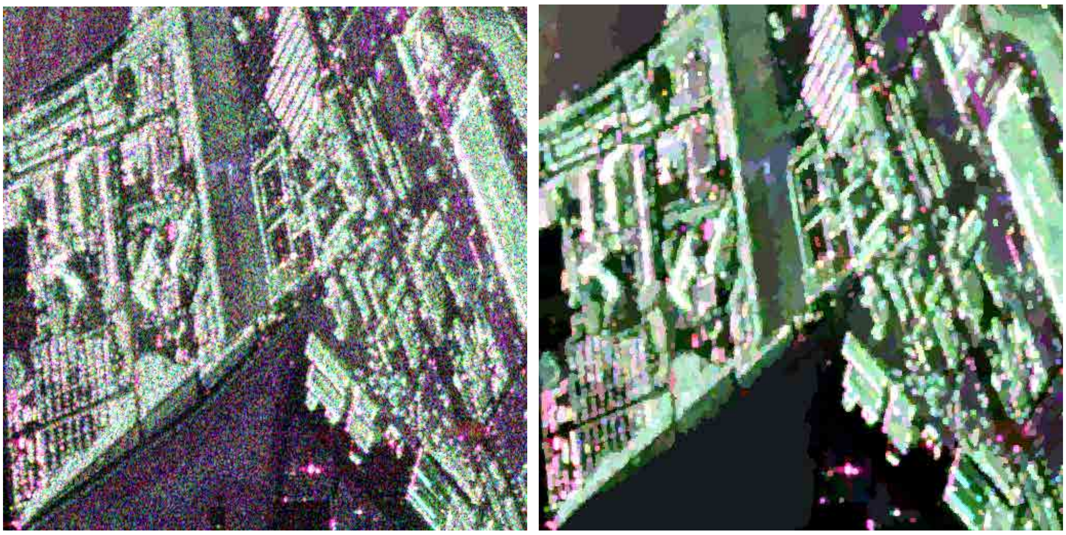

(a) Original crop **(b)** Filtered $(d_{sg}, \delta_p = -1dB)$

Figure 4.24: Pauli representation of the original and filtered images of an urban area $(|S_{hh} + S_{vv}|, |S_{hv} + S_{vh}|, |S_{hh} - S_{vv}|)$.

large and small regions with shapes and polarimetric information that may be close to the structure and content of a real PolSAR image.

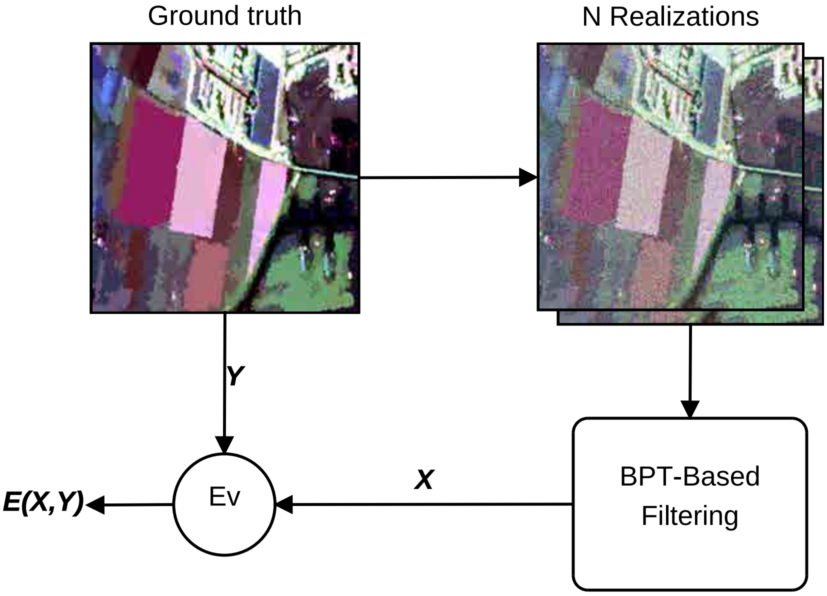

Figure 4.25: Evaluation process scheme for a simulated dataset.

A set of synthetic images may be generated from the ground truth images, represented in Figs 4.23b and 4.24b, that may be employed for testing the performance of the region homogeneity based pruning. The whole simulation and evaluation scheme has been represented in Fig. 4.25, which corresponds to the same evaluation process performed before for the 4-region images datasets.

In order to perform this analysis, the set of realizations are processed with the proposed BPT based technique employing different dissimilarity measures and pruning thresholds and they are compared against the simulated ground truth. For this comparison with the ground truth, which is denoted as $E(X, Y)$ in the scheme, the relative error measure E_R is employed, that has been defined previously in (4.18). Figs. 4.26a and 4.27a represent one simulated realization of the ground truth images described before. As outlined in Fig. 4.25, these images are processed with the BPT proposed technique in order to obtain filtered images, which are also depicted in Figs. 4.26b and 4.27b, respectively. It is worth noticing the similarity of these images with Figs. 4.23b and 4.24b, showing the ability of the BPT to obtain the originally simulated ground truth.

(a) One realization **(b)** Realization filtered $(d_{sg}, \delta_p = -5dB)$

Figure 4.26: One realization of the agricultural simulated ground truth and the corresponding filtered image $(|S_{hh} + S_{vv}|, |S_{hv} + S_{vh}|, |S_{hh} - S_{vv}|)$.

As a first step, the performance of the multilook filtering will be assessed in this complex simulated environment. Table 4.4 shows the E_R measure obtained for the original simulated realizations and after processing them with the multilook filtering employing various window sizes.

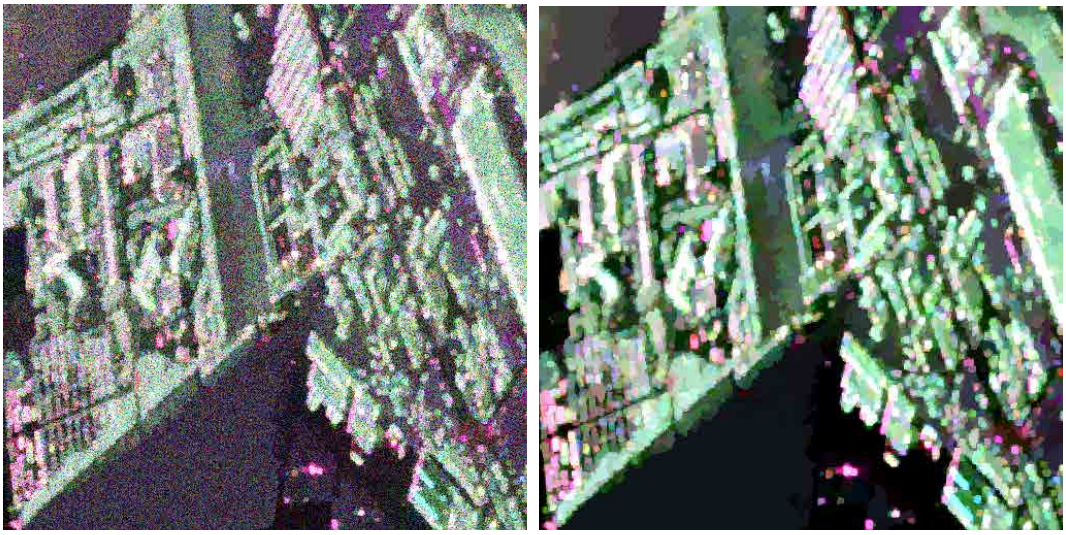

(a) One realization **(b)** Realization filtered $(d_{sg}, \delta_p = -5dB)$

Figure 4.27: One realization of the urban simulated ground truth and the corresponding filtered image ($|S_{hh} + S_{vv}|$, $|S_{hv} + S_{vh}|$, $|S_{hh} - S_{vv}|$).

	Agricultural zone	Urban zone
No filtering	1.451	1.565
3x3 multilook	-1.911	-0.251
5x5 multilook	-2.411	0.871
7x7 multilook	-1.895	2.616
9x9 multilook	-1.055	4.308

Table 4.4: Relative error E_R, in dB, for original and multilook filtered realizations.

As one might expect, similar relative error values are obtained for the original realizations in both zones. However, when applying the multilook, different trends are observed for both cases. On the agricultural zone the best window size is 5x5 whereas on the urban zone it is around 3x3. Moreover, the amount of error obtained in the agricultural area is much lower than the one obtained on the urban area. These differences are caused by the distinct spatial structure of both areas. The agricultural area is composed mainly by large homogeneous fields and, then, a higher amount of filtering may be performed without a significant inhomogeneous region mixture. On the other hand the urban area is composed by a large number of small regions and, consequently, the heterogeneous region mixture effect appears even for small window sizes, increasing the E_R measure.

The same analysis has also been performed to the region homogeneity based pruning, as depicted in Fig. 4.25. Results for the agricultural area are shown in Fig. 4.28 for the BPTs constructed employing the diagonal and full-matrix Wishart and geodesic dissimilarity measures: d_{dw}, d_{sw}, d_{dg} and d_{sg}. Figs. 4.28a and 4.28b show the achieved relative error E_R and the number of pruned regions in terms of the pruning threshold δ_p, respectively. Moreover, Fig. 4.28c shows the relative error in terms of the number of regions pruned in the BPT pruning process.

As it may be seen in Fig. 4.28a, there is a minimum value of E_R for a pruning threshold value slightly below $\delta_p = -5dB$, which is located at the same point for all the BPTs constructed employing various dissimilarity measures. This result is consistent with the previous results employing the 4 regions simulated datasets, as shown in Fig. 4.21. Moreover, for all the dissimilarity measures this minimum value of E_R is clearly below the best value obtained by the multilook, which is represented in Table 4.4, demonstrating its ability to outperform the multilook for speckle filtering by adapting to the spatial structure of the image, even in a complex scenario. When comparing the results obtained by the different dissimilarity measures, it may be seen that the geodesic set of measures achieves better results than the Wishart based measures. Additionally, the diagonal measures d_{dw} and d_{dg} attain slightly lower E_R values than their full-matrix counterparts d_{sw} and d_{sg}, respectively. This observation may seem contradictory as theoretically the full-matrix measures are sensitive to the full polarimetric information, being able to adapt to additional features than diagonal measures, as reported in the previous analysis with the 4 squares datasets. However, it may be related with the fact that the E_R measure is more sensitive to the power information, as stated before, which is contained in the diagonal elements of the covariance matrices. Note that nowadays there is not a clear measure to evaluate properly the full matrix information preservation and probably the relative error measure E_R presents some limitations in this regard. Nevertheless, the full-matrix measures have some important advantages in preserving the full polarimetric information under the Gaussian hypothesis, as it may be seen in Figs. 4.19 and 4.21.

Fig. 4.28b shows the number of pruned regions, or, equivalently, the leaves of the pruned tree, according to the pruning threshold δ_p value. For a better readability the vertical axis, corresponding to the number of pruned regions, is represented in logarithmic scale. It may be seen that, in general, the geodesic dissimilarity measures achieve a smaller number of regions for a given δ_p value than the Wishart based measures. Note that the pruning threshold δ_p parameter fixes the maximum amount of relative MSE accepted per region, corresponding to the homogeneity measure previously defined in (4.14). Then, a smaller number of regions means that the pruned regions obtained are larger while being equally homogeneous, as they have been pruned with the same relative MSE threshold, resulting in a simpler segmentation and a better polarimetric estimation. Consequently, it may be deduced that the geodesic based measures

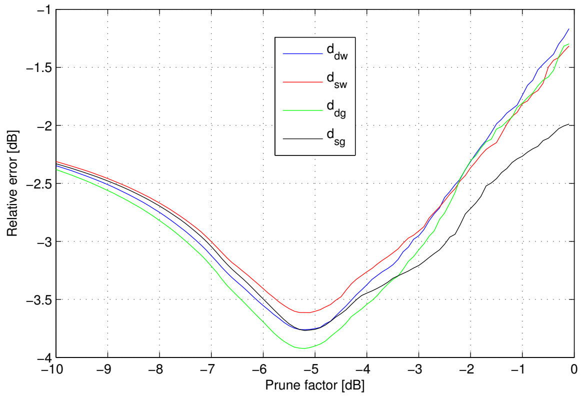

(a) E_R for different δ_p

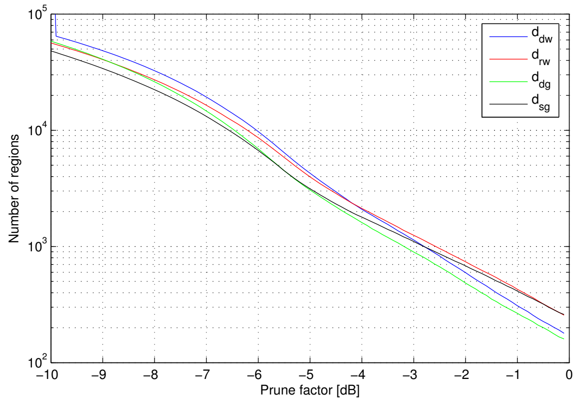

(b) Pruned regions for different δ_p

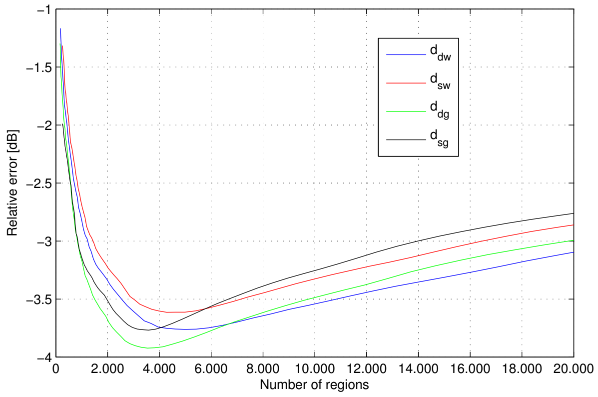

(c) E_R versus pruned regions

Figure 4.28: Parameter evolution for different values of δ_p and dissimilarity measures over the agricultural zone.

achieve a better adaptation to the scene spatial structure, as they obtain larger homogeneous regions than the Wishart based measures. Moreover, if full-matrix measures are compared with diagonal ones, two different situations are observed. For pruning threshold below the optimum, that is, $\delta_p < -5dB$, the full-matrix measures d_{sg} and d_{sw} achieve better results, having a smaller number of pruned regions, than their diagonal counterparts d_{dg} and d_{dw}, respectively. However, for larger values of the pruning threshold, $\delta_p > -5dB$, the opposite situation is noticed. This fact means that full-matrix measures are able to achieve a better adaptation to the structure of the scene when the regions obtained may be considered as homogeneous, specifically for small values of δ_p. As mentioned before, for a larger values of the pruning threshold, when the heterogeneous region mixture becomes evident, as it is represented by an increase in E_R, the sample covariance matrix $\mathbf{Z}$ is not able to properly represent statistically the scattering process of the region. For this pruning threshold values, the BPTs constructed employing full-matrix measures achieve a poorer performance in terms of spatial adaptation. Nonetheless, for this application we are usually interested in having homogeneous regions and, then, in this situation dissimilarity measures employing the full matrix information obtain larger homogeneous regions resulting in a better contour detection.

Additionally, Fig. 4.28c shows the relative error E_R measure versus the number of pruned regions that are obtained when varying the δ_p parameter. The set of E_R values obtained are the same that are represented in Fig. 4.28a, but it may be clearly seen that the minimum E_R value is obtained for a different number of pruned regions on each plot. In fact, the BPTs constructed employing Wishart based measures obtain the best E_R values at about 5000 regions, while if the geodesic measures are employed then this point is achieved at about 3500 regions. As mentioned before, the number of regions of the ground truth for the agricultural zone is 1939. This gives some idea of the spatial adaptation performance of the proposed technique. It can also be seen that the minimum point is attained at slightly lower number of regions for full matrix dissimilarities than for diagonal ones.

Fig. 4.29 shows the same figures than Fig. 4.28 for the urban area crop presented in Fig. 4.24. As in the previous case, the outcome of 25 realizations have been averaged to reduce the noise over the plots. Fig. 4.29a represents the E_R measure versus the pruning factor value δ_p. As it may be expected, there is a minimum for all the lines almost in the same position than in Fig. 4.28a, at $-6dB < \delta_p < -5dB$, but the values of these minimums in urban area are lower in terms of E_R than the values obtained in the agricultural area. Indeed, the difference between the E_R obtained at $\delta_p = -10dB$ and the minimum point is not as large as in Fig. 4.28a. This contrast between both results are produced by the distinct spatial structure of both images. As mentioned previously, the urban area is composed mainly by a large number of small regions and, then, there are a smaller number of homogeneous samples for each target to estimate its response. Consequently, the possible amount of speckle filtering is inherently reduced, as there is no opportunity to achieve such a large filtering as in the agricultural area. However, it is worth to mention that the obtained E_R values are still better than those obtained by the multilook, represented in Table 4.4, as the spatial adaptation avoids the mixture of adjacent targets. When comparing the results obtained employing different dissimilarity measures, the same conclusions extracted for the agricultural area dataset apply, although over urban area the differences in term of E_R between diagonal and full matrix dissimilarities are larger. This fact may be caused by the inability to estimate properly the off-diagonal elements of the covariance matrix over such a small regions having few samples available, confusing the full-matrix measures that rely on them for the region similarity computation.

Fig. 4.29b shows similar trends to Fig. 4.28b, having almost the same shape. However, the vertical axis scale, corresponding to the number of regions, presents larger values, since the structure of the urban areas is much more complex, resulting in a higher number of regions for a given pruning factor δ_p. An analogous effect may be observed on Fig. 4.29c, where the best results in terms of E_R are achieved at about 15000 regions for the geodesic based dissimilarities and at about 20000 for Wishart based dissimilarities. As described before, the ground truth for the urban area contains 6869 regions, so there is approximately the same relation between the number of pruned regions for the minimum E_R attained and the ground truth regions for the agricultural and the urban areas.

Comparing the results with simulated data presented in this section with those presented in Section 4.3.3 it may be seen that the δ_p values employed differ substantially. When dealing with real data, the typical pruning threshold values range from $-2dB < \delta_p < 0dB$ whereas on the previous analysis with simulated data the best E_R values are obtained for values around $-6dB < \delta_p < -4dB$. As an example, Figs. 4.23b and 4.26b correspond to similar results but the former has been obtained from real data at $\delta_p = -1dB$ whereas the latter from simulated data with $\delta_p = -5dB$. This disparity implies that the simulated data are more homogeneous, in terms of the homogeneity measure, than the real data. This fact may be caused due to additional features that are present in real data and are not taken into account within the region model simulated, which is the complex Gaussian polarimetric model. These additional features may be considered as the region texture and, since they are not properly modeled, the pruning threshold δ_p has to be increased in order to absorb these modeling errors when processing real data. When the synthetic data are generated, this texture is not reproduced as it is not contemplated in the model and, then, it is not necessary to increase the pruning factor to assimilate the modeling

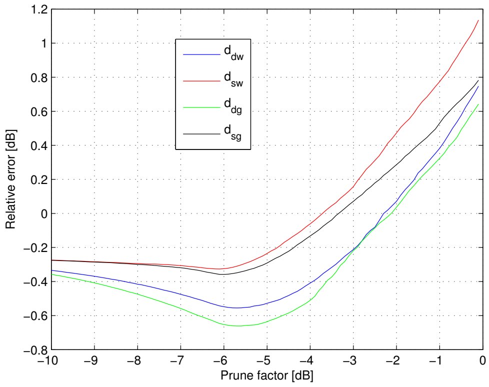

(a) E_R for different δ_p

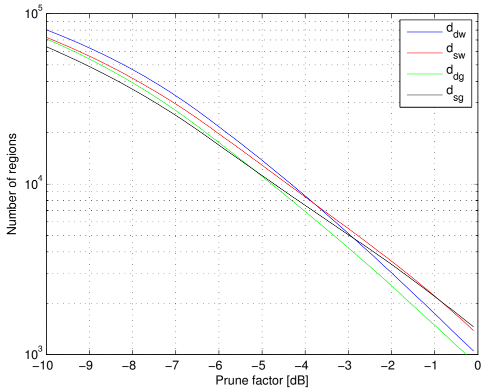

(b) Pruned regions for different δ_p

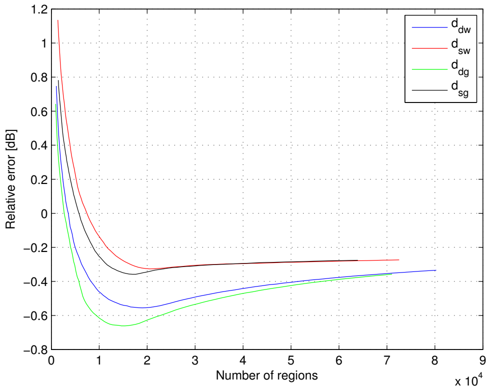

(c) E_R versus pruned regions

Figure 4.29: Parameter evolution for different values of δ_p and dissimilarity measures over the urban zone

errors.

4.4 BPT based Coastline Segmentation

As a multi-scale data abstraction, the BPT structure contains a large amount of useful information about the image structure at different detail levels, as mentioned before. In this section the coastline segmentation is briefly presented in order to illustrate a different application based on a completely different pruning mechanism than the polarimetric estimation presented in previous sections.

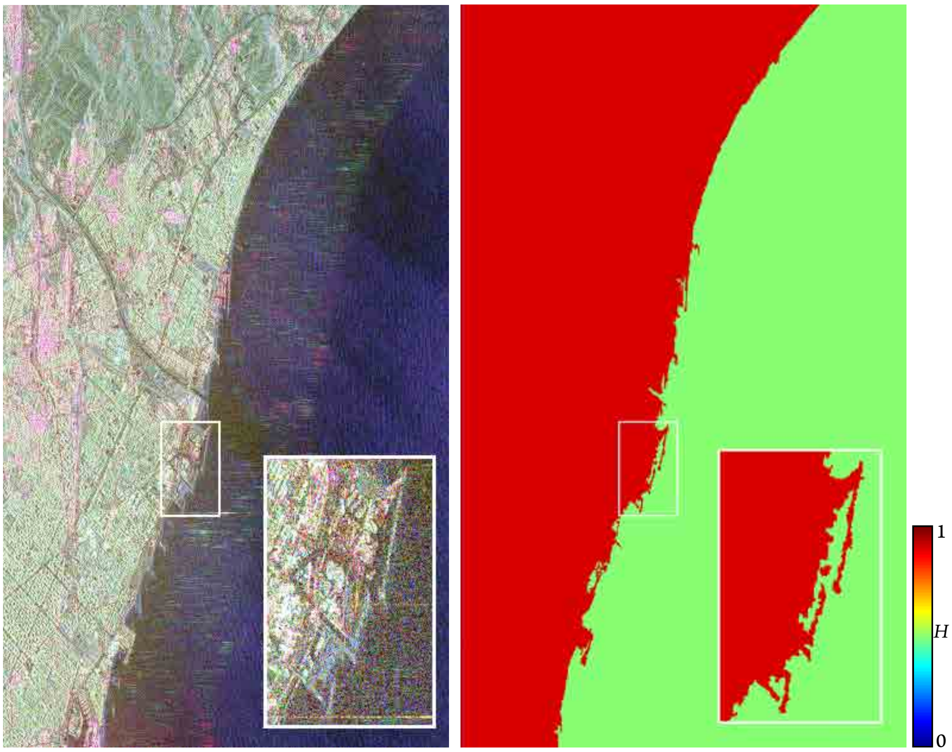

(a) Original Pauli **(b)** BPT based coastline segmentation

Figure 4.30: Pauli RGB image of Barcelona (a), and BPT based coastline segmentation (b). The revised Wishart dissimilarity d_{sw} has been employed for the BPT construction $(|S_{hh}+S_{vv}|, |S_{hv}+S_{vh}|, |S_{hh}-S_{vv}|)$.

Fig. 4.30a presents a PolSAR image of Barcelona, Spain. This image is a 1500 × 2500-pixel cut of a C-band Pauli RADARSAT-2 image that was acquired in November, 18th 2008, in fine quad polarization mode, with nominal resolution of $5.2m \times 7.6m$. Over the sea, a zoom rectangle shows a detailed area corresponding to the Forum harbor of Barcelona. The coastline segmentation result is shown on Fig. 4.30b, where 2 regions may be seen, corresponding to the sea and the land on the image. The color of each region corresponds to its Entropy (H) parameter in

Fig. 4.30b. To generate this result, the BPT has been constructed employing the symmetric Wishart dissimilarity measure d_{sw} (4.2) and, as a pruning strategy, the two most different of the tree has been extracted, that is, the two sons of the root node.

As it may be seen, the coastline is clearly detected as the contour between the two obtained regions. Additionally, due to the ability of the BPT to preserve contours and small details, some small and thin structures like the breakwaters of the Forum harbor are preserved in the segmentation. Indeed, all these details are detected on the lower levels of the tree and they are transfered to the larger regions of the BPT, as shown in Fig. 4.30b.

While the polarimetric estimation is based on the extraction of the homogeneous regions of the tree, corresponding to smaller regions, this application is focused on the largest ones. The example presented in Fig. 4.30 exhibits the benefits and usefulness of a multi-scale representation like the BPT for data representation and interpretation.

It is worth noticing that, as mentioned in Section 4.1.2, the sample covariance matrix $\mathbf{Z}$ employed as a region model, is not able to properly represent homogeneous regions of the image. In the coastline segmentation example, represented in Fig. 4.30b, the region corresponding to the land area, represented in red color, is strongly heterogeneous, as it contains a mixture of urban areas, agricultural fields, mountains, etc. Indeed, it may be seen that this area has a large Entropy, as red color correspond to $H = 1$, due to this combination of different types of scattering processes. Nevertheless, a meaningful segmentation result is obtained since, in this case, the other region containing the sea area corresponds to a quite homogeneous area. However, in general, for a proper representation of inhomogeneous areas more complex region models should be employed in the BPT representation. This issue will be further discussed and analyzed later, in Section 6.3, where some additional models are defined to handle, up to a certain point, with inhomogeneous regions.

We must use time as a tool, not as a coach.

John F. Kennedy

5

Polarimetric SAR Time Series BPT based Processing

In the last few years the construction of temporal series datasets has grown significantly, driven by the growing presence of space-borne SAR systems. These datasets consist of different acquisitions of the same area collected at different dates, due to the ability of space-borne sensors to revisit periodically and under the same geometry the scene. The importance of these data relies in that they contain useful information not only concerning the scene but also related to its temporal evolution and dynamics. Nevertheless, the analysis and exploitation of this information from SAR time series is a challenge that is only just beginning to be studied and developed.

This chapter deals with all the concepts related to the extension of the previously defined BPT data abstraction to represent and exploit PolSAR time series datasets. Two different alternatives are proposed for this extension and the strengths and limitations of both approaches are analyzed and discussed. Apart from the previously mentioned speckle filtering application, on which this thesis is focused, an additional application will be proposed in order to study the variability of the scene. This application gives an idea of the potentialities of the BPT abstraction and its usefulness for the analysis and interpretation of the temporal dimension of the data.

5.1 The Temporal Dimension of the Data

On the time series datasets, the temporal dimension comes into play. When considering these data, particular attention should be paid to the modeling of this dimension, as it will define the final representation obtained and its interpretation. In this work, two different BPT approaches are defined depending on the target modeling in terms of the temporal dimension. In order to simplify the processing and the analysis, in the following it will be assumed that all the acquisitions are properly co-registered, that is, the area of the scene represented by the pixel at position (i, j) is the same for each acquisition of the dataset.

The two proposed modeling alternatives differ on the way they characterize a target on these time series datasets. The additional information contained within the temporal dimension may be considered as an additional dimension of the data or as an additional feature of the target. The following sections give a more detailed description of these assumptions and their corresponding consequences in terms of data modeling and interpretation.

5.1.1 Time as an Additional Dimension of the Data

On the one hand, it may be assumed that a target is characterized by the statistics of its polarimetric response, as performed in single PolSAR image data processing, which has been described in Chapter 4. Note that, under this assumption, different target responses may be observed for a resolution cell on each acquisition, resulting into distinct targets detected at different time instants over the same area. This fact implies that time series datasets are composed by *three-dimensional data*, corresponding to the *space and time dimensions*. In this context, then, the temporal dimension is employed as an additional source of data [15].

The immediate consequence is that the amount of available samples gets increased according to the number of acquisitions of the dataset. A dataset having N acquisitions containing n_r and n_a pixels in range and azimuth dimensions, respectively, is composed of $n_r \cdot n_a \cdot N$ elements. It is worth noticing that, according to this assumption, the sample covariance matrix $\mathbf{Z}$ may be estimated, as described in (2.54), employing homogeneous samples of different acquisitions. This involves an improvement in terms of the estimated $\mathbf{Z}$ as the number of available samples may be increased while also reducing the effect of speckle noise. However, this also implies that an adaptation is needed in the space-time dimensions in order to avoid heterogeneous samples mixture, which might be more complex due to the higher dimensionality. Moreover, since samples of different acquisitions are combined, the interferometric information of the data cannot be exploited with this approach.

5.1.2 TIME AS AN ADDITIONAL DIMENSION OF THE TARGET

On the other hand, it may be assumed that a target is not defined by a constant response, but a particular temporal evolution is associated with each target. Then, its response changes among the temporal dimension following a particular trend defined by this evolution. Under this assumption, the target may be characterized by its response dynamics according to the temporal dimension. To this end, the statistics of the extended scattering vector $\mathbf{k}_e$ may be employed [15]

$$\mathbf{k}_e = \begin{bmatrix} \mathbf{k}_1^T & \mathbf{k}_2^T & \dots & \mathbf{k}_N^T \end{bmatrix}^T \tag{5.1}$$

where $\mathbf{k}_i$ represents the scattering vector at the i-th acquisition, as defined in Section 2.2.3 and N represents the number of acquisitions in the dataset.

Following the same rationale than in Section 2.2.4, the extended sample covariance matrix $\mathbf{Z}_e$ may be defined, corresponding to the estimation of the covariance matrix of $\mathbf{k}_e$, containing all the information to completely characterize it under the Gaussian hypothesis

$$\mathbf{Z}_e = \langle \mathbf{k}_e \mathbf{k}_e^H \rangle_n = \begin{pmatrix} \mathbf{Z}_{11} & \boldsymbol{\Omega}_{12} & \cdots & \boldsymbol{\Omega}_{1N} \\ \boldsymbol{\Omega}_{12}^H & \mathbf{Z}_{22} & \cdots & \boldsymbol{\Omega}_{2N} \\ \vdots & \vdots & \ddots & \vdots \\ \boldsymbol{\Omega}_{1N}^H & \boldsymbol{\Omega}_{2N}^H & \cdots & \mathbf{Z}_{NN} \end{pmatrix} \tag{5.2}$$

where $\mathbf{Z}_{ii}$ corresponds to the 3 by 3 sample covariance matrix representing the polarimetric information of the i-th acquisition, as expressed in (2.54), and $\boldsymbol{\Omega}_{ij}$ is a 3 by 3 complex matrix representing the correlation between the acquisitions i and j.

Note that, in this scenario, the additional information provided by the temporal dimension of the data is employed to improve the target characterization by including this information into its description, resulting into the extended matrix $\mathbf{Z}_e$. Then, the individual data elements are not the original pixels of each acquisition, but the complete set of collocated pixels among all the N acquisitions, as described by (5.2). Therefore, having N acquisitions containing n_r and n_a pixels in range and azimuth dimensions, respectively, results into a dataset having $n_r \cdot n_a$ elements with an extended sample covariance matrix $\mathbf{Z}_e$ composed of $N \times N$ 3 by 3 matrices. However, since $\mathbf{Z}_e$ is hermitian, it only contains $(N^2 + N)/2$ independent 3 by 3 matrices. So, this assumption results into *two-dimensional data*, corresponding to the *spatial dimensions*, similarly to the single PolSAR image case.

Comparing this approach with the one presented in Section 5.1.1, it has the disadvantage of not allowing the increase in the number of samples combined, as the number of samples in the dataset is independent of the number of acquisitions N. However, this concept allows a more detailed target characterization when employing the extended $\mathbf{Z}_e$ matrix, making possible, for instance, the exploitation of the interferometric information, which may be extracted from the $\mathbf{\Omega}_{ij}$ matrices.

5.2 BPT REPRESENTATIONS FOR POLSAR TIME SERIES

Two alternatives have been proposed for dealing with the temporal dimension of the data, as described in Sections 5.1.1 and 5.1.2. The BPT abstraction, described in Chapter 3, may be extended to represent PolSAR time series according to these hypotheses [15], as described in the following.

These sections are focused on the generation of the BPT structure from the original PolSAR time series, by defining the core concepts over these datasets, as described in Section 3.2. Additionally, these concepts are related with their equivalent notions when processing PolSAR data, as they have been defined previously in Section 4.1.

5.2.1 SPACE-TIME BPT

When considering the temporal information as an additional dimension of the data, just as described in Section 5.1.1, a three-dimensional dataset is obtained [10]. These correspond to the space and time dimensions and, consequently, this BPT representation will be called Space-Time BPT (ST BPT) [15].

In order to apply the BPT construction process, some elements have to be defined for this

1. *Data connectivity.* The obtained BPT will contain connected regions of the data. Then, in this case, the data connectivity has to be defined over the space-time domain. Over the spatial dimension, each pixel will be connected with its 8 neighbors, as it has been defined for PolSAR data in Section 4.1.1. In the temporal dimension, each pixel will be connected with the pixels located on the same position in the acquisitions just before and after in the temporal dimension, resulting into the *10-connectivity* [10][15], which has been represented in Fig. 5.1.

2. *Region model.* Under this approach, as described in Section 5.1.1, a target is characterized by its polarimetric response. Then, the sample covariance matrix $\mathbf{Z}$, defined in (4.1), may be employed for its description, as it completely describes the scattering process under the Gaussian hypothesis. However, note that in this case the sample covariance matrix

may be computed by combining samples of different acquisitions, as the connected regions of the data may cover different images by expanding over the temporal dimension.

3. *Similarity measure.* To apply the BPT construction process described in Algorithm 3.2, the similarity between adjacent regions has to be computed. Note that this is a measure defined over the region model space, which is the same model employed for processing PolSAR data. Then, all the dissimilarity measures previously defined in Section 4.1.3 may be employed to construct the ST BPT.

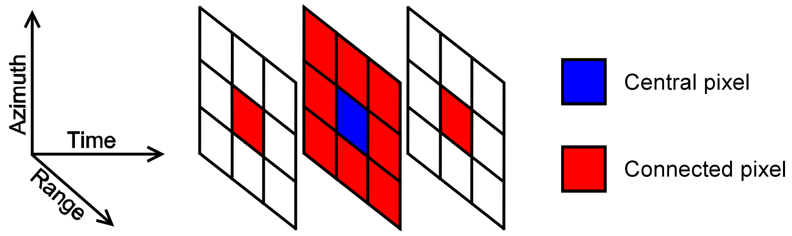

Figure 5.1: Space-Time BPT pixel connectivity. Each pixel, represented in blue, has 10 neighbors, colored in red.

As a consequence, the resulting ST BPT data abstraction is composed of connected regions of the data in the space and time dimensions presenting a *similar polarimetric response*. This means that the obtained regions cover pixels of different acquisitions having a similar **Z** matrices, according to the employed dissimilarity measure. As mentioned previously, this may allow an increase in the number of samples per region, improving the polarimetric information estimation by expanding regions in the temporal dimension. However, due to the adaptation to the data morphology, this expansion may only be possible if there are no changes in the target among the different acquisitions, as its **Z** matrix will change, resulting into the mixture of heterogeneous samples. Consequently, when there is a target change among two adjacent acquisitions, a contour in the temporal dimension is observed.

It is worth noticing that, since in the ST BPT approach the temporal information has been employed as an additional dimension of the data, a change in the data connectivity has to be performed to adapt to the new dimensionality, but the region model and dissimilarity measures have been maintained with respect to the single PolSAR image BPT abstraction. This fact may give an idea of the simplicity of the adaptation of the BPT processing scheme to a different data type or layout.

5.2.2 TEMPORAL EVOLUTION BPT

The temporal information may also be employed to improve the characterization of the target scattering process, as described in Section 5.1.2. As a consequence, each target is characterized by a particular temporal evolution [6], that may be described by the extended model $\mathbf{Z}_e$, as detailed before. Therefore, this approach will be called Temporal Evolution BPT (TE BPT) [15].

As for the ST BPT, the following elements have to be defined in order to construct the TE BPT from the original data [7]

1. *Data connectivity.* Note that in this case a two-dimensional dataset is obtained, as the temporal information is included within $\mathbf{Z}_e$. Then, the same 8-connectivity scheme employed before, shown in Fig. 4.1, may be applied for this data.

2. *Region model.* In this approach the whole temporal evolution of the target has to be taken into account, as mentioned in Section 5.1.2. The extended sample covariance matrix $\mathbf{Z}_e$ has been defined in (5.2) for this purpose and it may be employed as a region model in the TE BPT representation.

3. *Similarity measure.* This measure is defined in the region model space and, as a consequence, it has to be defined over the $\mathbf{Z}_e$ matrix. In Section 4.1.3, some dissimilarity measures have been defined over the sample covariance matrix for PolSAR data. The extended sample covariance matrix $\mathbf{Z}_e$ contains the polarimetric information of the target at the i-th acquisition on the sub-matrix $\mathbf{Z}_{ii}$, as explained before. Therefore, a modification of the previously defined dissimilarity measures is proposed to take into account the full sequence of polarimetric matrices. For instance, the extended geodesic dissimilarity measure d_g between two regions A and B may be defined as

$$d_g(A,B) = \sqrt{\sum_{i=1}^{N} \left\| \log\left(\mathbf{Z}_{A_{ii}}^{-1/2}\mathbf{Z}_{B_{ii}}\mathbf{Z}_{A_{ii}}^{-1/2}\right)\right\|_F^2 + \ln\left(\frac{2n_A n_B}{n_A + n_B}\right)} \tag{5.3}$$

   where $\mathbf{Z}_{A_{ii}}$ represents the $\mathbf{Z}_{ii}$ component of the A region, as shown on (5.2).

It is worth noticing that the first part of (5.3) corresponds to euclidean norm of the geodesic dissimilarity terms, the term depending on the covariance matrix in (4.3), corresponding to the entire sequence of $\mathbf{Z}_{ii}$ matrices. The term depending on the region size has been maintained unaltered as it only concerns the number of pixels within the region, having nothing to do with the polarimetric modeling. The same idea may also be applied to extend other similarity measures.

Moreover, the dissimilarity measure extension proposed in (5.3) ignores the information contained within the $\mathbf{\Omega}_{ij}$ matrices. Indeed, the d_{sg} dissimilarity measure defined in (4.3) could be applied directly to the whole $\mathbf{Z}_e$ matrix. However, this approach will involve some limitations as the information contained within the $\mathbf{\Omega}_{ij}$ is different to the one contained in the $\mathbf{Z}_{ii}$ matrices. The $\mathbf{\Omega}_{ij}$ matrices contain interferometric information, having a distinct nature than the polarimetric information, that depends on the spatial baselines, topography, subsidence, etc [34] which prevents a direct comparison between them. Additionally, in order to employ the whole $\mathbf{Z}_e$ matrix for a full-matrix measure, it is required to be full-rank, involving a large initial filtering of, at least, $3N$ independent samples for matrix regularization [60]. This may be a problem even for a small number of acquisitions N, requiring a large averaging and reducing the spatial resolution. On the other hand, the proposed extension in (5.3) employs the full polarimetric information among all the acquisitions, under the Gaussian hypothesis, and only requires a small matrix regularization process employing at least 3 independent samples, as in the single PolSAR image BPT based processing.

The nodes of the TE BPT represent spatial regions of the scene having a similar polarimetric temporal evolution, that is, regions presenting a similar sequence of $\mathbf{Z}_{ii}$ matrices according to the dissimilarity measure. Although it may not increase the number of averaged samples, as in the case of the ST BPT, the TE BPT may improve the target characterization, as it takes into account the temporal evolution information, resulting into a better identification of targets and a more accurate region contours over the scene.

In the TE BPT the region model has been changed and, as a consequence, the dissimilarity measure has been also modified accordingly. Despite these changes, the rest of the concepts and algorithms presented in Chapter 3 may be applied directly. This is possible thanks to the generic description of the BPT and its related modeling notions. Then, the adaptation performed on the TE BPT may serve as an example for the process of changing the region model in the BPT data abstraction.

It is worth mentioning that both ST BPT and TE BPT approaches, presented in Sections 5.1.1 and 5.1.2, may be seen as a generalization of the single PolSAR image BPT, presented and analyzed in Chapter 4, as both of them result into this representation for $N = 1$.

The computational complexity of the BPT construction process has been analyzed in Section 3.2.3, being the Algorithm 3.2 the most significant part. This algorithm has a complexity of $O(n \log n)$, depending on the number of leaves of the tree n. Note that for the two defined BPT approaches in Sections 5.1.1 and 5.1.2, the number of leaf nodes is different, being $n_r \cdot n_a \cdot N$ for the ST BPT and $n_r \cdot n_a$ for the TE BPT, where n_r and n_a represent the number of samples in range and azimuth, respectively. However, although the number of leaves does not depend on the number of acquisitions N in the TE BPT, the complexity of the dissimilarity measure computation increases linearly with N, as it may be observed on (5.3). When taking this into consideration, the asymptotic computational cost of the ST BPT may be expressed as $O\left(n_r n_a N \log(n_r n_a N)\right)$, whereas for the TE BPT this cost will be $O\left(n_r n_a N \log(n_r n_a)\right)$. Consequently, the computational cost of the TE BPT construction is slightly below the construction cost of the ST BPT, mainly due to the smaller number of nodes of the tree.

5.3 POLARIMETRIC SAR TIME SERIES BPT PRUNING

Section 5.2 has described two different BPT representations of a PolSAR time series dataset. Both of them differ on the target characterization in the temporal dimension, as explained in Sections 5.1.1 and 5.1.2, respectively. This section deals with the BPT exploitation of these two data abstractions.

A tree pruning process has been proposed in Section 3.3.1 for BPT exploitation. In order to achieve a good target characterization, we are usually interested in obtaining the largest homogeneous regions of the data, as it has been mentioned in Section 4.3. Note, however, that this results into different concepts for both approaches, as they contain distinct types of regions, as mentioned before. In this section, the region homogeneity based pruning, described in Section 4.3.2, will be adapted to the ST BPT and the TE BPT, as it has proven to be independent of the image content and to produce better results in practice.

The region homogeneity based pruning is based on the definition of a homogeneity measure $\Phi(A)$ that may be interpreted as the average error committed when representing all the samples of the region A by its region model, as defined in Section 4.3.2. For a single image PolSAR data, the homogeneity measure $\Phi(A)$ has been defined in (4.14) based on the relative MSE measured employing the euclidean matrix norm of the sample covariance matrices $\mathbf{Z}$. It is worth noticing that in the ST BPT representation the region model is exactly the same than in this case and, thus, the same (4.14) measure may be directly applied. Then, the pruning criterion may be obtained by fixing a threshold δ_p over this measure to obtain those regions with a homogeneity below the threshold, as expressed in (4.15) or (4.16). However, the nodes of both BPT representations may not be compared, as in the ST BPT they represent three-dimensional regions of the data, potentially containing samples of different acquisitions.

It is worth emphasizing at this point that although the BPT representation of a single PolSAR image and the ST BPT are different data abstractions of distinct types of datasets, the same pruning process and criteria may be directly applied for both of them without any change, as they share the same region model. Indeed, this is a good example of the decoupling performed by the BPT data abstraction between the application dependent and independent parts, as described in Section 3.1.4. As it has been depicted in the scheme on Fig. 3.6, the BPT pruning process for a particular application is defined in terms of the BPT structure itself, decoupling it with the underlying data. Then, when changing the underlying data structure for PolSAR time series in the ST BPT, only the BPT construction process has to be modified, whereas the same pruning process proposed in Section 4.3.2 may be applied directly over the resulting tree structure.

On the other hand, in the TE BPT representation the region model has been changed to the extended sample covariance matrix $\mathbf{Z}_e$ to represent the target temporal evolution, as expressed in (5.2). As expressed in Section 5.2.2 the previously mentioned $\Phi(A)$ measure may be applied to the $\mathbf{Z}_e$ matrix. However, this approach will have the same inconveniences previously mentioned, as it would mix polarimetric and interferometric information and it will require a stronger initial filtering for matrix regularization. Alternatively, the same extension method performed for the (5.3) dissimilarity measure may be applied for the homogeneity measure $\Phi(A)$ defined in (4.14), resulting into the extended homogeneity measure $\Phi_e(A)$ which employs the full polarimetric temporal evolution contained in the sequence of $\mathbf{Z}_{ii}$ matrices of the region A

$$\Phi_e(A) = \frac{1}{n_A} \sum_{i \in A} \frac{\sum_{j=1}^{N} \|\mathbf{Z}_{jj}^i - \mathbf{Z}_{A_{jj}}\|_F^2}{\sum_{j=1}^{N} \|\mathbf{Z}_{A_{jj}}\|_F^2} < \delta_p \tag{5.4}$$

where $\mathbf{Z}_{jj}^i$ is the $\mathbf{Z}_{jj}$ covariance matrix for the i-th pixel within region A and $\mathbf{Z}_{A_{jj}}$ is the $\mathbf{Z}_{jj}$ covariance matrix of the region model $\mathbf{Z}_e$ for the A region.

Again, the $\Phi_e(A)$ homogeneity measure may be interpreted as the relative MSE that is committed when representing all the individual pixels by its $\mathbf{Z}_e$ model when taking into account only the polarimetric information evolution, contained within the $\mathbf{Z}_{ii}$ matrices.

The pruning process has been described in Section 3.3.1, where Algorithms 3.3 and 3.5 have been defined for pruning the BPT in a top-down and bottom-up approaches, respectively. The complexity of these pruning processes has been defined as linear with respect to the number of nodes of the BPT, resulting in a computational complexity of $O(n_r n_a N)$ both for the ST BPT and the TE BPT. Note that although the number of nodes in the TE BPT is smaller, in the order of $O(n_r n_a)$, the computation of the homogeneity measure (5.4) has a linear complexity depending on the number of acquisitions $O(N)$, resulting into a total pruning cost in the order of $O(n_r n_a N)$.

To analyze the results obtained with the two different BPT based processing schemes proposed, a real PolSAR time series dataset is employed in this section. This dataset is composed by 8 RADARSAT-2 Fine Quad-Pol images corresponding to a test site in Flevoland, the Netherlands. It was acquired within the ESA AgriSAR 2009 campaign, devoted to analyze the agricultural fields temporal evolution employing PolSAR data. The selected set of images correspond to acquisitions with the same incidence angle, the beam FQ13 in this case, and in ascending passes of the satellite, from April 4th, 2009 to September 29th, 2009, with an acquisition every 24 days. From the original acquisitions, a crop of a common area of the scene having 4000 by 2000 pixels has been selected and co-registered, conforming the full Flevoland dataset, as represented in Fig. 5.2.

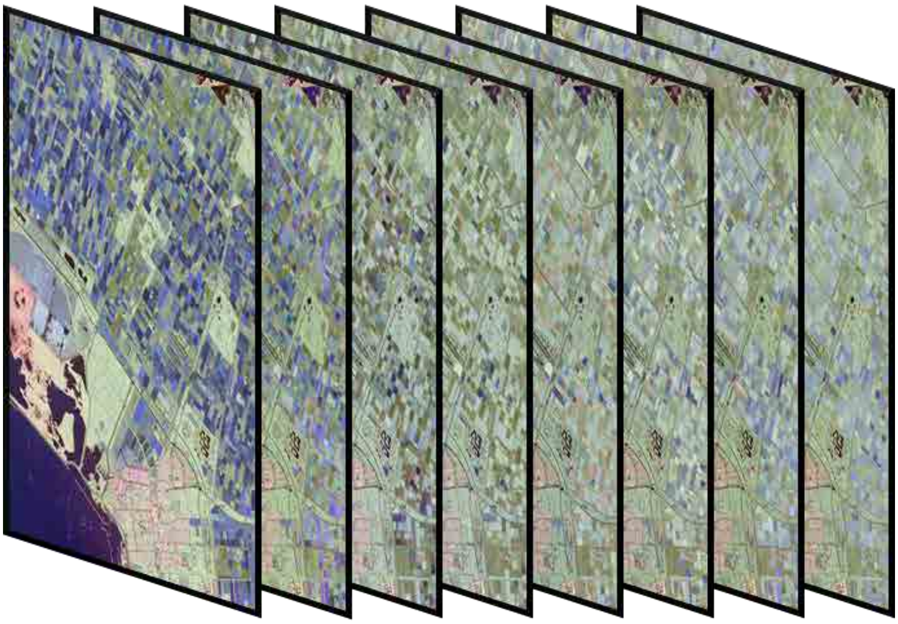

Figure 5.2: Composition with the 8 Pauli RGB images of the full PolSAR time series dataset of Flevoland ($|S_{hh} + S_{vv}|$, $|S_{hv} + S_{vh}|$, $|S_{hh} - S_{vv}|$).

Two of these images are shown on Fig. 5.3, corresponding to the acquisitions from April 14th, 2009 and June 25th, 2009, respectively. As it may be seen, the scene is composed mainly by a large area of agricultural fields, in the central and top part of the image, and some sea surface and urban areas at the bottom part. The difference between both images may be clearly observed specially in the agricultural fields, mostly appearing in blue color in Fig. 5.3a, corresponding to a surface scattering according to the Pauli basis, but appearing in green over Fig. 5.3b, representing a dominant volume scattering. This variation is caused by the plant growing process in the agricultural fields. Most of the plants in the agricultural fields are not grown on April, but they become near fully grown in June, resulting in an increase in the volume scattering component of the Pauli basis.

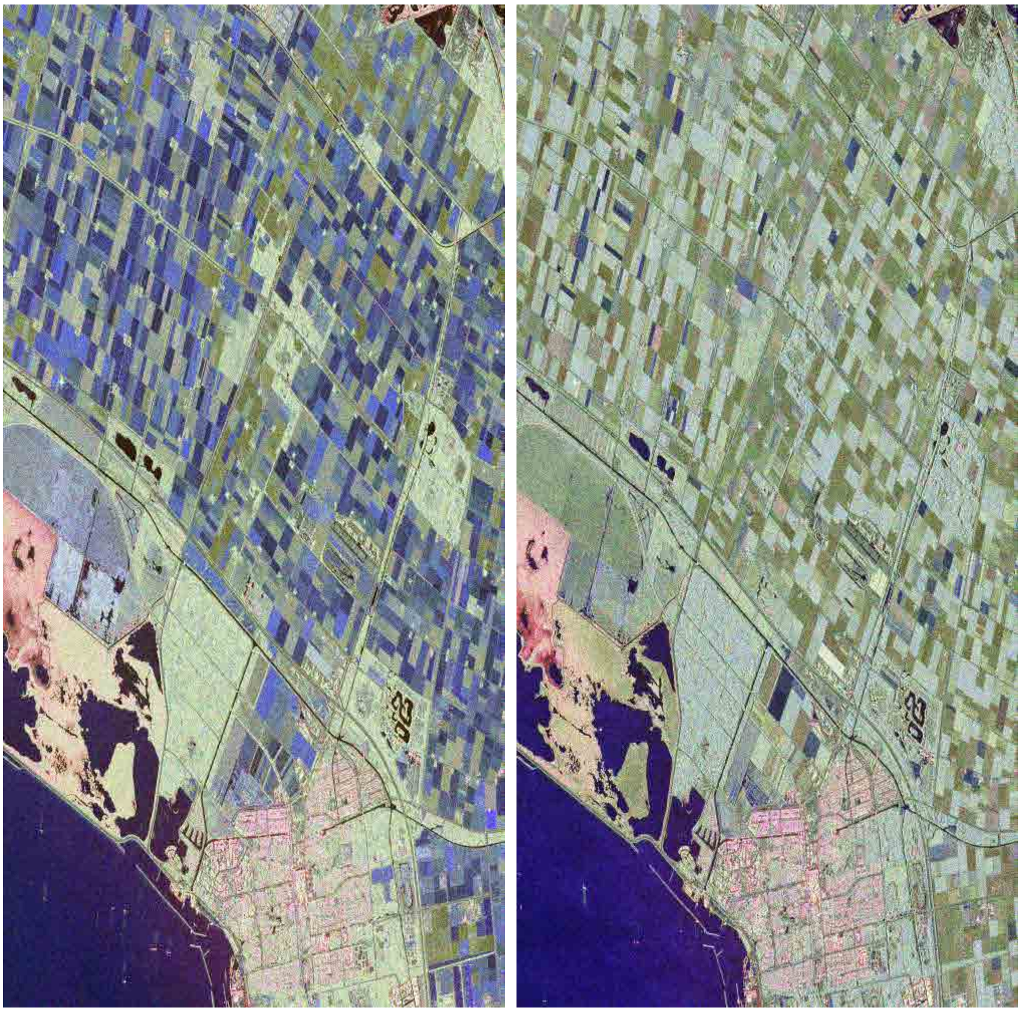

(a) April 14th, 2009 **(b)** June 25th, 2009

Figure 5.3: Pauli RGB crop images from two Flevoland acquisitions corresponding to April 14th, 2009 and June 25th, 2009 ($|S_{hh}+S_{vv}|$, $|S_{hv}+S_{vh}|$, $|S_{hh}-S_{vv}|$).

Fig. 5.4 shows the results obtained over the first acquisition of the dataset, corresponding to a fraction of the results, employing the two mentioned BPT approaches with a pruning threshold of $\delta_p = -3dB$. Note that the full dataset is difficult to represent for visual inspection, as it contains 8 different images, then, on Fig. 5.4 only a portion of it, corresponding to the first acquisition is shown, although the full dataset with the 8 acquisitions has been processed. Similarly, in the following, results will be shown over one of the acquisitions, for simplicity. Fig. 5.4a represents the results of the region homogeneity based pruning over the ST BPT constructed employing the geodesic dissimilarity measure d_{sg}, defined in (4.3), whereas Fig. 5.4b shows the same pruning results over the TE BPT constructed employing the extended geodesic

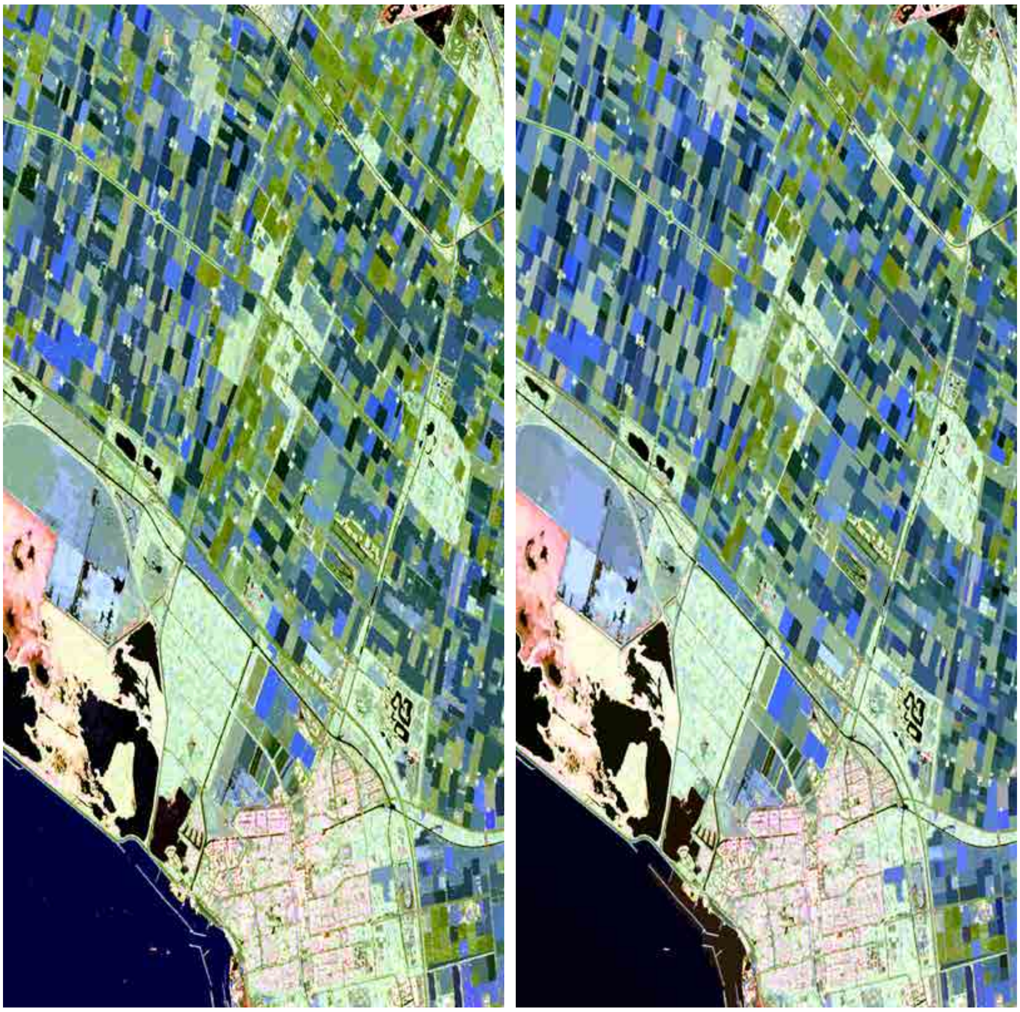

(a) ST BPT, d_{sg}, $\delta_p = -3dB$ (b) TE BPT, d_g, $\delta_p = -3dB$

Figure 5.4: Pauli representation of the first Flevoland acquisition after processing the full dataset with the Space-Time BPT constructed employing the d_{sg} measure (a), and with the Temporal Evolution BPT constructed with the d_g measure (b). Results shown are both for $\delta_p = -3dB$ ($|S_{hh} + S_{vv}|$, $|S_{hv} + S_{vh}|$, $|S_{hh} - S_{vv}|$).

dissimilarity d_g, as expressed in (5.3). Both cases have been pruned with a pruning threshold of $\delta_p = -3dB$ but, however, note that on the ST BPT the Φ homogeneity measure is employed whereas the corresponding extended measure Φ_e is employed for the TE BPT, as the region model for both approaches differs.

Qualitatively similar results may be observed when comparing Fig. 5.4a and Fig. 5.4b. With the employing pruning threshold both methods achieve a relatively large speckle reduction while also preserving the region contours. However, when the results are observed closely, some differences appear, specially on the agricultural fields region contours detected by both methods. To examine in detail the obtained contours, Fig. 5.5 shows a zoom over a small 512 x 512 pixel area of the dataset corresponding to the agricultural fields area of the previous results. Fig. 5.5a corresponds to the original acquisition, Fig. 5.5b shows the corresponding area of the results obtained with the ST BPT whereas Fig. 5.5c depicts the same area of the previous TE BPT results. In this case, the crop shown corresponds to the second acquisition for all the cases.

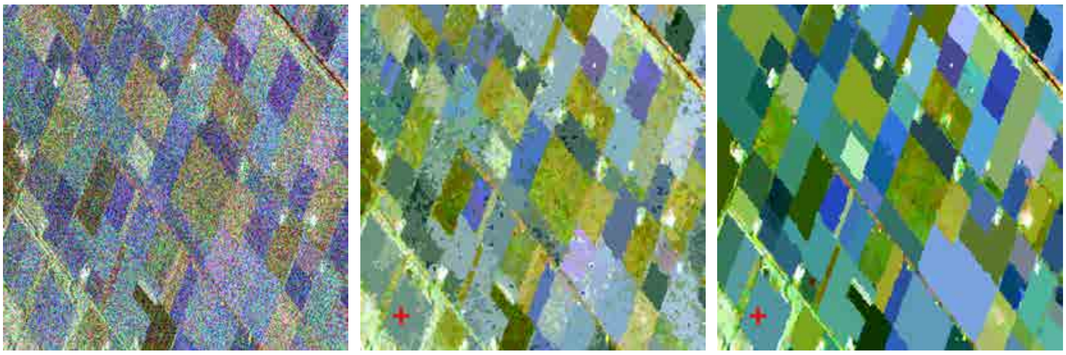
(a) Original **(b)** ST BPT **(c)** TE BPT

Figure 5.5: Pauli representation of a crop area of the second acquisition. Original (a) and results after processing the full dataset with the ST BPT (b) and with the TE BPT (c). Results are shown for $\delta_p = -3dB$ ($|S_{hh} + S_{vv}|$, $|S_{hv} + S_{vh}|$, $|S_{hh} - S_{vv}|$).

Analyzing the results shown in Fig. 5.5, it may be seen that although similar colors are obtained from both BPT approaches[1], the contours of the agricultural fields detected by the TE BPT, shown in Fig. 5.5c, seem to be more precise than the ones of the ST BPT, represented in Fig. 5.5b, where a larger number of contours may be observed within the fields. Indeed, the extended region model $\mathbf{Z}_e$ enhances the target characterization by taking into account the complete polarimetric temporal evolution, as mentioned before. Due to this improved characterization an increase in the region differentiation is obtained by a combination of two different factors. On the one hand, the extended model has N different realizations of the region contours, assuming that they appear over all the acquisitions, reducing the effect of the speckle noise over them and making easier their identification over the extended model with respect to the simpler classical one. On the other hand, there is a differentiation enhancement between adjacent regions if they are following a distinct temporal evolution, as this evolution is modeled by the extended sample covariance matrix $\mathbf{Z}_e$ and, consequently, the dissimilarity between re-

---

[1] The PolSARPro [3] software has been employed for Pauli image generation. Since this software applies an equalization for each RGB channel, small color differences are observed in the original and filtered Pauli images. These differences are caused buy this equalization process as the BPT based processing does not introduce any bias or distortion, as it has been shown in the previous Sections 4.3.3 and 4.3.4.

gions gets increased if they are following a different temporal evolution. However, in order to achieve this differentiation enhancement, the assumption that the region contours are spatially aligned among all the acquisitions, as the agricultural field contours, is essential.

In order to illustrate this differentiation enhancement that is obtained when taking into account the full temporal evolution of the target, Fig. 5.6 shows the results over another crop of the image containing some agricultural fields of the first acquisition. Fig. 5.6a shows the crop area over the original data, whereas Figs. 5.6b and 5.6c shows the same area processed with the TE BPT employing 1 and 8 acquisitions, respectively. In this case, the first acquisitions has been selected specifically due to the predominant surface scattering that may be observed over all the agricultural fields, as observed in Fig. 5.6a. When processing only one acquisition, most of the fields have a very similar polarimetric response and they are mixed together, as shown in Fig. 5.6b. However, if the whole polarimetric temporal evolution of the 8 acquisitions is employed for target characterization, they may be properly separated resulting in a better contour detection, as depicted in Fig. 5.6c.

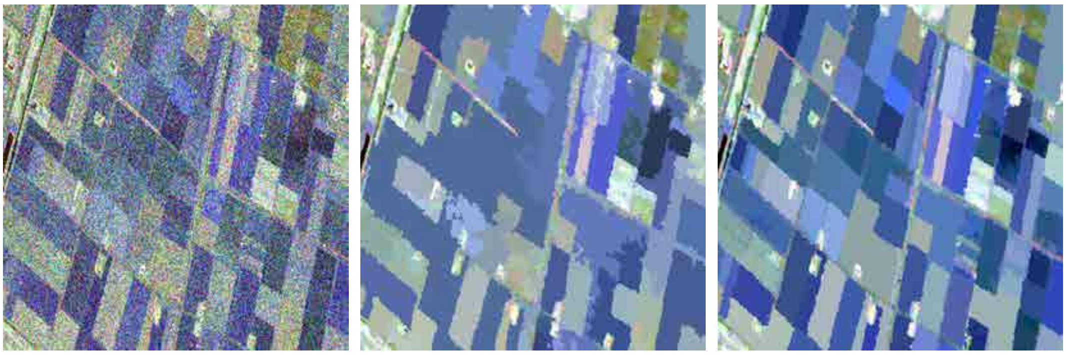
(a) Original **(b)** TE BPT, $N = 1$ **(c)** TE BPT, $N = 8$

Figure 5.6: Pauli representation of an agricultural area of the first acquisition. Original (a) and filtered with the TE BPT employing one image (b) and employing the full dataset (c) with $\delta_p = -3dB$ ($|S_{hh} + S_{vv}|$, $|S_{hv} + S_{vh}|$, $|S_{hh} - S_{vv}|$).

On the other hand, the main advantage of the ST BPT is that it may employ samples of different acquisitions in order to achieve a larger amount of filtering. This effect may not be clearly apparent when examining the results shown in Figs. 5.4 and 5.5, where the results from the ST BPT has been compared with those from the TE BPT. Indeed, these results are not directly comparable since they represent different information of the scene, as it has been mentioned in Sections 5.1.1 and 5.1.2. Whereas the TE BPT represents spatial regions of the scene following a similar polarimetric temporal evolution, the ST BPT represents regions of the dataset in the space-time domain and, consequently, they have contours in both, the spatial and the temporal domains. Consequently, it may not be expected that the ST BPT contours represent just the spatial features of the scene, as they also represent changes in the temporal dimension and, moreover, they may be different over each acquisition. For instance, on the results shown on Fig. 5.5b it may be seen that some contours appear within the agricultural fields apart from the field borders. In this case, they may be produced by small portions of the field that are connected with bigger regions on the acquisitions just before or after, representing zones of the field that start to change before or after than the rest of the field. It is worth noticing, then, that the interpretation of these region contours is more complex, as it may be done in the space-time domain.

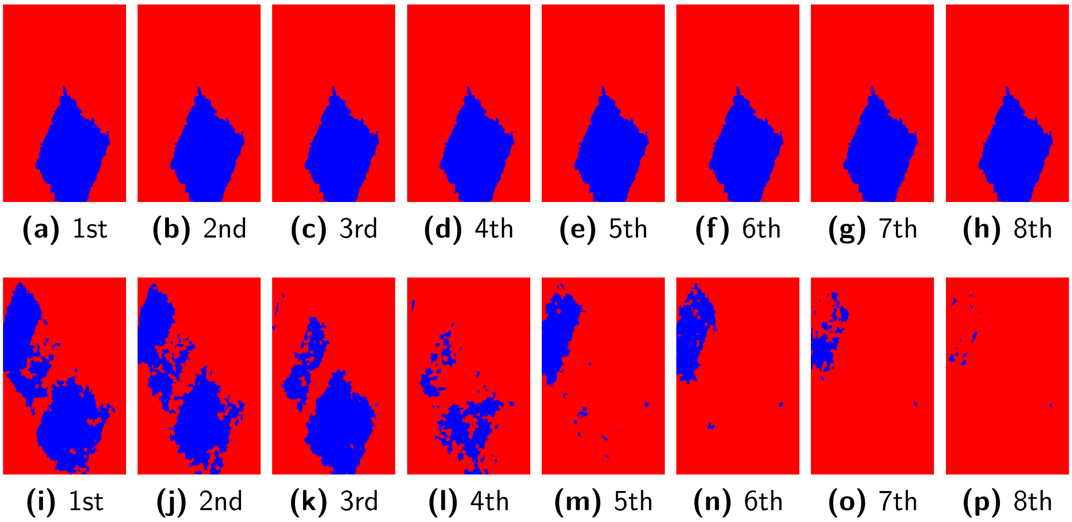
(a) 1st (b) 2nd (c) 3rd (d) 4th (e) 5th (f) 6th (g) 7th (h) 8th

(i) 1st (j) 2nd (k) 3rd (l) 4th (m) 5th (n) 6th (o) 7th (p) 8th

Figure 5.7: Region shape for the region marked in Fig. 5.5c, employing the TE BPT (first row), and for the region marked in Fig. 5.5b, employing the ST BPT (second row), for all the eight different acquisitions.

In order to see more clearly the differences between both representations and the type of information they represent, Fig. 5.7 shows the region shape of the field marked with a red cross on Figs. 5.5b and 5.5c over all the acquisitions for the ST BPT, on the first row, and for the TE BPT, on the second row. As it may be observed, the same region contours are achieved for the TE BPT among all the acquisitions, represented in Figs. 5.7a to 5.7h, as it is a spatial representation of the data. However, this is not the case for the ST BPT, as shown in Figs. 5.7i to 5.7p, where different shapes are obtained at each acquisition. Moreover, the regions of the ST BPT may have an arbitrary structure in the space-time domain, representing areas with similar polarimetric response on this domain. Then, as mentioned before, the ST BPT may combine samples of different acquisitions to achieve a better characterization of the target polarimetric response.

δ_p	Regions $\cap$ 1st acquisition	Average temporal depth
-5 dB	359371	2.067
-4 dB	223969	2.652
-3 dB	127957	4.068
-2 dB	52077	6.727
-1 dB	14660	7.758
0 dB	4666	7.921

Table 5.1: Number of regions and average region depth in the temporal dimension over pruned regions intersecting the first acquisition for different pruning factors in the results obtained employing the ST BPT.

To analyze this ability to increase the amount of available samples, Table 5.1 shows, for different pruning threshold δ_p values, the number of pruned regions over the first acquisition, that is, the pruned regions that intersect with this acquisition. Additionally, it shows the average temporal depth of all these regions, computed as the total number of samples contained within these regions with respect to the samples of one acquisition. When employing $\delta_p = -3dB$, as for the previously shown results, the ST BPT may employ approximately 4 times more samples than when filtering over one acquisition. As a result, this BPT representation may substantially improve the polarimetric response estimation by combining more homogeneous samples of different acquisitions.

From the previous results, it may be deduced that the ST BPT may improve the number of samples averaged by combining samples of different acquisitions. However, its results are more difficult to interpret as they are defined in the space-time domain and, thus, the obtained regions may not be directly related with an area of the scene, as their contours change among different acquisitions. On the other hand, the regions of the TE BPT represent spatial areas of the scene and, due to the improved target characterization attained when taking into account the complete temporal evolution, it may improve the contour detection over areas having spatially fixed contours. Additionally, the extended model $\mathbf{Z}_e$ is that it may be employed to exploit the interferometric information, contained within the $\mathbf{\Omega}_{ij}$ matrices, allowing a PolInSAR interpretation of the obtained regions.

It may be deduced, from the aforementioned conclusions, that the ST BPT may be a good representation for areas where almost no information can be extracted from the interferometric information, which may be produced by a strong temporal decorrelation, or where the contours are not spatially fixed as, for instance, over the sea or ocean areas. On the other hand, due the increase of region differentiation over fixed contours, the TE BPT may be the proper option for processing the land areas, where most of the contours are spatially fixed over time. Moreover, since the regions obtained by this representation uniquely correspond to spatial areas of the scene, it is easier to analyze and interpret.

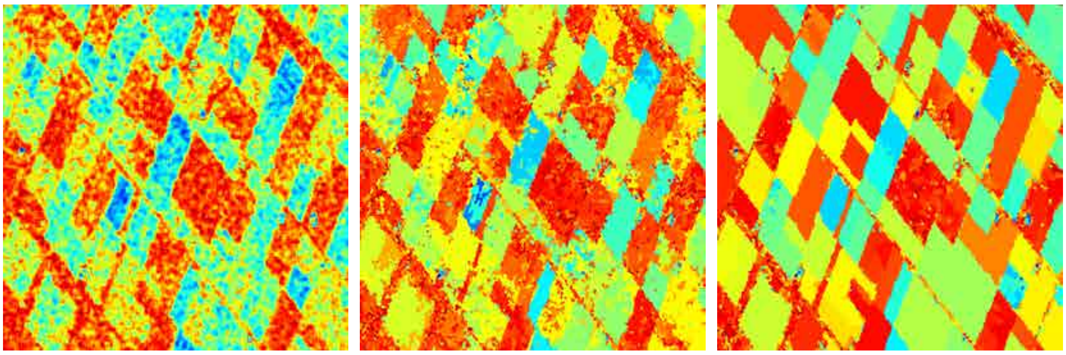

(a) H, 7x7 ML **(b)** H, ST BPT **(c)** H. TE BPT

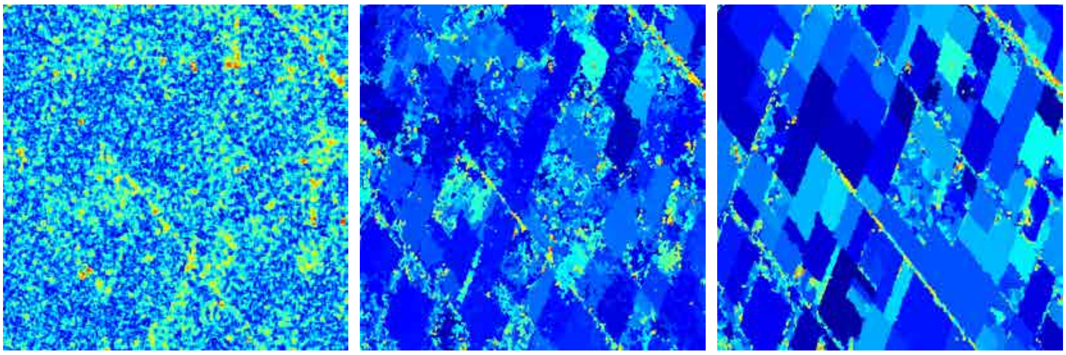

(d) A, 7x7 ML **(e)** A, ST BPT **(f)** A, TE BPT

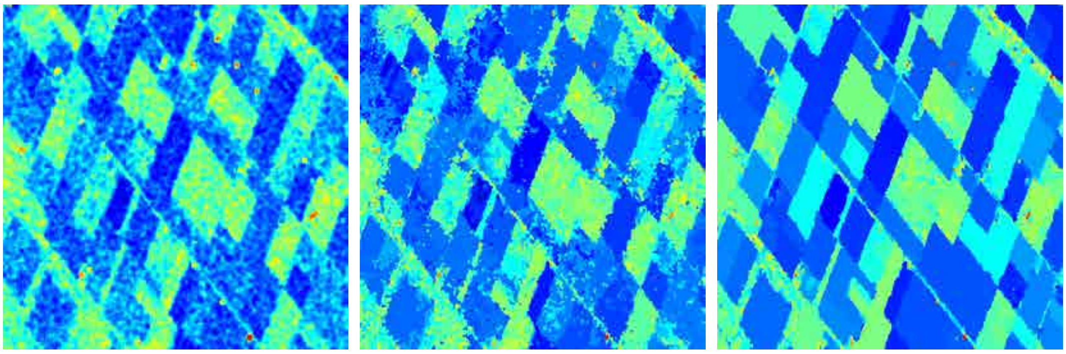

(g) $\bar{\alpha}$, 7x7 ML **(h)** $\bar{\alpha}$, ST BPT **(i)** $\bar{\alpha}$, TE BPT

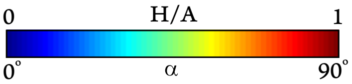

Figure 5.8: $H/A/\bar{\alpha}$ parameters of an agricultural area of the second acquisition processed with the ST BPT and with the TE BPT for $\delta_p = -3dB$.

As performed in Section 4.3.3, in order to analyze the capabilities of the proposed BPT approaches to correctly estimate and preserve the polarimetric information and its evolution in the scene, the $H/A/\bar{\alpha}$ eigendecomposition parameters [35] will be employed, described in Section 2.2.6. Fig. 5.8 shows the $H/A/\bar{\alpha}$ parameters for the agricultural area of the second acquisition presented in Fig. 5.5, for a pruning threshold $\delta_p = -3dB$. It compares the values obtained by the ST BPT and the TE BPT approaches with the 7x7 multilook (ML) filtering as a reference. A qualitative comparison of the results reveals that similar values are obtained by all the methods. However, as observed when processing a single PolSAR image, the BPT based approaches may obtain a better noise reduction due to employing a larger number of samples for polarimetric response estimation, while also preserving the contours. This effect is more noticeable in the TE BPT results, due to the increased region differentiation over temporally fixed contours, as mentioned previously.

Fig. 5.9 illustrates the temporal evolution of the Entropy H information for the TE BPT representation. The Pauli representation of the obtained results is shown in Figs. 5.9a to 5.9c for the 1st, 4th and 8th acquisitions, respectively. Figs. 5.9d to 5.9f show the Entropy parameter for the same acquisitions. It is worth mentioning that on the first acquisition, most of the agricultural fields are not grown, on the 4th acquisition they are almost fully grown and, finally, on the 8th acquisition most of them have already been harvested. This evolution may also be observed in the corresponding Pauli images, as mentioned before. Since the polarimetric response of these areas change substantially, the Entropy parameter varies accordingly over the different acquisitions, as can be seen on Figs. 5.9d to 5.9f, ranging from low Entropy when there is surface scattering to high Entropy when the volume scattering dominates.

To perform a more detailed analysis of the preservation of the polarimetric temporal evolution, Fig. 5.10 shows the evolution of the $H/A/\bar{\alpha}$ parameters for the field marked with a red cross on Fig. 5.9a among all the acquisitions. The evolution is shown for the ST BPT and the TE BPT, employing in both cases $\delta_p = -3dB$, and for the 7x7 multilook filtering, as a reference. For the multilook filter, the pixel located at the cross has been taken. In fact, the cross shown on Fig. 5.9a is far enough from the field edges in order to ensure that the multilook filter is not affected by the blurring of the region contours. Very similar trends are obtained for both the BPT approaches and also for the multilook filtering, meaning that the proposed time series BPT based processing techniques preserve also the polarimetric temporal evolution of the data. Additionally, the proposed methods may employ a much larger number of homogeneous samples with respect to the multilook filtering, resulting in a better estimation of the polarimetric response and evolution, while also having a better spatial resolution preservation, maintaining the region contours and small details of the scene. As stated in [90][91], the estimation of the

(a) 1st acquisition **(b)** 4th acquisition **(c)** 8th acquisition

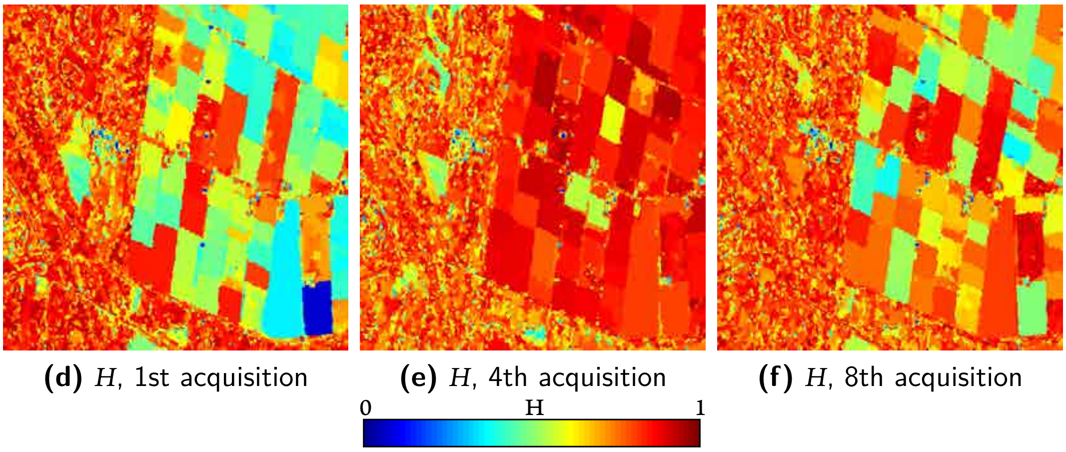

(d) H, 1st acquisition **(e)** H, 4th acquisition **(f)** H, 8th acquisition

Figure 5.9: Pauli and Entropy H images for different acquisitions processed with the TE BPT. The full dataset has been processed with a pruning threshold $\delta_p = -3dB$ ($|S_{hh} + S_{vv}|$, $|S_{hv} + S_{vh}|$, $|S_{hh} - S_{vv}|$).

$H/A/\bar{\alpha}$ parameters is biased when estimating the sample covariance matrices as an average of a finite number of samples. Due to this bias, the Entropy parameter is underestimated whereas the Anisotropy parameter is overestimated. As it may be seen, the Entropy values obtained by the multilook filtering are below those obtained by the BPT while in the Anisotropy the opposite is observed. Since the bias gets reduced when the amount of averaged samples gets increased, results on Fig. 5.10 are consistent with the fact that the BPT is employing a much larger number of samples and, thus, reducing the bias with respect to the multilook. More details about this bias and a mathematical characterization of the speckle noise effects over the estimation of the sample covariance matrix eigendecomposition and the $H/A/\bar{\alpha}$ parameters may be found in Appendix A.

Finally, in order to show the results over the complete dataset and the temporal evolution of the scene, the Pauli, Entropy (H), Anisotropy (A) and the averaged Alpha angle ($\bar{\alpha}$) is represented in Figs. 5.11 and 5.12, respectively, for all the acquisitions of the dataset.

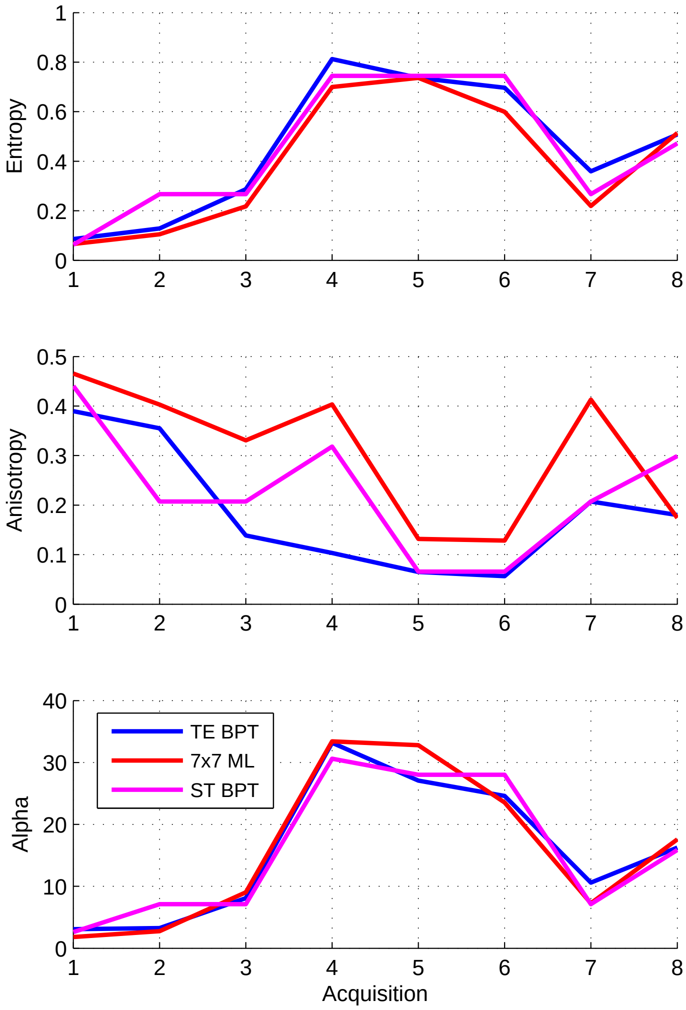

Figure 5.10: Evolution of the $H/A/\bar{\alpha}$ parameters for the agricultural field marked on Fig. 5.9a. The full dataset has been processed with the TE BPT, with a 7x7 multilook filter and with the ST BPT. For the BPT pruning $\delta_p = -3dB$ has been employed in both cases.

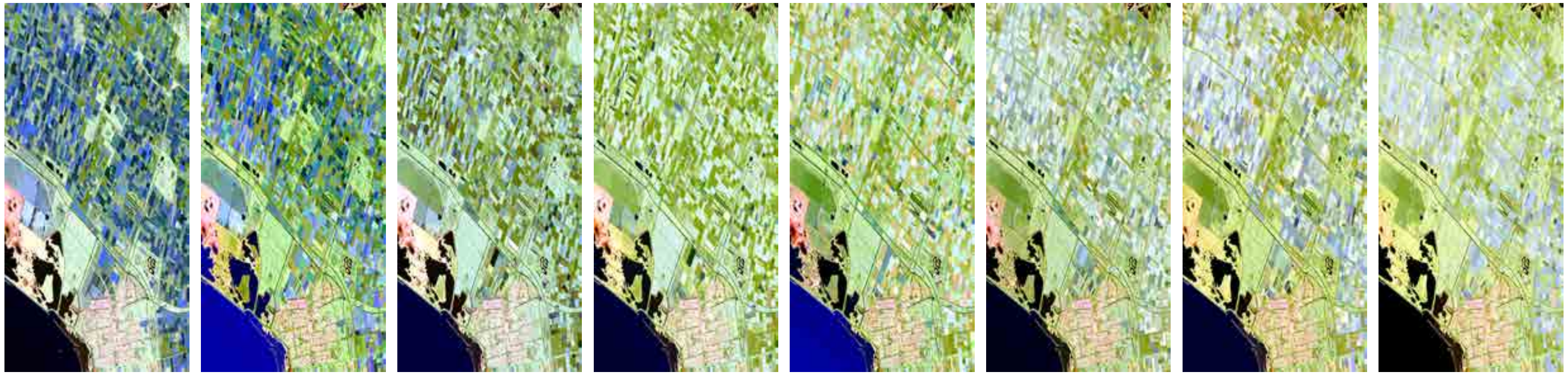

(a) Pauli 1st (b) Pauli 2nd (c) Pauli 3rd (d) Pauli 4th (e) Pauli 5th (f) Pauli 6th (g) Pauli 7th (h) Pauli 8th

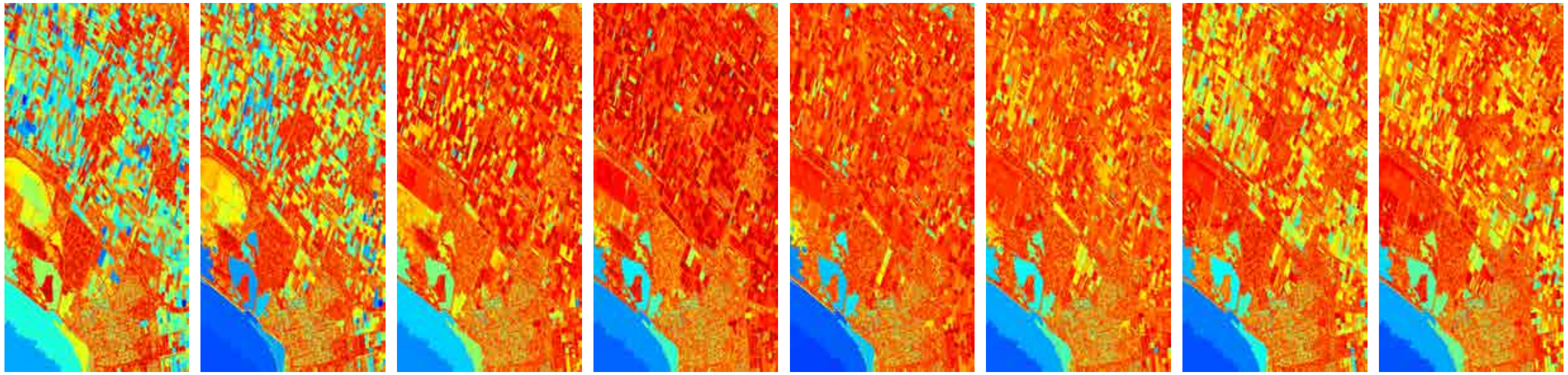

(i) H, 1st (j) H, 2nd (k) H, 3rd (l) H, 4th (m) H, 5th (n) H, 6th (o) H, 7th (p) H, 8th

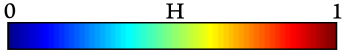

Figure 5.11: Pauli and Entropy H time series images over all the acquisitions of the results obtained with the TE BPT. The full dataset has been processed with a pruning threshold $\delta_p = -3dB$ ($|S_{hh} + S_{vv}|$, $|S_{hv} + S_{vh}|$, $|S_{hh} - S_{vv}|$).

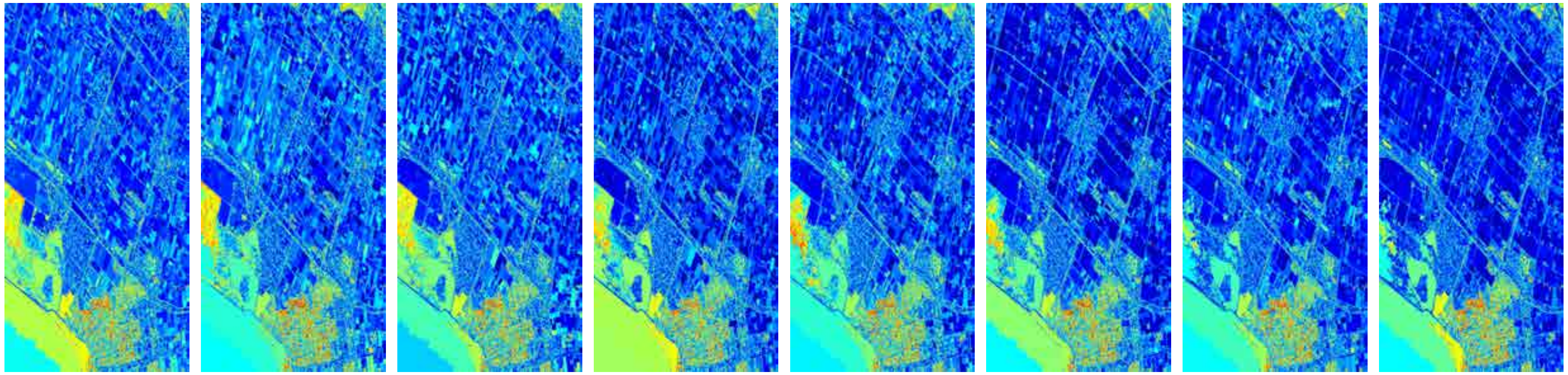

(a) A 1st **(b)** A 2nd **(c)** A 3rd **(d)** A 4th **(e)** A 5th **(f)** A 6th **(g)** A 7th **(h)** A 8th

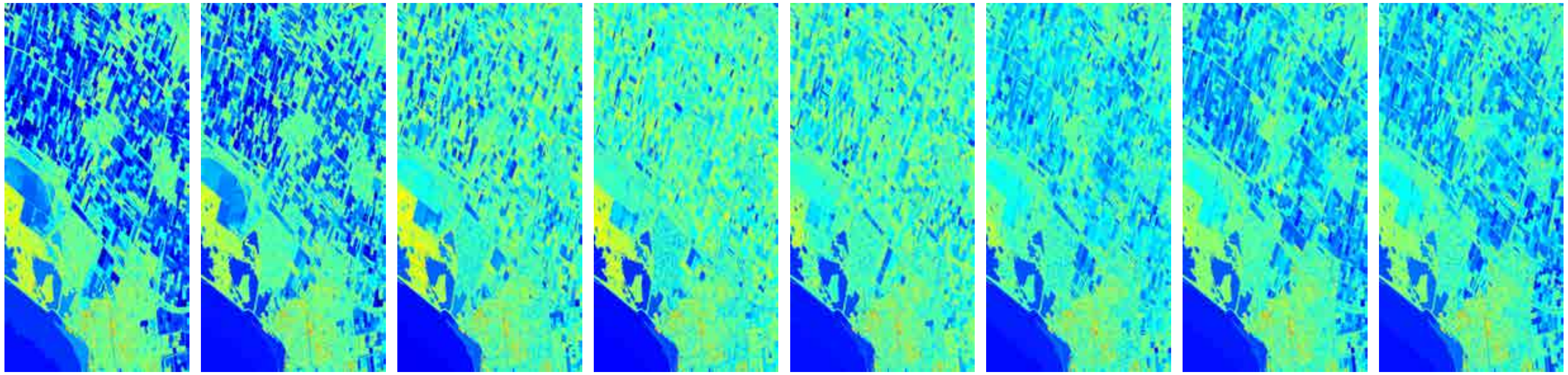

(i) $\bar{\alpha}$, 1st **(j)** $\bar{\alpha}$, 2nd **(k)** $\bar{\alpha}$, 3rd **(l)** $\bar{\alpha}$, 4th **(m)** $\bar{\alpha}$, 5th **(n)** $\bar{\alpha}$, 6th **(o)** $\bar{\alpha}$, 7th **(p)** $\bar{\alpha}$, 8th

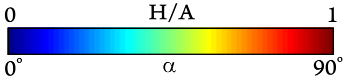

Figure 5.12: Anisotropy A and averaged Alpha angle $\bar{\alpha}$ time series images over all the acquisitions of the results obtained with the TE BPT. The full dataset has been processed with a pruning threshold $\delta_p = -3dB$.

5.4 TEMPORAL INFORMATION ANALYSIS

As shown in the previous section, the TE BPT and the ST BPT data structures have proven to be useful representations to process PolSAR time series. However, one of the main motivations for processing this type of datasets is to explore and analyze the evolution of the scene during the acquisition campaign. Consequently, this section is devoted to the analysis of the scene variability on the temporal dimension. For this purpose, two different applications are proposed, the temporal change detection and the temporal stability analysis, based on the ST BPT and the TE BPT, respectively. These applications are described and studied in the following.

5.4.1 TEMPORAL CHANGE DETECTION

In Section 5.1.1, the target characterization based on the classical sample covariance matrix **Z** model has been proposed for time series. In this case, it is assumed that a target is defined by its **Z** matrix and, consequently, a change in the obtained matrix among adjacent acquisitions may be interpreted as a target change. The ST BPT representation has been described in Section 5.2.1, based on this assumption, resulting into arbitrary regions in the space-time domain, which are composed of pixels of different acquisitions having similar polarimetric response. Then, having this type of representation, the change detection application naturally arises when examining the region contours in the temporal dimension, as proposed in [10]. Note that this application is focused on the temporal region contours, rather than on their spatial contours. Therefore, a map may be generated from the ST BPT results indicating, for each spatial pixel of the scene, the number of contours in the temporal dimension. Since on this representation a change in the polarimetric response may be interpreted as a target change, each time a temporal contour is observed among adjacent acquisitions it may be considered as a change. Then, the values of this map range from 0 changes, when the spatial pixel belongs to the same region and there is no change in the polarimetric response on all the acquisitions, to $N-1$, when there is a region change on every acquisition.

Fig. 5.13 represents the mentioned map, showing the number of contours in the temporal dimension per spatial pixel of the scene. The Flevoland dataset has 8 acquisitions and, consequently, the obtained values range ranging from no changes, represented in blue, to 7 changes, represented in red color. Results are shown for distinct pruning factor δ_p parameter values, corresponding to different prunes over the ST BPT constructed employing the geodesic dissimilarity measure d_{sg}. As seen before, when increasing the pruning factor δ_p, larger regions are also obtained in the temporal domain, resulting into a smaller number of temporal changes on

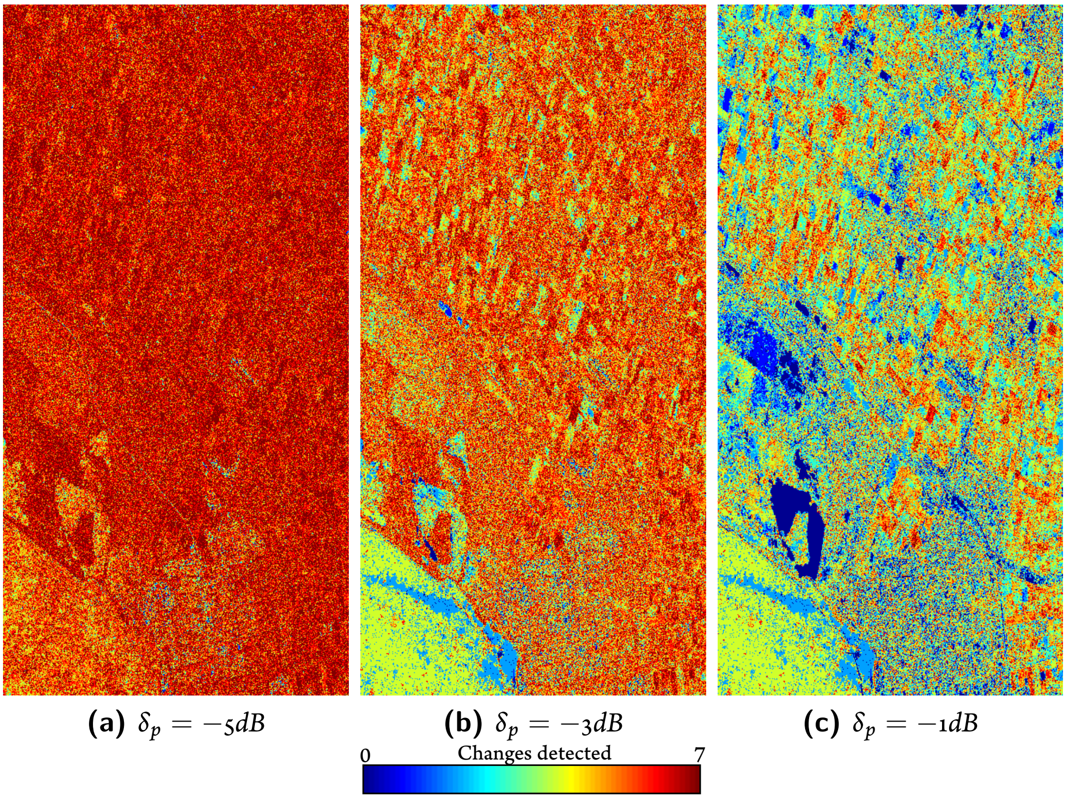
(a) $\delta_p = -5dB$ (b) $\delta_p = -3dB$ (c) $\delta_p = -1dB$

Figure 5.13: Number of temporal changes detected per spatial pixel for different pruning factors δ_p. No changes is represented in blue and 7 changes in red.

Fig. 5.13. Analyzing the results closely, it can be seen that there are small blue dots over urban area even for small values of the pruning factor, at $\delta_p = -5dB$. These small dots correspond to point scatterers of the buildings or human-made structures that present no-change during the different acquisitions. An enlarged image of an urban area and the corresponding changes detected map for $\delta_p = -5dB$ is shown on Fig. 5.14.

As it may be observed, the agricultural fields area, at the top-left part of the image, appears more reddish, indicating that a large number of temporal changes is detected. This is due to the small value of relative MSE that is admitted per region, as we are using $\delta_p = -5dB$, resulting into that most of the variability of the agricultural fields among acquisitions is considered as a target change. The urban areas, on the contrary, appears more yellowish, indicating a smaller number of changes, and, within these areas, there are small structures in blue, indicating no change in the whole sequence of acquisitions. These targets may be considered as point scatterers, as their polarimetric response presents a constant behavior among all the acquisitions.

When the pruning factor gets increased to $\delta_p = -3dB$, as shown on Fig. 5.13b, some other

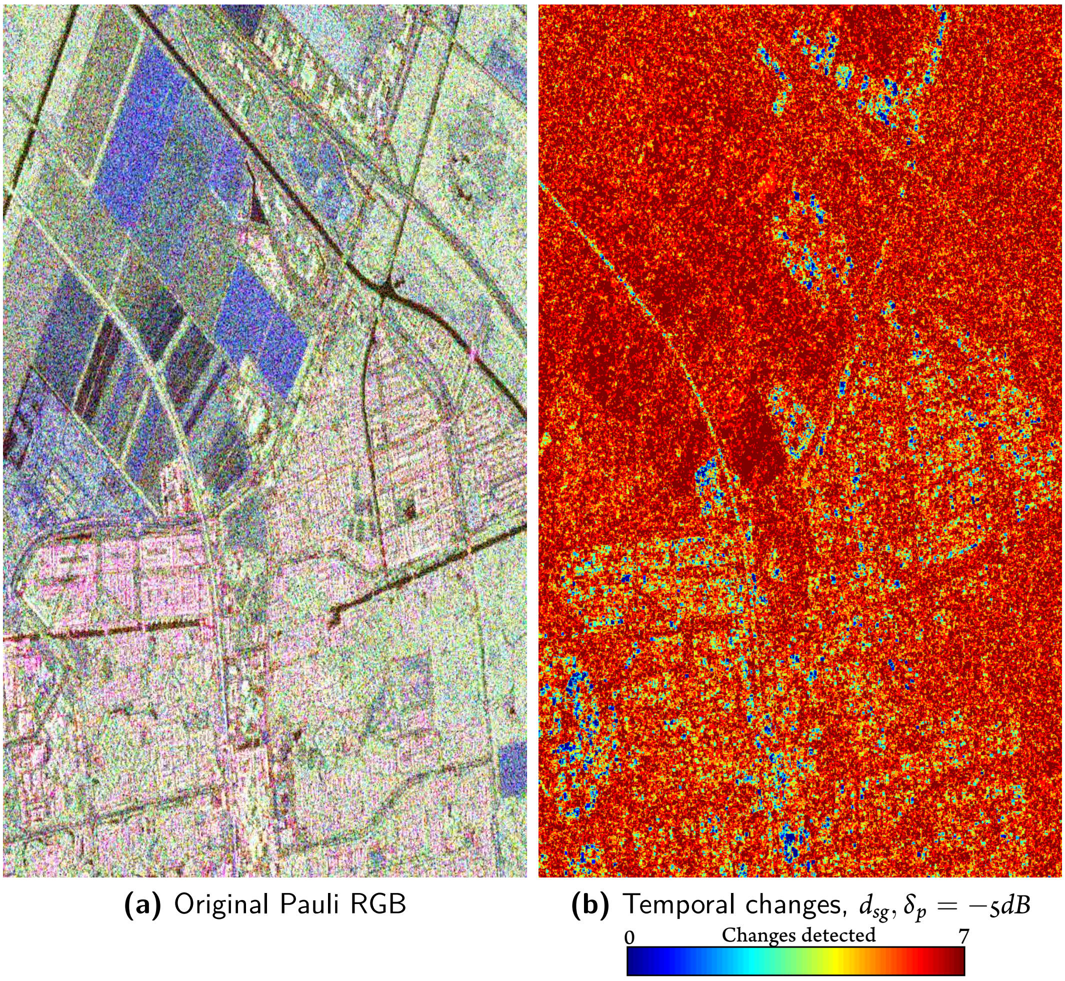

(a) Original Pauli RGB

(b) Temporal changes, d_{sg}, $\delta_p = -5dB$

Figure 5.14: Pauli RGB enlarged image of an urban area and the changes detected with a pruning threshold $\delta_p = -5dB$ $(|S_{hh} + S_{vv}|, |S_{hv} + S_{vh}|, |S_{hh} - S_{vv}|)$.

zones appear also in blue, like closed water areas, which roughness is less affected by wind than the sea, having a more stable polarimetric behavior. With this pruning factor, the agricultural fields also appear reddish and yellowish, presenting a large number of temporal changes. However, if the pruning factor is increased to $\delta_p = -1dB$, as depicted in Fig. 5.13c, then big differences in terms of temporal changes can be seen over the distinct fields of the agricultural areas.

It is worth noticing that the ST BPT construction process defined in Section 5.2.1 and the BPT pruning defined in Section 5.3 are sensitive to the fully polarimetric information under the Gaussian hypothesis and, consequently, these scene change maps are also sensitive to all this information.

However, although these maps may give an idea of the number of changes in the scene, they do not indicate the importance of these changes. For instance, although a small number of changes may be observed over urban areas, maybe some of them are more relevant in terms of the polarimetric response variation than the ones produced over the sea. Moreover, the results shown on Fig. 5.13 seems to be considerably noisy. This is produced by the fact that the obtained regions may have arbitrary shapes over time, as depicted on Fig. 5.7, which may result in different number of temporal contours for spatial pixels corresponding to the same agricultural field. Note that, in technical terms, the number of changes maps are pixel-based processing results, as the result is generated pixel by pixel. This reflects the difficulties in relating the regions in the space-time domain with the areas of the scene. Ideally, having results giving an idea of the amount of change for each field or structure of the scene could be more useful. When the aim is to have such results, a temporal analysis should be performed over the TE BPT, as it provides spatially fixed region contours, as shown on Fig. 5.7, which may be directly related to the same physical area of the scene among all the acquisitions.

5.4.2 Temporal Stability Analysis

As mentioned in Section 5.1.2, on the TE BPT it is assumed that the target is characterized by a particular polarimetric temporal evolution. In this case, then, the temporal information is included within the region model. As opossed to the ST BPT, the TE BPT performs a spatial segmentation of the data and, consequently, it does not have temporal contours. Therefore, in order to analyze the temporal information, the extended region model $\mathbf{Z}_e$ has to be examined. It contains the target response temporal evolution for the region, having the polarimetric response for each acquisition within the different $\mathbf{Z}_{ii}$ matrices. Then, a new temporal stability measure may be defined based on analyzing the amount of change between all the different $\mathbf{Z}_{ii}$ matrices of each region. Moreover, to be consistent with the BPT construction and processing, a similarity measure may also be employed to evaluate the similarity t_s between the different polarimetric matrices over all the acquisitions of the region A

$$t_s(A) = \frac{2}{N(N-1)} \sum_{i=1}^{N} \sum_{j=i+1}^{N} \left\| log\left(\mathbf{Z}_{ii}^{-1/2} \mathbf{Z}_{jj} \mathbf{Z}_{ii}^{-1/2}\right) \right\|_F . \tag{5.5}$$

where $\mathbf{Z}_{ii}$ correspond to the sample covariance matrix of the i-th acquisition of the extended model $\mathbf{Z}_e$ for the region A, described in (5.2).

The proposed t_s measure, as defined in (5.5), corresponds to the average geodesic similarity measure between the sample covariance matrices for all the acquisitions. A large value of the t_s measure indicates that strong changes are observed for the given region of the scene, whereas a small value indicates that the polarimetric response of the regions remains stable among the acquisition campaign. By contrast to the number of temporal contours, the t_s measure is not mathematically bounded, ranging from zero to infinity. However, in practice, since the radar measured values are bounded, the t_s measure values range approximately in the interval $[0, 6]$, but almost all the values are concentrated within the range $[0, 3]$.

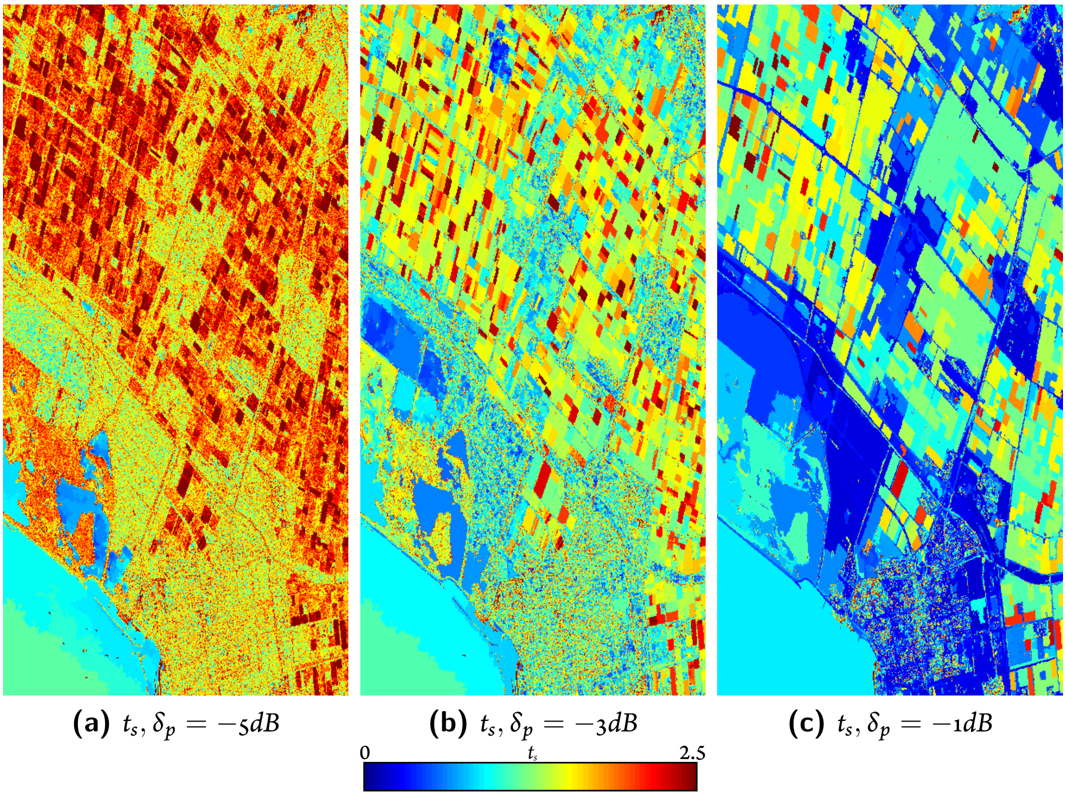

(a) $t_s, \delta_p = -5dB$ **(b)** $t_s, \delta_p = -3dB$ **(c)** $t_s, \delta_p = -1dB$

Figure 5.15: Temporal stability measure t_s over the Flevoland dataset for different pruning factors δ_p.

Fig. 5.15 shows the t_s measure over the Flevoland dataset. The TE BPT has been constructed with the extended geodesic d_g dissimilarity measure, defined in (5.3), and it has been pruned with different values of the δ_p parameter. As it may be seen, for lower values of δ_p the temporal stability measure obtains larger values, due to the smaller amount of speckle filtering, wich results resulting into larger variability of the obtained sample covariance matrices. However, as the pruning factor increases, larger regions are obtained, which results into a larger speckle filtering, reduces the variability of the estimated values and produces smaller t_s values over homogeneous areas. Analyzing the distribution of the t_s measure over the scene, it may be seen that larger variability in terms of the polarimetric temporal evolution is produced over the agricultural fields whereas closed waters, for instance, have a more stable polarimetric response.

These observations are, indeed, similar to the ones obtained by the number of changes in the temporal dimension, shown on Fig. 5.13. However, it is worth noticing that both results represent different information. The temporal contours give an idea of the number of changes in the polarimetric response over time, whereas t_s measures the amount of temporal polarimetric change for each region.

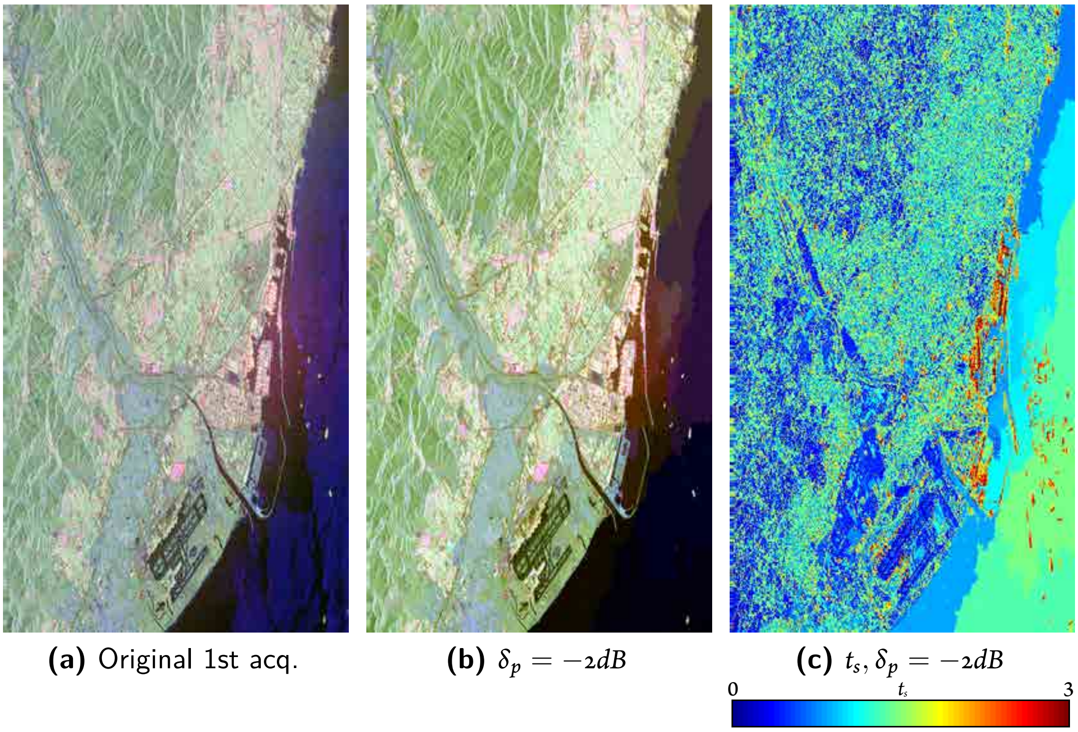
(a) Original 1st acq.

(b) $\delta_p = -2dB$

(c) $t_s, \delta_p = -2dB$

Figure 5.16: Pauli of the first acquisition of the Barcelona dataset (a), first acquisition processed with the TE BPT (b) and temporal stability measure t_s for $\delta_p = -2dB$ (c) ($|S_{hh} + S_{vv}|$, $|S_{hv} + S_{vh}|$, $|S_{hh} - S_{vv}|$).

In order to perform a more detailed analysis of the ability of the temporal stability measure to quantify relevant changes in the scene, a new dataset is employed, containing 35 RADARSAT-2 Fine Quad-Pol images of the city of Barcelona, in Spain. The images were acquired with the FQ9 beam, and the acquisition campaign goes from Januray 20th, 2010 to May 9th, 2012, with an acquisitions every 24 days. The Pauli representation of the first acquisition of the Barcelona dataset is represented in Fig. 5.16a. As it may be seen, the scene is mainly composed of the urban and industrial area of the Barcelona city, in the central part of the image, surrounded by the Mediterranean Sea on the right part and mountains on the left part. At the bottom part of the image, the Barcelona airport may be observed whereas on the center the Barcelona Harbor may be found. Fig. 5.16b shows the first acquisition of the results obtained after processing the full dataset employing the TE BPT representation and a pruning threshold $\delta_p = -2dB$. Fig. 5.16c presents the t_s measure defined in (5.5) over the pruned regions obtained. This dataset, then, has been chosen to detect changes in urban areas due to the availability of ground truth and knowledge of the scene.

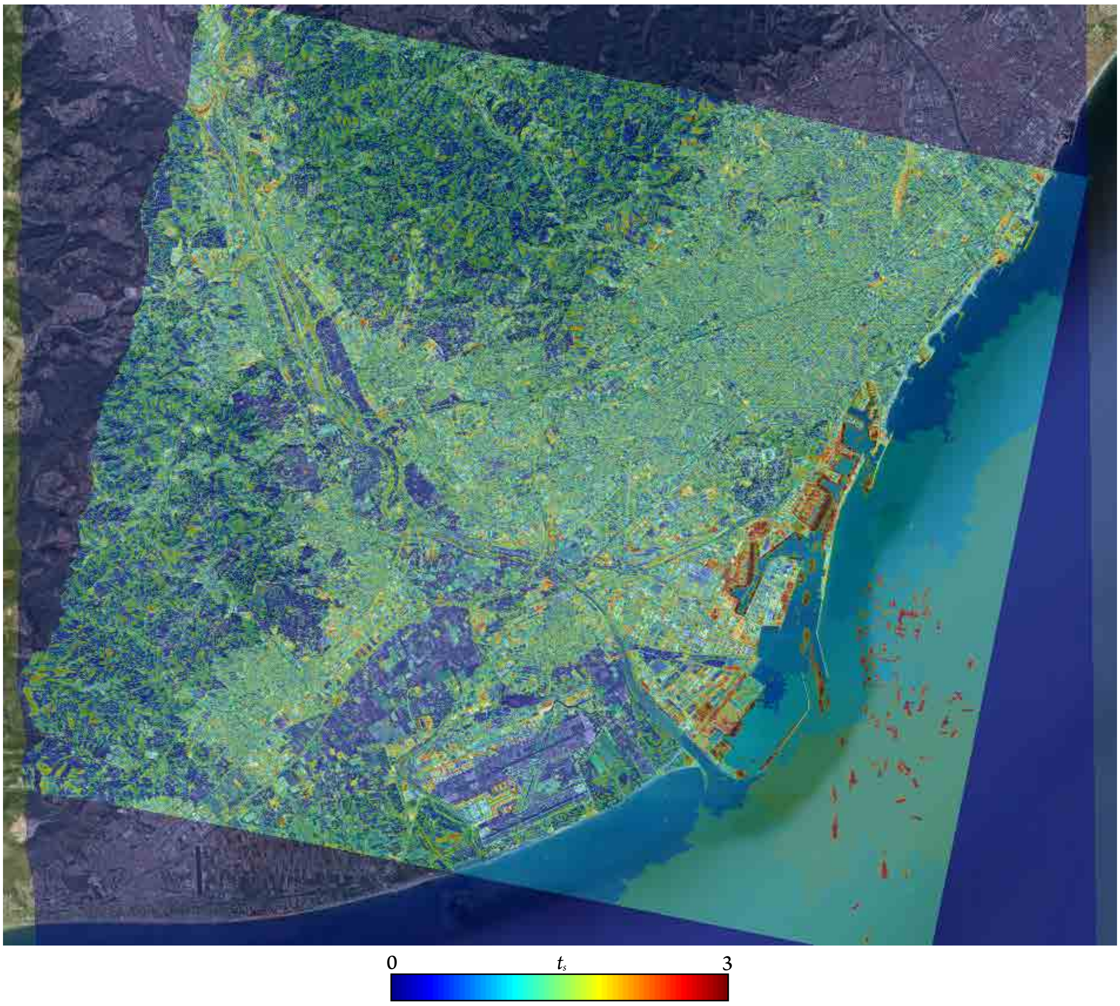

Figure 5.17: Geo-coded t_s measure for the Barcelona dataset as an overlay with an optical image [1].

Moreover, the temporal stability results shown in Fig. 5.16c have been geo-coded, in order to easily identify the obtained regions of the processed dataset over the ground. On Fig. 5.17 this information have been represented as an overlay with an optical image from [1], with a certain degree of transparency.

As it can be seen on Fig. 5.17, several red spots appear over the sea, in the lower right part of the image, corresponding to the different vessels that were present at some of the acquisitions.

Note that these vessels, since they are present only in one acquisition, represent a significant change in terms of the polarimetric response with respect to the underlying sea and, consequently, the t_s measure indicates a strong change with a large value, appearing in red. Over the land area some big red spots may also be seen, specially on the central part of the image, corresponding to the Barcelona harbor. In the rest of the image, some additional small red spots may also be seen, with correspond to changes in the urban area. In the following, these results are analyzed in detail.

(a) t_s over the Barcelona harbor area

(b) Container area **(c)** Ship loading bay and cranes

Figure 5.18: Geo-coded t_s measure over the Barcelona harbor (a) [1]. A container area (b) with a ship loading bay and cranes (c) may be seen [2].

Fig. 5.18a presents a zoom of the results shown on Fig. 5.17 corresponding to an area of the Barcelona harbor, where large red spots are obtained, as mentioned before. In the central part of the image, strong changes are detected corresponding to a ship container area. To see more clearly this zone, a photography taken from the ground is presented in Fig. 5.18b [2]. Note that on these areas the different containers are constantly stacked and unstacked from the ships, resulting in a completely different backscattering response from acquisition to acquisition. This task is performed by big cranes located near the loading bay, that may be seen on the photography in Fig. 5.18c [2], which are placed over rails along the loading bay and, consequently, their position change over different acquisitions, resulting into large changes detected by the radar. Moreover, on Fig. 5.18a red spots may also be seen all around the shore, corresponding to this cranes and also to the fact that different ships are docked at the loading bays on some acquisitions, as seen in Fig. 5.18c.

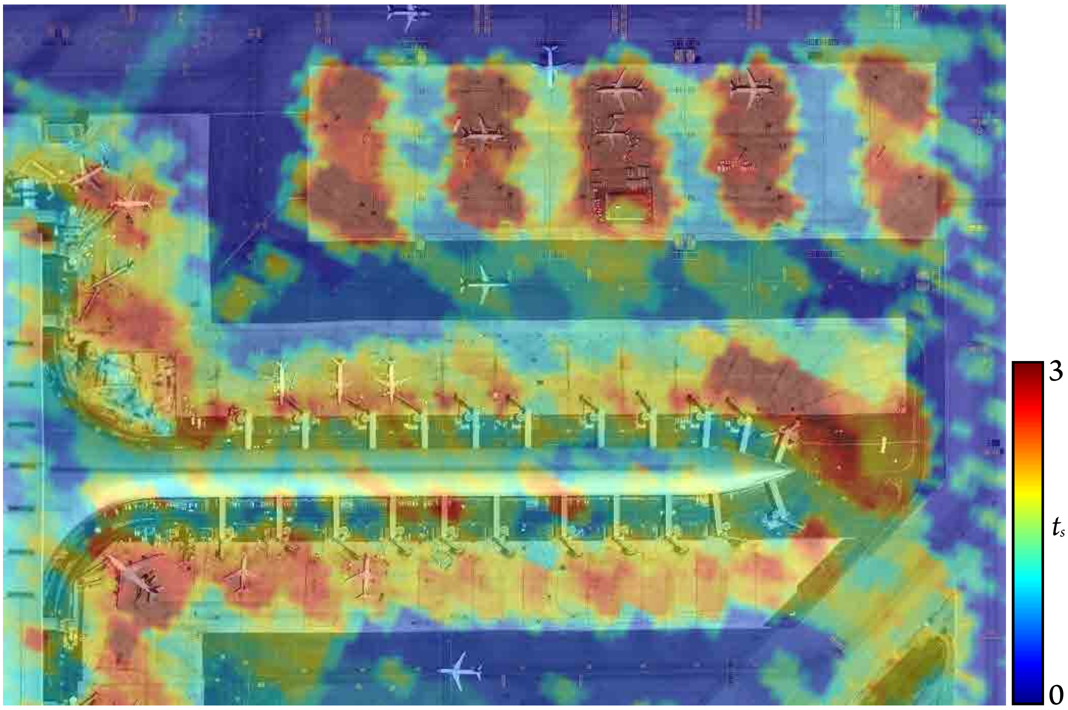

Figure 5.19: Geo-coded t_s measure over the Barcelona airport Terminal-1 area [1].

Another area of the scene where large changes may be detected correspond to the Barcelona airport. Fig. 5.19 presents a zoom of the geo-coded results shown in Fig. 5.17 corresponding to the Terminal 1 zone of the Barcelona airport. Some big rectangular red spots are observed on the top part of the image, where plane parking lots are located. On these zones the planes are placed temporally and, consequently, there is high probability of detecting different planes from acquisition to acquisition, resulting into large porlarimetric changes. Additionally, on the bottom part of the image a large building may be seen, corresponding to the Terminal 1 building. The fingers are connected to the building and it may be observed that small red dots are obtained over them. Indeed, the fingers are moved every time they are attached to a plane, resulting into these changes. In this case, the ability of the BPT structure to preserve small details of the data allows the identification of these changes. Some big spots may also be seen near the fingers, corresponding to some planes that were attached to them on some acquisitions of the dataset.

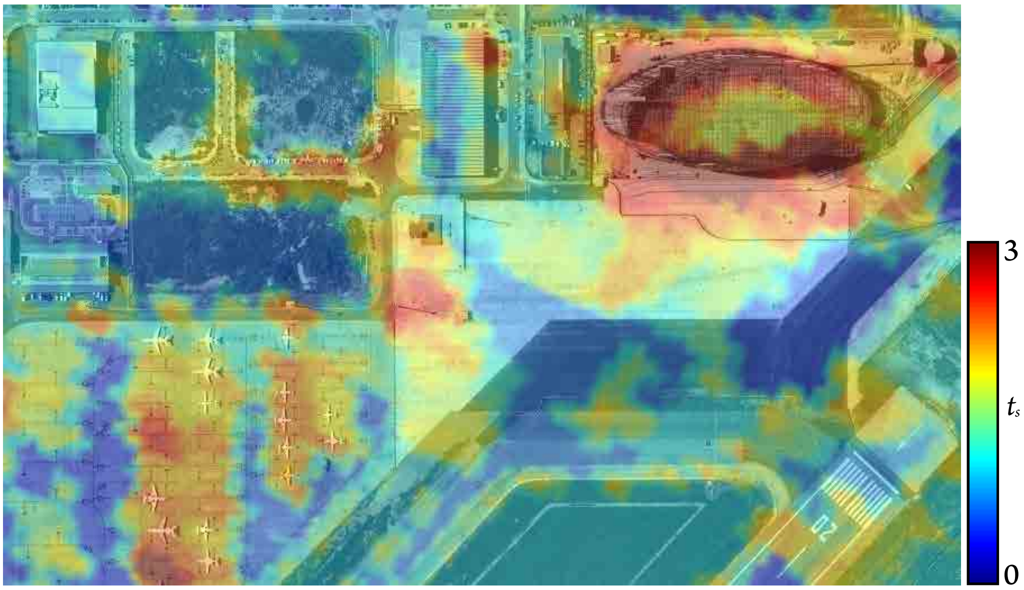

(a) t_s over the Barcelona airport hangar area

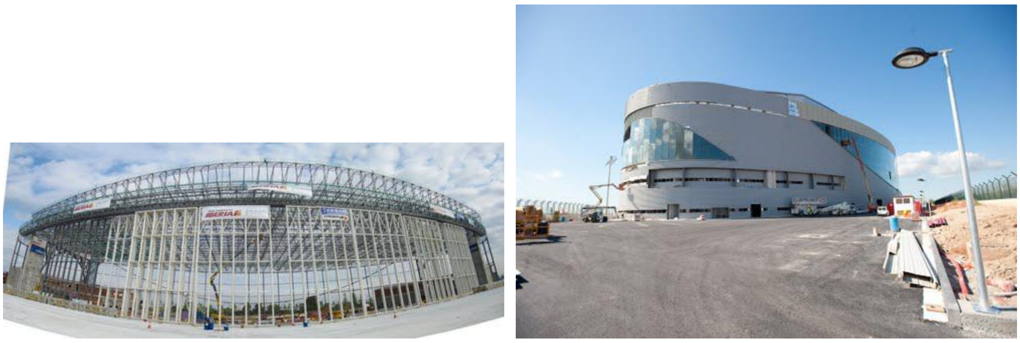

(b) Hangar in construction **(c)** Hangar finished

Figure 5.20: Geo-coded t_s measure over the Barcelona airport hangar area (a) [1]. Hangar under construction (b) and after the construction process has finished (c) photographies [2].

Fig. 5.20 presents the same results over a different area of the Barcelona airport where a big hangar is placed. The geo-coded results are shown in Fig. 5.20a. Another plane parking area may be seen in the bottom part of the image but the larger changes detected correspond to an hangar located at the top right part. In fact, this hangar has been constructed during the acquisition campaign, as it may be seen on the photographies taken from the ground Figs. 5.20b and 5.20c, presenting this hangar under construction and when the construction process has finished, respectively. Indeed, on the optical image employed on Fig. 5.20a as an overlay with the results the hangar was under construction. Note that these results show the ability of the TE BPT based temporal stability t_s analysis to detect and identify the scene changes related with the building activities.

Moreover, in the extended sample covariance model $\mathbf{Z}_e$, defined in (5.2), the complete set of PolSAR $\mathbf{Z}_{ii}$ and PolInSAR $\mathbf{\Omega}_{ij}$ matrices are available for target characterization. This additional information may be employed to describe the change in the scene. For instance, the Entropy H and averaged Alpha angle $\bar{\alpha}$ polarimetric parameters have been computed for the whole sequence of $\mathbf{Z}_{ii}$ matrices corresponding to the region of the hangar. The evolution of these two parameters for the different acquisitions of the campaign is shown in Fig. 5.20. As it may be observed, during the first 14 acquisitions the Entropy and Alpha parameters change substantially due to the building activities over the hangar. However, after the 14th acquisition, presumably when the hangar construction has finished, these parameters maintain a constant behavior. More specifically, the Entropy and the averaged Alpha angle present a low value, indicating surface scattering probably caused by the roof of the hangar.

The hangar that has been constructed in the Barcelona airport shows the ability of the TE BPT and the t_s measure to identify the changes on the scene corresponding to building activities. However, the hangar is a large building that might be also easily identified by other means. In order to analyze the ability of this technique to detect also more localized changes in the scene, Fig. 5.22 shows a zoom of the t_s results over the Montjuic area of Barcelona. A small red dot may be observed in the center of Fig. 5.22a. In these area a monument has been constructed during the acquisition campaign consisting in 4 columns, as it may be observed in the ground photographies Figs. 5.22b and 5.22c, corresponding to this area before and after the construction of the monument. Note that this monument is much smaller than the hangar presented in Figs. 5.20b and 5.20c, being, in fact, not much larger than the resolution of the sensor. However, due to the ability of the BPT structure to preserve small details of the data, as observed before, this change may be detected by the t_s measure.

In order to compare the proposed temporal stability t_s measure with a state-of-the-art polarimetric change detection technique, a modification of the log likelihood-ratio test statistic measure defined in [37] is proposed. However, the change measure $ln\ Q$ originally defined in

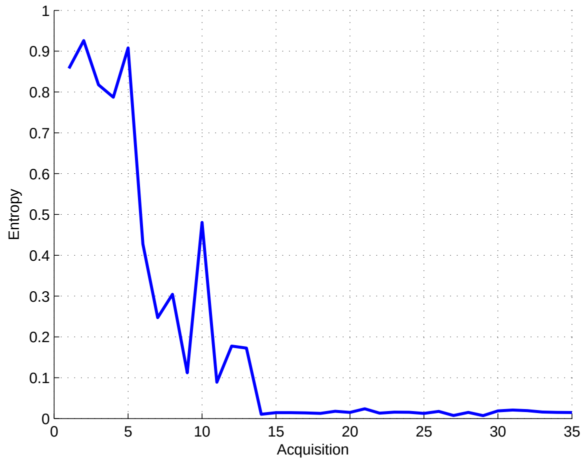

(a) H evolution for the hangar

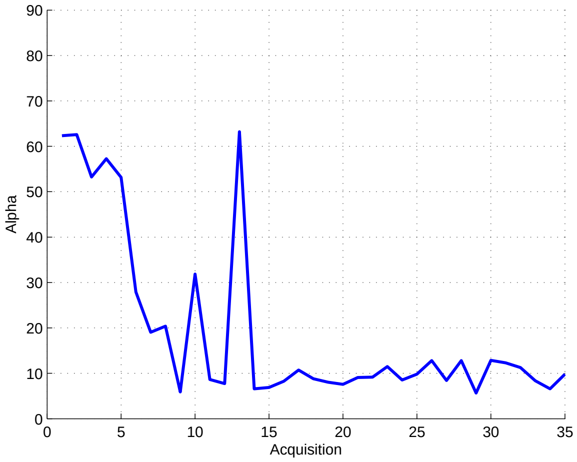

(b) $\bar{\alpha}$ evolution for the hangar

Figure 5.21: Entropy (a) and averaged Alpha angle (b) temporal evolution for the hangar among different acquisitions.

[37] was intended to determine the change between two different acquisitions. Then, it has to be generalized to process PolSAR time series, having N different acquisitions. According to [97], we have defined the extended log likelihood-ratio test statistic measure $ln\ Q_e$

$$-ln\ Q_e = -n_l \left(\sum_{i=1}^{N} ln|\mathbf{Z}_{ii}| - Nln|\mathbf{Z}_s| + pNlnN \right) \tag{5.6}$$

where n_l represents the number of looks, $|\mathbf{Z}_{ii}|$ represents the determinant of the p by p matrix $\mathbf{Z}_{ii}$ and $\mathbf{Z}_s = \sum_{i=1}^{N} \mathbf{Z}_{ii}$.

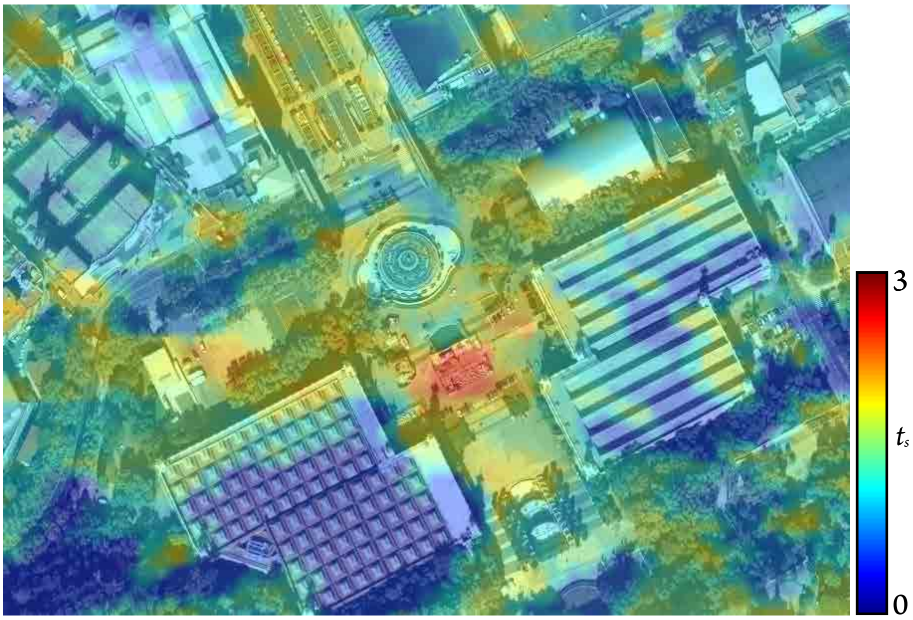

(a) t_s over the Montjuic area in Barcelona

(b) Before **(c)** After

Figure 5.22: Geo-coded t_s measure over the Montjuic area in Barcelona (a) [1]. Ground photographies before (b) and after (c) the construction of the 4 columns monument [2].

The $-ln\ Q_e$ measure (5.6) indicates no change between the $\mathbf{Z}_{ii}$ matrices with a 0 value, i.e. when $Q_e = 1$, and it denotes a strong change with a value tending to ∞ when $Q_e = 0$. It is worth noticing that, since this measure is based on the determinant, it requires full rank matrices. This means that some initial filtering must be applied to the data. In order to obtain a constant amount of filtering, as the $-ln\ Q_e$ measure depends on the number of looks n_l, an initial multilook filter will be performed in order to apply (5.6). The amount of initial filtering plays an important role in the obtained results. Note that a small amount of filtering will produce noisy results whereas a large filtering will reduce the spatial resolution. Fig. 5.23 shows the results of applying (5.6) after a 3x3 and a 7x7 multilook filter over the Barcelona dataset.

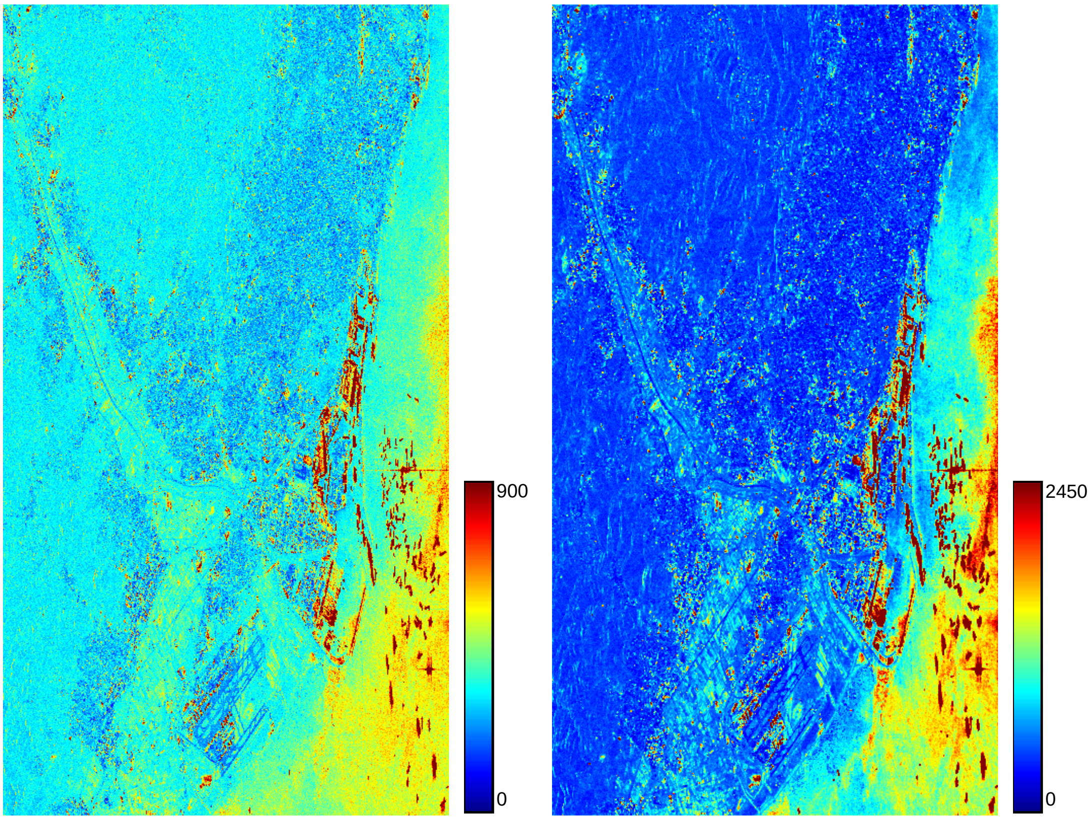

(a) $-ln\ Q_e$, 3x3 multilook **(b)** $-ln\ Q_e$, 7x7 multilook

Figure 5.23: $-ln\ Q_e$ test statistic results for change detection over the Barcelona dataset.

It may be observed that the contrast increases when increasing the amount of initial filtering. Fig. 5.23b has much more contrast than Fig. 5.23a. This effect is particularly visible when observing the contrast between the land and sea areas, which is larger with a 7x7 multilook than with a smaller 3x3 filtering. However, as explained before, this increase in contrast is attained at the expense of a spatial resolution loss. Moreover the values obtained by this measure are strongly affected by the amount of filtering, which may be seen on the colorbar.

Then, in order to make a quantitative evaluation of the t_s and the $-ln\ Q_e$ measures, a relative separation measure S is proposed to evaluate the ability to separate the change and no-change areas of the scene

$$S = \frac{\sigma_c + \sigma_{nc}}{|\mu_c - \mu_{nc}|} \tag{5.7}$$

where σ_c, σ_{nc} and μ_c, μ_{nc} stand for the standard deviation and the mean of the change and no-change areas, respectively.

A lower value of the S measure indicates that change and no-change areas can be better separated. To see more clearly the differences between the TE BPT temporal stability measure t_s

and the $-ln\ Q_e$ test statistic, two zoom areas of the geo-coded results are shown in Fig. 5.24.

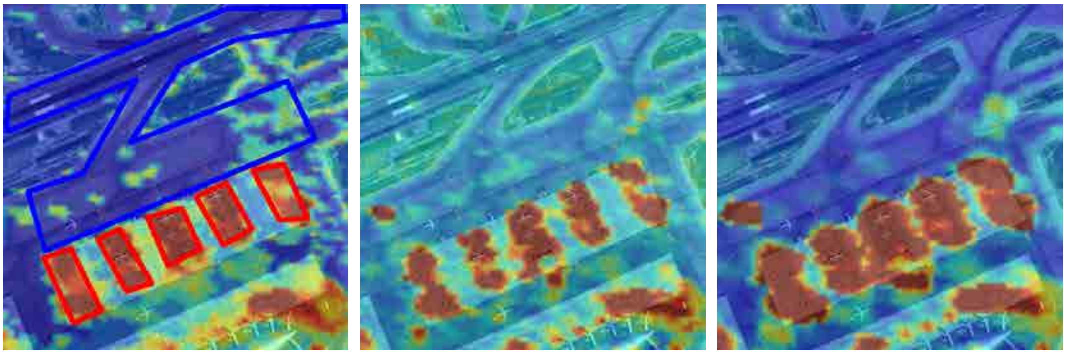

(a) t_s, $\delta_p = -2dB$ **(b)** $-ln\ Q_e$, 3x3 ML **(c)** $-ln\ Q_e$, 7x7 ML

(d) Before **(e)** After **(f)** Zones for S test

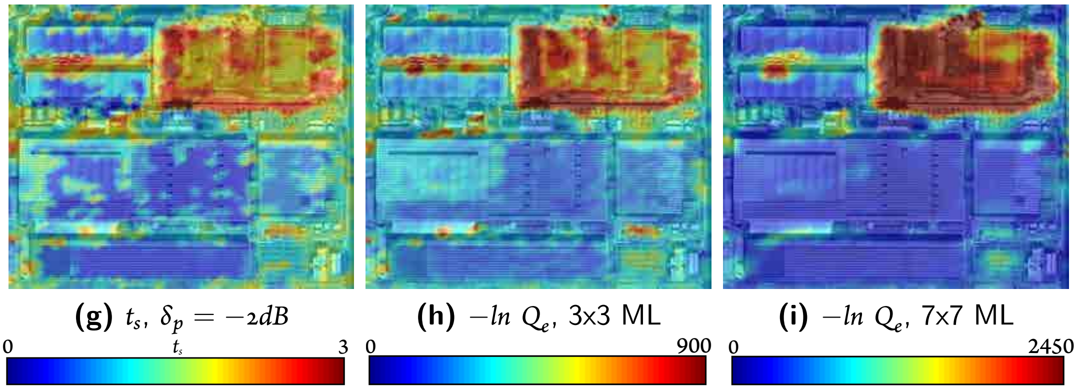

(g) t_s, $\delta_p = -2dB$ **(h)** $-ln\ Q_e$, 3x3 ML **(i)** $-ln\ Q_e$, 7x7 ML

Figure 5.24: Geo-coded t_s and $-ln\ Q_e$ comparison over the airport and a building area in the Barcelona harbor as an overlay with an optical image [1].

To evaluate the separability of both measures, two areas of the Barcelona dataset have been analyzed in detail, shown on Fig. 5.24. Figs. 5.24a to 5.24c correspond to an area of the Barcelona airport, where the plane parking lots previously analyzed may be seen. On the other hand, Figs. 5.24g to 5.24i show an area of the harbor where one industrial building has been demolished, as it may be observed on the optical photographies in Figs. 5.24d and 5.24e. In order to evaluate the statistics of the change and no-change zones, which are required for the S measure, some areas have to be manually labeled accordingly. In Figs. 5.24a and 5.24f, the change areas have been marked with a red contour whereas the no-change zones are represented with a blue contour. Note that the changes appearing in both areas have a different layout: the plane parking lots on Fig. 5.24a are relatively small when compared with the industrial building that has been demolished in Fig. 5.24g.

Measure	μ_c	μ_{nc}	σ_c	σ_{nc}	S
$t_s, \delta_p = -2dB$	3.034	0.4207	0.7578	0.3785	0.4348
$t_s, \delta_p = -1dB$	2.993	0.2944	0.8023	0.1900	0.3678
$-ln\ Q_e$, 3x3 ML	1095	259.1	462.0	52.87	0.6157
$-ln\ Q_e$, 7x7 ML	4478	489.7	2179	460.1	0.6615

Table 5.2: Separability between change and no-change areas for the Barcelona airport zone shown on Fig. 5.24a.

Measure	μ_c	μ_{nc}	σ_c	σ_{nc}	S
$t_s, \delta_p = -2dB$	2.222	0.6224	0.2920	0.3408	0.3956
$t_s, \delta_p = -1dB$	2.077	0.4459	0.2760	0.1832	0.2816
$-ln\ Q_e$, 3x3 ML	710.8	209.0	145.6	62.23	0.4143
$-ln\ Q_e$, 7x7 ML	2611	279.2	643.5	82.27	0.3112

Table 5.3: Separability between change and no-change areas for the Barcelona harbor industrial area shown on Fig. 5.24f.

Tables 5.2 and 5.3 show the values of σ_c, σ_{nc}, μ_c, μ_{nc} and the separation measure S over the areas shown on Figs. 5.24a and 5.24f for the t_s measure with $\delta_p = -2dB$ and $\delta_p = -1dB$ pruning thresholds and for the $-ln\ Q_e$ measure with 3x3 and 7x7 multilook as initial filtering. For the airport area, whose results are shown in Table 5.2, the separation attained by the BPT based method outperforms the $-ln\ Q_e$ in all cases. Since on this situation the change areas are relatively small, increasing the multilook filtering size results into a mixture of zones having different temporal evolution and, consequently, degrading the separability. Conversely, the TE BPT is able to adapt to the spatial structure of the targets in the scene, avoiding the mixture of targets having a different evolution and achieving a better separability. On the other hand, Table 5.3 shows the same results for the industrial buildings near the harbor. In this case, the BPT based t_s measure achieves slightly better separability for low and high filtering, that is, t_s with $\delta_p = -2dB$ vs. $-ln\ Q_e$ with 3x3 multilook and t_s with $\delta_p = -1dB$ vs. $-ln\ Q_e$ with a 7x7 multilook, respectively. Note that since the building are that has been demolished is large, the effect of the inhomogeneous samples mixture is more negligible here, resulting into a performance of the $-ln\ Q_e$ measure more similar to the t_s measure in terms of the separability S measure. The improvement of the BPT-based technique is produced in this case by a combination of a better spatial resolution preservation and a larger amount of filtering over large homogeneous areas.

5.4.3 OBSERVED EXECUTION TIMES

The computational complexity of the BPT construction and pruning algorithms has been analyzed and described in Sections 3.2.3 and 3.3.1. Moreover, the cost of these algorithms has been detailed in Section 5.3 for processing PolSAR time series when employing the ST BPT and the TE BPT representations. However, to give a more clear idea of the processing time in practice, Table 5.4 shows the observed execution times of different processing stages of the BPT-based processing. In order to generate these results, a processing server has been employed for computation, having 12 Intel® Xeon® processors. It may be seen, as stated in Chapter 3, that the most time consuming part is the BPT construction, due mainly to the similarity measures computation. Nevertheless, it is worth mentioning that this step only has to be performed once per dataset, as it is application independent. Once the BPT data abstraction has been constructed, it may be pruned many times for different applications and, in fact, this step is fast, as it may be seen on Table 5.4. It may also be seen, as stated in Section 5.3, that the ST BPT construction has a larger computational complexity than the TE BPT generation, since its number of nodes gets increased by a factor of N. However, the pruning process over the ST BPT may be performed faster than on the TE BPT, since the computation of the (4.14) measure is simpler than the extended homogeneity (5.4).

Processing	Flevoland ST BPT	Flevoland TE BPT	Barcelona TE BPT
BPT Construction	5h 24m	37m 29s	5h 34m
Prune $\delta_p = -2dB$	0.24s	0.52s	6.2s
Prune $\delta_p = -1dB$	0.04s	0.19s	3.4s
Prune $\delta_p = 0dB$	0.02s	0.08s	2.3s

Table 5.4: Observed execution times for different processing stages of the proposed techniques.

A person who never made a mistake never tried anything new.

Albert Einstein

6

BPT Related Enhancements and Other Contributions

THIS CHAPTER COLLECTS some other contributions that have been developed during the course of this thesis in order to enhance the detected limitations related with the different aspects of the BPT based processing.

On the first section, the problem related with the resolution loss implied by the initial filtering needed for matrix regularization is analyzed. A new speckle filtering method is developed in order to improve this limitation of the 3 by 3 multilook previously applied. Moreover, this technique is defined in the same terms than the BPT processing scheme, employing analogous similarity measures in order to combine similar pixels of the image, while avoiding the heterogeneous sample mixture. The second section deepens into the understanding of the changes detected from a polarimetric point of view. The mathematical background to perform this analysis is defined and, then, tested with real data. The third section describes the limitations of the sample covariance model for representing inhomogeneous or textured data. Then, a new model, not based on the centroid representation approach is proposed in order to mitigate this limitation.

6.1 MATRIX REGULARIZATION AND INITIAL FILTERING

As mentioned in Section 2.2.4, the sample covariance matrix $\mathbf{Z}$ is the estimation of the covariance matrix that determined the statistical distribution of the polarimetric data, assuming the Gaussian hypothesis. However, the estimation of this matrix, as expressed in (2.54), only makes sense over homogeneous samples of the data. The problem here is that PolSAR data is usually strongly heterogeneous, since it reflects the complexity of the scene.

An additional complication when processing PolSAR data is that most processing schemes require that the estimated $\mathbf{Z}$ values are full-rank matrices. This inconvenience also applies to the proposed BPT based techniques as it has been indicated, for instance, in the full-matrix dissimilarity measures defined in Section 4.1.3. In order to circumvent this limitation, an initial filtering may be applied to the data, just as a matrix regularization. In the results shown in Chapters 4 and 5, an initial 3 by 3 multilook filtering has been applied for this purpose. This pre-processing step ensures full-rank matrices at the expense of a small spatial resolution loss. In general, this may be a reasonable price to be paid, but for the BPT based processing, which aims to preserve as much as possible the spatial resolution, this effect undermines one of its most valuable benefits. Then, in the following, a new speckle filtering technique is presented, based on the Bilateral filtering [116] applied to PolSAR data [14][12][13], in order to mitigate, as much as possible, this spatial resolution loss produced during this matrix regularization pre-processing step. It is worth mentioning that this approach has, in practice, some similarities to the Non-Local Means filtering [28][42], presented in Section 2.3.4, while reducing the size of the patch to one pixel.

6.1.1 BILATERAL AND DISTANCE-BASED FILTERING

The multilook filtering, as mentioned in Section 2.3.1, is assuming spatial locality on the data. Then, for each pixel of the image, a local window is considered, and it is assumed that all the pixels within this window are homogeneous. Obviously, this is not true near contours or for small areas, where different type of targets may appear together.

The bilateral filter [116] introduces also the domain locality. Note that it may be assumed, for PolSAR data, that homogeneous samples will also have similar response values. Then, the homogeneous data will be found close in the spatial domain and also in the polarimetric domain. Therefore, the sample averaging (2.54) performed by the multilook may be replaced by a weighted averaging according to the sample closeness in both domains [14][12]. As a consequence, the sample covariance matrix $\hat{\mathbf{Z}}^{ij}$ obtained at position (i, j) may be expressed as [13]

$$\hat{\mathbf{Z}}^{ij} = \frac{1}{k(i,j)} \sum_{m,n \in V(i,j)} \mathbf{Z}^{mn} w_s(i,j,m,n) w_p\left(\mathbf{Z}^{mn}, \mathbf{Z}^{ij}\right) \tag{6.1}$$

where $V(i,j)$ stands for the local window around the pixel located at (i,j) position, $\mathbf{Z}^{ij}$ represents the sample covariance matrix of the input image at (i,j), w_s and w_p are the weighting functions on the spatial and polarimetric domains, respectively, and $k(i,j)$ is the normalization factor, defined as

$$k(i,j) = \sum_{m,n \in V(i,j)} w_s(i,j,m,n) w_p\left(\mathbf{Z}^{mn}, \mathbf{Z}^{ij}\right). \tag{6.2}$$

In order to obtain valuable results, the proper definition of the w_s and w_p weighting functions is crucial. The role of these functions is to exploit the spatial and polarimetric locality and, accordingly, they should exhibit the following characteristics:

1. The weighting functions w_s and w_p should be within the finite interval $[0,1]$, presenting higher values for closer values in the spatial and polarimetric domains, respectively.

2. As a consequence, from the previous condition it may be assumed that

$$w_s(i,j,i,j) = 1, \ \forall\, i,j \tag{6.3}$$

$$w_p\left(\mathbf{Z},\mathbf{Z}\right) = 1, \ \forall\, \mathbf{Z} \tag{6.4}$$

3. Additionally, symmetry is considered in data closeness for both domains, thus, w_s and w_p should be symmetric, that is,

$$w_s(i,j,m,n) = w_s(m,n,i,j) \ \forall\, i,j,m,n \tag{6.5}$$

$$w_p\left(\mathbf{Z}^{mn}, \mathbf{Z}^{ij}\right) = w_p\left(\mathbf{Z}^{ij}, \mathbf{Z}^{mn}\right) \ \forall\, i,j,m,n. \tag{6.6}$$

In short, the w_s and w_p weights should be functions based on the data closeness in the spatial and polarimetric domains, respectively. In order to employ a simple and known mathematical concept, and also to be consistent with the BPT based conception, a definition of those weights is proposed in terms of a spatial and a polarimetric distances d_s and d_p, respectively

$$w_s(i,j,m,n) = \frac{1}{1+\frac{d_s^2(i,j,m,n)}{\sigma_s^2}} \tag{6.7}$$

$$w_p\left(\mathbf{Z}^{mn},\mathbf{Z}^{ij}\right) = \frac{1}{1+\frac{d_p^2(\mathbf{Z}^{mn},\mathbf{Z}^{ij})}{\sigma_p^2}} \tag{6.8}$$

where σ_s and σ_p control the weights sensitivity in the spatial and polarimetric domains, respectively. Mathematically, d_s and d_p are metric functions that quantify the sample closeness on their domains, following the properties:

1. $d(x,y) \geq 0$. Non-negativity.
2. $d(x,y) = 0$ if and only if $x = y$. Identity of indiscernibles.
3. $d(x,y) = d(y,x)$. Symmetry.
4. $d(x,z) \leq d(x,y) + d(y,z)$. Triangle inequality.

Some similarity measures have been defined in Section 4.1.3 and analyzed in Sections 4.3.3 and 4.3.4 with real and simulated PolSAR data. On that section, two main types of measures were identified: full-matrix and diagonal measures. Although only full-matrix measures are able to fully exploit the complete polarimetric information under the Gaussian hypothesis, these functions require full-rank matrices. If this technique is intended to be used as a matrix regularization step, that is, without any kind of initial filtering, only diagonal measures may be employed as the matrices estimated from original pixels $\mathbf{Z} = \mathbf{k}\mathbf{k}^H$ are singular, having rank equal to 1.

In the proposed technique, the classical euclidean distance may be employed in the spatial domain

$$d_s^2(i,j,m,n) = (i-m)^2 + (j-n)^2. \tag{6.9}$$

On the other hand, for the polarimetric domain, some of the diagonal dissimilarity measures defined in Section 4.1.3 may be employed. However, special attention must be paid to them in order to fulfill the previously defined mathematical properties of a metric measure. Since this was not a requisite for the dissimilarity measures for the BPT construction, some of them have to be modified. Moreover, the term depending on the region size has no sense for the bilateral filter which is, indeed, a pixel-based approach. Then, the revised Wishart dissimilarity measure [68], on which is based the d_{dw} measure defined in (4.10), may be applied with some modifications for the bilateral filtering, resulting into the the d_{pw} measure

$$d_{pw}^2\left(\mathbf{Z}^{mn},\mathbf{Z}^{ij}\right)=\left(\sum_{k=1}^{3}\left(\frac{(Z_{kk}^{mn})^2+(Z_{kk}^{ij})^2}{Z_{kk}^{mn}Z_{kk}^{ij}}\right)-6\right) \tag{6.10}$$

where Z_{ij} is the index notation for the (i,j)-th element of the 3 by 3 matrix $\mathbf{Z}$.

Another relevant measure that has been defined in Section 4.1.3 is the geodesic dissimilarity, based on the Riemannian geometry of the hermitian positive definite cone of matrices [22]. As in the previous case, a modification of the diagonal version d_{dg}, which has been defined in (4.11), will be employed. Note that this measure is defined in terms of the natural logarithm of the diagonal elements quotient. This fact reduces considerably the rate of growth of the measure having not enough separability between different matrices to prevent the heterogeneous region mixture when employed for the bilateral filter. Thus, a modification d_{pg} is proposed to compensate this rate of growth reduction caused by the logarithm

$$d_{pg}^2\left(\mathbf{Z}^{mn},\mathbf{Z}^{ij}\right)=\exp\left(\sqrt{\sum_{k=1}^{3}\ln^2\left(\frac{Z_{kk}^{ij}}{Z_{kk}^{mn}}\right)}\right)-1 \tag{6.11}$$

where ln stands for the natural logarithm.

Additionally, when dealing with PolSAR data, special attention must be given to the system noise. This noise may be caused by different sources as, for instance, thermal noise, discretization errors, etc [53]. However, from the statistical point of view, it is usually modeled as a zero-mean uncorrelated Gaussian noise. This noise may degrade the performance of the polarimetric weights computation when the backscattered power is comparable to the noise power. Then, a modified d_{pt} measure may be applied, based on the previous measures (6.10) and (6.11)

$$d_{pt}^2\left(\tilde{\mathbf{Z}}^{mn},\tilde{\mathbf{Z}}^{ij}\right)=d_p^2\left(\mathbf{Z}^{mn}+\sigma_t^2\mathbf{I},\mathbf{Z}^{ij}+\sigma_t^2\mathbf{I}\right) \tag{6.12}$$

where $\mathbf{I}$ represents the 3 by 3 identity matrix, σ_t^2 stands for the power of the system noise and d_p^2 may be d_{pw}^2 or d_{pg}^2.

In practice, the effect of the d_{pt} measure modification is that it reduces the sensitivity of the polarimetric measures when the backscattered power, contained within the diagonal elements of the $\mathbf{Z}$ matrix, is close to the system noise power σ_t. However, it has the inconvenience of introducing it as a new parameter to be fixed. The σ_t value may be obtained from the parameters of the sensor. Additionally, it may be estimated from the data, as proposed in [53], by manually selecting a dark area of the image, where presumably there is no radar backscattered power, and, consequently, the mean power of this area may be considered as the system noise power σ_t. In fact, an automatic method for estimating the σ_t is proposed based on this rationale. The whole image is decomposed into large enough blocks to reduce the effect of speckle noise, for instance 9 by 9 pixels, and the minimum retrieved power from all the blocks among all the channels is considered as the σ_t parameter for the image. Note that this method is assuming that some dark areas are present in the image. If this is not the case, this method may lead to an incorrect parameter estimation. Then, it is generally safer to employ the parameters of the sensor when available.

It is worth noticing that the bilateral filtering, as described in (6.1), results into a different amount of averaged pixels per pixel. This may be a difficulty for further processing of the data but, however, this information is still available for analysis and interpretation, being related with the k parameter (6.2). Moreover this parameter may also hold information related with the spatial structure of the image, as it will be seen later on.

As mentioned previously, the bilateral filter is a pixel-based processing scheme, as it relies on the pixel values for the computation of the different w_p weights. Then, the speckle noise present in the data that contaminates the original SAR data will also affect the weight computation, resulting into a noisy w_p values and, consequently, a noisy filtered image. In order to mitigate this effect, an iterative weight refinement scheme is proposed, which is represented in Fig 6.1.

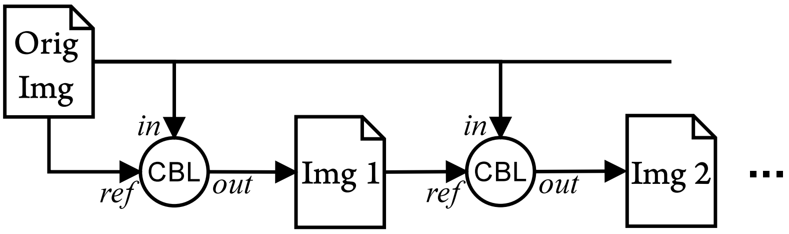

Figure 6.1: Iterative weight refinement approach diagram.

In the diagram presented in Fig 6.1, 'Orig Img' stands for the original input image and the subsequent 'Img i' represent the output result obtained after the i-th iteration. The filtering process is performed on the circular boxes marked as 'CBL', an acronym for *Cross-Bilateral Filter* [47] based on the filter previously defined in (6.1). The weighted average is performed over the input image *in*, whereas the weight computation is performed over the reference image *ref*

$$\hat{\mathbf{Z}}^{ij} = \frac{1}{k(i,j)} \sum_{m,n \in V(i,j)} \mathbf{Z}_{\text{in}}^{mn} w_s(i,j,m,n) w_p \left(\mathbf{Z}_{\text{ref}}^{mn}, \mathbf{Z}_{\text{ref}}^{ij} \right) \tag{6.13}$$

where $\mathbf{Z}_{\text{in}}^{ij}$ and $\mathbf{Z}_{\text{ref}}^{ij}$ represent the estimated covariance matrix of the input and reference images at position (i, j), respectively.

It is worth stressing that the proposed iterative weight computation scheme in Fig. 6.1 does not correspond to an iterative filtering. Iterative filtering may produce a stronger level of filtering but it usually tends to produce overfiltering by mixing similar non-homogeneous areas and blurring some details due to the propagation of errors. On the other hand, the proposed scheme processes the original image at each iteration. Consequently, the propagation of errors is avoided. This scheme is intended to generate a more reliable estimation of the polarimetric weights w_p based on filtered images. Additionally, iterative filtering would have the inconvenience of combining samples with different amounts of filtering among the different iterations, producing a k parameter that does not correspond to the real number of samples averaged from the original image, making the further analysis and interpretation of the obtained results more difficult.

In the following, this approach will be called the Distance Based Filtering (DBF) [13]. This proposed technique is evaluated in this section as a speckle filter itself, in order to analyze the ability of this approach to adapt to the structure of the scene and preserve its spatial resolution. In Section 6.1.2 this technique will be combined with the BPT, employed as a pre-processing step for matrix regularization.

Fig. 6.2 shows the results obtained after applying the proposed DBF technique to the first acquisition of the Flevoland dataset described in Section 5.3. The original image is presented in Fig. 6.2a and the corresponding DBF filtering result is shown in Fig. 6.2b. For this processing, the d_{pw} similarity measure has been employed, the local window V corresponds to a 11 by 11 pixel square window, and the weights sensitivity has been set to $\sigma_s = 3$ and $\sigma_p = 0.6$. These values have been chosen experimentally, as they have demonstrated to produce a good level of speckle filtering while also preserving the details of the image. The automatic method for σ_t^2 calculation has been applied, as stated before. In this case, the original image contains dark areas, as seen on Fig. 6.2a, corresponding to closed and calm water, where this parameter may be estimated correctly. Finally, 5 iterations of the weight refinement scheme presented on Fig. 6.1 have been performed.

As it may be observed, the noise has been substantially reduced in Fig. 6.2b in comparison with Fig. 6.2a. However, in order to see more clearly the differences, a detail of these images is depicted in Figs. 6.3a and 6.3e, including the obtained number of averaged pixels k parameter, represented in Fig. 6.3f. This detail area is composed by some forest and agricultural areas in the top part and urban and sea areas in the bottom part. Moreover, the results of this filtering strategy are compared with those obtained from the 7 by 7 multilook filter, the Refined Lee filter

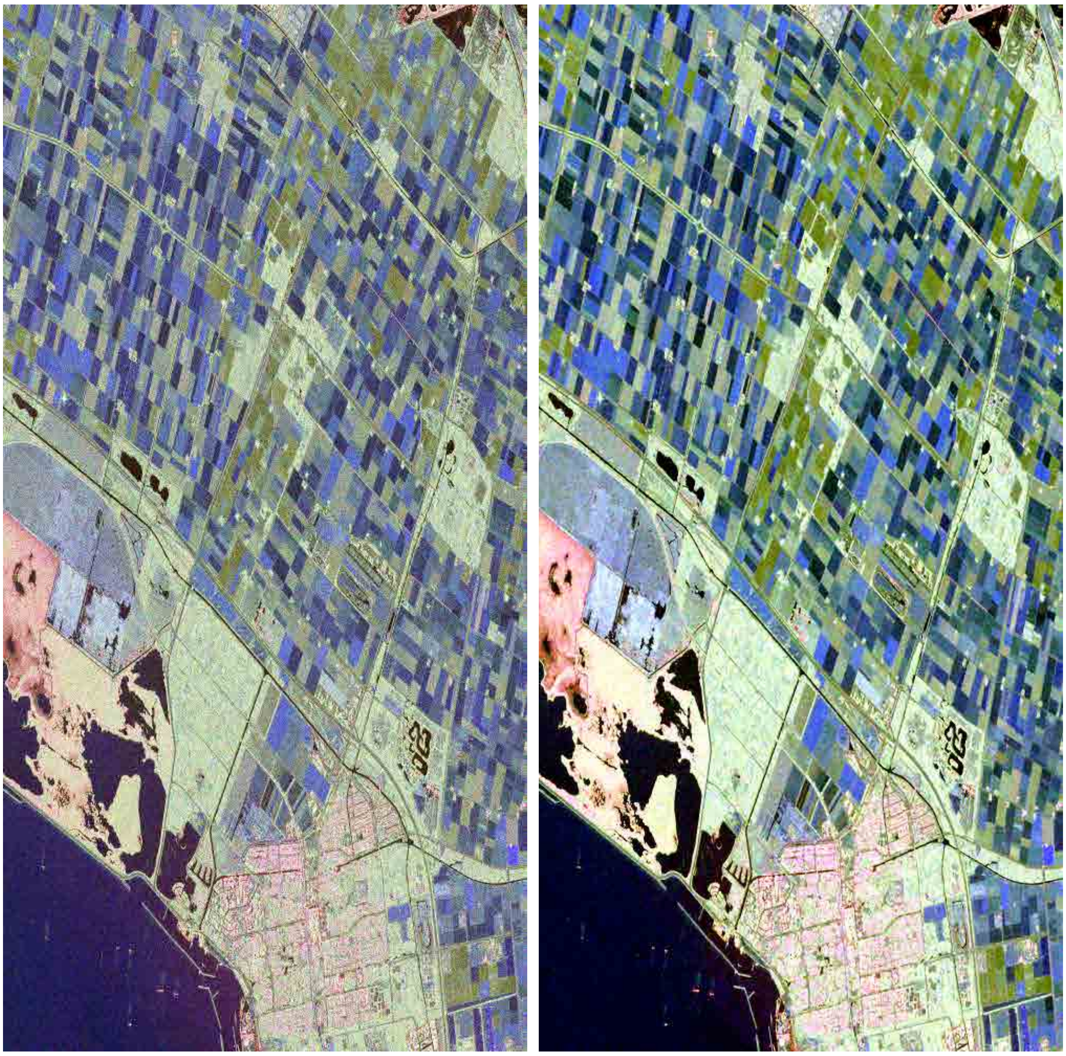

(a) Original **(b)** DBF Filtered, 5it, d_{pw}, σ_s=3, σ_p=0.6

Figure 6.2: Original (a) and DBF filtered (b) Pauli RGB images of the first acquisition of the Flevoland dataset. For the DBF, 5 weight refinement iterations have been employed with the d_{pw} measure and $\sigma_s = 3, \sigma_p = 0.6$ parameters ($|S_{hh} + S_{vv}|$, $|S_{hv} + S_{vh}|$, $|S_{hh} - S_{vv}|$).

[74], described in Section 2.3.2, and the IDAN filter[1] [125], explained in Section 2.3.3. Additionally, a zoom is shown in bottom right corner, corresponding to the central part of the image, in order to see the obtained results at pixel level. The 7 by 7 multilook filtering may achieve a good level of filtering, as observed in Fig. 6.3b, but it blurs the edges on the image and enlarges the small point scatters or details of the image, mixing, then, heterogeneous samples of the im-

---

[1] The PolSARPro software [3] has been employed to process this data and for Pauli image generation. For the IDAN filtering, a maximum AN size parameter of 100 pixels has been employed.

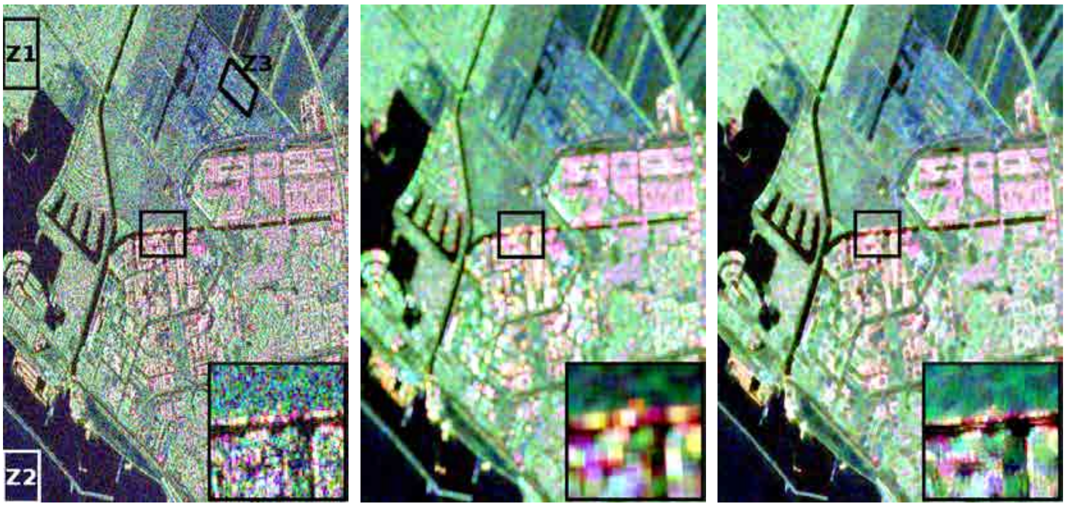

(a) Original **(b)** 7x7 multilook **(c)** Refined Lee filter

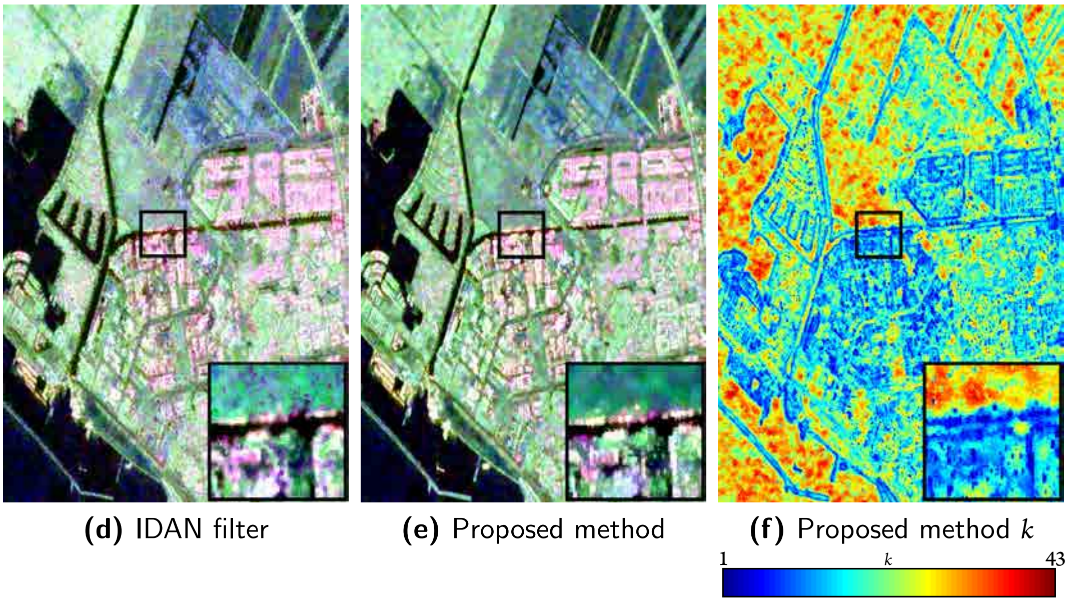

(d) IDAN filter **(e)** Proposed method **(f)** Proposed method k

Figure 6.3: Pauli RGB for the original detail image (a) and filtered images employing 7x7 multilook (b), refined Lee (c), IDAN (d) and the proposed method (e). The k parameter for the proposed method is represented in (f), corresponding to the number of averaged pixels ($|S_{hh}+S_{vv}|$, $|S_{hv}+S_{vh}|$, $|S_{hh}-S_{vv}|$).

age. As mentioned in Section 2.3.1, this is caused by the fact that the multilook is a low pass filter that reduces the spatial resolution. The refined Lee filtering, shown in Fig. 6.3c achieves a good spatial resolution reservation but, due its intrinsic limitations to adapt to complex spatial structures, it introduces some artifacts that distort the obtained image. The IDAN filter also achieves a good level of filtering while also preserves some of the image contours but, however, it blurs small details as point scatters. On the other hand, the proposed technique does not introduce artifacts and preserves the edges and the small details. Furthermore, it achieves a good level of filtering over homogeneous areas, similar to the multilook. The edge preservation may be clearly seen over the coastline while its capability to preserve small details may be observed in the zoom over the urban area. The amount of filtering performed for each pixel is represented in Fig. 6.3f, corresponding to the k parameter. Note that this parameter may not be directly assumed as the Equivalent Number of Looks [18], but it is related with it, as it correspond to the number of averaged pixels per pixel. It may be observed that small k values are obtained near contours while large values are retrieved over homogeneous areas. Indeed, the values obtained over homogeneous areas are in the order of 40, which is a similar number to the multilook filter, that would have a number of averaged pixels per pixel constant over the whole image and equal to $7 \cdot 7 = 49$ pixels.

To see more clearly the effect of the iterative weight refinement scheme presented in Fig. 6.1, the obtained k parameter for each iteration has been represented in Fig. 6.4. The number of averaged pixels per pixel is represented for the 1st to the 4th iterations, as the last iteration corresponds to Fig. 6.3f, presented before. Note that the color scale is different in each image, in order to increase the contrast, as reflected by the corresponding color bars. Additionally, Fig. 6.5 shows the histogram of the obtained k parameter for each iteration.

As it may be observed, in the first iteration the amount of filtering achieved is low, as small k values are obtained. Moreover, the k values retrieved are very noisy since it is difficult to estimate correctly the w_p weights over the original image due to the speckle noise. This effect is specially visible over the zoomed area. In the successive iterations of the weight refinement process, larger values of k are progressively obtained while the noise over this parameter gets reduced. It may also be seen that contours, small details and homogeneous areas of the image are more clearly detected. Similar conclusions may be extracted from the k histograms shown in Fig. 6.5. It may be observed that the k values gets increased with the successive weight refinement iterations and, additionally, the difference between them gets reduced as the number of iterations increases. Then, a convergence pattern may be observed which may induce to continue this process. However, very small differences are observed in the following iterations and, consequently, we have decided to stop it after the 5th iteration, in order to reduce the computational time needed for this processing.

In order to perform a detailed analysis of the polarimetric information preservation of a filtering technique, additional information than the one contained in the Pauli images should be considered. Fig. 6.6 analyzes the obtained Entropy (H) and averaged Alpha angle ($\bar{\alpha}$) polari-

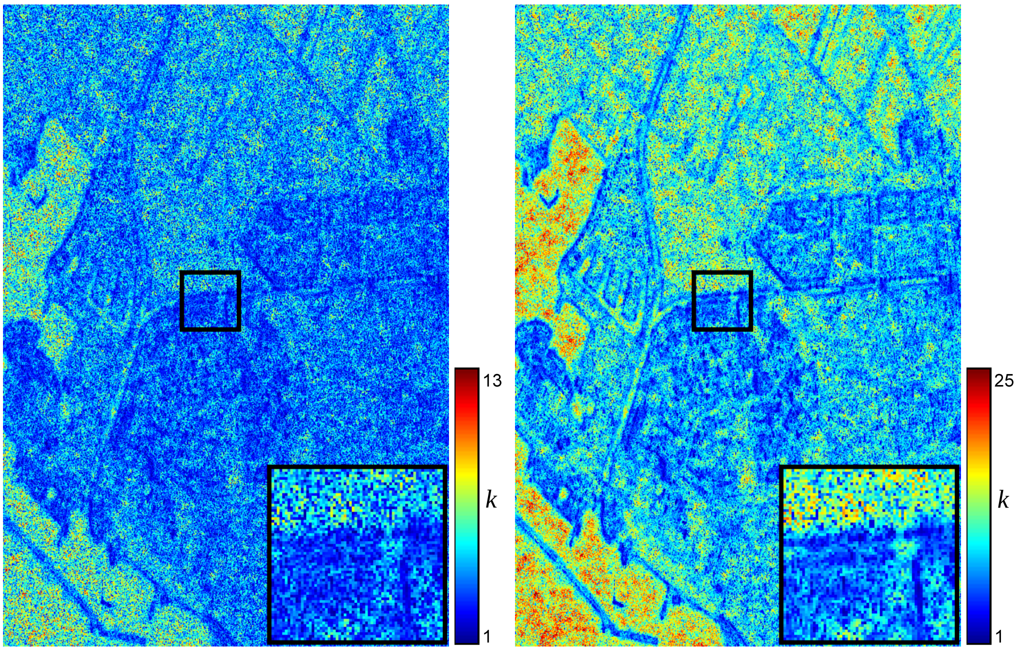

(a) k, 1st it **(b)** k, 2nd it

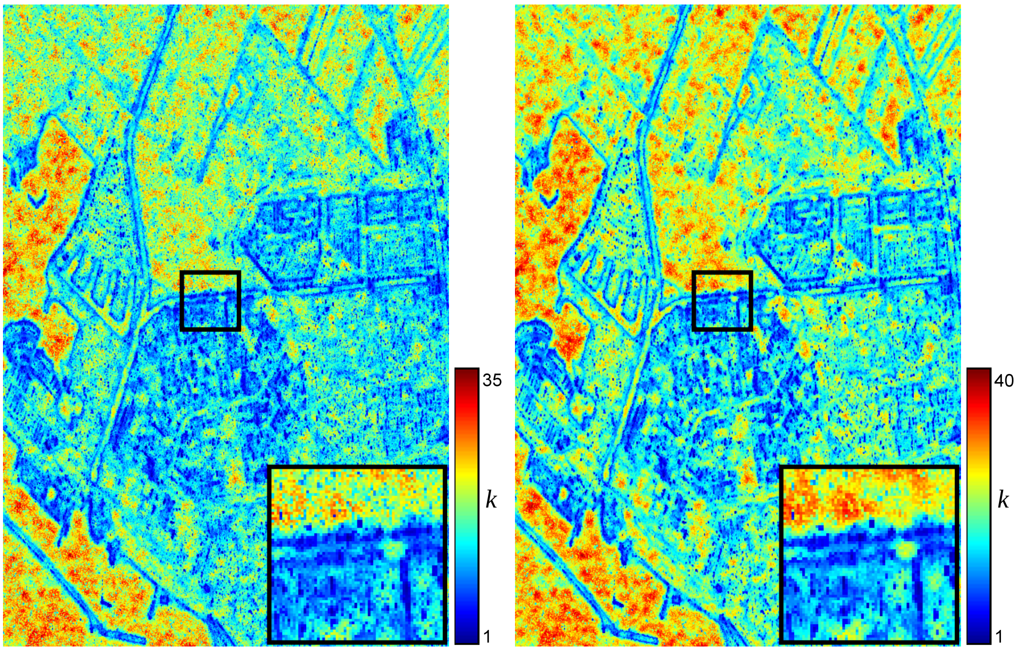

(c) k, 3rd it **(d)** k, 4th it

Figure 6.4: Evolution of the k parameter, corresponding to the number of averaged pixels per pixel, among the different iterations of the weight refinement scheme presented in Fig. 6.1. The k parameter of the final iteration corresponds to Fig. 6.3f.

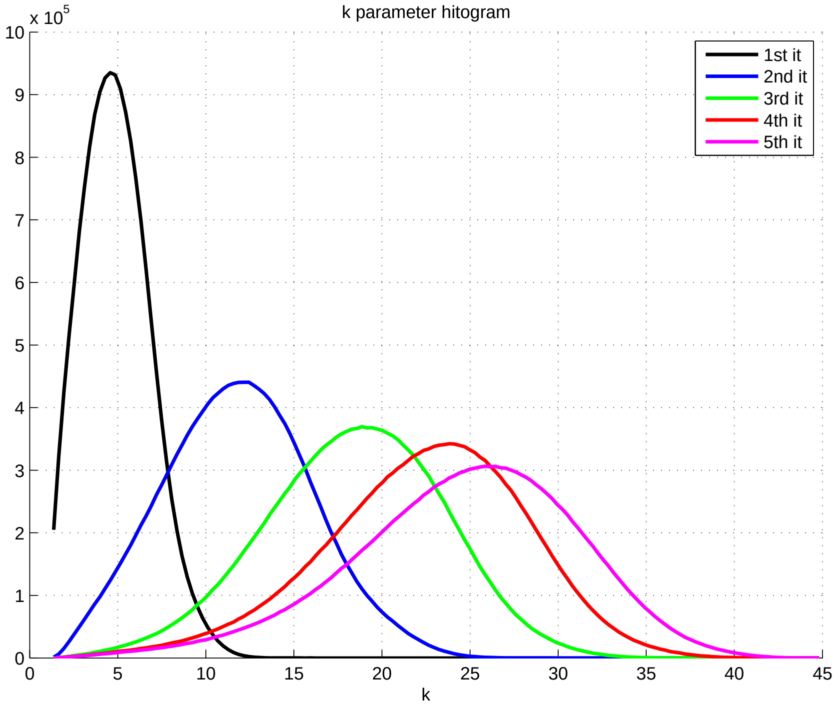

Figure 6.5: Number of averaged pixels per pixel histograms, the k parameter, for each iteration of the weight refinement scheme.

metric parameters [35], which has been described in Section 2.2.6, for the multilook, the refined Lee, the IDAN and the proposed DBF filtering strategies. The same area than on Fig. 6.3 is shown, for comparison purposes. Qualitatively similar colors may be observed in all cases, meaning that similar values are obtained over homogeneous areas. However, when looking at the results in detail some important differences may be noticed. The ability of the different methods to preserve the spatial resolution may be clearly stated over the small details of the image, specially over the urban area, as seen on the zoomed area, where the multilook filter enlarges those details according to its window. The Refined Lee filter results, shown on Figs. 6.6b and 6.6f, demonstrates a good preservation of the small details of the image whereas the IDAN filter, whose results are represented on Figs. 6.6c and 6.6g, almost destroys these small details that appear as small blue and red dots in H and $\bar{\alpha}$, respectively, when employing the refined Lee. On the other hand, the proposed DBF filter preserves the structure of the small details, similarly to the refined Lee, while also has the advantage over this technique of attaining a higher amount of filtering over homogeneous areas while not introducing distortion to the image.

As performed in Section 4.3.3, some homogeneous areas may be manually defined over the image in order to perform a quantitative evaluation of the preservation of the polarimetric information. Three homogeneous zones have been manually selected from this data crop that

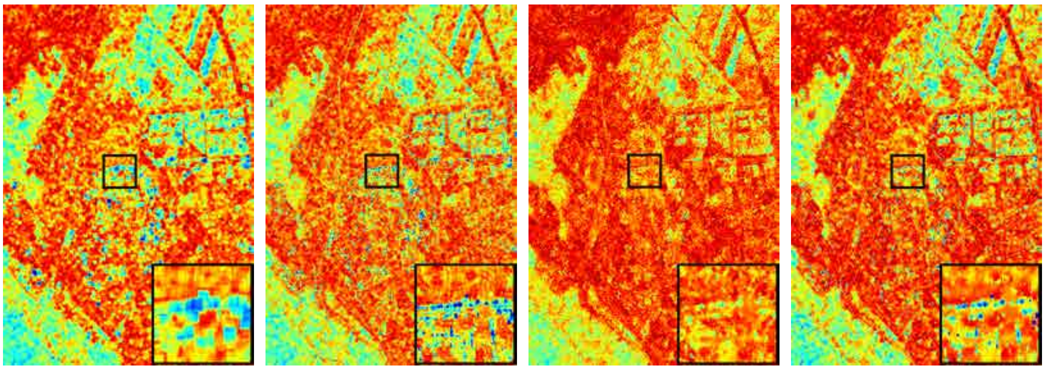

(a) H, 7x7 multilook **(b)** H, refined Lee **(c)** H, IDAN **(d)** H, Proposed

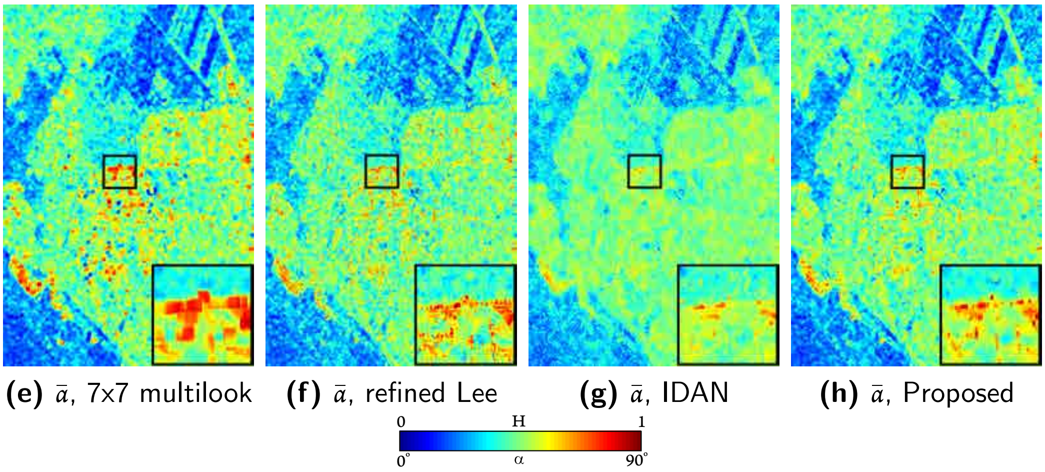

(e) $\bar{\alpha}$, 7x7 multilook **(f)** $\bar{\alpha}$, refined Lee **(g)** $\bar{\alpha}$, IDAN **(h)** $\bar{\alpha}$, Proposed

Figure 6.6: Entropy (H) and averaged Alpha angle ($\bar{\alpha}$) for 7x7 multilook and the proposed filtering method.

have been marked in Fig. 6.3a. These zones correspond to forest, water and an agricultural crop areas, respectively. Table 6.1 shows the mean values obtained for the diagonal elements of the sample covariance matrix over these areas for the original image and for the different speckle filtering methods previously commented. Additionally, the same results for the proposed DBF method are presented, when employing the d_{pw} and d_{pg} measures. Moreover, the magnitude and phase of the correlation coefficient ρ_{13} over HH and VV polarization states and the $H/A/\bar{\alpha}$ polarimetric decomposition parameters are also shown. All these values may not be computed over the original image and, then, they are not represented in the table. It may be observed that all the adaptive filters analyzed have an underestimation bias over the diagonal elements of the covariance matrix. However, the bias of the proposed method is the smaller of those filters, obtaining mean values that are close to the ones obtained for the multilook. Nonetheless, for the $H/A/\bar{\alpha}$ all the filters obtain values that are similar to those obtained by the multilook. In addition, a further analysis of the filtering capability of those filters may be found in [13].

Region	Filtering	C_{11}	C_{22}	C_{33}	$\lvert\rho_{13}\rvert$	$\arg(\rho_{13})(^\circ)$	H	A	$\bar{\alpha}(^\circ)$
Z1 Forest 5000 pixels	Original	$2.302 \cdot 10^{-1}$	$1.125 \cdot 10^{-1}$	$1.906 \cdot 10^{-1}$	-	-	-	-	-
	7x7 Multilook	$2.305 \cdot 10^{-1}$	$1.130 \cdot 10^{-1}$	$1.933 \cdot 10^{-1}$	0.4194	1.670	0.8504	0.2599	42.87
	Refined Lee	$1.879 \cdot 10^{-1}$	$9.965 \cdot 10^{-2}$	$1.623 \cdot 10^{-1}$	0.3971	2.873	0.8442	0.3063	44.51
	IDAN	$1.471 \cdot 10^{-1}$	$7.353 \cdot 10^{-2}$	$1.252 \cdot 10^{-1}$	0.2993	2.339	0.8878	0.2513	46.03
	Proposed d_{pw}	$2.227 \cdot 10^{-1}$	$1.090 \cdot 10^{-1}$	$1.869 \cdot 10^{-1}$	0.3865	1.569	0.8698	0.2244	43.46
	Proposed d_{pg}	$2.210 \cdot 10^{-1}$	$1.082 \cdot 10^{-1}$	$1.853 \cdot 10^{-1}$	0.3869	1.550	0.8661	0.2290	43.52
Z2 Water 3900 pixels	Original	$1.787 \cdot 10^{-2}$	$1.280 \cdot 10^{-3}$	$2.552 \cdot 10^{-2}$	-	-	-	-	-
	7x7 Multilook	$1.801 \cdot 10^{-2}$	$1.271 \cdot 10^{-3}$	$2.552 \cdot 10^{-2}$	0.7443	3.088	0.4351	0.6407	19.30
	Refined Lee	$1.492 \cdot 10^{-2}$	$1.255 \cdot 10^{-3}$	$2.099 \cdot 10^{-2}$	0.7062	2.535	0.4701	0.6438	21.89
	IDAN	$1.158 \cdot 10^{-2}$	$8.901 \cdot 10^{-4}$	$1.667 \cdot 10^{-2}$	0.6263	2.473	0.5248	0.6967	24.32
	Proposed d_{pw}	$1.749 \cdot 10^{-2}$	$1.263 \cdot 10^{-3}$	$2.479 \cdot 10^{-2}$	0.7094	2.872	0.4689	0.6381	20.59
	Proposed d_{pg}	$1.732 \cdot 10^{-2}$	$1.254 \cdot 10^{-3}$	$2.458 \cdot 10^{-2}$	0.7079	2.871	0.4693	0.6392	20.75
Z3 Crop 2200 pixels	Original	$1.862 \cdot 10^{-1}$	$3.195 \cdot 10^{-2}$	$1.771 \cdot 10^{-1}$	-	-	-	-	-
	7x7 Multilook	$1.855 \cdot 10^{-1}$	$3.170 \cdot 10^{-2}$	$1.758 \cdot 10^{-1}$	0.7489	8.423	0.5444	0.2998	22.87
	Refined Lee	$1.434 \cdot 10^{-1}$	$2.862 \cdot 10^{-2}$	$1.393 \cdot 10^{-1}$	0.7059	7.478	0.5781	0.3653	25.86
	IDAN	$1.020 \cdot 10^{-1}$	$1.948 \cdot 10^{-2}$	$1.006 \cdot 10^{-1}$	0.6187	8.641	0.6514	0.3783	27.84
	Proposed d_{pw}	$1.765 \cdot 10^{-1}$	$3.087 \cdot 10^{-2}$	$1.679 \cdot 10^{-1}$	0.7062	8.474	0.5880	0.2933	24.50
	Proposed d_{pg}	$1.757 \cdot 10^{-1}$	$3.058 \cdot 10^{-2}$	$1.671 \cdot 10^{-1}$	0.7072	8.470	0.5808	0.2987	24.53

Table 6.1: Mean estimated values over homogeneous areas for the proposed DBF in comparison with other speckle filtering techniques. For the proposed technique, an 11x11 local window has been employed with 5 weight refinement iterations and $\sigma_s = 3, \sigma_p = 0.6$.

As mentioned previously, some parameters are involved into the DBF filtering process. The effect of the weight refinement scheme and the number of iterations has been analyzed previously. In the following, the impact of the σ_s and σ_p weight sensitivity parameters is evaluated. Fig. 6.7 shows the results of applying the proposed method to the Flevoland dataset with different combination of σ_s and σ_p parameters. The same detail area is shown than on Fig. 6.3, for comparison purposes. Figs 6.7a and 6.7b show the effect of changing the σ_s parameter, whereas Figs 6.7d and 6.7e depict changes on σ_p. If these results are compared with the previous filtering results, shown in Fig. 6.3e, it may be observed that when the weight sensitivity is increased, by reducing the values of σ_s or σ_p, the amount of speckle filtering attained gets reduced. Conversely, when those parameters are increased the opposite effect is obtained. Additionally, Figs. 6.7b and 6.7c and Figs. 6.7e and 6.7f show the effect of changing the dissimilarity measure employed for computing the polarimetric weights. Note that smaller differences are observed between these image, which means that this parameter has a lower impact on the obtained results.

Nevertheless, the σ_s and σ_p parameters are dealing with different domains and, consequently, they have a different impact on the filtering. The 50-bin histogram of the number of averaged pixels per pixel, the k parameter, is shown in Fig. 6.8 for distinct values of σ_s and σ_p. When changing the σ_s parameter the spatial decay of the w_s weights is modified but the sensitivity to the polarimetric domain remains unaltered. Then, as it may be observed in Figs. 6.8a to 6.8c, all the k values gets increased but the shape of the histograms remains almost unaffected. On the other hand, when the σ_p parameter is modified, a similar trend is observed in terms of k but in this case, as it may be seen in Figs. 6.8d to 6.8i, the shape of the histograms is substantially changed. It is worth noticing that the σ_p parameter plays an important role in the polarimetric information preservation, as the adaptation to the spatial content of the image is achieved due to the polarimetric locality assumption. Then, the selection of this parameter is a trade-off between the amount of speckle filtering and the contours and details preservation. In fact, if this parameter is set to a high value, as it may be observed in Figs. 6.7e and 6.7f, a larger amount of filtering is achieved at a cost of some heterogeneous samples mixture and resolution loss. Moreover, the proposed DBF filtering scheme may be considered as a generalization of the multilook as it tends to this filter over the V window when $\sigma_s \to \infty$ and $\sigma_p \to \infty$.

6.1.2 DBF AS MATRIX REGULARIZATION FOR THE BPT

In the previous section the DBF technique has been defined and analyzed as a speckle filter. However, it may be employed also as a matrix regularization pre-processing step for the BPT based processing scheme, in order to obtain full-rank $\mathbf{Z}$ matrices. According to the previous

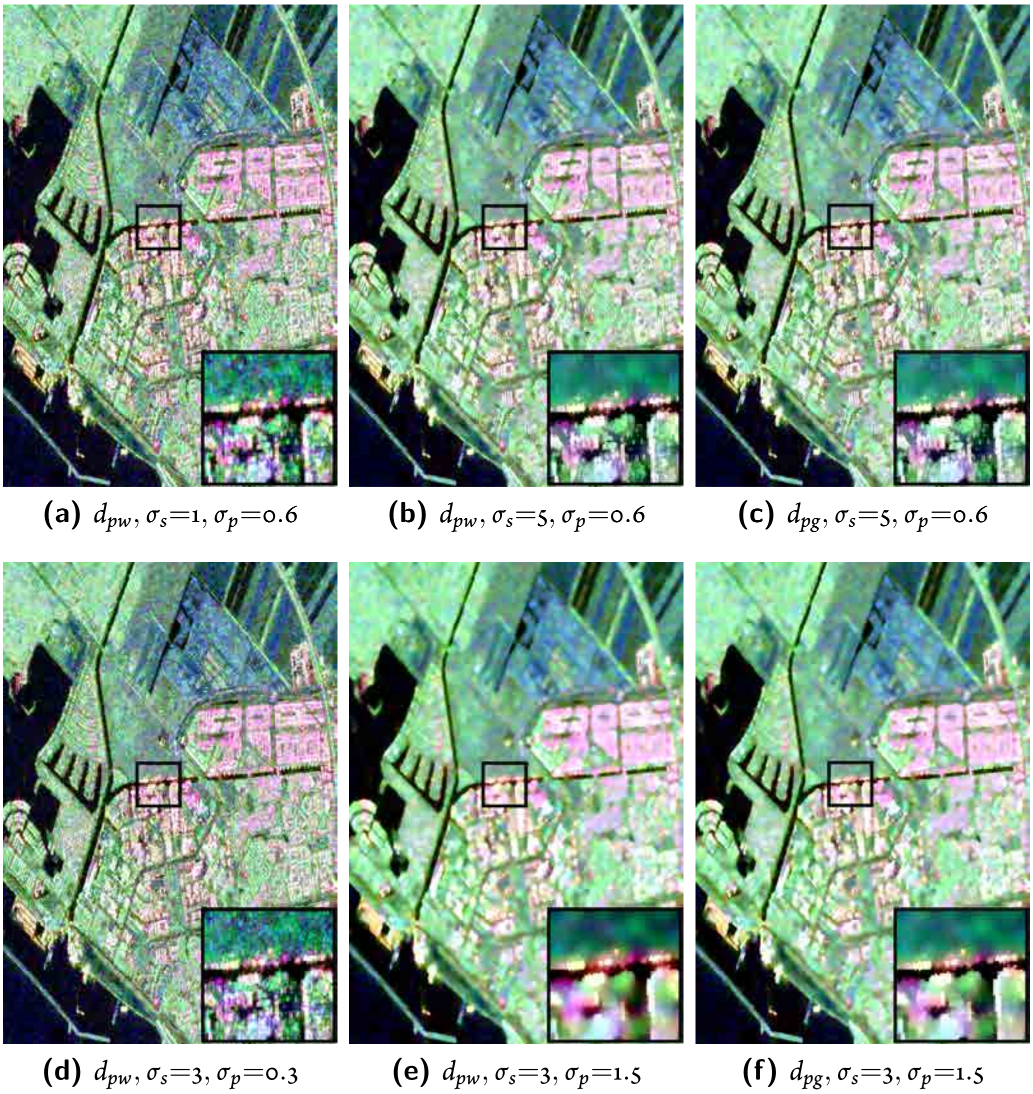

(a) d_{pw}, σ_s=1, σ_p=0.6 **(b)** d_{pw}, σ_s=5, σ_p=0.6 **(c)** d_{pg}, σ_s=5, σ_p=0.6

(d) d_{pw}, σ_s=3, σ_p=0.3 **(e)** d_{pw}, σ_s=3, σ_p=1.5 **(f)** d_{pg}, σ_s=3, σ_p=1.5

Figure 6.7: Pauli RGB detail image of the filtered results for different σ_s and σ_p with 5 weight refinement iterations and 11x11 local window V ($|S_{hh} + S_{vv}|$, $|S_{hv} + S_{vh}|$, $|S_{hh} - S_{vv}|$).

analysis, when employing it instead of the classical 3 by 3 multilook filtering, the spatial resolution loss of the multilook may be avoided.

Nevertheless, the goal of this matrix regularization step is not to reduce the speckle noise of the data but to obtain full-rank matrices in order to be able to apply dissimilarity measures that exploit the full polarimetric information under the Gaussian hypothesis. In this situation, then, the amount of filtering required is much smaller, just to regularize the sample covariance matrices.

Fig. 6.9 shows the BPT region homogeneity based pruning results employing a $\delta_p = -2dB$

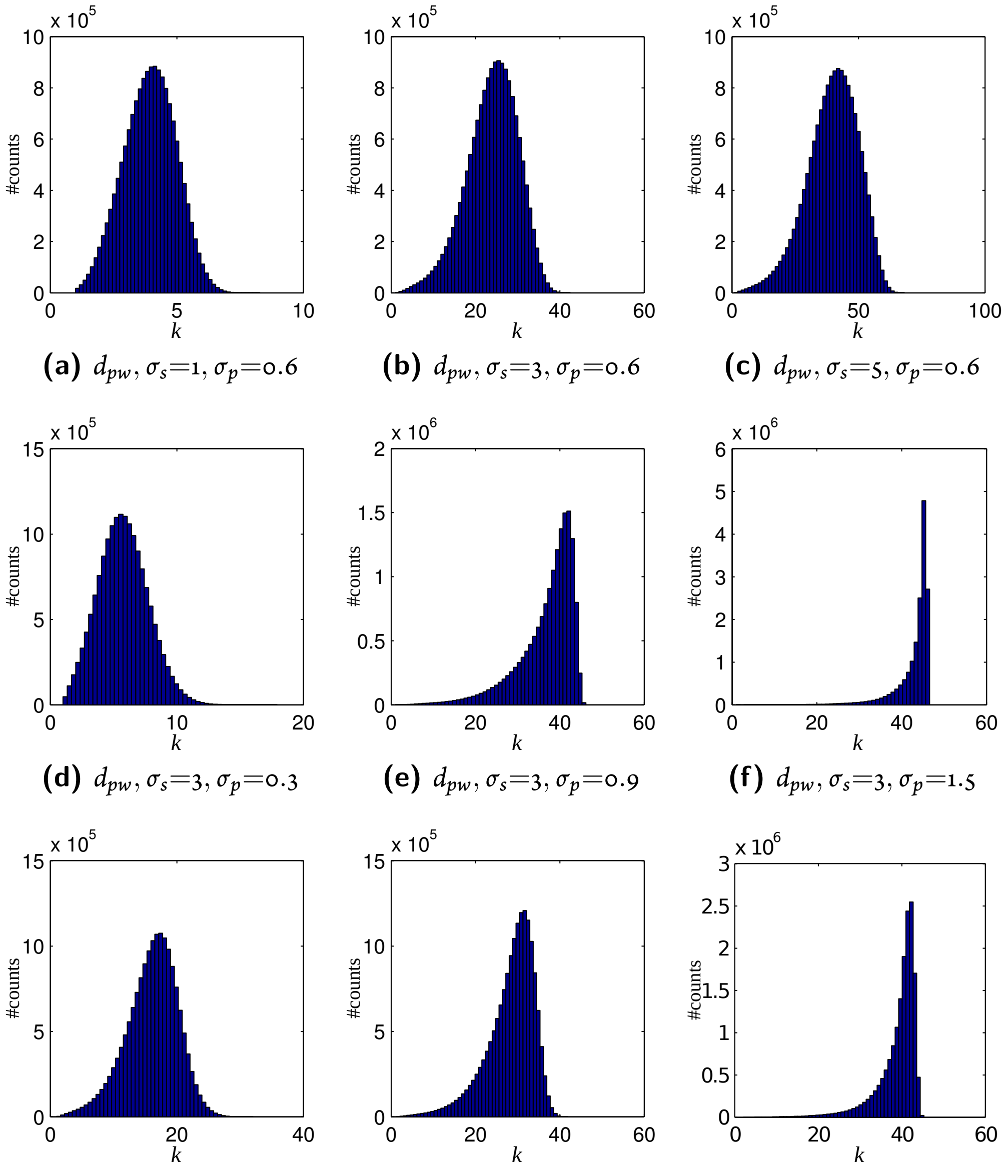

(a) $d_{pw}, \sigma_s{=}1, \sigma_p{=}0.6$ **(b)** $d_{pw}, \sigma_s{=}3, \sigma_p{=}0.6$ **(c)** $d_{pw}, \sigma_s{=}5, \sigma_p{=}0.6$

(d) $d_{pw}, \sigma_s{=}3, \sigma_p{=}0.3$ **(e)** $d_{pw}, \sigma_s{=}3, \sigma_p{=}0.9$ **(f)** $d_{pw}, \sigma_s{=}3, \sigma_p{=}1.5$

(g) $d_{pg}, \sigma_s{=}3, \sigma_p{=}0.6$ **(h)** $d_{pg}, \sigma_s{=}3, \sigma_p{=}0.9$ **(i)** $d_{pg}, \sigma_s{=}3, \sigma_p{=}1.5$

Figure 6.8: Histograms of the number of averaged pixels k for different σ_s and σ_p with 5 weight refinement iterations and 11x11 local window V

pruning threshold and the d_{sg} dissimilarity measure, as described in Section 4.3.2, of the first acquisition of the Flevoland dataset. Fig. 6.9a shows the BPT results obtained when the classical 3 by 3 multilook filtering is applied as a regularization step. On the other hand, Fig. 6.9b shows those results when the proposed DBF technique is applied for matrix regularization. As it may be seen, the amount of filtering required for this purpose is much smaller, as the local window V has been reduced to 5 by 5 pixels and also the corresponding filter parameters to $\sigma_s = 2, \sigma_p =$

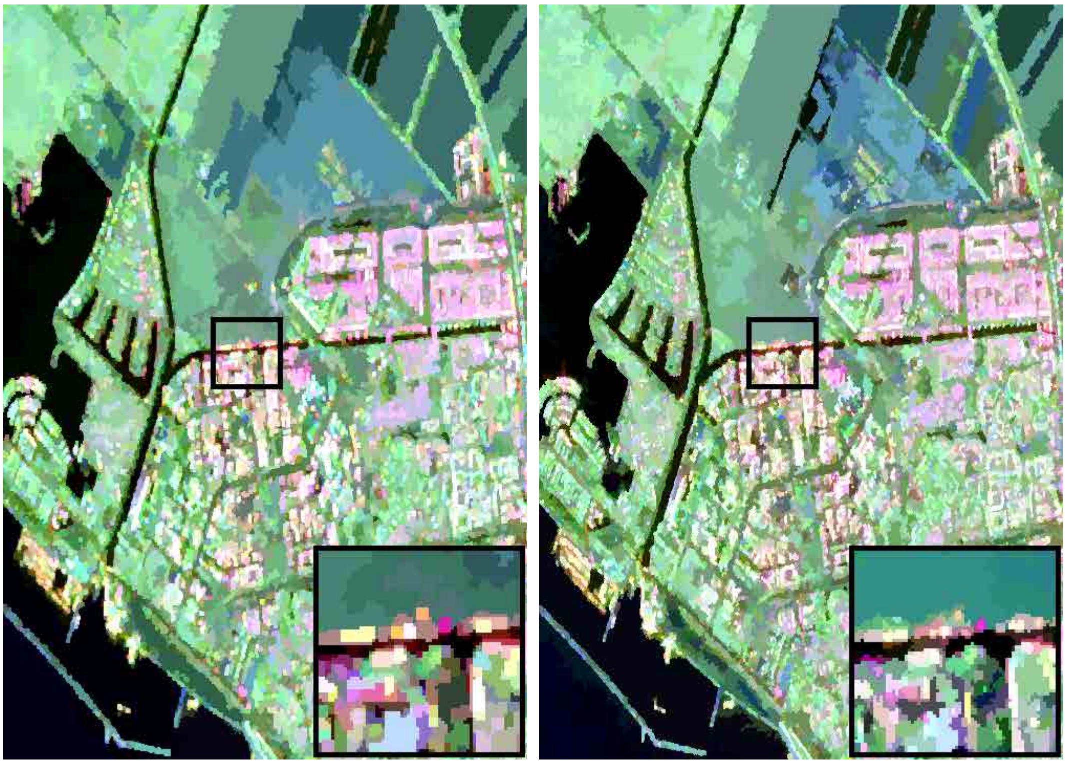

(a) BPT pruning $\delta_p = -2dB$ with 3x3 multilook

(b) BPT pruning $\delta_p = -2dB$ with 5x5 DBF, 3it, $d_{pw}, \sigma_s = 2, \sigma_p = 0.4$

Figure 6.9: Pauli RGB of the BPT region homogeneity based pruning results with $\delta_p = -2dB$ for 3x3 multilook and the proposed DBF method with 5x5 local window V, 3 iterations of the weight refinement scheme, and $d_{pw}, \sigma_s = 2, \sigma_p = 0.4$ parameters as initial filtering for matrix regularization ($|S_{hh} + S_{vv}|$, $|S_{hv} + S_{vh}|$, $|S_{hh} - S_{vv}|$).

0.4. Additionally, only 3 iterations of the weight refinement scheme have been performed, as they are enough to produce a reliable result. Comparing the results on Figs. 6.9a and 6.9b it may be clearly observed that the small resolution loss of the 3 by 3 multilook is also transfered to the BPT representation, specially on the small details in the urban area that appear enlarged in the zoom area. When the DBF is employed, the resolution preservation observed in details of the urban area gets improved. This effect may also be seen in thin structures like the breakwaters in the coastline. Moreover, due to the better contour preservation also achieved by the DBF technique, some field contours of the image are better retrieved by the BPT, as it may be seen in the top part of the image, for instance.

Another example of the benefits of employing the proposed DBF technique for matrix regularization may be observed in Fig. 6.10. In this case, the whole Barcelona time series dataset has been processed with the TE BPT representation. Fig. 6.10a shows the geo-coded results of the

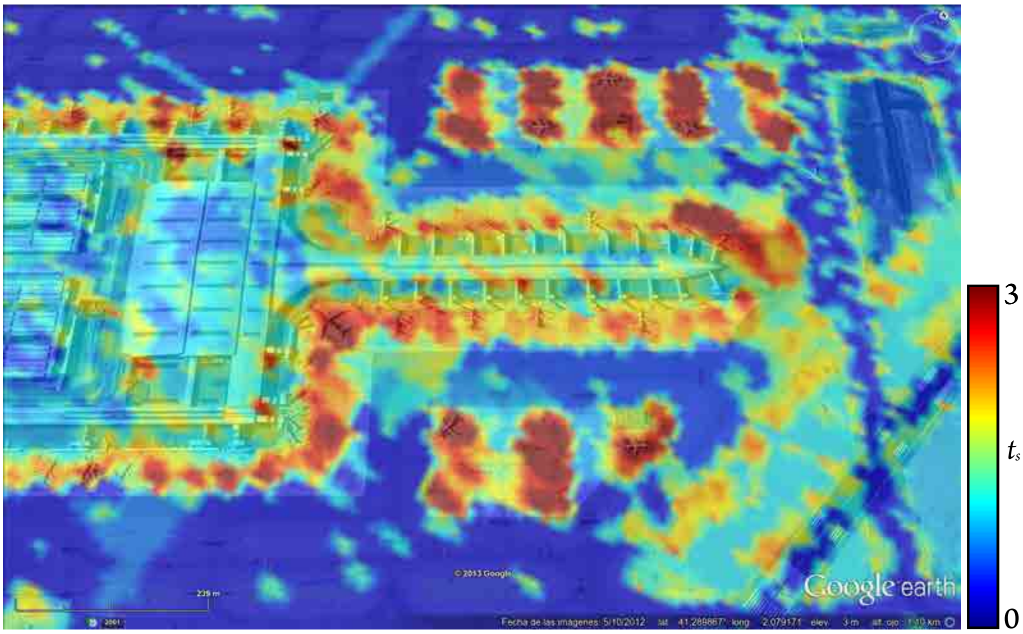

(a) Geo-coded t_s measure with 3x3 multilook regularization

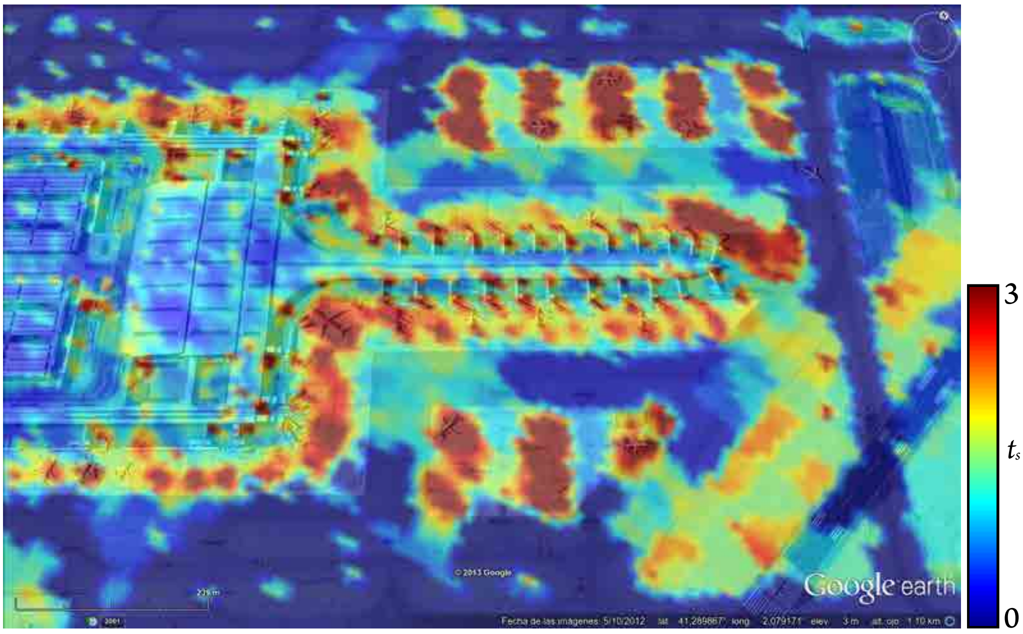

(b) Geo-coded t_s measure with 5x5 DBF, 3it, $d_{pw}, \sigma_s = 2, \sigma_p = 0.4$ regularization

Figure 6.10: Geo-coded temporal stability measure t_s over the Barcelona dataset employing the TE BPT for the 3x3 multilook and the proposed DBF method with 5x5 local window V, 3 iterations of the weight refinement scheme, and $d_{pw}, \sigma_s = 2, \sigma_p = 0.4$ parameters as initial filtering for matrix regularization.

temporal stability t_s measure, described in Section 5.4.2, over the Terminal-1 Barcelona airport area when employing the 3 by 3 multilook on each one of the 35 images as matrix regularization. On the other hand, Fig. 6.10b shows the same results when applying the proposed DBF technique over each image. The increase in spatial resolution on the t_s results when applying the DBF may be clearly observed, specially in the zone of the fingers, those details appear blurred in Fig. 6.10a but not in Fig. 6.10b, where a small red dot may be clearly seen for each finger. Moreover, since the heterogeneous sample mixture gets avoided due to a better preservation of the contours when employing the DBF for matrix regularization, some small or thin structures appear better represented in Fig. 6.10b. This effect is particularly evident on the runway in the right part of the image, which appear very noisy in Fig. 6.10a and much more clear in Fig. 6.10b. Note that since this runway presents a thin structure, the 3 by 3 multilook mixes its samples with those around it, resulting in a poorer performance for the BPT representation. This example, indeed, may serve as an example of the improvement achieved by applying the DBF technique as a pre-processing step for PolSAR time series datasets.

6.2 POLARIMETRIC CHANGE ANALYSIS

6.2.1 THE $\mathbf{B}^{-1}\mathbf{A}$ MATRIX

When analyzing the term depending on the sample covariance matrices in the different dissimilarity measures defined in Section 4.1.3, it may be observed that some of them are based in the matrix $\mathbf{Z}_B^{-1}\mathbf{Z}_A$. The revised Wishart measure d_{sw}, defined in (4.2), is based on the trace of this matrix $\mathrm{tr}(\mathbf{Z}_B^{-1}\mathbf{Z}_A)$, whereas the geodesic dissimilarity measure d_{sg} is based on the Frobenius norm of this matrix, as it is defined in (4.3) in terms of the expression $\| \log \left(\mathbf{Z}_B^{-1/2}\mathbf{Z}_A\mathbf{Z}_B^{-1/2} \right) \|_F$. Indeed, this expression is equivalent to $\| \log \left(\mathbf{Z}_B^{-1}\mathbf{Z}_A \right) \|_F$, since the eigenvalues of $\mathbf{Z}_B^{-1/2}\mathbf{Z}_A\mathbf{Z}_B^{-1/2}$ are the same than those of $\mathbf{Z}_B^{-1}\mathbf{Z}_A$.

In fact, this is not a coincidence, as the Wishart probability density function, defined in (2.55) is also based on the exponential of the trace of this matrix. Then, in the following sections, this matrix is studied from the point of view of its eigenvectors and eigenvalues, in order to obtain a physical interpretation of the information contained within.

6.2.2 GENERALIZED EIGENVALUES AND POLARIMETRIC CONTRAST

As mentioned in Section 2.2, one of the most important properties of wave polarimetry is that it allows to explore the target response at any other polarization state, through the polarization synthesis [24]. Then, one of the first approaches proposed to explore the difference between two targets characterized by **A** and **B** covariance matrices was through the *polarimetric constrast*, defined as the ratio between the radar power backscattered by the two targets at a particular polarization state, denoted by **w** [70]

$$P_c(\mathbf{A}, \mathbf{B}, \mathbf{w}) = \frac{\mathbf{w}^H \mathbf{A} \mathbf{w}}{\mathbf{w}^H \mathbf{B} \mathbf{w}}. \tag{6.14}$$

Note that the polarimetric contrast P_c is the ratio between two power measures and, consequently it is real and positive valued. For each polarization state, the polarimetric contrast indicates an increment of power in **A** respect to **B** with a value $P_c > 1$, whereas in the case of a decrease in power $P_c < 1$ is obtained. If there is no change in the retrieved power a value equal to 1 is retrieved. This measure may be optimized in order to obtain the *optimum* polarization state $\mathbf{w}_{opt}$ that maximizes the contrast between the two targets [70]. The mathematical solution to this optimization process may be found by the Lagrange multipliers method, that corresponds to the generalized eigenvalues for **A** and **B** covariance matrices [70][33]

$$\mathbf{A}\mathbf{w} = \lambda \mathbf{B}\mathbf{w} \tag{6.15}$$

which may be obtained by solving the following equation

$$\det(\mathbf{A} - \lambda \mathbf{B}) = 0. \tag{6.16}$$

Note that, if the matrix **B** is invertible, then (6.15) may be pre-multiplied by $\mathbf{B}^{-1}$ in order to obtain [20]

$$\mathbf{B}^{-1}\mathbf{A}\mathbf{w} = \lambda \mathbf{w} \tag{6.17}$$

corresponding to the classical eigenvalue equation of the $\mathbf{B}^{-1}\mathbf{A}$ matrix, that may be obtained solving

$$\det(\mathbf{B}^{-1}\mathbf{A} - \lambda \mathbf{I}) = 0. \tag{6.18}$$

Then, the eigenvalues λ_i of the $\mathbf{B}^{-1}\mathbf{A}$ matrix define the polarimetric contrast P_c values that may be obtained. If the eigenvalues are assumed to be sorted $\lambda_1 \geq \lambda_2 \geq \ldots \geq \lambda_p \geq 0$ then the maximum contrast corresponds to λ_1 whereas the minimum contrast corresponds to λ_p [70][33]. Moreover, the polarization states that produce the mentioned polarimetric contrast values denoted by the eigenvalue λ_i corresponds to its associated eigenvector $\mathbf{v}_i$. In the case of the 3 by 3 covariance matrices, λ_1 corresponds to the maximum polarimetric contrast, λ_3 to the minimum contrast and λ_2 corresponds to a contrast in between these two. It is worth mentioning that, since the $\mathbf{B}^{-1}\mathbf{A}$ matrix is not necessarily hermitian, then the corresponding eigenvectors $\mathbf{v}_i$ are not orthogonal to each other.

6.2.3 PHYSICAL INTERPRETATION OF POLSAR DISSIMILARITY MEASURES

According to the mathematic analysis performed in Section 6.2.2, the eigenvalues of the $\mathbf{B}^{-1}\mathbf{A}$ matrix may be interpreted in terms of the polarimetric contrast. Consequently, the dissimilarity measures that are based on these matrices may also be interpreted in these terms.

The revised Wishart dissimilarity measure d_{sw}, is defined in the form $\mathrm{tr}(\mathbf{Z}_B^{-1}\mathbf{Z}_A) + \mathrm{tr}(\mathbf{Z}_A^{-1}\mathbf{Z}_B)$. Accordingly, this measure may also be expressed as

$$\mathrm{tr}(\mathbf{Z}_B^{-1}\mathbf{Z}_A) + \mathrm{tr}(\mathbf{Z}_A^{-1}\mathbf{Z}_B) = \sum_{i=1}^{p} \lambda_i + \lambda_i^{-1} \tag{6.19}$$

where $\mathbf{Z}_A$ and $\mathbf{Z}_B$ are assumed to be p by p covariance matrices and λ_i represent the generalized eigenvalues of $\mathbf{Z}_A$ and $\mathbf{Z}_B$ matrices. Note that the eigenvalues of $\mathbf{Z}_A^{-1}\mathbf{Z}_B$ are the inverse of the eigenvalues from $\mathbf{Z}_B^{-1}\mathbf{Z}_A$.

Then, the revised Wishart dissimilarity measure may also be interpreted as the sum of the polarimetric contrasts and their inverse. In fact, as expressed before, a power reduction in a particular polarization state will be represented by a polarimetric contrast value $0 < P_c < 1$, having less importance on $\mathrm{tr}(\mathbf{Z}_B^{-1}\mathbf{Z}_A)$ than a power increment, represented by $P_c > 1$. To solve this issue, the sum is performed over the polarimetric contrast and its inverse in (6.19), in order to give equal importance to changes due to power increments or decrements.

On the other hand, the term corresponding to the covariance matrices of the geodesic dissimilarity measure d_{sg}, as mentioned before, may be expressed as $\| \log \left(\mathbf{Z}_B^{-1}\mathbf{Z}_A\right) \|_F$. Then, this measure may be interpreted in terms of the polarimetric contrast interpretation of the $\mathbf{Z}_B^{-1}\mathbf{Z}_A$ matrix as

$$\| \log \left(\mathbf{Z}_B^{-1/2}\mathbf{Z}_A\mathbf{Z}_B^{-1/2}\right) \|_F = \| \log \left(\mathbf{Z}_B^{-1}\mathbf{Z}_A\right) \|_F = \sqrt{\sum_{i=1}^{p} \ln^2 \lambda_i}. \tag{6.20}$$

As it may be observed in (6.20), in the geodesic dissimilarity measure the logarithm of the polarimetric contrast is taken. Then, an increment or decrement of power by the same factor would naturally have the same contribution to the measure, represented by the same positive or negative logarithm value, respectively. Afterwards, the euclidean norm of all the $\ln \lambda_i$ values is computed, giving equal weight to positive or negative values.

6.2.4 CHANGE ANALYSIS RESULTS

The previous analysis of the $\mathbf{B}^{-1}\mathbf{A}$ matrices in terms of the polarimetric contrast motivates the employment of these matrices to characterize the changes that are produced over the different acquisitions in PolSAR time series. In the following an example is shown over two images of the Flevoland dataset, presented in Section 5.3, corresponding to the acquisitions from April 14th, 2009 and June 25th, 2009, respectively. The two original Pauli images of these two acquisitions may be seen in Fig. 5.3, in page 129.

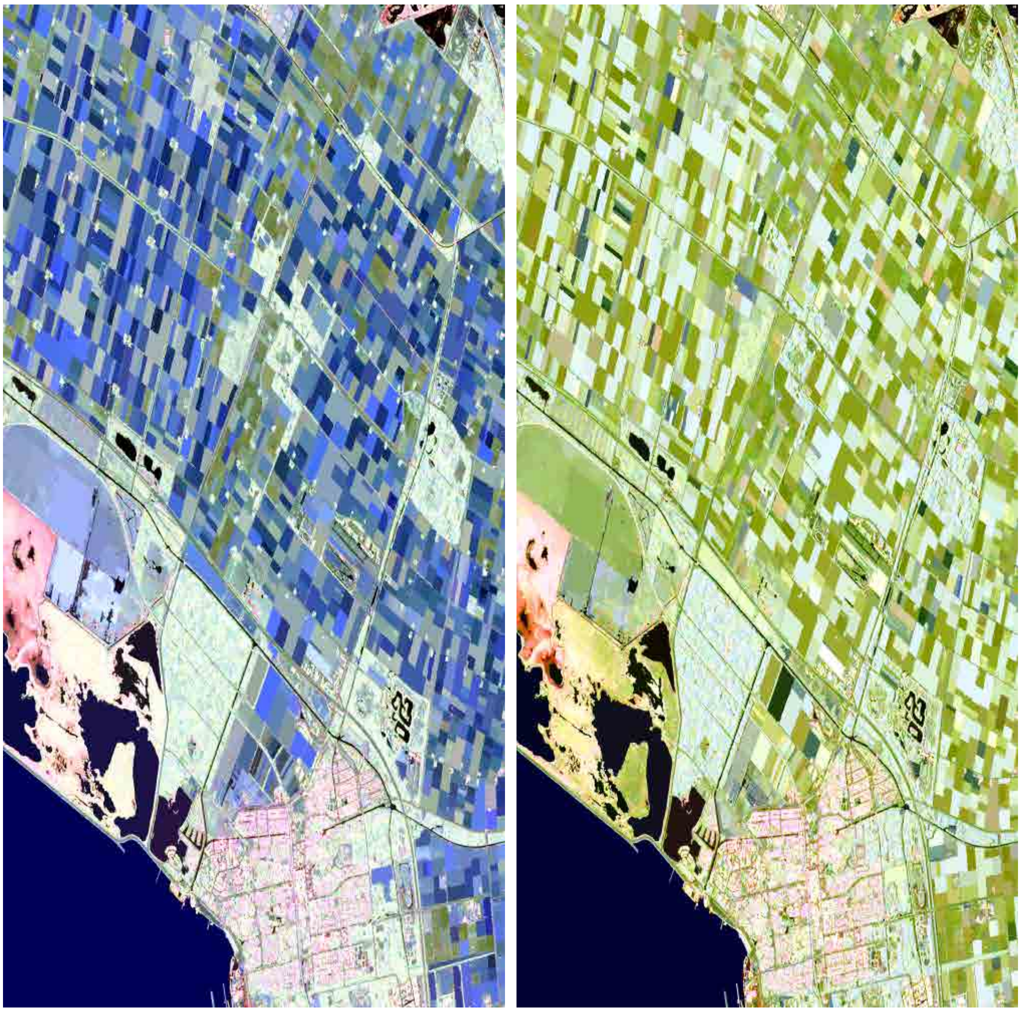
(a) April 14th, 2009 filtered **(b)** June 25th, 2009 filtered

Figure 6.11: Pauli RGB images from the TE BPT results with $\delta_p = -3dB$ pruning threshold of two Flevoland acquisitions corresponding to April 14th, 2009 and June 25th, 2009 ($|S_{hh}+S_{vv}|$, $|S_{hv}+S_{vh}|$, $|S_{hh}-S_{vv}|$).

The entire Flevoland dataset has been processed with the TE BPT representation, as described in Section 5.3, and the Pauli representation of the results obtained when employing a pruning threshold of $\delta_p = -3dB$ is shown in Figs. 6.11a and 6.11b, for the same acquisitions shown in Fig. 5.3, corresponding to April 14th, 2009 and June 25th, 2009, respectively. As it may be seen, there are significant changes in terms of the observed polarimetric response among the two acquisitions. On April, as shown in Fig. 6.11a, most of the agricultural field plants are not grown, resulting into a predominant surface scattering, appearing in blue color. On the other hand, in the acquisition from June, in Fig. 6.11b, most of these fields are grown, resulting into a predominant volume scattering from the plants, represented in green color in the Pauli RGB composition.

With these results from the BPT based approach, having almost a region per agricultural field, the speckle noise reduction achieved over them is considerable, resulting into a reliable estimation of the polarimetric response of the field. Then, the previous analysis of the polarimetric change based on the estimated sample covariance matrices of the two acquisitions $\mathbf{Z}_A^{-1}\mathbf{Z}_B$ may be employed to interpret the differences among these two acquisitions.

Fig. 6.12 shows the histograms of each one of the generalized eigenvalues λ_i between the two acquisitions depicted in Fig. 6.11. The horizontal axis represents the value of each eigenvalue in expressed in dB, according to $10 \log_{10}(\lambda_i)$. As it may be observed, most of the λ_1 values, shown in Fig. 6.12a, are greater than 0, as they correspond to the maximum polarimetric contrast, which represents an increase of the retrieved power in their corresponding polarization state. On the other hand, most of the values of λ_3, in Fig. 6.12c, are below 0, which implies the opposite effect. The peak of the second generalized eigenvector λ_2, represented in Fig. 6.12b, is located around 0, indicating no change in terms of the polarimetric contrast. However, most of the λ_2 values are located over the positive values.

In order to see the distribution of the generalized eigenvalues among the scene, Fig. 6.13 shows the generalized eigenvalues corresponding to the change between these two acquisitions. As in Fig. 6.12, the λ_i values are represented in dB, as depicted in the color bar. The 0 dB, corresponding to no change, is represented in green, the reddish colors represent an increase whereas the blueish values represent a decrease in the retrieved power. As observed in Fig. 6.12, it may be seen that on λ_1 most of the values are positive whereas on λ_3 most are negative. However, some positive values may also be observed in λ_3 over some agricultural fields, which implies that the retrieved power has increased for all the polarization states. On λ_2 some red areas may be observed in the agricultural fields, whereas most of the other areas appear in green, corresponding to a polarimetric contrast equal to 1, indicating no change.

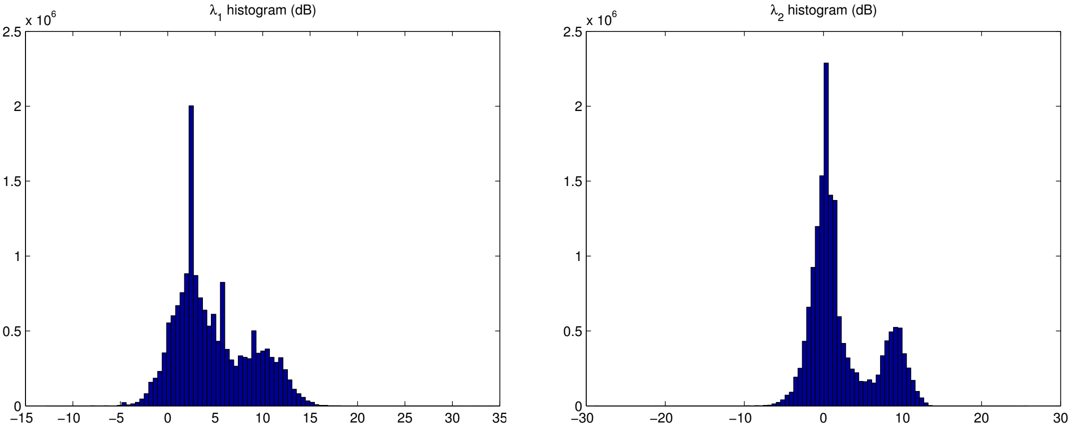

(a) λ_1 (b) λ_2

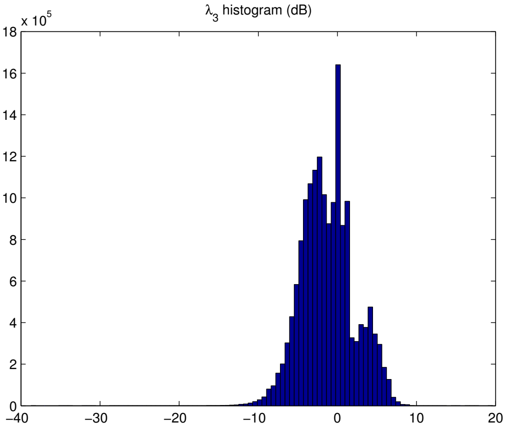

(c) λ_3

Figure 6.12: Histograms of the λ_i generalized eigenvalues among the two acquisitions shown in Fig. 6.11 expressed in dB.

Fig. 6.14 depicts the obtained generalized eigenvectors in the Pauli RGB color composition associated with the eigenvalues represented in Fig. 6.13. Then, Fig. 6.14a represents the Pauli of the polarization state that produces the maximum contrast whereas Fig. 6.14c correspond to the polarization state achieving the minimum polarimetric contrast. As it may be observed, the predominant component of the first eigenvectors $\mathbf{v}_1$ is the volume scattering, appearing in green. On the $\mathbf{v}_2$ eigenvector, representing also an increase in the retrieved power, more reddish colors are seen, corresponding to double bounce. On the other hand, the third eigenvector $\mathbf{v}_3$, is clearly blue over the agricultural fields. Accordingly, it may be deduced that over the agricultural fields the volume and double bounce scattering processes have increased, mostly corresponding to the first and second eigenvalues, whereas the smaller contrast is obtained for the surface scattering,

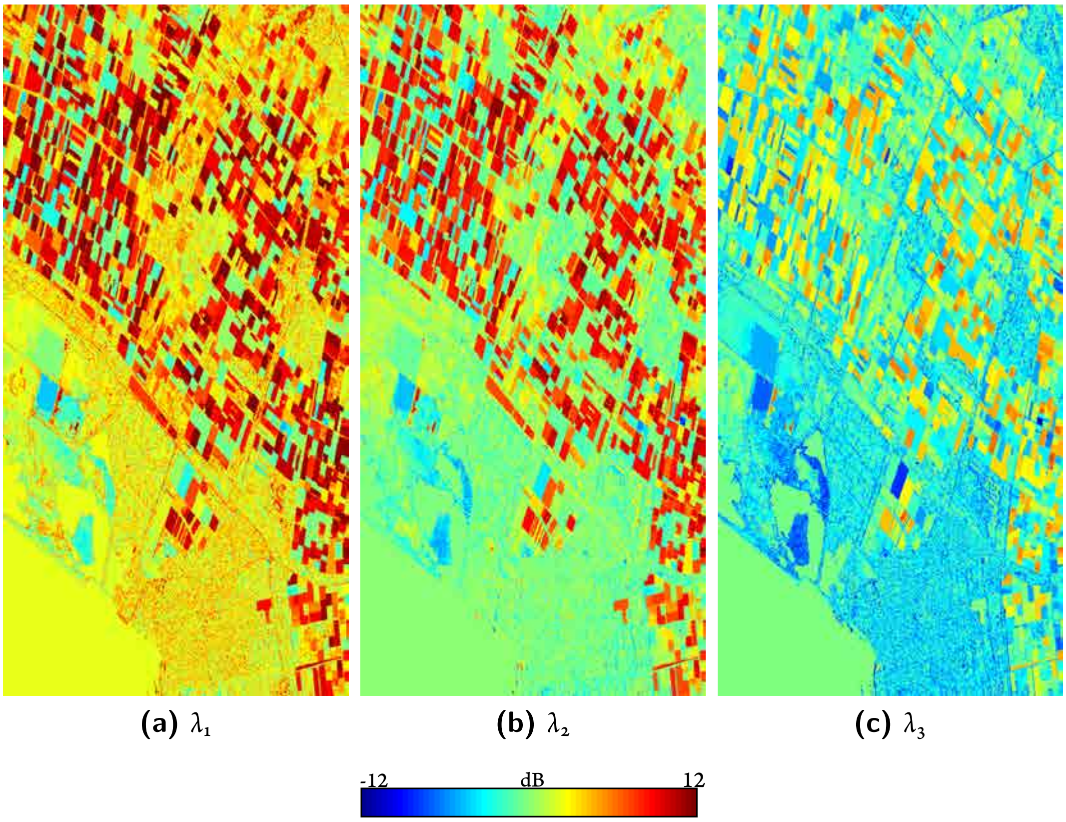
(a) λ_1 (b) λ_2 (c) λ_3

Figure 6.13: Distribution of the different λ_i generalized eigenvalues among the two acquisitions shown in Fig. 6.11. Results are shown in dB scale.

represented by the third eigenvector. This conclusion in consistent with the physical changes described before, corresponding to the growing process of the plants in the agricultural fields.

6.3 REGION SIMILARITY AND HOMOGENEITY

In Section 4.3.2 the region homogeneity based pruning has been defined. This pruning process is defined in terms of a region homogeneity measure which may be interpreted as the average error that is committed when representing all the pixels of the region by its region model. In this section, a more generic definition of this measure is proposed from a mathematical point of view. Then, the limitation of the previously defined homogeneity measure are identified and some improvements are proposed to solve them.

In the more general case, a region model space is supposed, denoted by S, and a metric d is assumed over this space

$$d : S \times S \rightarrow \mathbb{R}. \tag{6.21}$$

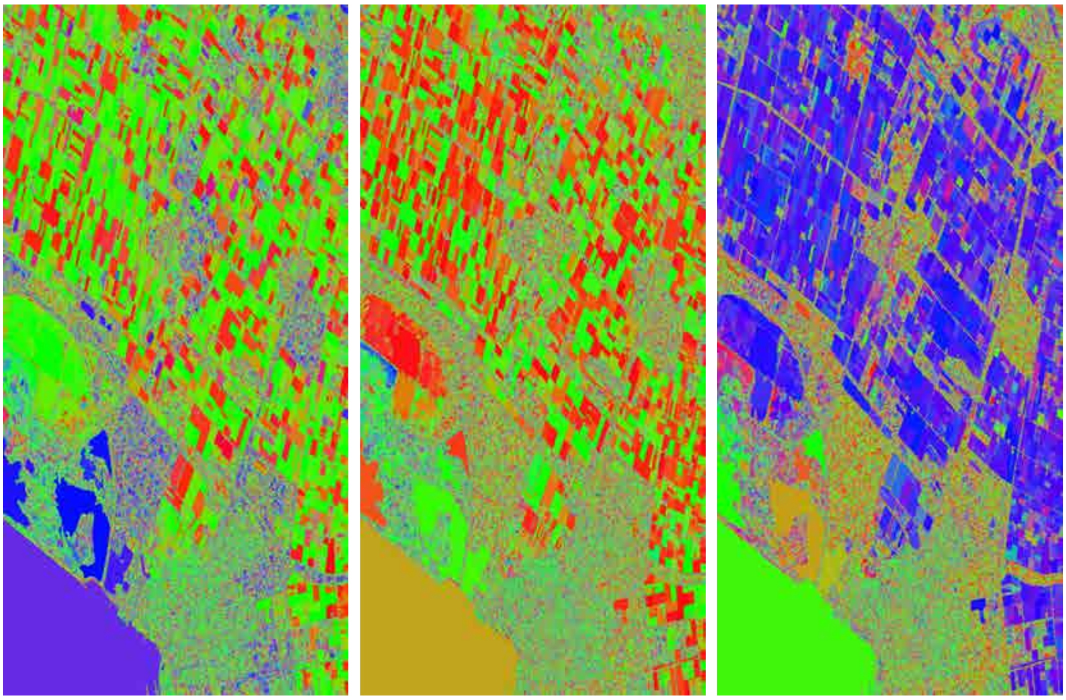

(a) Pauli RGB $\mathbf{v}_1$ **(b)** Pauli RGB $\mathbf{v}_2$ **(c)** Pauli RGB $\mathbf{v}_3$

Figure 6.14: Pauli RGB representation of the different $\mathbf{v}_i$ generalized eigenvectors among the two acquisitions shown in Fig. 6.11 ($|S_{hh}+S_{vv}|$, $|S_{hv}+S_{vh}|$, $|S_{hh}-S_{vv}|$).

This measure is, in fact, the point on which all the knowledge of the S space may be included, while focusing on the particular properties of the region model space on that we are interested on.

Then, a set C of N points in this region model space is assumed $C = \{\mathbf{Z}_1, \mathbf{Z}_2, \ldots, \mathbf{Z}_N\}$, where $\mathbf{Z}_1, \mathbf{Z}_2, \ldots, \mathbf{Z}_N \in S$. Note that the mathematical concept of a set of samples may be directly related with the region concept within the BPT structure or, generally, in any region-based approach. Accordingly a set homogeneity $H(C)$ measure may be defined in terms of the corresponding d metric. First, it is assumed that $\mathbf{Z}_C$ is the center of mass of C, defined as, for instance,

$$\mathbf{Z}_C = \frac{1}{N}\sum_{i=1}^{N}\mathbf{Z}_i. \tag{6.22}$$

Then, the set homogeneity $H(C)$ may be defined in terms of the metric d as

$$H(C) = \frac{1}{N}\sum_{i=1}^{N} d(\mathbf{Z}_i, \mathbf{Z}_C). \tag{6.23}$$

Fig. 6.15 represents the set C and the computation of $H(C)$ in terms of the metric d. Indeed, $H(C)$ may be interpreted as the average distance d from all the C samples to its center of mass $\mathbf{Z}_C$.

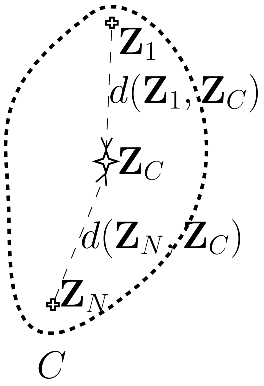

Figure 6.15: Set homogeneity measure definition. The set C and its center of mass $\mathbf{Z}_C$ are represented.

For the region homogeneity based BPT pruning, the relative error homogeneity Φ, has been defined in (4.14). With the aforementioned notation it may be expressed as

$$\Phi(C) = \frac{1}{N} \sum_{i=1}^{N} \frac{||\mathbf{Z}_i - \mathbf{Z}_C||_F^2}{||\mathbf{Z}_C||_F^2}, \tag{6.24}$$

that corresponds to the relative MSE of the region. According to the previous generic homogeneity definition, in (6.23), it corresponds to the $H(C)$ measure that is obtained when employing the relative euclidean distance as the d_Φ metric

$$d_\Phi(\mathbf{A}, \mathbf{B}) = \frac{||\mathbf{A} - \mathbf{B}||_F^2}{||\mathbf{B}||_F^2}. \tag{6.25}$$

The distance measure d employed for the region homogeneity measure pays an important role in the obtained results, presumably as important as the role it plays in the BPT construction process. In fact, the (6.25) measure is not adapted to the complex covariance matrix space, which may result into a bad estimation of the region homogeneity. As opposite, an homogeneity measure could be defined employing a distance measure adapted to the complex covariance matrix space as, for instance, the revised Wishart similarity measure [68]

$$d_{rw}(\mathbf{A}, \mathbf{B}) = \mathrm{tr}(\mathbf{A}^{-1}\mathbf{B}) + \mathrm{tr}(\mathbf{B}^{-1}\mathbf{A}) - 2p \tag{6.26}$$

where p is the size of the p by p matrices $\mathbf{A}$ and $\mathbf{B}$. If the d_{rw} measure is employed to define an homogeneity measure, as expressed in (6.23), then the homogeneity measure $H_{rw}(C)$ is obtained as

$$H_{rw}(C) = \frac{1}{N}\sum_{i=1}^{N} \mathrm{tr}(\mathbf{Z}_i^{-1}\mathbf{Z}_C) + \mathrm{tr}(\mathbf{Z}_C^{-1}\mathbf{Z}_i) - 2p \tag{6.27}$$

In order to analyze the effects of the distance measure employed on the homogeneity measure, an evaluation process is proposed. For this experiment, two different covariance matrices $\mathbf{C}_1$ and $\mathbf{C}_2$ are defined

$$\mathbf{C}_1 = \begin{bmatrix} 1 & 0 & 0.1 \\ 0 & 0.1 & 0 \\ 0.1 & 0 & 1 \end{bmatrix}, \mathbf{C}_2 = \begin{bmatrix} 1 & 0 & 0.9 \\ 0 & 0.1 & 0 \\ 0.9 & 0 & 1 \end{bmatrix}. \tag{6.28}$$

These matrices are employed to generate two reference sets, A and B, having each one 5000 samples following a Wishart distribution with a particular covariance matrix and a number of looks equal to 9. Then, a new set C is computed taking 5000 samples with different proportion from A and B and its homogeneity is computed. Fig. 6.16 shows the evolution of the homogeneity measures $\Phi(C)$ and $H_{rw}(C)$, depending on the amount of samples, in %, taken from the B set. The rest of the required samples to complete the set are taken from the A set.

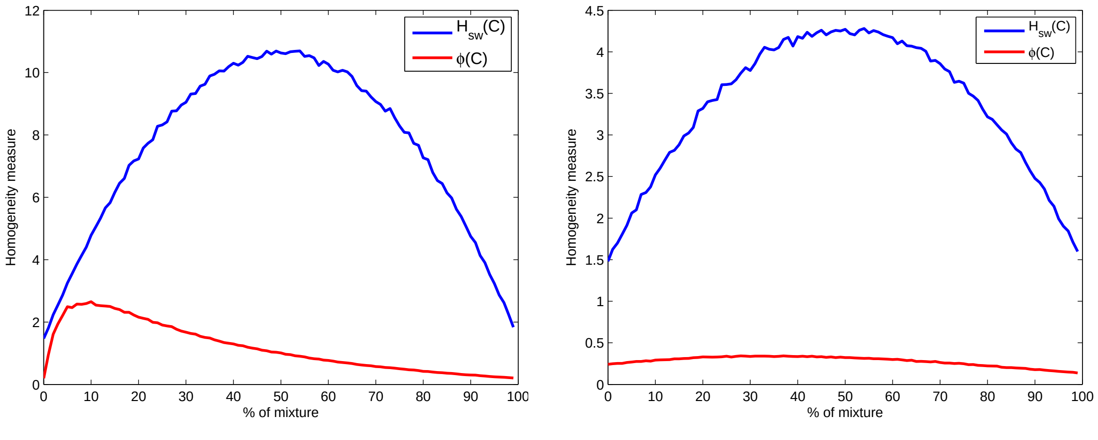

(a) $\mathbf{Z}_A = \mathbf{C}_1, \mathbf{Z}_B = 10\mathbf{C}_1$ **(b)** $\mathbf{Z}_A = \mathbf{C}_1, \mathbf{Z}_B = \mathbf{C}_2$

Figure 6.16: Evolution of the homogeneity measure versus % of mixture; 0% and 100% of mixture correspond to selecting all the samples from A and B, respectively.

Fig. 6.16a shows the evolution of the $\Phi(C)$ and $H_{rw}(C)$ homogeneity measures, defined in (6.24) and (6.27), when the samples of A and B are following a Wishart distribution characterized by the $\mathbf{C}_1$ and $10\mathbf{C}_1$ matrices, respectively. As it may be seen, the $\Phi(C)$ measure do not characterize properly the homogeneity of the C set, as it should present a maximum when 50% of samples are taken from each set. On the contrary, the $H_{rw}(C)$ measure, based on the Wishart metric d_{rw}, obtains a better plot as it presents a behavior more analogous to the amount of mixture. Moreover, since the $\Phi(C)$ measure is not adapted to the covariance matrix space, it may have low significance when there are changes only on the off-diagonal elements, as it is dominated by the power. This effect is shown on Fig. 6.16b, having A and B characterized by $\mathbf{C}_1$ and $\mathbf{C}_2$ matrices, respectively, where the $\Phi(C)$ measure obtains an almost flat curve, whereas the Wishart homogeneity $H_{rw}(C)$ obtains a much better characterization of the C set homogeneity.

In a split and merge scenario, as it is the case in the BPT construction algorithm, where different sets are frequently merged, an efficient computation of the homogeneity measure H is essential to obtain a reasonable computing time. Specifically, when the set C is constructed as the merging of two disjoint sets A and B, that is $C = A \cup B$, $H(C)$ should be computed in constant time in terms of $\mathbf{Z}_A$, $\mathbf{Z}_B$, $H(A)$ and $H(B)$. As mentioned in Section 3.2.3, in order to maintain the BPT construction algorithm complexity at $O(nlogn)$, the region merging merging process, including the region model and homogeneity calculation, should be computed at constant time.

For an efficient computation of the Φ measure defined in (6.24) the Total Sum of Squares (TSS) [128] is employed in the BPT construction process. For a given set C, the $TSS(C)$ is defined as the sum of squared euclidean distances from all samples to its center of mass. In the case of the sample covariance matrices employed as a region model, this corresponds to

$$TSS(C) = \sum_{i=1}^{N} \|\mathbf{Z}_i - \mathbf{Z}_C\|_F^2. \tag{6.29}$$

Having this measure, when a new set C is generated by merging A and B, expressed as $C = A \cup B$, then the corresponding measures $\Phi(C)$ and $TSS(C)$ of the new set may be computed in terms of $TSS(A)$ and $TSS(B)$ as [128]

$$TSS(C) = TSS(A) + TSS(B) + \|\mathbf{Z}_A - \mathbf{Z}_B\|_F^2 \frac{N_A N_B}{N_A + N_B} \tag{6.30}$$

where N_A and N_B are the number of samples of the sets A and B, respectively. Note that (6.30) does not contain any summation depending on the number of samples and, consequently, it may be computed in constant time as long as the TSS values for each set are stored. With the

$TSS(C)$ value, the homogeneity measure $\Phi(C)$ may be directly computed in constant time as

$$\Phi(C) = \frac{1}{N_C\|\mathbf{Z}_C\|_F^2} TSS(C) \tag{6.31}$$

where $N_C = N_A + N_B$ correspond to the number of samples of the C set.

6.3.1 THE PROBLEM OF THE CENTROID REPRESENTATION

When having a set of pixels A, they are usually characterized by the average sample covariance $\mathbf{Z}_C^A$, as mentioned before. When comparing the set A with another set of pixels B, their central values $\mathbf{Z}_C^A$ and $\mathbf{Z}_C^B$ are compared through the metric measure d, for instance, the revised Wishart dissimilarity d_{rw} defined in (6.26). This cluster center comparison is depicted in Fig. 6.17, where the enveloping of the set of pixels has been marked with a dashed line and its central value with a cross.

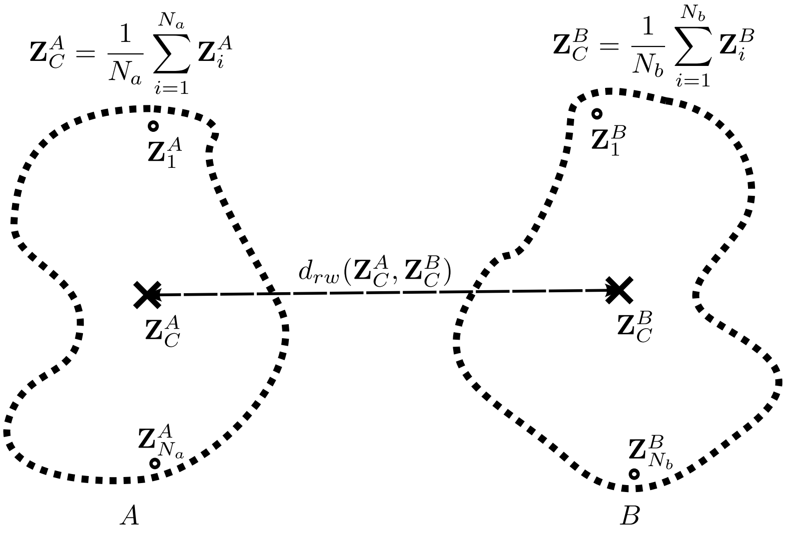

Figure 6.17: Representation of the similarity computation between cluster centers employing the centroid model.

In some situations, the central value of a cluster may not be a good representative of the set of pixels, specially if it is composed by not homogeneous samples. This effect has been stated in Section 4.1.2, where the limitations of the sample covariance matrix as a region model were discussed. In this situation, the central value may even fall outside the cloud of points it represent, as illustrated in Fig. 6.18. As it may be seen, a set of pixels composed by $A \cup B$ has been compared with another D employing the central value, as stated before. In this case, the obtained mean value $\mathbf{Z}_C^{A\cup B}$ falls outside the two sets A and B which it represents. Consequently, the obtained similarity measure $d_{rw}(\mathbf{Z}_C^{A \cup B}, \mathbf{Z}_C^D)$ becomes completely unrealistic, as it not represents properly the similarity between the sets $A \cup B$ and D.

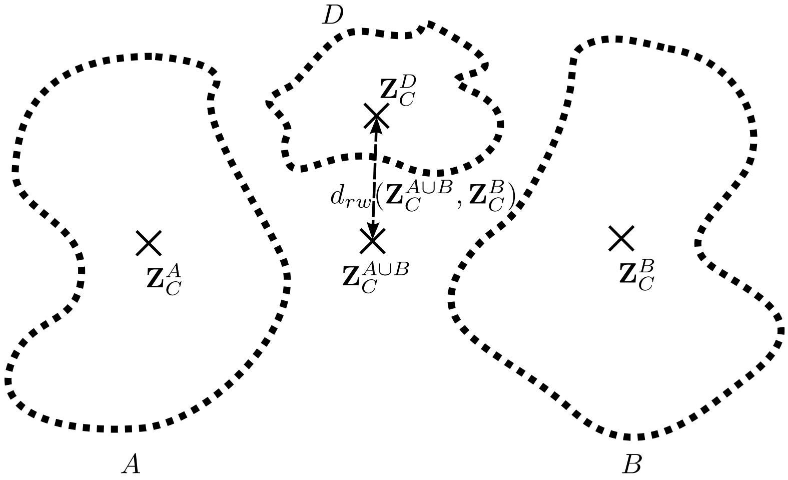

Figure 6.18: Similarity comparison between cluster centers may obtain unrealistic results over inhomogeneous sets.

The issue of the centroid representation previously mentioned, is not a problem of the d_{rw} measure itself, but it is a limitation of the employed model, which is not able to represent such a situation. More complex models may be employed as a descriptors, taking into account a mixture of distributions or the data texture, for instance. However, more complicated models require a larger number of parameters and, consequently, they are more difficult to determine, requiring a larger number of samples for a reliable estimation.

6.3.2 AVERAGE LINKAGE DISSIMILARITY MEASURES

In order to solve the previous problem, instead of defining a more complex model, another possibility is to avoid the need for a parametric model and the necessity of cluster similarity computation within this model space. Having defined the d_{rw} similarity between points, the *average linkage* between all the cluster values, also known as Unweighted Pair Group Method with Arithmetic mean (UPGMA) [113], may be used, in order to avoid the employment of a representative value. This similarity measure, denoted as d_{al} may be defined as

$$d_{al}(A, B) = \frac{1}{N_a N_b} \sum_{i=1}^{N_a} \sum_{j=1}^{N_b} d_{rw}(\mathbf{Z}_i^A, \mathbf{Z}_j^B) \tag{6.32}$$

As it may be seen, it is a similar concept to the generic homogeneity measure (6.23) but, in this case, the distance is evaluated between each possible pair of values of the two sets compared. This idea has been represented in Fig. 6.19.

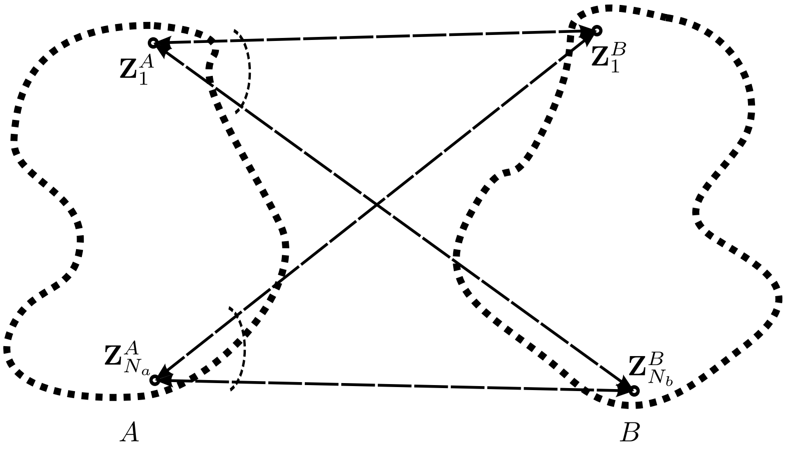

Figure 6.19: Similarity comparison between two sets employing an average linkage Wishart measure.

If this average linkage measure is employed to analyze the similarity between not homogeneous sets, as in the scenario depicted in Fig. 6.18, a more appropriate measure may be obtained. This situation has been represented in Fig. 6.20

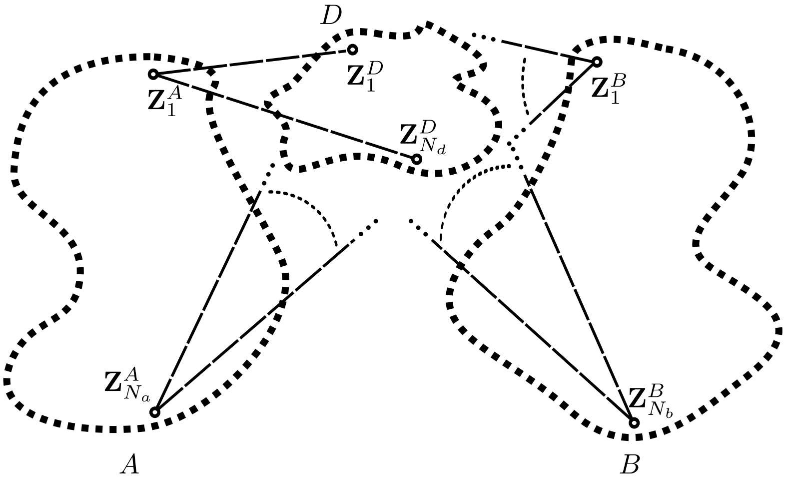

Figure 6.20: Similarity comparison between the inhomogeneous sets $A \cup B$ and D employing the average linkage measure.

The previous average linkage Wishart similarity measure between two sets may take into account data inhomogeneity and also the texture of the two different pixel sets. Moreover, it is not assuming any shape over the points sets, being able to compute the similarity between arbitrary collections of points. The only assumption performed is embedded within the metric d employed for the computation, which corresponds to the geometry of the space. However, the computation of d_{al} may be very resource consuming as it requires to compare all the possible pixel pairs through the d_{sw} measure, that is $N_a \cdot N_b$ comparisons, as it may be deduced from (6.32).

Nonetheless, in order to avoid this computational explosion, an extension to the centroid representation is proposed. Expanding the d_{rw} measure (6.26) into (6.32)

$$d_{al}(A,B) = \frac{1}{N_a N_b}\left(\sum_{i=1}^{N_a}\sum_{j=1}^{N_b}\operatorname{tr}(\mathbf{Z}_i^{A^{-1}}\mathbf{Z}_j^B) + \sum_{i=1}^{N_a}\sum_{j=1}^{N_b}\operatorname{tr}(\mathbf{Z}_j^{B^{-1}}\mathbf{Z}_i^A)\right) - 2p \tag{6.33}$$

the linear properties of the matrix trace may be applied to obtain

$$\begin{aligned} d_{al}(A,B) &= \frac{1}{N_a N_b}\left(\operatorname{tr}\left(\sum_{i=1}^{N_a}\sum_{j=1}^{N_b}\mathbf{Z}_i^{A^{-1}}\mathbf{Z}_j^B\right) + \operatorname{tr}\left(\sum_{i=1}^{N_a}\sum_{j=1}^{N_b}\mathbf{Z}_j^{B^{-1}}\mathbf{Z}_i^A\right)\right) - 2p \\ &= \frac{1}{N_a N_b}\left(\operatorname{tr}\left(\sum_{i=1}^{N_a}\mathbf{Z}_i^{A^{-1}}\sum_{j=1}^{N_b}\mathbf{Z}_j^B\right) + \operatorname{tr}\left(\sum_{j=1}^{N_b}\mathbf{Z}_j^{B^{-1}}\sum_{i=1}^{N_a}\mathbf{Z}_i^A\right)\right) - 2p. \end{aligned} \tag{6.34}$$

Note that, as stated before, the center of a set of pixels A may be computed as

$$\mathbf{Z}_C^A = \frac{1}{N_a}\sum_{i=1}^{N_a}\mathbf{Z}_i^A. \tag{6.35}$$

Similarly, the average of its inverses may be defined, which in the following will be referred to as $\mathbf{Y}_C^A$

$$\mathbf{Y}_C^A = \frac{1}{N_a}\sum_{i=1}^{N_a}\mathbf{Z}_i^{A^{-1}}. \tag{6.36}$$

With this notation, the average linkage Wishart similarity measure d_{al} defined in (6.34) may also be expressed in terms of these matrices

$$\begin{aligned}d_{al}(A,B) &= \frac{1}{N_a N_b}\left(\mathrm{tr}\left(N_a N_b \mathbf{Y}_C^A \mathbf{Z}_C^B\right) + \mathrm{tr}\left(N_a N_b \mathbf{Y}_C^B \mathbf{Z}_C^A\right)\right) - 2p \\ &= \mathrm{tr}\left(\mathbf{Y}_C^A \mathbf{Z}_C^B\right) + \mathrm{tr}\left(\mathbf{Y}_C^B \mathbf{Z}_C^A\right) - 2p. \qquad (6.37)\end{aligned}$$

In the following, this set representation based on the $\mathbf{Y}_C$ and the $\mathbf{Z}_C$ average matrices will be called the ZY model. Employing this idea, as it may be seen, the computation of the d_{al} measure may be as simple as the computation of the classical symmetric Wishart similarity measure (4.2) or even faster, as it just requires two matrix multiplication and trace computations, not requiring any matrix inversion. On the other hand, it has the disadvantage of requiring a larger amount of memory, as two different matrices, $\mathbf{Z}$ and $\mathbf{Y}$, are stored in the model. The computation of the union model of two sets $A \cup B$ may also be easily obtained as

$$\mathbf{Z}_C^{A\cup B} = \frac{N_a \mathbf{Z}_C^A + N_b \mathbf{Z}_C^B}{N_a + N_b} \qquad (6.38)$$

$$\mathbf{Y}_C^{A\cup B} = \frac{N_a \mathbf{Y}_C^A + N_b \mathbf{Y}_C^B}{N_a + N_b}. \qquad (6.39)$$

It is worth mentioning that this model requires an initial filtering or matrix regularization of the original data, in order to have full-rank matrices. The computation of the $\mathbf{Y}$ matrix requires invertible original pixel matrices. This problem may be circumvented by applying an initial small multilook filtering or by a more complex adaptive filtering in order to preserve the resolution of the original data, as, for instance, the proposed DBF technique [13], proposed in Section 6.1.1.

Additionally, the $\mathbf{Y}_C^A \mathbf{Z}_C^B$ matrices allow a similar interpretation to the $\mathbf{A}^{-1}\mathbf{B}$ matrices studied in Section 6.2, as they correspond to the average of these matrices for each pair of points of the two sets.

The proposed ZY model also allows the efficient computation of the Wishart homogeneity measure $H_{rw}(A)$ defined in (6.27). To do so, the same mathematical development may be applied to compare all the points of the region A with its average sample covariance matrix $\mathbf{Z}_C^A$

$$\begin{aligned}
H_{rw}(A) &= \frac{1}{N_A}\sum_{i=1}^{N_A} d(\mathbf{Z}_i^A, \mathbf{Z}_C^A) \\
&= \frac{1}{N_A}\sum_{i=1}^{N_A}\left(\mathrm{tr}\left(\mathbf{Z}_i^{A^{-1}}\mathbf{Z}_C^A\right) + \mathrm{tr}\left(\mathbf{Z}_C^{A^{-1}}\mathbf{Z}_i\right)\right) - 2p \\
&= \frac{1}{N_A}\left(\sum_{i=1}^{N_A}\mathrm{tr}\left(\mathbf{Z}_i^{A^{-1}}\mathbf{Z}_C^A\right) + \sum_{i=1}^{N_A}\mathrm{tr}\left(\mathbf{Z}_C^{A^{-1}}\mathbf{Z}_i^A\right)\right) - 2p \\
&= \frac{1}{N_A}\left(\mathrm{tr}\left(\sum_{i=1}^{N_A}\mathbf{Z}_i^{A^{-1}}\mathbf{Z}_C^A\right) + \mathrm{tr}\left(\mathbf{Z}_C^{A^{-1}}\sum_{i=1}^{N_A}\mathbf{Z}_i^A\right)\right) - 2p \\
&= \frac{1}{N_A}\left(\mathrm{tr}\left(\sum_{i=1}^{N_A}\mathbf{Z}_i^{A^{-1}}\mathbf{Z}_C^A\right) + N_A\mathrm{tr}\left(\mathbf{Z}_C^{A^{-1}}\mathbf{Z}_C^A\right)\right) - 2p \\
&= \frac{1}{N_A}\left(\mathrm{tr}\left(\sum_{i=1}^{N_A}\mathbf{Z}_i^{A^{-1}}\mathbf{Z}_C^A\right)\right) - p \\
&= \mathrm{tr}\left(\frac{1}{N_A}\sum_{i=1}^{N_A}\mathbf{Z}_i^{A^{-1}}\mathbf{Z}_C^A\right) - p
\end{aligned}$$

which yields to the expression

$$H_{rw}(A) = \mathrm{tr}(\mathbf{Y}_C^A\mathbf{Z}_C^A) - p. \tag{6.40}$$

If instead of the Wishart homogeneity $H_{rw}(A)$, the average distance among all the A points is evaluated, that is, $d_{al}(A, A)$, then it may be obtained

$$d_{al}(A, A) = 2\mathrm{tr}(\mathbf{Y}_C^A\mathbf{Z}_C^A) - 2p = 2H_{rw}(A). \tag{6.41}$$

This expression may be easily obtained from (6.37) when $\mathbf{Z}_C^B = \mathbf{Z}_C^A$ and $\mathbf{Y}_C^B = \mathbf{Y}_C^A$.

However, in this case, the eigenvalues of the $\mathbf{Y}_C^A\mathbf{Z}_C^A$ matrix do not correspond to the average polarimetric contrast. Note that this measure is defined among all the points within the same set A and, consequently, instead of change, it may be interpreted as the homogeneity or variability within A. As it may be deduced from (6.27), in this case, $\mathbf{Y}_C^A\mathbf{Z}_C^A$ corresponds to the average of $\mathbf{Z}_i^{A^{-1}}\mathbf{Z}_j^A + \mathbf{Z}_j^{A^{-1}}\mathbf{Z}_i^A$, for each pair of points $\mathbf{Z}_i^A$ and $\mathbf{Z}_j^A$ within A. Equivalently, its eigenvalues correspond to the average of the generalized eigenvalues and its inverse $\lambda_i + \lambda_i^{-1}$ as it is based on the Wishart measure, that may be defined in the same terms, as denoted in (6.19). Consequently, the eigenvalues of the $\mathbf{Y}_C^A\mathbf{Z}_C^A$ matrix, denoted as λ_{YZ_i}, are always larger than 1, that is, $\lambda_{YZ_i} \geq 1 \ \forall i$. Then, their value may be interpreted as amount of variability in the A set, in terms of the Wishart dissimilarity measure. The larger the λ_{YZ_i}, the larger the variability on the corresponding polarization state defined by the associated eigenvector $\mathbf{v}_{YZ_i}$.

6.3.4 PolSAR Time Series ZY Region Model Extension

When processing PolSAR time series, as described in Section 5.1.2, the temporal evolution of the target may be included within the region model in order to improve its characterization, assuming that a target is defined by its polarimetric temporal evolution. This assumption, then, leads to the extended $\mathbf{Z}_e$ model, defined in (5.2), on page 121.

Similarly, the extended $\mathbf{Y}_e$ matrix can be defined, following the same rationale

$$\mathbf{Y}_e = \begin{pmatrix} \mathbf{Y}_{11} & - & \cdots & - \\ - & \mathbf{Y}_{22} & \cdots & - \\ \vdots & \vdots & \ddots & \vdots \\ - & - & \cdots & \mathbf{Y}_{NN} \end{pmatrix} \tag{6.42}$$

where N represents the number of acquisitions in the dataset and $\mathbf{Y}_{ii}$ represents the $\mathbf{Y}$ matrix corresponding to the i-th acquisition, as expressed in (6.36). On (6.42), the off-diagonal elements other than the ones contained within the $\mathbf{Y}_{ii}$ matrices are not considered, as only the polarimetric information will be employed in the following. With the $\mathbf{Z}_e^A$ and $\mathbf{Y}_e^A$ matrices, the extended Wishart homogeneity measure $H_{rw_e}(A)$ of the region A can be computed as

$$H_{rw_e}(A) = \frac{1}{N} \sum_{i=1}^{N} \mathrm{tr}(\mathbf{Y}_{ii}^A \mathbf{Z}_{ii}^A) - p \tag{6.43}$$

Similarly, the extended average linkage $d_{al_e}(A, B)$ dissimilarity measure may also be defined in terms of the extended $\mathbf{Z}_e$ and $\mathbf{Y}_e$ matrices of the A and B regions

$$d_{al_e}(A, B) = \frac{1}{N} \sum_{i=1}^{N} \left(\mathrm{tr}(\mathbf{Y}_{ii}^A \mathbf{Z}_{ii}^B) + \mathrm{tr}(\mathbf{Y}_{ii}^B \mathbf{Z}_{ii}^A) \right) - 2p. \tag{6.44}$$

Additionally, a temporal stability measure $t_{s_{al}}(A)$ may be defined in the same way as the t_s measure defined in (5.5), on page 144, but in terms of the average linkage dissimilarity measure d_{al}

$$t_{s_{al}}(A) = \frac{2}{N(N-1)} \sum_{i=1}^{N} \sum_{j=i+1}^{N} \left(\mathrm{tr}(\mathbf{Y}_{ii}^A \mathbf{Z}_{jj}^A) + \mathrm{tr}(\mathbf{Y}_{jj}^A \mathbf{Z}_{ii}^A) \right) - 2p. \tag{6.45}$$

6.3.5 COMPARISON WITH COVARIANCE MATRIX AND SIMILARITIES

To see the benefits obtained when employing the ZY region model in combination the average linkage similarity measures, the Flevoland and Barcelona datasets, presented in Sections 5.3 and 5.4.2 have been processed with the TE BPT employing the average linkage d_{al_e} dissimilarity measure for BPT construction and the extended Wishart homogeneity H_{rw_e} for pruning.

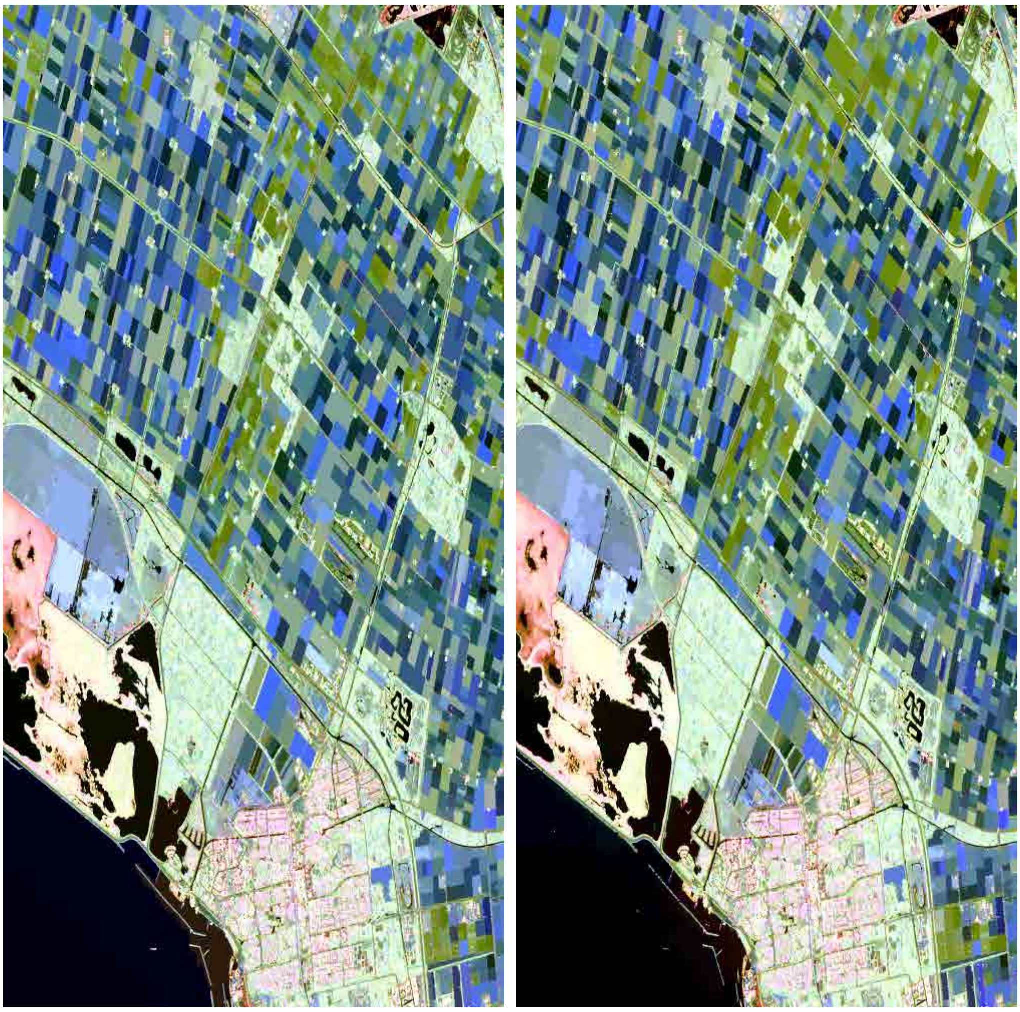

(a) TE BPT, d_g, Φ_e, $\delta_p = -3dB$ **(b)** TE BPT, d_{al_e}, H_{rw_e}, $\delta_p = 6dB$

Figure 6.21: Pauli RGB images of the first acquisition from the TE BPT results over the Flevoland dataset processed with the d_g and Φ_e measures over the classical model and with d_{al_e} and H_{rw_e} dissimilarity and homogeneity measures over the ZY model ($|S_{hh} + S_{vv}|$, $|S_{hv} + S_{vh}|$, $|S_{hh} - S_{vv}|$).

Fig. 6.21 shows the first acquisition of the processed Flevoland dataset when employing the previously proposed extended region model $\mathbf{Z}_e$, dissimilarity and homogeneity measures, defined in Sections 5.2.2 and 5.3, in comparison with the ZY model and the d_{al_e} and H_{rw_e} measures defined in Section 6.3.4. It is worth mentioning that since the extended Wishart homogeneity measure H_{rw_e} is based on a different measure than Φ_e, a different range of values of the pruning threshold δ_p parameter are required in both situations in order to obtain a similar result. Then, in Fig. 6.21a a pruning threshold $\delta_p = -3dB$ has been employed whereas on Fig. 6.21b a $\delta_p = 6dB$ value has been set in order to obtain a comparable level of detail in the results.

Apparently Fig. 6.21a and 6.21b present similar results but, when they are examined in detail, some differences may be observed. Figs. 6.22a and 6.22b show a detail of these results over the first acquisition. It may be observed, in the left part of the image, some green fields corresponding to zones that are vegetated among all the acquisitions of the Flevoland dataset. These areas presumably have a larger spatial variability or texture and, consequently, they appear segmented into many regions in Fig. 6.22a. Due to this larger variability, the classical $\mathbf{Z}_e$ is not able to properly group all these small regions as it is not able to model inhomogeneous regions accurately. When the ZY model is employed better results are obtained, as observed in Fig. 6.22b, since the average linkage dissimilarity measure d_{al_e} and the revised Wishart homogeneity measure H_{rw_e} are more suited for the comparison and modeling of heterogeneous regions, as they are not based on the centroid representation, as stated in Section 6.3.2. With this approach these areas are properly merged together and they appear as a single region. To see more clearly this effect, Figs. 6.22c and 6.22d show only the contours between the regions obtained. It may be observed that over the agricultural areas on the right part of the image both approaches achieve similar results whereas, for these fields having high spatial variability, only the ZY model is able to properly identify and separate them. Indeed, when employing the ZY model, no significant difference is observed on the results obtained among these fields and the other ones.

The Barcelona dataset has been also processed employing the TE BPT with the ZY model and the d_{al_e} and H_{rw_e} dissimilarity and homogeneity measures. Fig. 6.23b shows the temporal stability $t_{s_{al}}$ measure results, defined in (6.45), obtained employing this representation. These results are compared with the ones obtained in Fig. 6.23a employing the classical model, dissimilarity and homogeneity measures for the TE BPT and the temporal stability measure t_s, as described in Section 5.4.2. In these results, the DBF technique, defined in Section 6.1.1, has been employed for matrix regularization in both cases.

As it may be observed in Fig. 6.23, the average linkage concept may also improve the results obtained in terms of the temporal stability measure. When employing the $t_{s_{al}}$ measure based on this notion, the same changes are detected but a much larger contrast may be observed between the change and no change areas. Note that with the ZY model the different regions of the scene

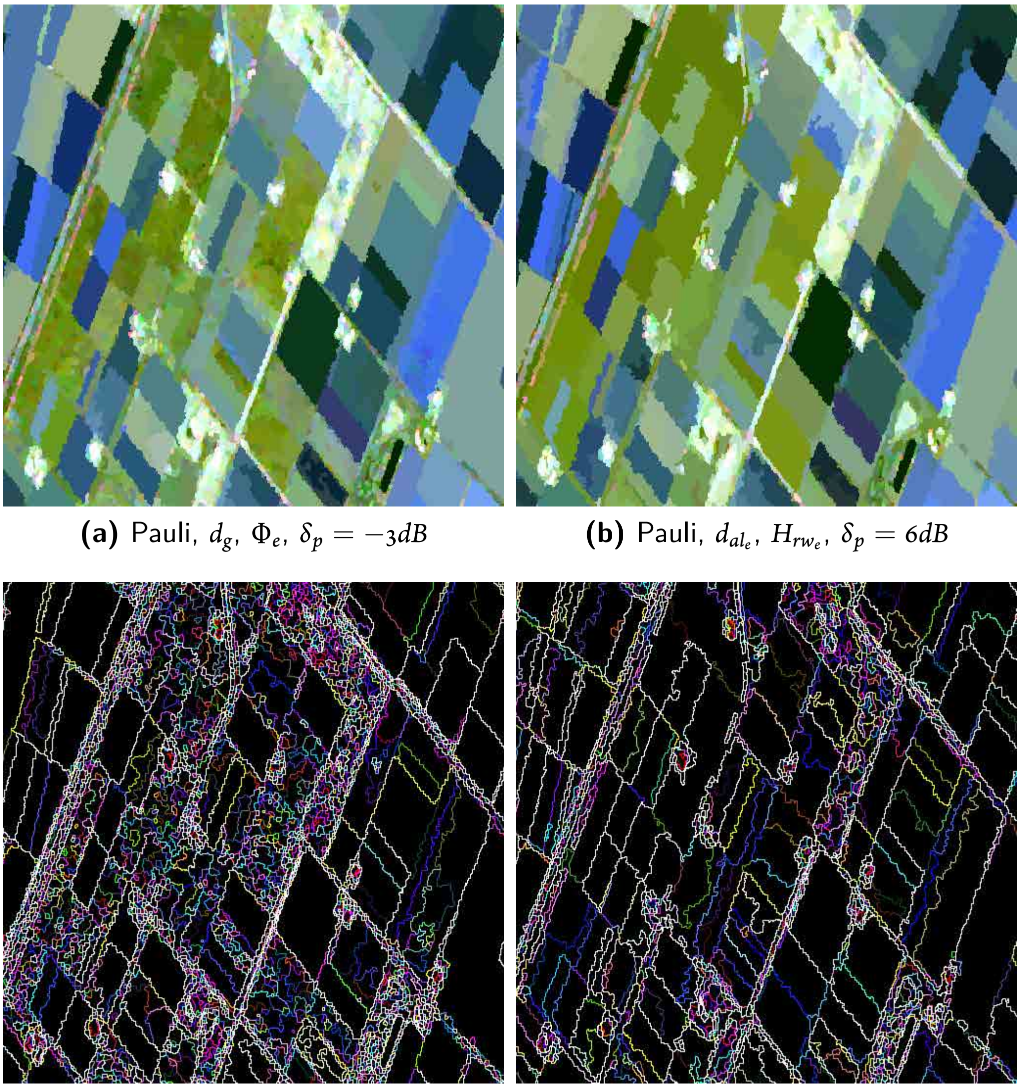

(a) Pauli, d_g, Φ_e, $\delta_p = -3dB$ **(b)** Pauli, d_{al_e}, H_{rw_e}, $\delta_p = 6dB$

(c) Contours, d_g, Φ_e, $\delta_p = -3dB$ **(d)** Contours, d_{al_e}, H_{rw_e}, $\delta_p = 6dB$

Figure 6.22: Pauli RGB detail images and contours of the first acquisition from the TE BPT results over the Flevoland dataset processed with the d_g and Φ_e measures over the classical model and with d_{al_e} and H_{rw_e} dissimilarity and homogeneity measures over the ZY model ($|S_{hh} + S_{vv}|$, $|S_{hv} + S_{vh}|$, $|S_{hh} - S_{vv}|$).

may be better identified, specially those having large spatial variability, as seen before. Additionally, the $t_{s_{al}}$ measure is able to calculate more accurately the polarimetric changes among these regions, as it employs all the pixel values instead of the centroid, resulting into a more reliable temporal stability outcome. In fact, the results in Fig. 6.23b are less noisy and more contrasted than those on Fig. 6.23a, being easier to identify the corresponding changes over the scene.

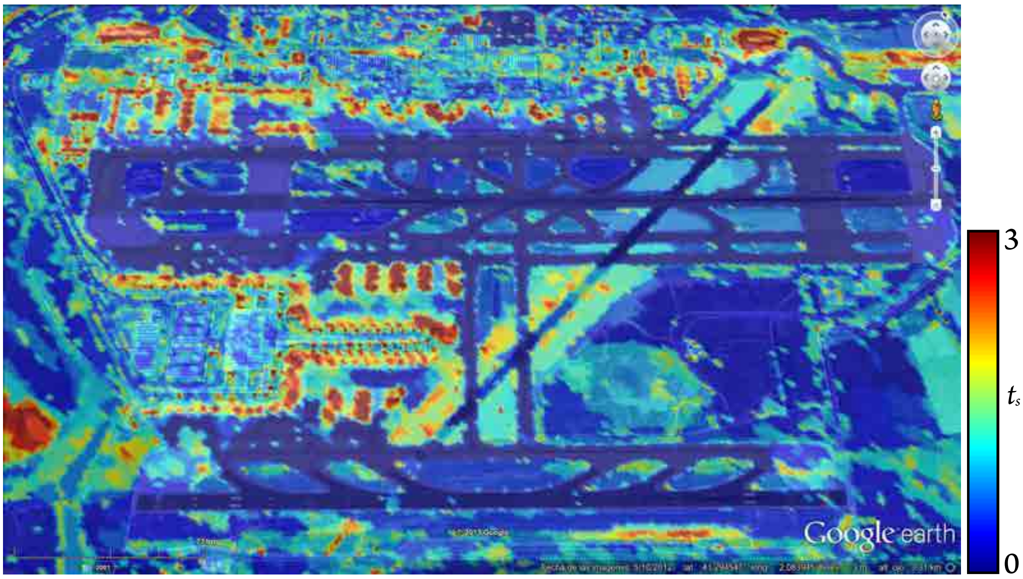

(a) Geo-coded t_s, TE BPT with the classical model and d_g and Φ_e

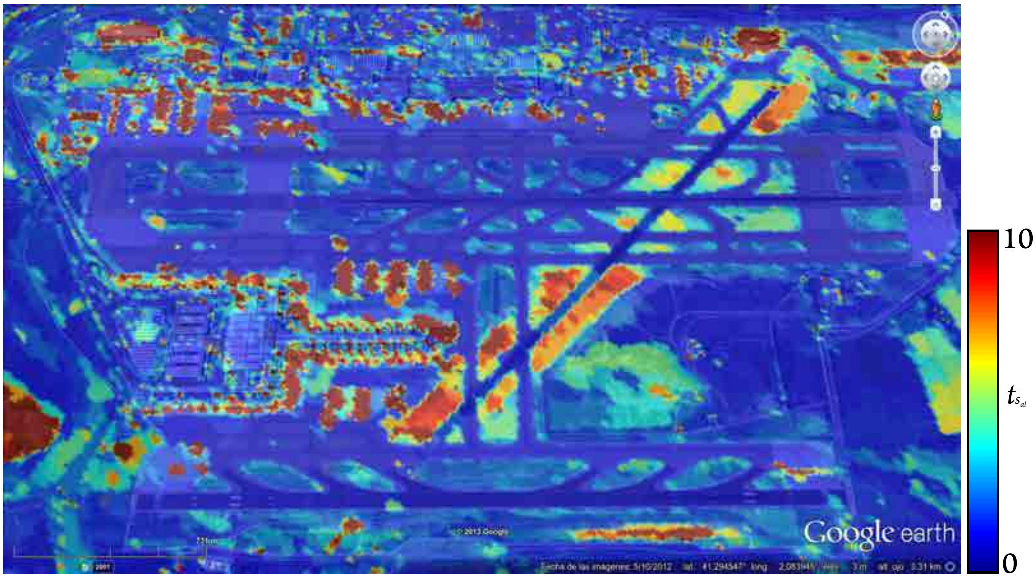

(b) Geo-coded $t_{s_{al}}$, TE BPT with the ZY model and d_{al_e} and H_{rw_e}

Figure 6.23: Geo-coded temporal stability measures t_s and $t_{s_{al}}$ over the Barcelona dataset employing the TE BPT with the classical model and d_g and Φ_e measures and the ZY model with d_{al_e} and H_{rw_e} dissimilarity and homogeneity measures. In both cases the DBF technique has been employed for matrix regularization with 5x5 local window V, 3 iterations of the weight refinement scheme, and $d_{pw}, \sigma_s = 2, \sigma_p = 0.4$ parameters.

To get different results, you have to do something different.

Albert Einstein

7

Multidimensional SAR Data Classification

The BPT has proven to be a useful multidimensional SAR data representation for different applications. As described in Chapter 3, it is a region-based approach that describes homogeneous connected areas of the image. Going one step further in this direction, different areas of the scene identified by some particular traits may be grouped together into *classes*. The process of assigning the different samples, or regions, from the data into a finite set of classes is known as *classification*. This chapter introduces some progress that has been developed within the course of this thesis in this field, based on the BPT representation and concepts.

As indicated in Section 2.4, classification techniques may be decomposed into two main types: supervised and unsupervised classification. On supervised classification, an initial knowledge of the scene is required in order to provide the training set, which is a set of regions that are known to belong to each class. Then, the rest of the data is assigned into one of the supplied classes by the technique. On unsupervised classification no a priori knowledge of the scene or classes is assumed and, consequently, the technique automatically defines the classes according to the most differentiated areas of the data.

The first section of this chapter defines a supervised classification technique taking into account the same similarity measures that have been employed for the BPT based processing. The second section employs the k-means clustering approach to obtain unsupervised classification results from the BPT pruning results. It is worth mentioning that, since these techniques are defined in terms of the BPT, they may also be applied to the previously described representations for PolSAR images and also for PolSAR time series datasets, providing a classification technique that naturally takes into account the temporal evolution of the scene.

7.1 Similar Regions Supervised Classification

The proposed BPT construction process, described in Section 3.2, is based on an iterative merging of the two most similar adjacent regions on the scene. The conceptual framework behind this idea is based on the similarity measures, which evaluate the closeness among two regions. Moreover, these measures have been adapted to the extended model for processing PolSAR time series, as described in Section 5.2.2. It has been shown that taking into account the polarimetric temporal evolution of the target results into an increase of region differentiation. In fact, this information may also be useful for classifying the different regions of the scene.

As mentioned before, the BPT pruning process results into a set of homogeneous regions of the image. Note that, for a region-based supervised classification approach, a training set should be provided consisting of a collection of regions for each class. Accordingly, in order to obtain a supervised classification technique based on the BPT, the same similarity measures employed for its construction may be employed also to identify the closest training region of any pruned node, but, in this case, without the term depending on the region size. Note that this term was incorporated for the BPT construction process, in order to ensure a proper multi-scale structure while favoring the merging of smaller regions first. In this case, the aim is to define a classification technique independent of the region size. Then, the geodesic similarity measure d_{gc}, for instance, may be employed for classification, based on the geodesic measure d_g, defined in (5.3) on page 124

$$d_{gc}(A,B) = \sqrt{\sum_{i=1}^{N} \left\| \log\left(\mathbf{Z}_{A_{ii}}^{-1/2} \mathbf{Z}_{B_{ii}} \mathbf{Z}_{A_{ii}}^{-1/2} \right) \right\|_F^2} \tag{7.1}$$

where $\mathbf{Z}_{A_{ii}}$ stands for the sample covariance matrix of the i-th acquisition within the extended region model $\mathbf{Z}_e$ of the region A.

Fig. 7.1 shows an example of this classification procedure in the Flevoland PolSAR time series dataset, described in Section 5.3. In this case, the classical 3 by 3 multilook has been employed as initial filtering and the extended geodesic d_g and Φ_e measures for TE BPT construction and pruning, respectively. In the pruning process a $\delta_p = -3dB$ threshold parameter has been employed, corresponding, then, to the same results shown previously in Fig. 5.4b, on page 130, and analyzed in Section 5.3. Fig. 7.1a shows the value of the proposed d_{gc} measure, as described in (7.1), corresponding to the similarity to the region marked in magenta in this figure. In order to obtain the similar regions to a given one, a maximum value may be set over the similarity measure in order to obtain a mask, as shown in Figs. 7.1b and 7.1c. As it may be observed, a larger value of this threshold parameter results into a larger amount of similar regions. Note that these results correspond to the set of regions of the dataset that are following a similar polarimetric temporal evolution among all the 8 different acquisitions of the dataset.

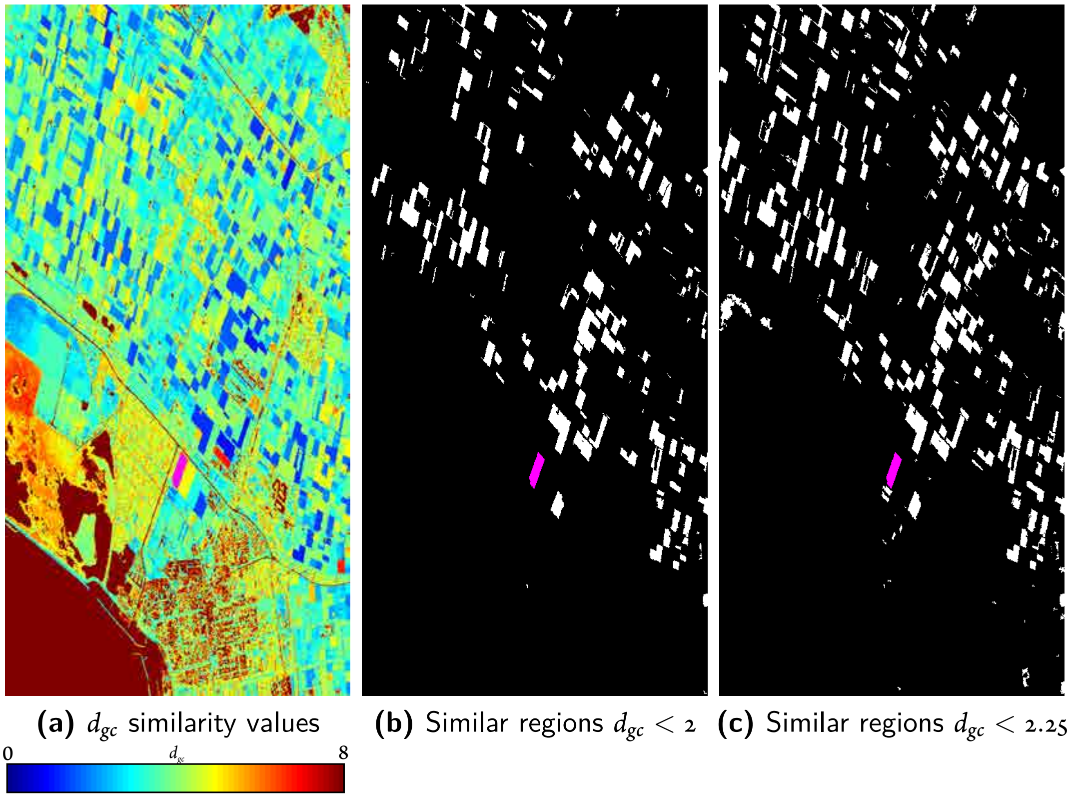

(a) d_{gc} similarity values **(b)** Similar regions $d_{gc} < 2$ **(c)** Similar regions $d_{gc} < 2.25$

Figure 7.1: Region similarity to the field marked in magenta in (a). A threshold over the similarity measure conforms a similar regions classification, as represented in (b) and (c).

In order to obtain a supervised classification of the data a certain number of classes are provided within the training set and, consequently, each region is assigned to the class of the most similar region of this set. Over the Flevoland dataset, a ground truth classification of the agricultural fields is available, represented in Fig. 7.2. This ground truth has been built by collecting the information related with the crop type in ground, provided as part of the ESA AgriSAR

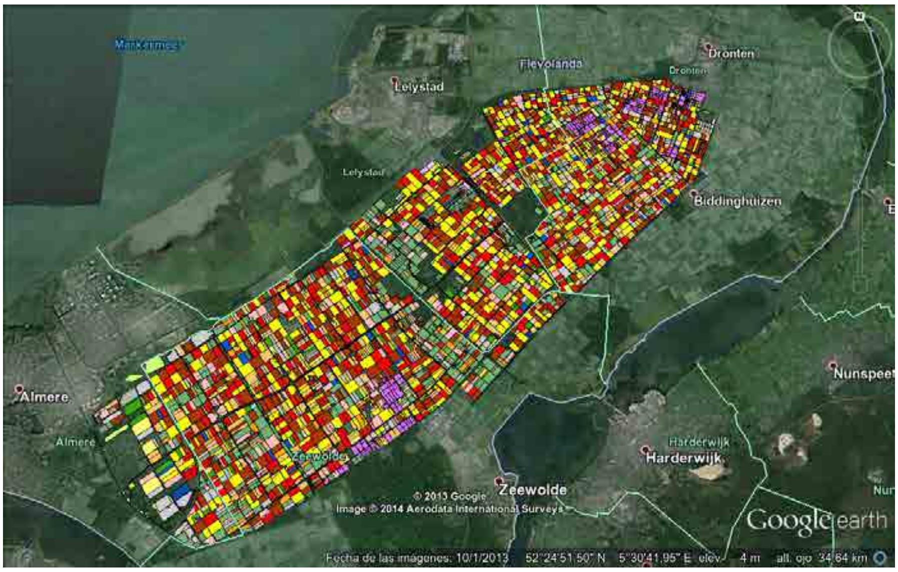

Figure 7.2: Flevoland agricultural crop type ground truth. Each color represents a type of crop.

2009 campaign. Note that only a part of this ground truth falls within the scene covered by the Flevoland dataset, shown in Fig. 5.3.

From the ground truth presented in Fig. 7.2, 4 different types of crop has been selected for classification: winter wheat, onions, sugar beet and potatoes. These crop types has been selected since a large number of these fields may be found within the scene of the Flevoland dataset presented before. As a training set, two fields have been randomly selected for each crop type. Then, the obtained polarimetric temporal evolution for each pruned region of the TE BPT has been tested for similarity, according to the d_{gc} measure, to these training set fields. Accordingly, they have been assigned to the class of the most similar training field. In order to avoid the labeling of very different areas of the scene, a threshold of $d_{gc} < 2.5$ has been set for all the region similarity, as represented in Fig. 7.1. Thus, those regions that have a similarity above 2.5 from all the fields of the training set are not labeled.

The corresponding supervised classification results are shown in Fig. 7.3. On this figure, the pruned regions have been filled according to the color of the class they have been assigned to, whereas the contours of the fields have been colored according to the ground truth data. Although there are some regions miss-classified, a high degree of success may be observed among the agricultural fields. From this results it may be inferred that a reliable supervised classification results may be obtained when employing the TE BPT for scene type classification, specially over agricultural fields.

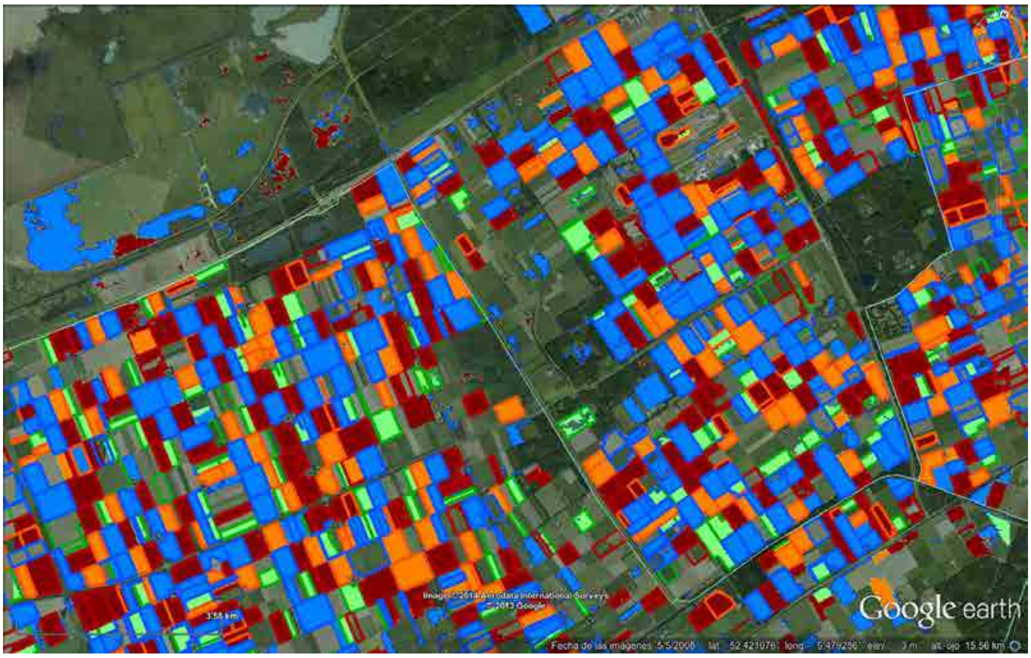

Figure 7.3: Geo-coded Flevoland agricultural crop type supervised classification results and ground truth. The regions are filled according to their classification result whereas the contours of each field are represented with the color of the ground truth data. Colors correspond to **Winter wheat**, **Sugar beet**, **Potatoes** and **Onions**.

This performance is mainly achieved due to taking into account the complete polarimetric temporal evolution of the agricultural fields, as it increases substantially the differentiation among them, as it has been stated in Section 5.3. In order to see clearly the benefits of employing this information in practice, the same supervised classification approach has been employed over the dataset conformed only by the first acquisition. Fig. 7.4 shows a detail of the results obtained after applying this technique with different types of filtering processes. Fig. 7.4a correspond to the detail of the results shown in Fig. 7.3, employing the TE BPT over the whole time series dataset, having 8 acquisitions. On the other hand, Fig. 7.4b shows the results obtained when applying the same TE BPT and supervised classification techniques over the first acquisition only of the Flevoland dataset. Note that on each result of Fig. 7.4 a different type of data or filtering is employed and, then, the applied threshold values for the d_{gc} similarity measure have been tuned in each case in order to obtain comparable results. As it may be observed, the performance of the obtained classification decreases substantially when only one acquisition is available, specially for Winter wheat and Onions classes. Probably, these classes are mainly distinguished by their polarimetric temporal evolution and only one image may be not enough in order to properly identify them.

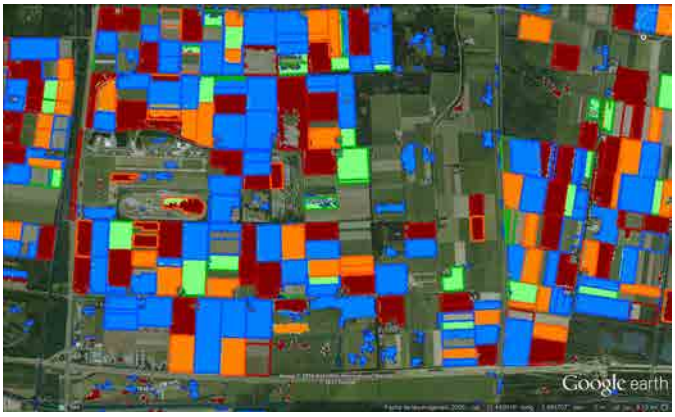

(a) TE BPT employing 8 acquisitions, $d_{gc} < 2.5$

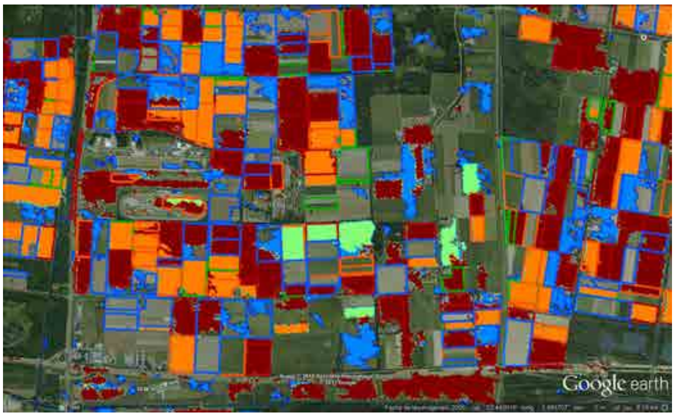

(b) TE BPT employing 1 acquisition, $d_{gc} < 0.5$

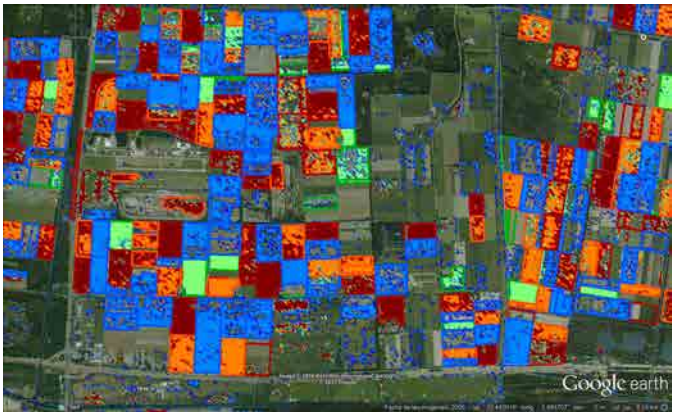

(c) 7x7 multilook employing 8 acquisitions, $d_{gc} < 3.5$

Figure 7.4: Comparison of geo-coded Flevoland agricultural crop type supervised classification results for the TE BPT employing 8 and 1 acquisition and for the 7 by 7 multilook employing the 8 acquisitions. Colors correspond to **Winter wheat**, **Sugar beet**, **Potatoes** and **Onions**.

Additionally, in order to reflect the benefits of employing the TE BPT representation for homogeneous region segmentation and filtering, Fig. 7.4c shows the results obtained after applying the same supervised classification employed in Figs. 7.3 and 7.4a over the 8 original images filtered with a 7 by 7 multilook. Note that, in this case, the polarimetric temporal evolution among all the acquisitions is also available but estimated employing the multilook instead of the TE BPT. Therefore, roughly the same areas than on Fig. 7.4a may be guessed in Fig. 7.4c but they are considerably more noisy as they are more contaminated due to the speckle. This example clearly shows the advantage of employing the TE BPT for segmentation and polarimetric estimation. Since it results into almost one region per agricultural field, the effect of the speckle noise over the data is strongly reduced producing a noticeably clearer result. Moreover, as it is a region-based approach, the classification process over the BPT is significantly more efficient from a computational point of view, as it has to test the d_{gc} measure only once per region instead of once per pixel as in the case of the 7 by 7 multilook.

7.2 K-Means Unsupervised Classification

This section is focused on the definition of an unsupervised classification technique based on the BPT representation. Indeed, the results shown on the previous section suggest that, due to the clear differentiation among the different agricultural fields, an unsupervised classification technique may be useful to determine automatically the different areas of the scene.

In machine learning and data mining the *clustering* or *cluster analysis* is the process of grouping samples in such a way that the samples within a group or cluster are more similar to each other than those in other groups. Then, it corresponds to the unsupervised classification procedure. The *k-means* is a well-known method for cluster analysis in data mining [92]. Moreover this technique may be also defined in similar terms to those of the BPT based processing. The following sections describe and analyze a PolSAR classification technique based on the k-means clustering.

7.2.1 K-Means Definition and Limitations

The k-means concept was originally employed for signal processing [114] as proposed by S. Lloyd [86]. However, the first algorithm was published by E.W. Forgy [51] and, consequently, it is also referred to as the Lloyd-Forgy algorithm.

Originally, in the k-means clustering approach, a set of n multidimensional observations, which are denoted by $(\mathbf{x}_1, \mathbf{x}_2, \ldots, \mathbf{x}_n)$, are assigned to a finite k sets $\mathbf{S} = (S_1, S_2, \ldots, S_k)$, having

$k \leq n$, in order to minimize the within-cluster sum of squares

$$\arg\min_{\mathbf{S}} \sum_{i=1}^{k} \sum_{\mathbf{x}_j \in S_i} \|\mathbf{x}_j - \boldsymbol{\mu}_i\|^2 \tag{7.2}$$

where $\boldsymbol{\mu}_i$ refers to the mean of all the observations assigned to S_i. For region-based PolSAR data and time series datasets, the $\mathbf{x}_j$ and $\boldsymbol{\mu}_i$ may be considered as region models, corresponding to the sample covariance matrices $\mathbf{Z}$ or the extended $\mathbf{Z}_e$ matrices.

The k-means is an iterative algorithm that may be decomposed into two main alternating stages, assignment and update steps:

1. During the assignment step, each observation is tested for similarity among all the cluster centers $\boldsymbol{\mu}_i$. Finally, it is assigned to the set S_i having the closest center $\boldsymbol{\mu}_i$. That is, for the iteration t, the set $S_i^{(t)}$ may be defined as

   $$S_i^{(t)} = \left\{\mathbf{x}_p : d(\mathbf{x}_p, \boldsymbol{\mu}_i^{(t)}) \leq d(\mathbf{x}_p, \boldsymbol{\mu}_j^{(t)}) \ \forall j, 1 \leq j \leq k\right\} \tag{7.3}$$

   where $d(\mathbf{x}_p, \boldsymbol{\mu}_i^{(t)})$ denotes the distance between the p observation and the mean of the i-th cluster at iteration t.

   Originally, the distance d refers to the squared euclidean distance d_e, defined as

   $$d_e(\mathbf{x}_p, \boldsymbol{\mu}_i^{(t)}) = \|\mathbf{x}_p - \boldsymbol{\mu}_i^{(t)}\|^2, \tag{7.4}$$

   but for PolSAR data any of the previously defined dissimilarity measures without the region size term may be employed as, for instance, the d_{gc} measure defined in (7.1). Note, however, that this fact involves that (7.2) is not fulfilled, as they correspond to distinct measures. Additionally, in order to fulfill a similar expression when substituting the euclidean d_e by the geodesic d_{gc} measure, the cluster means $\boldsymbol{\mu}_i$ should also be computed according to the geodesic mean [22], to be consistent with the space geometry employed in the similarity measure, which is not the case.

2. In the update step the means or centroids $\boldsymbol{\mu}_i$ are re-computed for each cluster S_i, according to the new assignments performed during the previous assignment step. This may also be expressed as

   $$\boldsymbol{\mu}_i^{(t+1)} = \frac{1}{|S_i^{(t)}|} \sum_{\mathbf{x}_j \in S_i^{(t)}} \mathbf{x}_j \tag{7.5}$$

   where $|S_i^{(t)}|$ denotes the cardinality of the $S_i^{(t)}$ set.

These two steps are repeated until a convergence criterion is achieved, usually when there is no change among the assignments or when a given number of iterations has been performed.

It is worth mentioning that finding the exact or optimum solution of the k-means method is a NP-hard problem [45]. This means that no solution is known in a polynomial execution time and, consequently, an exact solution may not be found in practice even for relatively small datasets due to the large computational complexity. The Lloyd-Forgy algorithm previously described corresponds to an approximation of the problem. Therefore, this algorithm typically converges to a local optimum but, however, there is no guarantee that it converges to the global optimum. In fact, the performance of the results obtained strongly depends on the initial cluster assignments, also called *seeds*. As a consequence, some initialization methods have been proposed in order to perform a robust initialization for different types of data. Accordingly, in Section 7.2.2, an initialization method is adapted for the PolSAR data BPT pruning results.

It should be noted that the Wishart classification technique [81], previously described in Section 2.4.2, may also be considered as a k-means clustering algorithm, as it is based on the same principles. In this case, the employed polarimetric distance $d_{wc}(\mathbf{Z}_p, \mathbf{C}_i)$ between the estimated covariance matrices of the p sample $\mathbf{Z}_p$ and the cluster center $\mathbf{C}_i$ may be considered as

$$d_{wc}(\mathbf{Z}_p, \mathbf{C}_i) = \ln|\mathbf{C}_i| + \mathrm{tr}(\mathbf{C}_i^{-1}\mathbf{Z}_p). \tag{7.6}$$

Note, however, that this technique is limited to 8 or 16 classes, depending on the initialization employed, that is, the $H/\bar{\alpha}$ or the $H/A/\bar{\alpha}$ classification. Indeed, since PolSAR data are strongly contaminated by speckle noise, a good initialization of the cluster centers is crucial in order to obtain meaningful results. Then, the initial classification based on $H/A/\bar{\alpha}$ parameters is employed as it provides a reasonably good initialization at the cost of restricting the number of classes parameters k.

7.2.2 Robust Initialization for K-Means: K-Means++

As mentioned previously, the initialization or seeding process is crucial for the k-means method. Moreover, this process is even more important for PolSAR data, since it is strongly contaminated by speckle.

Recently, the k-means++ [19] method has been proposed in order to generate a robust initialization for the k-means technique. It specifies a randomized procedure to initialize the cluster centers, prior to the k-means clustering. A randomized algorithm employs some degree of randomness to guide its behavior in order to achieve a good performance in the *average case* [96]. Under some situations, only randomized algorithms are able to ensure a certain level of approximation to general problems [46]. In this regard, with the k-means++ initialization, the Lloyd-Forgy algorithm previously described is guaranteed to find an expected approximation ratio $O(\log k)$ to the optimal k-means solution [19], where k refers to the number of clusters. Note that the original k-means algorithm may find clusters arbitrarily worse than the optimum [67].

In order to obtain a good initialization of the k cluster centers, they should be spread out around the range of values of the dataset. This is, indeed, the intuition behind the k-means++ approach. It initializes each of the cluster centers to one sample of the dataset, trying to ensure that all the obtained centers are far away from each other. The k-means++ initialization algorithm may be described according to the following steps:

1. The first cluster S_1 gets initialized to one sample taken uniformly random among all the samples of the dataset. If the sample $\mathbf{x}_k$ has been chosen, the corresponding first cluster center is set to it accordingly $\boldsymbol{\mu}_1 = \mathbf{x}_k$.

2. For each data sample $\mathbf{x}_i$, the minimum distance $D_m(i)$ between it and the nearest center $\boldsymbol{\mu}_j$ of the already chosen sets $\mathbf{S}_c$ already chosen is computed

$$D_m(i) = \underset{j \in \mathbf{S}_c}{\arg\min}\, d(\mathbf{x}_i, \boldsymbol{\mu}_j). \tag{7.7}$$

3. A new cluster S_n is assigned to a new sample $\mathbf{x}_i$, which is chosen randomly according to a weighted probability proportional to $D_m(i)^2$ for each sample i. That is, the probability $P(i)$ of choosing the $\mathbf{x}_i$ sample as the new cluster center $\boldsymbol{\mu}_n$ may be defined as

$$P(i) = \frac{D_m(i)^2}{\sum_{j=1}^{n} D_m(j)^2}. \tag{7.8}$$

4. The steps 2 and 3 are repeated until the k different sets have been initialized.

5. Finally, the standard k-means clustering process, defined in Section 7.2.1, is applied with this initialization.

In order to apply the k-means++ method previously described for PolSAR data and temporal series, the dissimilarity measures may be employed over the sample covariance matrices. For instance, the d_{gc} measure, defined in (7.1), may be applied. However, in order to apply this algorithm over the regions obtained from the BPT, some changes have to be made. Note that the k-means++ is a randomized algorithm and, since regions of different sizes may be found, the number of samples for each region has to be taken into account.

The k-means++ is a randomized algorithm that defines a probability for choosing each one of the input samples. However, the BPT is a region-based approach and, consequently, each region is composed by an arbitrary number of samples. Then, the probability $P(i)$ of selecting the sample i, defined in (7.8), may be redefined in a region-based fashion as $P_r(i)$, taking into account the region size parameter

$$P_r(i) = \frac{D_m(i)^2 \cdot N_i}{\sum_{j=1}^{N_R} D_m(j)^2 \cdot N_j} \tag{7.9}$$

where N_i refers to the number of samples of the region i and N_R refers to the total number of pruned regions.

The computation of this initialization may be much more complex than employing a random or fixed seeding as, for instance, the fixed $H/\bar{\alpha}$ or $H/A/\bar{\alpha}$ initial classification. Then, the k-means++ requires an additional amount of time to the classical k-means technique. However, according to the authors, the k-means classification may converge faster due to a better initialization, resulting into a global processing time reduction [19].

7.2.3 OUTLIER DETECTION AND REMOVAL FOR K-MEANS

In statistics, an outlier may be considered as an observation that is unusually distant from other observations [62]. An outlier observation may be produced due to the inherent variability in the observation or due to an experimental error. In the later case, those samples are usually excluded from the dataset.

For unsupervised classification techniques, the outliers may pose a problem. Since they are far away from all of the other data, this situation may result into one big cluster grouping almost all the data within and small clusters around it for the outliers themselves. Then, for this application, the elimination of the outliers may be interpreted as the removal of non-significant small details in order to obtain a more detailed analysis over the significant data.

In order to define a reliable outlier removal technique, a clear definition of this concept should be available. However, up to date there is no rigid mathematical definition of what constitutes an outlier. There are different methods for outlier detection [83][64]. Typically, a model is employed to characterize the data, assuming a normal distribution, and the observations that are considered as *unlikely* based on the mean and standard deviation are removed. However, these approaches have the inconvenience of resulting into a systematic elimination of a part of the data. Other applications are based on a distance measure in order to remove those samples that are relatively far from the closest sample [69][105]. Nevertheless, these techniques only work for isolated samples. When a group of samples constitute an outlier, these distance-based approaches do not detect them properly.

Consequently, a different approach for outlier detection and removal is proposed. In a general sense, within the context of the unsupervised classification an outlier may be considered as group or class that is small enough to be considered as not significant. When a dataset composed of N samples is classified into k clusters, it may be considered that the average size per cluster is N/k. Then, a set S_i will be considered as not significant if it contains less than 1% samples of this average size. Consequently, the k-means algorithm, described in Section 7.2.1, is modified in order to remove the samples corresponding to each stable cluster S_i having less than $N/(100k)$ samples. When the samples assigned to the non-significant S_i cluster have not changed among two consecutive iterations, these samples are labeled as outliers and removed from the classification. The free S_i cluster is then re-assigned according to the k-means++ method, as described in (7.9).

7.2.4 BPT based Unsupervised Classification Results

In this section, the proposed unsupervised classification technique, based on the k-means++ initialization method and the Lloyd-Forgy algorithm is evaluated with real PolSAR data. Fig. 7.5 shows the results of applying the proposed unsupervised classification method to the Oberpfaffenhofen PolSAR image presented in Fig. 4.10a, on page 88. Fig. 7.5a shows the result obtained after classifying the image into 8 clusters employing the BPT with the classical sample covariance matrix $\mathbf{Z}$ model, as presented in Chapter 4, and the d_{gc} measure (7.1) for classification. On the other hand, Fig. 7.5b shows the same result when employing the ZY model, described in Section 6.3.3, and the d_{al} measure (6.32) for classification. In both cases, the number and, consequently, the color of each class is random, as it depends on the k-means++ randomized initialization method.

It may be observed from Fig. 7.5 that the structure of the image is much less clear from Fig. 7.5a than from Fig. 7.5b. The obtained classes when employing the ZY model have a better correspondence with the different areas of the scene, as some parts like the runway and agricultural fields are distinguished into different classes. Indeed, as mentioned in Section 4.1.2, the classical model has the limitation of being unable to properly represent inhomogeneous areas of the image. This effect becomes more dramatic for the classification application, as all the different targets of the scene are grouped into a small number of groups, resulting into a mixture of different statistics within each cluster. In this situation, the classical model is unable to properly represent the different clusters and, consequently, the dissimilarity measurements obtained are also affected, resulting into a poor final performance. On the other hand, the ZY model and the

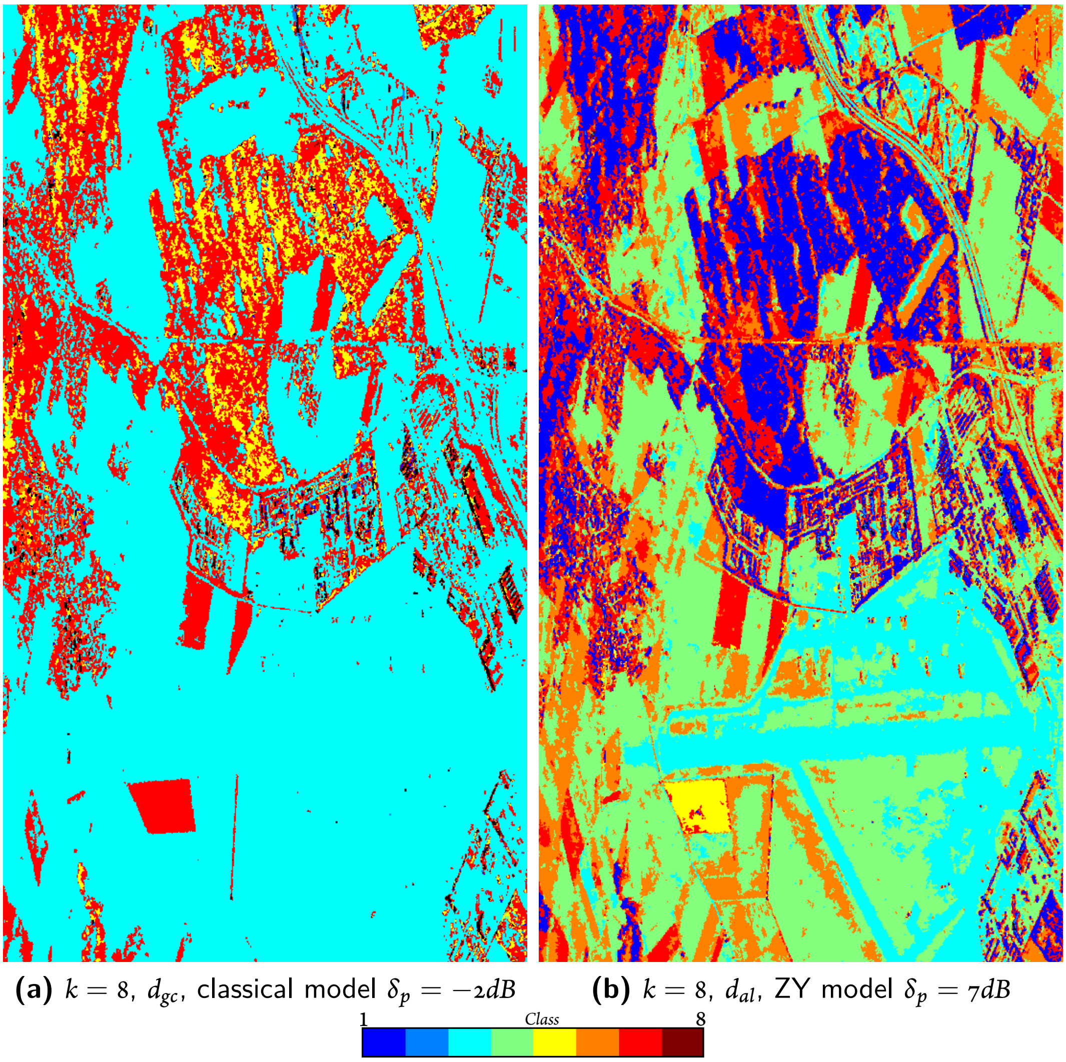

(a) $k = 8$, d_{gc}, classical model $\delta_p = -2dB$ **(b)** $k = 8$, d_{al}, ZY model $\delta_p = 7dB$

Figure 7.5: Clustering into 8 classes of the Oberpfaffenhofen PolSAR image presented in Fig. 4.10a. The classical model and d_{gc} measure has been employed in (a) whereas the ZY model and the d_{al} dissimilarity measure has been employed in (b).

average linkage dissimilarity measure have been proposed in Sections 6.3.3 and 6.3.2 in order to circumvent this limitation, resulting into better unsupervised classification results as they are able to deal more effectively with inhomogeneous statistics.

The outlier removal method presented in Section 7.2.3 has been employed in the results shown in Fig. 7.5. On these images, the outliers are not represented, as they are not classified, appearing in black color. To see them more clearly, Fig. 7.6 shows the outlier pixels obtained from these two results. As it may be observed, much more outliers are detected when employing the classical model, in Fig. 7.6a, than with the ZY model, in Fig. 7.6b. Again, this is a consequence of

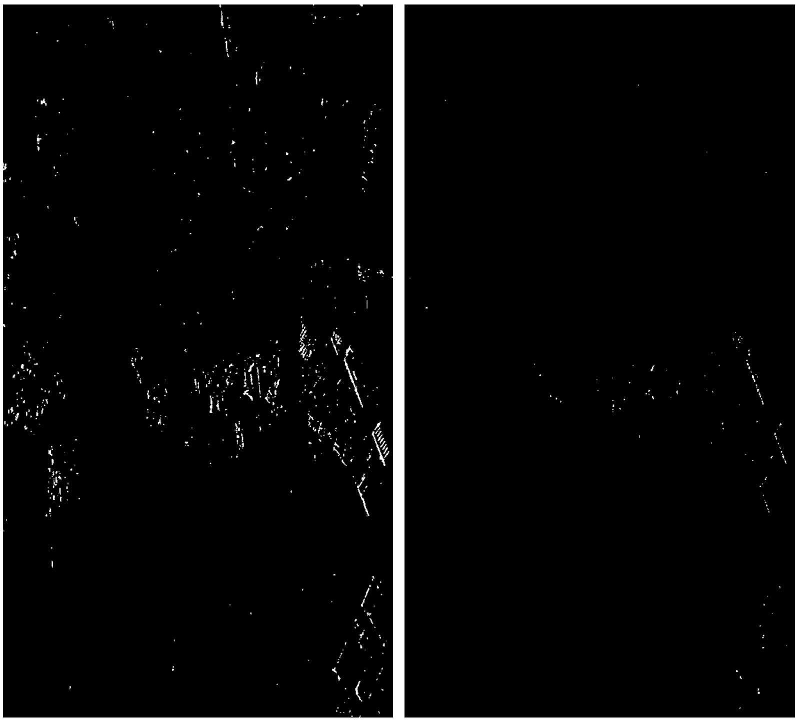

(a) Outliers $k = 8$, d_{gc}, classical model $\delta_p = -2dB$ **(b)** Outliers $k = 8$, d_{al}, ZY model $\delta_p = 7dB$

Figure 7.6: Outliers detected during the clustering into 8 classes of the Oberpfaffenhofen PolSAR image presented in Fig. 4.10a. The classical model and d_{gc} measure has been employed in (a) whereas the ZY model and the d_{al} dissimilarity measure has been employed in (b).

the inability of the classical model to deal properly with the different inhomogeneous clusters. In Fig. 7.6b it may be observed that most of the outliers correspond to strong targets in urban areas that are very different to the rest of the image, according to the d_{al} measure, and they are not enough representative to constitute a cluster by themselves. The number of detected outliers in Fig. 7.6a is 38330 pixels (0.88%), whereas on Fig. 7.6b only 3214 pixels (0.074%) have been labeled as outliers.

One of the main advantages of the k-means++ initialization algorithm, as described in Section 7.2.2, is that it may be employed to initialize the Lloyd-Forgy unsupervised classification algorithm with an arbitrary number of classes while providing a reasonably robust results. This eliminates the limitation of the Wishart classifier, that only produces 8 or 16 classes, as it has to rely on the fixed $H/\bar{\alpha}$ or $H/A/\bar{\alpha}$ polarimetric segmentation in order to obtain a robust initialization. To show this ability, Fig. 7.7 shows the results obtained when clustering the Oberpfaffenhofen PolSAR image into 2, 4 and 12 clusters. In these cases, the ZY model and the d_{al} measure

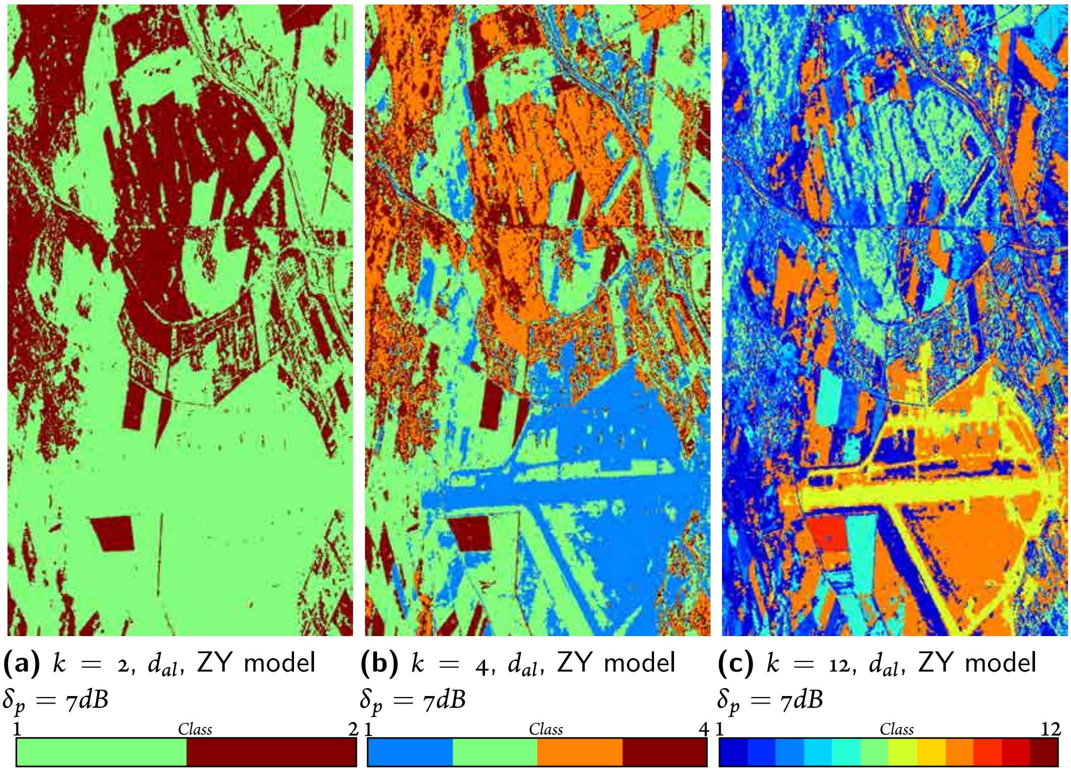

(a) $k = 2$, d_{al}, ZY model $\delta_p = 7dB$ **(b)** $k = 4$, d_{al}, ZY model $\delta_p = 7dB$ **(c)** $k = 12$, d_{al}, ZY model $\delta_p = 7dB$

Figure 7.7: Clustering into 2, 4 and 12 classes of the Oberpfaffenhofen PolSAR image presented in Fig. 4.10a. The ZY model and the d_{al} dissimilarity measure has been employed in all cases.

have been employed for the BPT processing and classification. It may be seen that when the number of clusters k gets increased, the additional classes are spread into further details of the image.

This classification procedure may also be extended to process PolSAR time series, employing the BPT structures defined in Chapter 5. Fig. 7.8 shows the classification results obtained over the complete Flevoland dataset for $k = 16$. On Fig. 7.8a the extended $\mathbf{Z}_e$ region model, the d_g dissimilarity and the Φ_e homogeneity measures have been employed for BPT processing whereas the d_{gc} measure has been employed for the unsupervised classification. On the other hand, Fig. 7.8b presents the results when employing the extended **ZY** model and d_{al_e} and H_{rw_e} dissimilarity and homogeneity measures for BPT based processing, described in Section 6.3.4, and d_{al_e} also for the clustering process. In both cases the 3 by 3 multilook has been employed as initial filtering for matrix regularization. It may be observed that in this dataset, the d_{gc} measure and the classical extended model obtain a more reliable results than over one single image, as previously seen in Fig. 7.6, since having the polarimetric temporal evolution information increases the separability among the different regions of the scene. However, it may also be seen that employing the extended ZY model results in an improvement, as a better separation into different clusters is observed within the agricultural crop fields area. Moreover, the number of outliers, appearing in black color, is larger in Fig. 7.8a than on Fig. 7.8b, specially over the urban areas.

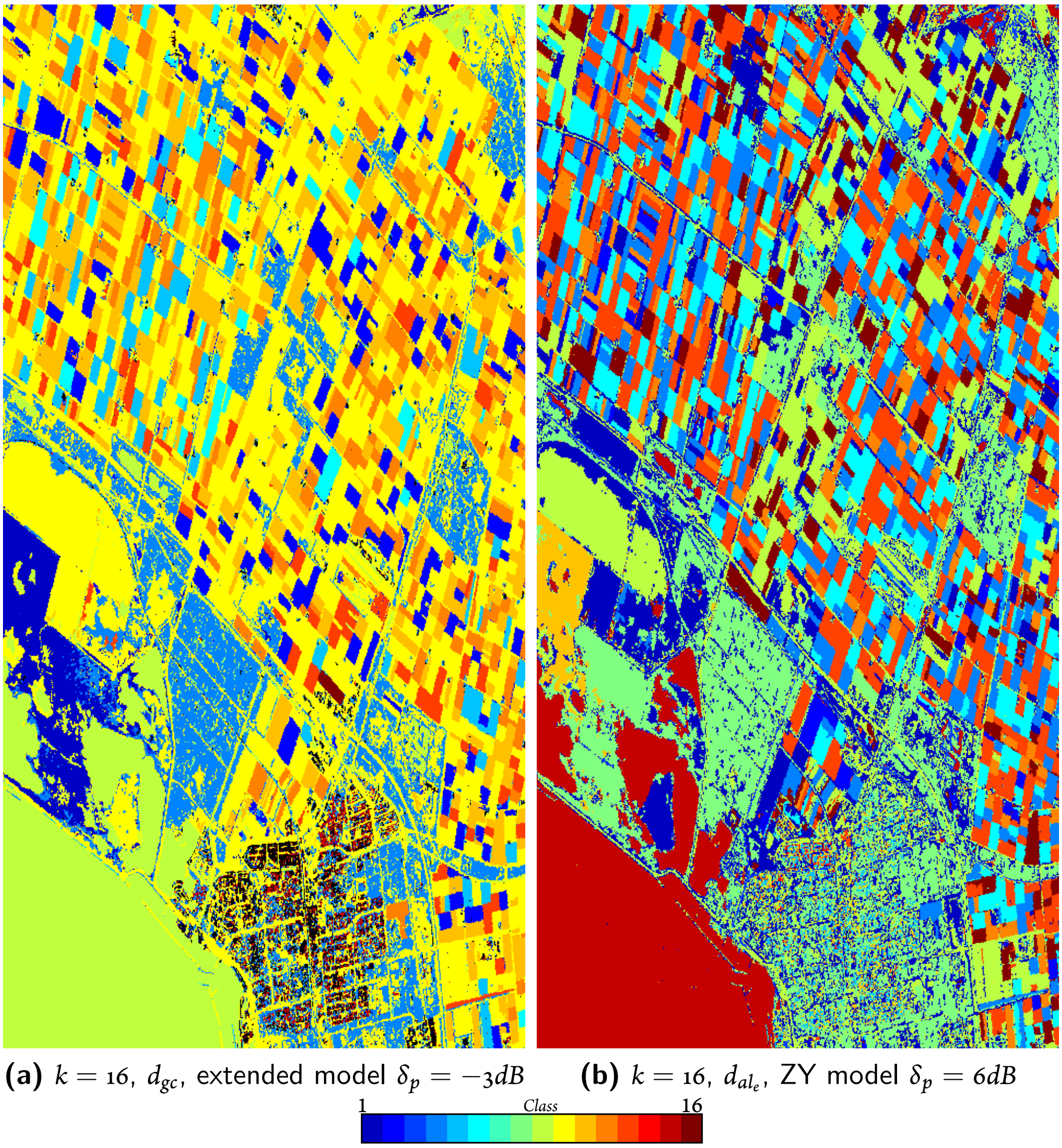

(a) $k = 16$, d_{gc}, extended model $\delta_p = -3dB$ **(b)** $k = 16$, d_{al_e}, ZY model $\delta_p = 6dB$

Figure 7.8: Clustering into 16 classes of the complete Flevoland dataset. The classical model and d_{gc} measure has been employed in (a) whereas the ZY model and the d_{al_e} dissimilarity measure has been employed in (b).

Fig. 7.9 depicts the clustering results for different k values over the Flevoland dataset. The ZY region model has been employed, with the d_{al_e} measure for BPT construction and pruning, as in the results shown in Fig. 7.8b. It may be seen that for $k = 2$, in Fig. 7.9a, the two obtained classes correspond to the sea and land areas of the scene. Additionally, some roads of the scene are also included in the class representing the sea, as they present a similar polarimetric temporal evolution, dominated by surface scattering among all the acquisitions. When two more classes are allowed, as shown in Fig. 7.9b, the land area of the scene is divided into three distinct classes. Two of them correspond to different types of agricultural fields, whereas the third one groups the forest and urban areas having a larger backscattering power. For $k = 8$, represented in Fig. 7.9c, more classes are observed over the fields and urban areas. This behavior continues when the number of classes k parameter gets further increased, as it may be seen in Fig. 7.8b, specially over the agricultural crops area, as different polarimetric temporal evolution trends are detected in this part of the scene.

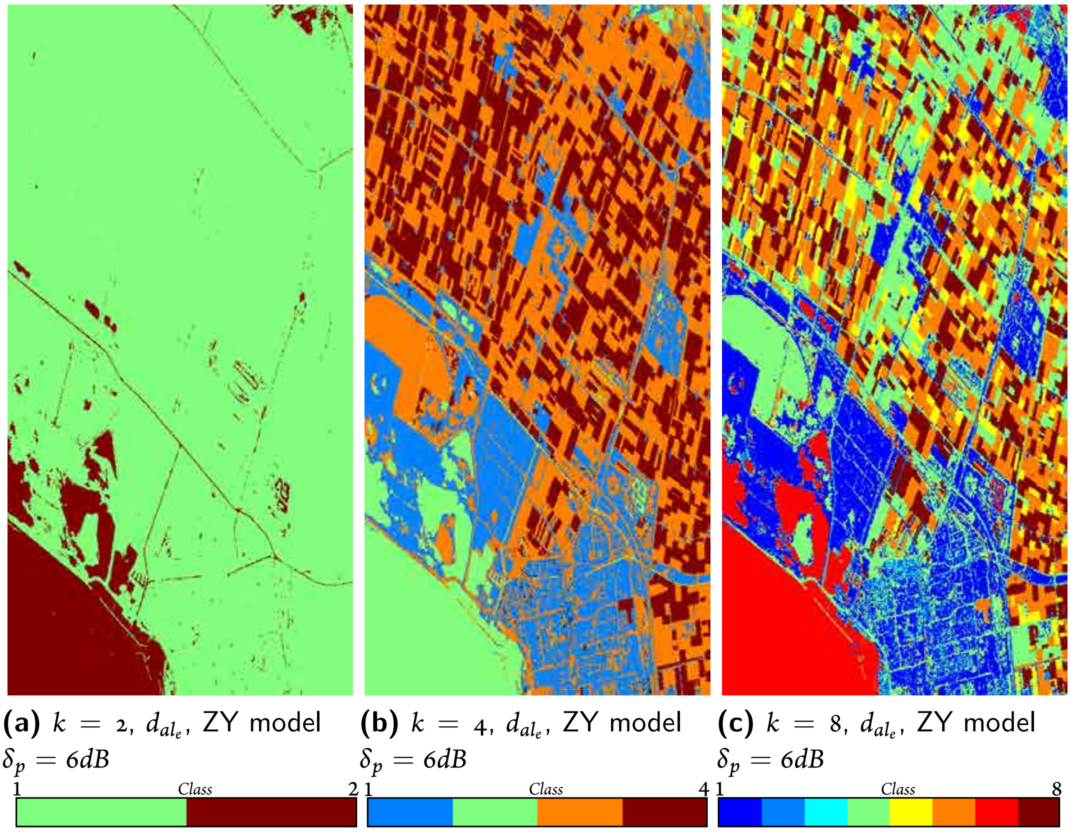
(a) $k = 2$, d_{al_e}, ZY model $\delta_p = 6dB$ **(b)** $k = 4$, d_{al_e}, ZY model $\delta_p = 6dB$ **(c)** $k = 8$, d_{al_e}, ZY model $\delta_p = 6dB$

Figure 7.9: Clustering into 2, 4 and 8 classes of the Flevoland PolSAR time series dataset presented in Fig. 5.3. The ZY model and the d_{al_e} dissimilarity measure has been employed in all cases.

In order to evaluate the correspondence of the obtained classes with the ground truth information and, consequently, with the real content of the scene, Fig. 7.10 shows a detail of the geo-coded results shown in Fig. 7.8b, corresponding to the classification into 16 clusters. On Figs. 7.10a to 7.10f, the contours of different crops types have been marked in black color, according to the ground truth information. It may be observed that the different classes obtained by the classification technique correspond to the different types of agricultural crops of the scene, specially for those crop types having a larger number of fields over the image, as for onions, potatoes, sugar beet and winter wheat, marked on Figs. 7.10c to 7.10f, respectively. It is worth mentioning that, in this case, no training information has been provided, as the proposed technique is an unsupervised classification method. Then, the different polarimetric temporal evolution of the distinct agricultural fields is automatically detected and separated into different clusters.

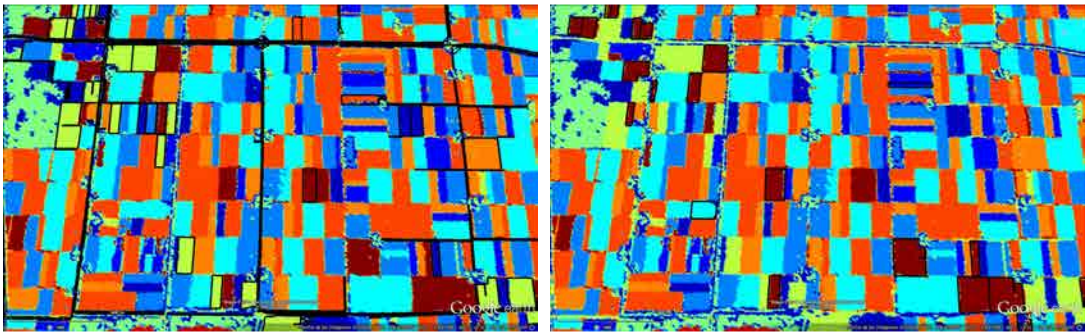

(a) Grass **(b)** Maize

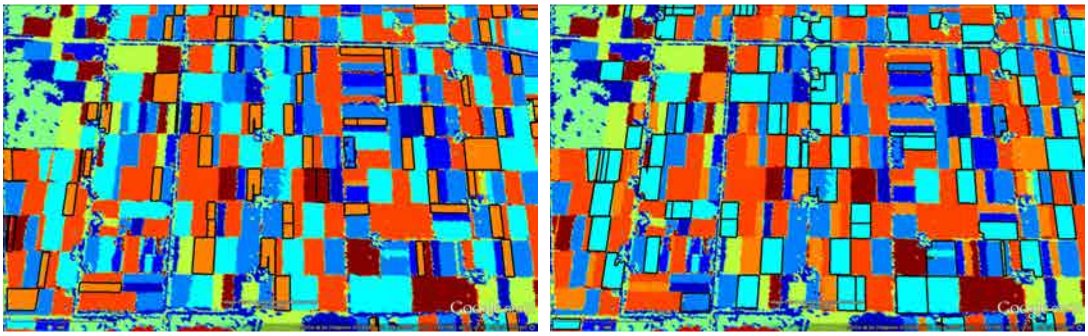

(c) Onions **(d)** Potato

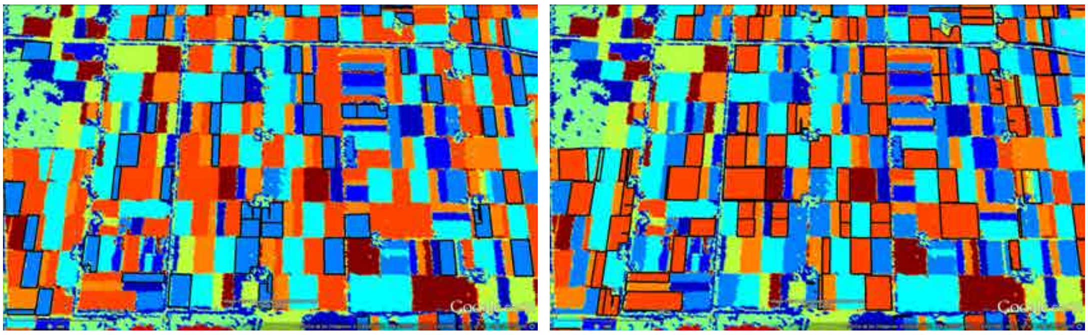

(e) Sugar beet **(f)** Winter wheat

Figure 7.10: Detail of the geo-coded clustering results of the Flevoland dataset into 16 classes and the region contours of some agricultural fields from the the ground truth data. The ZY model and the d_{al_e} dissimilarity measure has been employed.

I think what a life in science really teaches you is the vastness of our ignorance.

David Eagleman

8

Conclusions and Future Research Lines

8.1 CONCLUDING REMARKS

The processing of multidimensional and multitemporal SAR data has been addressed in this thesis. Instead of performing this task directly over the original pixels, a data abstraction has been proposed, the Binary Partition Tree (BPT). It is a hierarchical representation of the data, which may be considered as a region-based and multi-scale description of the data. This work has dealt with the adaptation and the exploitation of this novel representation for PolSAR data and also for polarimetric time series datasets. After this detailed study, the BPT has proven to be a useful representation for the processing and analysis of multidimensional SAR data.

A generic BPT based processing scheme has been proposed, which is composed of two different steps: the BPT construction and its exploitation. Moreover, these two steps isolate the application dependent and independent parts of the technique. Then, the application independent part only has to be performed once per dataset, as it only exploits the internal relationships within the data. Additionally, the exploitation of this abstraction is defined in terms of a BPT pruning mechanism, dissociating the application rationale from the data arrangement. This fact has allowed, for instance, the employment of the same algorithms for speckle filtering and segmentation over PolSAR images and over time series datasets. It is worth mentioning that all these methods have been defined in terms of two straightforward mathematical concepts: a region model and a similarity measure within the space defined by this model. Then the BPT based processing scheme may be considered as a framework for the systematic exploitation of these two concepts.

The BPT based processing scheme has been adapted to process PolSAR data. To do so, the sample covariance matrix **Z** has been proposed as a region model, as it corresponds to the statistical descriptor employed in most of the PolSAR techniques and parameter inversion models. Some similarity measures have been proposed over this covariance matrix space, being the most successful the Wishart measure, based on the statistical distribution of the data under the Gaussian hypothesis, and the geodesic measure, which is based on the geometry of the positive definite matrix cone. However, it is worth mentioning that the variation observed among the different similarity measures is relatively subtle, showing the robustness of the BPT in this sense. Conceptually, the similarity measure encapsulates all the knowledge about the region model space and, in practice, it allows the systematic employment of all the polarimetric information contained within the covariance matrices, which was one of the limitations of some of the speckle filtering techniques in the literature.

Different applications have been developed based on the BPT abstraction during the course of this thesis. Nonetheless, special attention has been paid to the polarimetric information estimation or speckle filtering of the data. This application may be considered as the main pillar of this thesis. After an extensive analysis of the literature on this topic, a common trend has been observed on some state-of-the-art techniques towards the adaptation of their local window to the structure of the scene. The ultimate goals of this tendency are both to increase the amount of available samples for estimation and to avoid the mixture of heterogeneous sample distributions. The BPT structure continues with the same essential approach in a region-based fashion, assuming that although a SAR image is composed by heterogeneous data, it may be decomposed into a set of homogeneous regions, which are the basic entities of this technique. In this regard, the proposed region homogeneity based pruning strategy has proven to be capable of adapting to the structure of the scene independently of its content complexity. This independence has allowed the employment of the same pruning threshold values for different images and datasets, resulting into similar degree of filtering. Thanks to the multi-scale nature of the BPT representation, this technique has shown its ability to obtain, simultaneously, large regions over homogeneous areas while also preserving the small details and the spatial resolution of the scene. Distinct pruning processes over the same tree have shown that the image morphology may be extracted at different detail levels and they have also demonstrated the large amount of useful information contained within the BPT representation of the data.

Detailed analyses have been conducted, including real and simulated data, to evaluate the performance of the proposed BPT based speckle filtering approaches. It has been proven that it does not introduce any bias or distortion over the data, as the estimation process is based on the Maximum Likelihood Estimator (MLE) within each homogeneous region. Additionally, since it has the ability to achieve arbitrarily large regions over homogeneous areas, a massive amount of filtering may be attained over these areas, unparalleled in other pixel-based approaches. As a consequence, the BPT based approach has outperformed other speckle filtering techniques in the conducted analysis in terms of noise reduction and spatial adaptation capabilities.

Additionally, the flexibility of the BPT structure has allowed the development of another additional application: coastline segmentation. In this case, the whole PolSAR image has been divided into the two most different regions, corresponding automatically to the land and sea areas. Thanks to the capability of the BPT to preserve the small features of the scene and the spatial resolution of the data, all the details and thin structures of the coastline are also preserved in the obtained results. Unlike in the speckle filtering application, which is focused on the homogeneous regions of the BPT, this application is focused on the larger nodes of the tree and, thus, it shows that the BPT exploitation may be performed at completely different detail scales and, consequently, it may be useful for a wide range of applications.

This thesis has also studied the processing of PolSAR time series datasets. The analysis and exploitation of the temporal information in PolSAR data is a big challenge that is now starting to be studied and developed. In this thesis, two different alternatives have been proposed to deal with the temporal dimension of the data. On the one hand, it may be assumed that a target is characterized by its particular PolSAR response. Under this assumption, samples from different acquisitions may be combined as long as there is no substantial changes in their response, since they correspond to the same target. Consequently, this approach results into a three-dimensional filtering in the space and time dimensions. The data abstraction that is obtained under this assumption is called the Space-Time BPT (ST BPT). On the other hand, it may be assumed that targets are evolving among the temporal dimension and, thus, they may be characterized by their particular polarimetric temporal evolution. Then, this evolution is a feature of the target which should be included within the model for its proper characterization and exploitation. In this context, the objective is to combine samples of the scene following the same polarimetric temporal evolution. Employing this concept, the Temporal Evolution BPT (TE BPT) representation is defined.

The main advantage of the ST BPT is that it may combine samples from different acquisitions in order to enlarge the available data and improve the polarimetric response estimation. Additionally, as it is a three-dimensional data representation, it has the flexibility to properly represent details of the scene not having fixed contours among the temporal dimension. However, as a counterpart, this flexibility hinders the interpretation of the obtained results as, due to the changing contours, the obtained regions may not be directly related with a particular area of the scene. Moreover, the combination of samples among acquisitions prevents the exploitation of the interferometric information of the data. Conversely, the TE BPT improves the characterization of the target by taking into account its complete temporal evolution. The main inconvenience in respect to the ST BPT is that it is only capable to properly represent spatially fixed contours. However, most of the contours over the land areas of the scene may be considered as spatially fixed, limiting the impact of this inconvenience. Furthermore, its results may be easily interpreted as its regions uniquely correspond to a spatial area of the scene and, additionally, the interferometric information is naturally included within the region model, allowing the exploitation of the PolInSAR information. In this regard, it is worth mentioning that exploiting the temporal evolution for target characterization improves significantly the ability to distinguish among the different areas of the scene and the accuracy of the obtained contours.

According to the aforementioned findings, it has been deduced that the space-time representation may be more suitable for areas not having spatially fixed contours or where no significant information may be extracted from the interferometric information. This is particularly the case, for instance, of the sea or water areas. However, over the land areas, most of the contours may be considered as fixed and, in this situation, employing the polarimetric temporal evolution for target characterization may result into more precise results. Furthermore, these results are simpler to interpret as they uniquely correspond to an area of the scene. It is worth noticing that some of these conclusions related with the temporal information characterization can be extrapolated to other processing techniques and, consequently, they are contributions of this thesis that go beyond the BPT based processing of the data.

The two BPT time series data representations have been analyzed in the context of the speckle filtering application with real time series datasets. A region homogeneity based pruning has been defined over these structures, in the same fashion as in the single PolSAR image BPT exploitation. The adaptation of this exploitation procedure has been straightforward due to the decoupling of the application rationale from the data achieved thanks to the BPT as an intermediate layer in the processing scheme. The TE BPT and the ST BPT have proven to achieve a large amount of noise reduction while also preserving the polarimetric information and its evolution. Additionally, the TE BPT extended model has demonstrated a better region and contour differentiation thanks to the improved characterization due to the complete polarimetric temporal evolution.

The analysis of the variability of the scene has been studied, resulting into the change detection application. On the ST BPT the changes are directly detected, appearing as temporal contours. Consequently, a map indicating the number of temporal contours per pixels has been proposed to analyze the variations over the scene. However, this approach does not take into account the significance of the detected changes. Conversely, the TE BPT contains the target evolution information within the region model. Then, the temporal stability measure has been proposed over the extended model to assess the relevance of the temporal changes of each region among all the acquisitions. This approach has proven to be able to precisely detect human made changes as, for instance, the building construction and transportation activities. For this application, the ability of aggregating samples having the same polarimetric temporal evolution into the regions of the TE BPT is essential, as it avoids the mixture of pixels having different dynamics. Moreover, the region-based BPT change detection approach has also proven to outperform a pixel-based state-of-the-art polarimetric change detection technique in terms of separability between change and no-change areas.

This thesis has also attempted to overcome some of the detected limitations of the developed techniques. One of these limitations of the BPT based and most PolSAR techniques is that, in order to exploit the full polarimetric information, they require an initial filtering for matrix regularization. A 3 by 3 multilook is employed as a pre-processing step in the BPT, resulting into a small spatial resolution loss. In this thesis, the Distance-Based Filtering (DBF) technique has been proposed to circumvent this drawback. It has been analyzed as a standalone speckle filtering technique, resulting into a good polarimetric estimation and an improved spatial resolution preservation with respect to the multilook, the adaptive Lee and IDAN filters. It is worth mentioning that this technique is based on the same similarity measures and models than the BPT but, in this case, in a pixel-based fashion. This contributes to give an idea of the great potential of these simple concepts in practice. In conjunction with the BPT, it has improved the spatial resolution of the obtained results both in speckle filtering and change detection applications. Additionally, the mathematical concepts for the sample covariance matrix generalized eigenvalues have been proposed to perform a fully polarimetric analysis of the changes between two different acquisitions.

Another downside analyzed has been the inability of the polarimetric Gaussian model to properly represent inhomogeneous regions. The mean sample covariance matrix is based on the centroid representation, which may not be sufficient when heterogeneous samples are mixed. More complex statistical distributions may be applied as region models but, usually, they involve a larger number of elements in order to properly initialize and estimate the model. Conversely, a non-parametric representation has been proposed, the ZY region model, allowing the estimation of the average Wishart similarity measure among all the sample pairs. The linear properties of the trace are exploited in order to achieve an efficient computation of these measures. When employed for the BPT based processing, since this measure is not based on the centroid representation, it has demonstrated an improved capability to identify and represent areas of the scene having large spatial variability or texture. Moreover, an improvement has been also observed for the change detection application, when this model and the associated full-linkage measures are employed for the temporal stability measurements.

Finally, the supervised and unsupervised BPT based classification have also been developed applying the same notions previously exploited: a region-based approach employing a polarimetric model and a similarity measure in this space. For the supervised classification application, the previously employed dissimilarity measures have been capable of detecting similar agricultural fields to a given one. Moreover, the region-based BPT approach has been compared with the multilook pixel-based approach in this framework, showing a clear improvement when employing the BPT-based technique. For the unsupervised classification, the k-means method has been proposed to exploit the similarity measures for grouping similar regions into clusters. Special attention has been paid to the initialization process, employing the k-means++ randomized method, and to the outlier detection and removal, which have been defined in a region-based fashion in order to achieve reliable results. The proposed technique has proven to be able to obtain a good separation of the scene content into an arbitrary number of classes. Additionally, thanks to the BPT generalization for PolSAR time series, the classification of the scene taking into account the temporal evolution of the different targets has been achieved. The temporal information has demonstrated to produce a considerable improvement in the classification of agricultural fields, as different types of crops may be properly identified according to their polarimetric temporal dynamics. Another important conclusion extracted from this analysis is that, in the unsupervised classification, the obtained clusters are composed of a mixture of different targets, as all the scene content is grouped into a small set of classes. Then, the employment of a region model being able to properly deal with heterogeneous distributions, as the ZY model, is even crucial for this application.

8.2 Future Research Lines

As mentioned previously, the central topic of this thesis is the employment of the BPT data abstraction for the speckle filtering of multidimensional SAR data. However, as this structure has proven its usefulness for many other fields, some additional applications have been proposed and analyzed. In fact, the employment of the BPT representation for different multidimensional SAR applications seems very promising. Then, one future line of research would be the exploitation of this framework for additional applications as, for instance, vessel detection, mapping land-use and cover, agriculture monitoring, forestry, city planning and control, or, in general, object identification and segmentation.

Additionally, when the different proposed BPT pruning mechanisms have been analyzed with simulated data, it has been shown that an optimum value exist for the pruning parameter. Although this information may not be clearly obtained from real data, since no ground truth information is available, it might seem reasonable to investigate an automatic prune criteria to avoid the need for the pruning parameter. This method could be based, for instance, on the evolution of the homogeneity measure from the tree leaf to the root node in order to identify automatically the better pruning location for each branch of the BPT.

One of the advantages of the TE BPT representation is that the interferometric information is naturally contained within the extended region model, as mentioned before. However, this information has not been employed for the BPT construction or processing. Then, in the future this information may be taken into account to generate region-based PolInSAR processing techniques, which might also benefit from the improved estimation capabilities of the BPT over homogeneous areas and the ability to preserve small details as point scatters. This future line fits perfectly with some forthcoming SAR missions that are focused on this direction, as the ESA BIOMASS mission or the TanDEM-X and TamDEM-L missions. Moreover, this information might also be specially useful for classification, as it may help to differentiate and characterize different types of targets, particularly human-made structures.

During the course of this thesis, the limitations of the classical sample covariance matrix have been stated and the ZY region model has been introduced to overcome some of these limitations. However, this model could also be employed to characterize the texture within the region, in conjunction with the generalized eigenvalues and eigenvectors study proposed. Moreover, an automatic fully polarimetric change analysis and characterization among all the acquisitions could be performed, by extending the generalized eigenvalue decomposition to N acquisitions.

If people do not believe that mathematics is simple, it is only because they do not realize how complicated life is.

John Von Neumann

A

Eigendecomposition Perturbation Analysis

As mentioned previously, the statistical characterization of PolSAR data is based on the sample covariance matrix statistical descriptor. This appendix describes briefly the study of the stability of the different eigendecomposition parameters of this matrix based on the perturbation analysis. Additionally, some conclusions are presented relating the obtained results with the Entropy (H), Anisotropy (A) and averaged alpha angle $(\bar{\alpha})$ decomposition, described in Section 2.2.6.

After the matrix estimation or filtering process, the matrix $\widehat{\mathbf{T}}$ is obtained, which, in fact, will be different to the real covariance matrix $\mathbf{T}$ due the estimation errors produced due to the employment of a finite number of samples. Since the sum of two Hermitian matrices is a Hermitian matrix, it is possible to model this error as $\mathbf{E}$ [71][89]

$$\widehat{\mathbf{T}} = \mathbf{T} + \mathbf{E}. \tag{A.1}$$

The objective, then, is to determine the eigendecomposition of $\widehat{\mathbf{T}}$ and its relation with $\mathbf{T}$ in terms of the perturbation $\mathbf{E}$. The perturbation matrix $\mathbf{E}$ may be interpreted as the speckle contributions that corrupt the estimation of $\mathbf{T}$. Consequently, the influence of this term will decrease by increasing the number of averaged independent samples or improving the speckle filtering technique. In order to quantify the effect of the error matrix, (A.1) may be expressed as

$$\widehat{\mathbf{T}} = \mathbf{T} + \varepsilon \mathbf{B} \tag{A.2}$$

where $\varepsilon = ||\mathbf{E}||$ quantifies the perturbation magnitude and $\mathbf{B} = \mathbf{E}/\varepsilon$.

According to [129] the sample eigenvalues $\widehat{\lambda}_i(\varepsilon)$ may be expressed as a function of the true eigenvalues λ_i, for an ε sufficiently small, as a convergent power series in ε

$$\widehat{\lambda}_i(\varepsilon) = \lambda_i + k_{i1}\varepsilon + k_{i2}\varepsilon^2 + \ldots . \tag{A.3}$$

The quantities $\widehat{\lambda}_i(\varepsilon)$ correspond to the eigenvalues of $\widehat{\mathbf{T}}$ or, equivalently, $\mathbf{T} + \varepsilon\mathbf{B}$. As observed, when $\varepsilon \rightarrow 0$, $\widehat{\lambda}_i(\varepsilon) \rightarrow \lambda_i$ and $|\widehat{\lambda}_i(\varepsilon) - \lambda_i| = O(\varepsilon)$, where $O(\varepsilon)$ is the big O or Landau notation describing the limiting behavior of a function. In a similar way [129], the sample eigenvectors $\widehat{\mathbf{u}}_i(\varepsilon)$ may be expressed as a convergent power series in ε, for ε sufficiently small, where the constant term corresponds to true eigenvector $\mathbf{u}_i$

$$\widehat{\mathbf{u}}_i(\varepsilon) = \mathbf{u}_i + \mathbf{z}_{i1}\varepsilon + \mathbf{z}_{i2}\varepsilon^2 + \ldots . \tag{A.4}$$

Since the set of eigenvectors $\mathbf{u}_i$, for $i = 1, \ldots, m$ forms a basis of $\mathbb{C}^m$, $\mathbf{z}_{ij}$ may be expressed as

$$\mathbf{z}_{ij} = \sum_{k=1}^{m} s_{ikj}\mathbf{u}_k \tag{A.5}$$

where s_{ikj} is a scalar. Introducing (A.5) into (A.4)

$$\begin{aligned} \widehat{\mathbf{u}}_i(\varepsilon) &= \left(1 + \varepsilon s_{ii1} + \varepsilon^2 s_{ii2} + \ldots\right)\mathbf{u}_i \\ &+ \sum_{k=1,k\neq i}^{m} \left(\varepsilon s_{ik1} + \varepsilon^2 s_{ik2} + \ldots\right)\mathbf{u}_k . \end{aligned} \tag{A.6}$$

In order to eliminate the multiplicative factor, one may divide the previous expression by the factor $(1 + \varepsilon s_{ii1} + \varepsilon^2 s_{ii2} + \ldots)$ as this term in not zero for sufficiently small ε. Then

$$\widehat{\mathbf{u}}_i(\varepsilon) = \mathbf{u}_i + \sum_{k=1,k\neq i}^{m} \left(\varepsilon t_{ik1} + \varepsilon^2 t_{ik2} + \ldots\right)\mathbf{u}_k \tag{A.7}$$

that holds for unitary vectors $\mathbf{u}_i$. Nevertheless, it only holds for a normalized $\widehat{\mathbf{u}}_i(\varepsilon)$ when $\varepsilon = 0$. When $\varepsilon \neq 0$, $\widehat{\mathbf{u}}_i(\varepsilon)$ needs to be normalized to norm one.

The eigenvector $\mathbf{u}$, or right-eigenvector, of a square matrix $\mathbf{T}$ is a vector $\mathbf{u} \neq 0$ such that

$$\mathbf{T}\mathbf{u} = \lambda \mathbf{u} \tag{A.8}$$

where λ is the eigenvalue associated with the eigenvector $\mathbf{u}$. Similarly, the left-eigenvector $\mathbf{f}$ is a vector $\mathbf{f} \neq 0$ such that $\mathbf{f}^H\mathbf{T} = \lambda \mathbf{f}^H$. In case of Hermitian matrices, left and right-eigenvectors are equal. When considering (A.8) for the perturbed case

$$(\mathbf{T} + \varepsilon \mathbf{B})\,\widehat{\mathbf{u}}_i(\varepsilon) = \widehat{\lambda}_i(\varepsilon)\widehat{\mathbf{u}}_i(\varepsilon). \tag{A.9}$$

According to [91], the first order perturbation of the eigenvalues is [129]

$$\widehat{\lambda}_i(\varepsilon) = \lambda_i + \varepsilon \beta_{ii} + O(\varepsilon^2). \tag{A.10}$$

where

$$\begin{aligned} \beta_{ij} &= \mathbf{f}_i^H \mathbf{B} \mathbf{u}_j && \text{(A.11)} \\ s_i &= \mathbf{f}_i^H \mathbf{u}_i. && \text{(A.12)} \end{aligned}$$

Finally, the first order perturbation of the eigenvectors is [129]

$$\widehat{\mathbf{u}}_i(\varepsilon) = \mathbf{u}_i + \varepsilon \sum_{k=1,k\neq i}^{m} \frac{\beta_{ki}}{\lambda_i - \lambda_k}\mathbf{u}_k + O(\varepsilon^2). \tag{A.13}$$

The same analysis may be performed to obtain the second-order perturbation approximation [91]. For the eigenvalues this approximation may be expressed as [129]

$$\widehat{\lambda}_i(\varepsilon) = \lambda_i + \varepsilon \beta_{ii} + \varepsilon^2 \sum_{k=1,k\neq i}^{m} \frac{|\beta_{ik}|^2}{\lambda_i - \lambda_k} + O(\varepsilon^3). \tag{A.14}$$

Similarly, the second order perturbation of the eigenvectors is

$$\begin{aligned} \widehat{\mathbf{u}}_i(\varepsilon) = \mathbf{u}_i &+ \varepsilon \sum_{k=1,k\neq i}^{m} \frac{\beta_{ki}}{\lambda_i - \lambda_k}\mathbf{u}_k \\ &+ \varepsilon^2 \sum_{k=1,k\neq i}^{m} \left(\frac{\left(\sum_{j=1,j\neq i}^{m} \frac{\beta_{ji}\beta_{kj}}{\lambda_i-\lambda_j}\right) - \frac{\beta_{ii}\beta_{ki}}{\lambda_i-\lambda_k}}{\lambda_i - \lambda_k}\mathbf{u}_k \right) + O(\varepsilon^3). \end{aligned} \tag{A.15}$$

In order to relate the perturbation with the speckle, the statistical model of the speckle noise has to be included within the expression (A.2) [91]. Then, the perturbation magnitude ε^2 is equivalent to the inverse of the number of looks n^{-1} and the expectation of the perturbed eigenvalues may be defined as

$$\widehat{\lambda}_i = E\{\widehat{\lambda}_i(\varepsilon)\} = \lambda_i + \frac{1}{n} \sum_{k=1, k\neq i}^{m} \frac{\lambda_i \lambda_k}{\lambda_i - \lambda_k} + O\left(n^{-2}\right). \tag{A.16}$$

Similarly, the expectation of the perturbed eigenvectors may be defined as

$$\widehat{\mathbf{u}}_i = E\{\widehat{\mathbf{u}}_i(\varepsilon)\} = \mathbf{u}_i + \frac{1}{n} \sum_{k=1, k\neq i}^{m} \frac{\lambda_i \lambda_k}{(\lambda_i - \lambda_k)^2} \mathbf{u}_k + O\left(n^{-2}\right). \tag{A.17}$$

With this information, the expected values for the $H/A/\bar{\alpha}$ polarimetric decomposition parameters may also be extracted

$$\begin{aligned} \widehat{H} = E\{\widehat{H}(\varepsilon)\} \simeq H - \left(\frac{1}{n} \sum_{i=1}^{3} p_i \log_3(p_i) \sum_{k=1, k\neq i}^{m} \frac{\lambda_k}{\lambda_i - \lambda_k} \right) \\ - \frac{1}{2n \ln(3)} + O\left(n^{-2}\right). \end{aligned} \tag{A.18}$$

$$k_s = \sum_{k=1, k\neq 2}^{m} \frac{\lambda_2 \lambda_k}{\lambda_2 - \lambda_k} + \sum_{k=1, k\neq 3}^{m} \frac{\lambda_3 \lambda_k}{\lambda_3 - \lambda_k} \tag{A.19}$$

$$k_d = \sum_{k=1, k\neq 2}^{m} \frac{\lambda_2 \lambda_k}{\lambda_2 - \lambda_k} - \sum_{k=1, k\neq 3}^{m} \frac{\lambda_3 \lambda_k}{\lambda_3 - \lambda_k} \tag{A.20}$$

$$\begin{aligned} \widehat{A} \simeq A - \frac{1}{n} \frac{\lambda_2 - \lambda_3}{(\lambda_2 + \lambda_3)^2} k_s + \frac{1}{n} \frac{\lambda_2 - \lambda_3}{(\lambda_2 + \lambda_3)^3} (\lambda_2^2 + \lambda_3^2) \\ - \frac{1}{n} \frac{\lambda_2^2 - \lambda_3^2}{(\lambda_2 + \lambda_3)^2} + \frac{1}{n} \frac{1}{(\lambda_2 + \lambda_3)} k_d + O\left(n^{-2}\right). \end{aligned} \tag{A.21}$$

$$\begin{aligned} \widehat{\bar{\alpha}} \simeq \bar{\alpha} - \sum_{i=1}^{3} \frac{p_i}{2n} \left(|\mathbf{u}_i(1)| + \frac{|\mathbf{u}_i(1)|^3}{2} \right) \sum_{k=1, k\neq i}^{m} \frac{\lambda_i \lambda_k}{(\lambda_i - \lambda_k)^2} \\ \cdot \left(2\Re \left\{ \frac{\mathbf{u}_k(1)}{\mathbf{u}_i(1)} \right\} - 1 \right) + O(n^{-2}). \end{aligned} \tag{A.22}$$

As mentioned in [82], the entropy bias has a linear dependence with its value. Then, a linear regression may be performed for the estimation and further removal of this bias [91], as it may be observed on Fig. A.1.

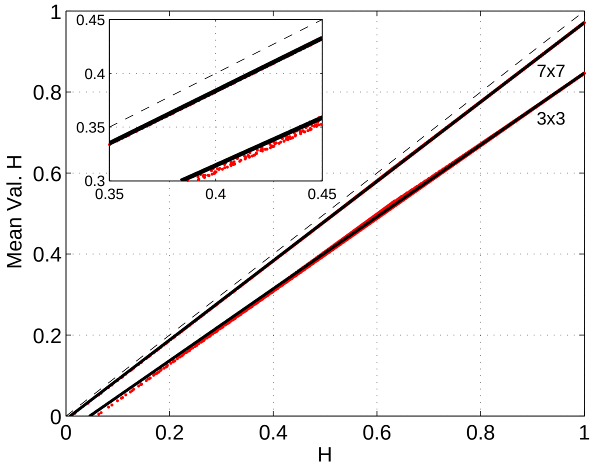

Figure A.1: $\widehat{H}$ is represented by red dots and regression curves by black lines [91].

The effect of this bias correction in practice may be observed in Fig. A.2, over a portion of the Oberpfaffenhofen dataset, presented in Section 4.3.3.

Another important conclusion that may be extracted from the perturbation analysis of the matrix eigendecomposition is that, if the eigenvalues are sufficiently separated, the eigenvectors are more stable with respect to the speckle than eigenvalues, as the denominator of (A.17) depends on the square of the eigenvalue separation $(\lambda_i - \lambda_k)^2$, whereas (A.16) depends only in this separation $(\lambda_i - \lambda_k)$.

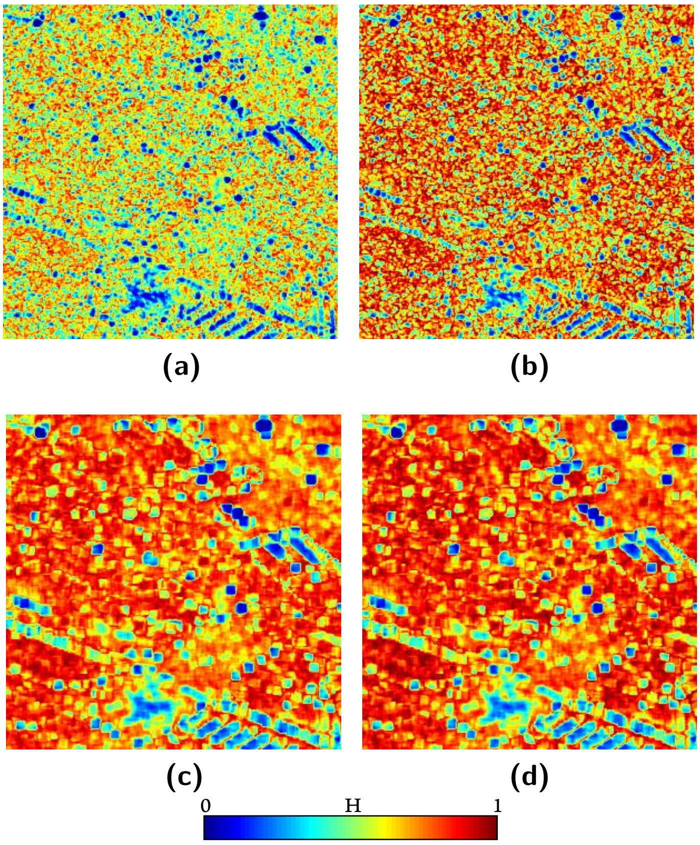

(a) (b)

(c) (d)

Figure A.2: Original and corrected entropies employing the multilook filter. (a) Entropy estimated with a 3 × 3 multilook, (b) Corrected entropy estimated with a 3 × 3 multilook, (c) Entropy estimated with a 7 × 7 multilook, (b) Corrected entropy estimated with a 7 × 7 multilook [91].

B

Additional Results

This appendix presents some additional results from other datasets that have been obtained during the course of this thesis. In many cases, these results have not been analyzed as in detail as those presented in Chapters 4 and 5. However, they have been included in this thesis in order to show the ability of the proposed technique to process different types of data from different SAR sensors.

B.1 ALOS Fully Polarimetric SAR Data

Fig. B.1a shows the Pauli representation of the original fully polarimetric SAR data acquired by the ALOS sensor, at L-band, from Catalunya, Spain. This acquisition was acquired the 13th of April, 2007. Figs. B.1b and B.1c show the obtained results with the BPT region homogeneity based pruning, employing the Φ measure, with pruning threshold parameter values of $\delta_p = -3dB$ and $\delta_p = -1dB$, respectively, as described in Section 4.3.2. The 3 by 3 multi-look initial filtering and the geodesic dissimilarity measure d_{sg} have been employed for the BPT construction process.

As it may be seen, the amount of speckle reduction achieved in this case is also noticeable, resulting into a more contrasted image. The effect of changing the pruning threshold parameter

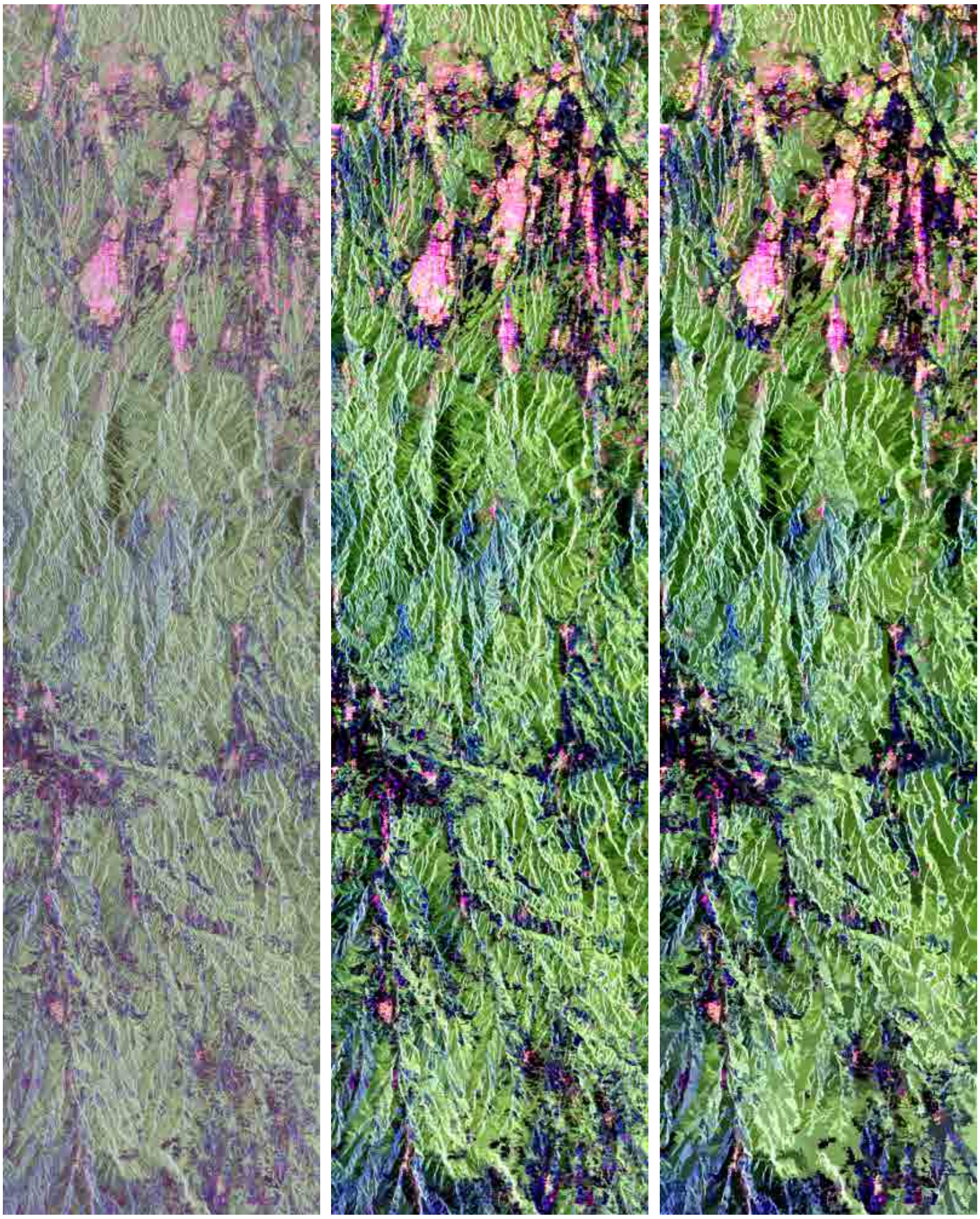

(a) Original **(b)** BPT $\delta_p = -3dB$ **(c)** BPT $\delta_p = -1dB$

Figure B.1: Pauli representation of the results obtained from the ALOS dataset from Catalunya, Spain. The original image is presented in (a), whereas (b) and (c) present the results obtained employing the BPT region homogeneity based pruning with $\delta_p = -3dB$ and $\delta_p = -1dB$ pruning thresholds, respectively. The images have been reduced in the azimuth direction, represented in the vertical direction, by a factor of 25% ($|S_{hh} + S_{vv}|$, $|S_{hv} + S_{vh}|$, $|S_{hh} - S_{vv}|$).

may be seen specially at the bottom part of the image, where some of the details are filtered for high values, as for $\delta_p = -1dB$ in Fig. B.1c.

B.2 FSAR AIRBORNE FULLY POLARIMETRIC SAR DATA

A portion of a PolSAR image acquired by the FSAR airborne sensor, from the DLR, is represented in Fig. B.2a. It was acquired at X-band with a 25 cm by 25 cm spatial resolution near Kaufbeuren, in Germany. This image have much better resolution than the other images employed previously and, then, it a good example of the results obtained with the BPT based processing scheme over very high resolution images. In this case, the ZY region model and the d_{al} dissimilarity and H_{rw} homogeneity measures have been employed for the BPT construction and pruning, as described in Section 6.3.3. Additionally, the DBF filtering has been employed for matrix regularization, employing a 9 by 9 local window, $\sigma_s = 2$ and $\sigma_p = 0.65$ parameters and 3 iterations of the weight refinement scheme, as described in Section 6.1.1. The results obtained for a pruning threshold of $\delta_p = -2dB$ are shown in Fig. B.2b.


(a) Original **(b)** BPT $\delta_p = -2dB$

Figure B.2: Pauli of the results obtained from the FSAR dataset at X-band from Kaufbeuren, Germany. Original Pauli image (a) and results obtained with the BPT region homogeneity based pruning (b) at $\delta_p = -2dB$ ($|S_{hh} + S_{vv}|$, $|S_{hv} + S_{vh}|$, $|S_{hh} - S_{vv}|$).

Additionally, in order to see more clearly the results, a detailed area of these results is shown in Fig. B.3a. The BPT based obtained results for $\delta_p = -2dB$ and $\delta_p = 0dB$ are represented in

(a) Original detail

(b) BPT $\delta_p = -2dB$ **(c)** BPT $\delta_p = 0dB$

Figure B.3: Pauli representation of a detailed area of the results obtained from the FSAR dataset at X-band from Kaufbeuren, Germany. The original image is presented in (a), whereas (b) and (c) present the results obtained employing the BPT region homogeneity based pruning with $\delta_p = -2dB$ and $\delta_p = 0dB$ pruning thresholds, respectively ($|S_{hh} + S_{vv}|$, $|S_{hv} + S_{vh}|$, $|S_{hh} - S_{vv}|$).

Figs B.3b and B.3c, respectively. The effect of speckle reduction may be clearly seen from these results and also the larger amount of filtering when increasing the pruning threshold δ_p up to 0dB. The ability of the proposed technique to obtain large regions over homogeneous areas while also maintaining the spatial resolution and the small details of the image may be clearly seen on Fig. B.3c.

B.3 TerraSAR-X Dual Polarimetric Time Series Data

The TE BPT representation and the temporal stability t_s measure, defined in Chapter 5, have also been employed to process a dual polarimetric TerraSAR-X time series dataset. This dataset consists of 49 acquisitions having HH and VV polarization states from the city of Murcia, Spain. The acquisition campaign started the 19th, February 2009 and ended the 24th, January 2011. A crop having 3000 by 3000 pixels has been selected for each image and they have been co-registered. The extended model and geodesic dissimilarity measure d_g have been employed for BPT construction. The DBF method has been employed for matrix regularization, with a 5 by 5 local window, $\sigma_p = 2$ and $\sigma_s = 0.5$ parameters and 3 weight refinement iterations. Fig. B.4 shows the geo-coded temporal stability measure t_s, as described in Section 5.4.2, as an overlay with an optical image of the area [1].

Fig. B.5c shows a detailed area of the results shown in Fig. B.4. In order to identify the changes detected, two optical images of the zone from 2008 and 2011 are represented in Figs. B.5a and B.5b, respectively. As it may be seen, in this area a street has been constructed in the top part of the image and two buildings have been erected over the right part. These buildings are clearly detected, appearing as red areas. Over the street, however, there is no detected polarimetric change as in both optical images, shown in Figs. B.5a and B.5b, the observed type of scattering may be, from 2008 to 2011, surface scattering, resulting into no change from the radar response point of view among all the acquisitions of the dataset. However, due to the good spatial resolution of the sensor, some small dots are observed over the street, corresponding to the streetlights that have been built. These small details may be detected thanks to the good spatial resolution preservation of the DBF and the TE BPT.

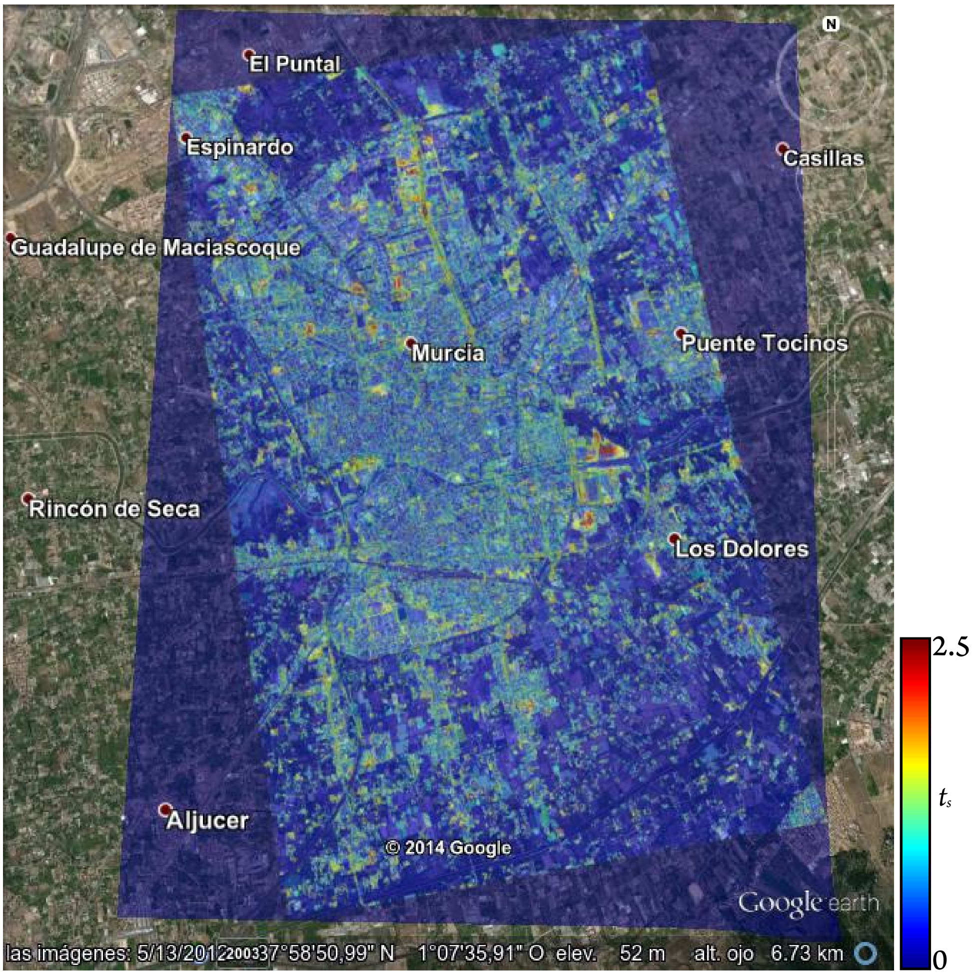

Figure B.4: Geo-coded t_s measure for the Murcia dual-pol TerraSAR-X time series dataset, in Spain [1]. The TE BPT with extended region model has been employed with a $\delta_p = -2dB$ pruning threshold.

(a) Optical image 2008

(b) Optical image 2011

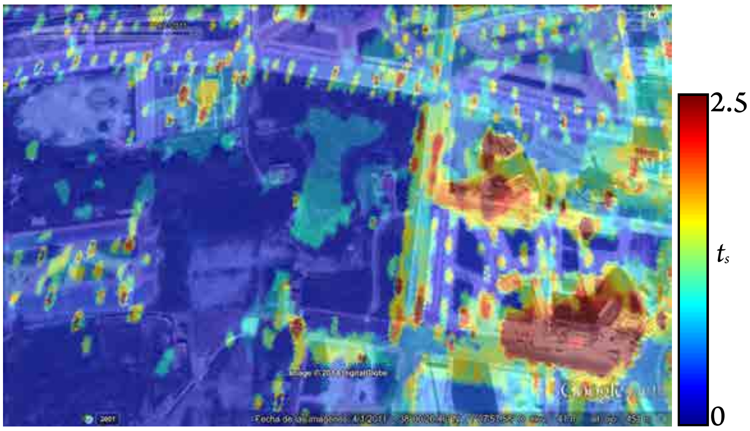

(c) Geo-coded t_s measure

Figure B.5: Optical images from 2008 (a) and 20011 (b) and geo-coded t_s measure (c) for the Murcia dual-pol TerraSAR-X time series dataset, in Spain [1]. The TE BPT with extended region model has been employed with a $\delta_p = -2dB$ pruning threshold.

C

Publications

C.1 PUBLICATIONS IN PEER-REVIEWED INTERNATIONAL JOURNALS

[JP1] A. Alonso-González, C. López-Martínez, and P. Salembier. Filtering and segmentation of polarimetric sar data based on binary partition trees. *Geoscience and Remote Sensing, IEEE Transactions on*, 50(2):593–605, 2012. ISSN 0196-2892. doi: 10.1109/TGRS.2011.2160647.

[JP2] A. Alonso-González, C. López-Mart ínez, P. Salembier, and X. Deng. Bilateral distance based filtering for polarimetric sar data. *Remote Sensing*, 5(11):5620–5641, 2013. ISSN 2072-4292. doi: 10.3390/rs5115620. URL `http://www.mdpi.com/2072-4292/5/11/5620`.

[JP3] A. Alonso-González, S. Valero, J. Chanussot, C. López-Martínez, and P. Salembier. Processing multidimensional sar and hyperspectral images with binary partition tree. *Proceedings of the IEEE*, 101(3):723–747, 2013. ISSN 0018-9219. doi: 10.1109/JPROC.2012.2205209.

[JP4] A. Alonso-González, C. López-Martínez, and P. Salembier. Polsar time series processing with binary partition trees. *Geoscience and Remote Sensing, IEEE Transactions on*, 52(6): 3553–3567, June 2014. ISSN 0196-2892. doi: 10.1109/TGRS.2013.2273664.

[JP5] C. López-Martínez and A. Alonso-González. Assessment and estimation of the rvog model in polarimetric sar interferometry. *Geoscience and Remote Sensing, IEEE Transactions on*, 52(6):3091–3106, June 2014. ISSN 0196-2892. doi: 10.1109/TGRS.2013.2269614.

[JP6] C. López-Martínez, A. Alonso-González, and X. Fabregas. Perturbation analysis of eigenvector-based target decomposition theorems in radar polarimetry. *Geoscience and Remote Sensing, IEEE Transactions on*, 52(4):2081–2095, April 2014. ISSN 0196-2892. doi: 10.1109/TGRS.2013.2257802.

C.2 Publications in International Conferences

[CA1] A. Alonso-González and C. López-Martínez. Space-time PolSAR data temporal series processing based on Binary Partition Trees. In *Synthetic Aperture Radar, 2012. EUSAR. 9th European Conference on*, pages 705–708, April 2012. This paper received the **First place Student Paper Award**.

[CA2] A. Alonso-González and C. López-Martínez. PolSAR Time Series temporal change detection and analysis with Binary Partition Trees. In *Geoscience and Remote Sensing Symposium (IGARSS), 2013 IEEE International*, pages 2321–2324, July 2013. doi: 10.1109/IGARSS.2013.6723283.

[CA3] A. Alonso-González, C. López-Martínez, and P. Salembier. Filtering and segmentation of polarimetric SAR images with Binary Partition Trees. In *Proc. IEEE Int. Geoscience and Remote Sensing Symp. (IGARSS)*, pages 4043–4046, 2010. doi: 10.1109/IGARSS.2010.5653466.

[CA4] A. Alonso-González, C. López-Martínez, and P. Salembier. PolSAR speckle filtering and segmentation based on Binary Partition Tree representation. In *Proc. ESA Int. Workshop on Science Applications of SAR Polarimetry and Polarimetric Interferometry. (PolInSAR)*, 2011.

[CA5] A. Alonso-González, C. López-Martínez, and P. Salembier. Binary Partition Tree as a polarimetric SAR data representation in the space-time domain. In *Proc. IEEE Int. Geoscience and Remote Sensing Symp. (IGARSS)*, pages 3819–3822, 2011. doi: 10.1109/IGARSS.2011.6050063.

[CA6] A. Alonso-González, C. López-Martínez, and P. Salembier. Variable local weight filtering for PolSAR data speckle noise reduction. In *Geoscience and Remote Sensing Symposium (IGARSS), 2012 IEEE International*, pages 2133 –2136, july 2012. doi: 10.1109/IGARSS.2012.6351082.

[CA7] A. Alonso-González, C. López-Martínez, and P. Salembier. Temporal PolSAR image series exploitation with Binary Partition Trees. In *Geoscience and Remote Sensing Symposium (IGARSS), 2012 IEEE International*, pages 1493–1496, July 2012. doi: 10.1109/IGARSS.2012.6351252.

[CA8] A. Alonso-González, C. López-Martínez, and P. Salembier. PolSAR time series processing and analysis based on Binary Partition Trees. In *Proc. ESA Int. Workshop on Science Applications of SAR Polarimetry and Polarimetric Interferometry. (PolInSAR)*, 2013.

[CA9] R. Iglesias, X. Fabregas, A. Aguasca, C. López-Martínez, and A. Alonso-González. Advanced polarimetric optimization for DInSAR applications with Ground-Based SAR. In *Synthetic Aperture Radar, 2012. EUSAR. 9th European Conference on*, pages 513–516, April 2012.

[CA10] R. Iglesias, X. Fabregas, A. Aguasca, C. López-Martínez, A. Alonso-González, and J.J. Mallorqui. Polarimetric optimization for DInSAR pixel selection with ground-based SAR. In *Geoscience and Remote Sensing Symposium (IGARSS), 2012 IEEE International*, pages 3122–3125, July 2012. doi: 10.1109/IGARSS.2012.6350764.

[CA11] C. López-Martínez and A. Alonso. Statistical study of the H/A/Alpha decomposition based on a perturbation analysis of the coherency matrix. In *Geoscience and Remote Sensing Symposium (IGARSS), 2013 IEEE International*, pages 4154–4157, July 2013. doi: 10.1109/IGARSS.2013.6723748.

[CA12] C. López-Martínez and A. Alonso. A study of the RVoG coherent scattering model validity in PolInSAR for forests studies. In *Geoscience and Remote Sensing Symposium (IGARSS), 2013 IEEE International*, pages 2349–2352, July 2013. doi: 10.1109/IGARSS.2013.6723290.

[CA13] C. López-Martínez, A. Alonso, X. Fàbregas, and K. P. Papathannassiou. Ground topography estimation over forests considering Polarimetric SAR Interferometry. In *Geoscience and Remote Sensing Symposium (IGARSS), 2010 IEEE International*, pages 3612–3615, July 2010. doi: 10.1109/IGARSS.2010.5653364.

[CA14] C. López-Martínez, X. Fabregas, A. Alonso, and K. P. Papathanassiou. Ground Topography Retrieval on Forested Areas Based on Polarimetric SAR Interferometry. In *Synthetic Aperture Radar (EUSAR), 2010 8th European Conference on*, pages 1–4, June 2010.

[CA15] C. López-Martínez, A. Alonso, X. Fabregas, and K. P. Papathannassiou. Analysis of volumetric scatters based on TanDEM-X polarimetric interferometric SAR data. In *Geoscience and Remote Sensing Symposium (IGARSS), 2011 IEEE International*, pages 2574–2577, July 2011. doi: 10.1109/IGARSS.2011.6049767.

[CA16] C. López-Martínez, Papathanassiou K., and A. Alonso-González. Separation of scattering contributions in Polarimetric SAR Interferometry. In *Proc. ESA Int. Workshop on Science Applications of SAR Polarimetry and Polarimetric Interferometry. (PolInSAR)*, 2011.

[CA17] C. López-Martínez, X. Fabregas, and A. Alonso-González. Analysis and validity of the PolInSAR line model on forested areas. In *Synthetic Aperture Radar, 2012. EUSAR. 9th European Conference on*, pages 697–700, April 2012.

[CA18] C. López-Martínez, A. Alonso-González, and Fabregas X. Study of speckle noise effects over the eigen decomposition of Polarimetric SAR Data: A Review & Update. In *Proc. ESA Int. Workshop on Science Applications of SAR Polarimetry and Polarimetric Interferometry. (PolInSAR)*, 2013.

[CA19] C. López-Martínez, A. Alonso-González, and Fabregas X. Maximum Likelihood Analysis of the RVoG Model for Forestry Studies in PolInSAR. In *Proc. ESA Int. Workshop on Science Applications of SAR Polarimetry and Polarimetric Interferometry. (PolInSAR)*, 2013.

[CA20] A. Reppucci, X. Banque, Y. Zhan, A. Alonso, and C. López-Martinez. Estimation of snow pack characteristics by means of polarimetric SAR data. In *SPIE Remote Sensing*, pages 85310Z–85310Z. International Society for Optics and Photonics, October 2012.

References

[1] Google Earth. [Online]. Available: `http://earth.google.com`.

[2] Panoramio. [Online]. Available: `http://www.panoramio.com`.

[3] PolSARPro v. 4.0.3. [Online]. Available: `http://earth.esa.int/polsarpro`.

[4] R. Adams and L. Bischof. Seeded region growing. *Pattern Analysis and Machine Intelligence, IEEE Transactions on*, 16(6):641–647, 1994. doi: 10.1109/34.295913.

[5] A.V. Aho, J.E. Hopcroft, and J.D. Ullman. *The design and analysis of computer algorithms*. Reading: Addison-Wesley, 1974.

[6] A. Alonso-González and C. López-Martínez. Space-time PolSAR data temporal series processing based on Binary Partition Trees. In *Synthetic Aperture Radar, 2012. EUSAR. 9th European Conference on*, pages 705–708, April 2012.

[7] A. Alonso-González and C. López-Martínez. PolSAR time series temporal change detection and analysis with binary partition trees. In *Geoscience and Remote Sensing Symposium (IGARSS), 2013 IEEE International*, pages 2321–2324, July 2013. doi: 10.1109/IGARSS.2013.6723283.

[8] A. Alonso-González, C. López-Martínez, and P. Salembier. Filtering and segmentation of polarimetric SAR images with Binary Partition Trees. In *Proc. IEEE Int. Geoscience and Remote Sensing Symp. (IGARSS)*, pages 4043–4046, 2010. doi: 10.1109/IGARSS.2010.5653466.

[9] A. Alonso-González, C. López-Martínez, and P. Salembier. PolSAR speckle filtering and segmentation based on Binary Partition Tree representation. In *Proc. ESA Int. Workshop on Science Applications of SAR Polarimetry and Polarimetric Interferometry. (PolInSAR)*, 2011.

[10] A. Alonso-González, C. López-Martínez, and P. Salembier. Binary Partition Tree as a polarimetric SAR data representation in the space-time domain. In *Proc. IEEE Int. Geoscience and Remote Sensing Symp. (IGARSS)*, pages 3819–3822, 2011. doi: 10.1109/IGARSS.2011.6050063.

[11] A. Alonso-González, C. López-Martínez, and P. Salembier. Filtering and Segmentation of Polarimetric SAR Data Based on Binary Partition Trees. *Geoscience and Remote Sensing, IEEE Transactions on*, 50(2):593–605, 2012. doi: 10.1109/TGRS.2011.2160647.

[12] A. Alonso-González, C. López-Martínez, and P. Salembier. Variable local weight filtering for PolSAR data speckle noise reduction. In *Geoscience and Remote Sensing Symposium (IGARSS), 2012 IEEE International*, pages 2133 –2136, july 2012. doi: 10.1109/IGARSS.2012.6351082.

[13] A. Alonso-González, C. López-Martínez, P. Salembier, and X. Deng. Bilateral Distance Based Filtering for Polarimetric SAR Data. *Remote Sensing*, 5(11):5620–5641, 2013. ISSN 2072-4292. doi: 10.3390/rs5115620. URL http://www.mdpi.com/2072-4292/5/11/5620.

[14] A. Alonso-González, S. Valero, J. Chanussot, C. López-Martínez, and P. Salembier. Processing Multidimensional SAR and Hyperspectral Images With Binary Partition Tree. *Proceedings of the IEEE*, 101(3):723–747, 2013. ISSN 0018-9219. doi: 10.1109/JPROC.2012.2205209.

[15] A. Alonso-González, C. López-Martínez, and P. Salembier. PolSAR Time Series Processing With Binary Partition Trees. *Geoscience and Remote Sensing, IEEE Transactions on*, 52 (6):3553–3567, June 2014. doi: 10.1109/TGRS.2013.2273664.

[16] S.N. Anfinsen and T. Eltoft. Application of the Matrix-Variate Mellin Transform to Analysis of Polarimetric Radar Images. *Geoscience and Remote Sensing, IEEE Transactions on*, 49(6):2281–2295, June 2011. ISSN 0196-2892. doi: 10.1109/TGRS.2010.2103945.

[17] S.N. Anfinsen, R. Jenssen, and T. Eltoft. Spectral clustering of polarimetric SAR data with Wishart-derived distance measures. In *PolInSAR 2007*, 2007.

[18] S.N. Anfinsen, A.P. Doulgeris, and T. Eltoft. Estimation of the Equivalent Number of Looks in Polarimetric Synthetic Aperture Radar Imagery. *Geoscience and Remote Sensing, IEEE Transactions on*, 47(11):3795–3809, 2009. ISSN 0196-2892. doi: 10.1109/TGRS.2009.2019269.

[19] D. Arthur and S. Vassilvitskii. k-means++: The advantages of careful seeding. In *Proceedings of the eighteenth annual ACM-SIAM symposium on Discrete algorithms*, pages 1027–1035. Society for Industrial and Applied Mathematics, 2007.

[20] Z. Bai, J. Demmel, J. Dongarra, A. Ruhe, and H. van der Vorst. *Templates for the solution of algebraic eigenvalue problems: a practical guide*, volume 11. Siam, 2000.

[21] C.A. Balanis. *Advanced engineering electromagnetics*. Wiley New York, 1989.

[22] F. Barbaresco. Interactions between Symmetric Cone and Information Geometries: Bruhat-Tits and Siegel Spaces Models for High Resolution Autoregressive Doppler Imagery. In Frank Nielsen, editor, *Emerging Trends in Visual Computing*, volume 5416 of *Lecture Notes in Computer Science*, pages 124–163. Springer Berlin / Heidelberg, 2009.

[23] P. Beckmann and A. Spizzichino. The scattering of electromagnetic waves from rough surfaces. *Norwood, MA, Artech House, Inc., 1987, 511 p.*, 1, 1987.

[24] W. M. Boerner. Optimal polarization concept in radar imaging. Technical report, May 1981.

[25] L. Bombrun and J.-M. Beaulieu. Fisher Distribution for Texture Modeling of Polarimetric SAR Data. *Geoscience and Remote Sensing Letters, IEEE*, 5(3):512–516, July 2008. ISSN 1545-598X. doi: 10.1109/LGRS.2008.923262.

[26] M. Borgeaud, R. T. Shin, and J. A. Kong. Theoretical models for polarimetric radar clutter. *Journal of Electromagnetic Waves and Applications*, 1(1):73–89, 1987.

[27] W.M. Brown. Synthetic aperture radar. *Aerospace and Electronic Systems, IEEE Transactions on*, (2):217–229, 1967.

[28] A. Buades, B. Coll, and J.-M. Morel. A non-local algorithm for image denoising. In *Proc. IEEE Computer Society Conf. Computer Vision and Pattern Recognition CVPR 2005*, volume 2, pages 60–65, 2005.

[29] W.L. Cameron and L.K. Leung. Feature motivated polarization scattering matrix decomposition. In *Radar Conference, 1990., Record of the IEEE 1990 International*, pages 549–557. IEEE, 1990.

[30] A. Cardama, L.J. Roca, J.M. Rius, J. Romeu, and S. Blanch. *Antenas*. Edicions UPC, Edicions de la Universitat Politècnica de Catalunya, 1993.

[31] A.B. Carlson, P. Crilly, and J. Rutledge. *Communication systems*. McGraw-Hill New York etc., 1986.

[32] S.R. Cloude. Group theory and polarisation algebra. *Optik*, 75(1):26–36, 1986.

[33] S.R. Cloude. *Polarisation: applications in remote sensing*. Oxford University Press, USA, 2009.

[34] S.R. Cloude and K.P. Papathanassiou. Polarimetric SAR interferometry. *Geoscience and Remote Sensing, IEEE Transactions on*, 36(5):1551 –1565, sep 1998. doi: 10.1109/36.718859.

[35] S.R. Cloude and E. Pottier. A review of target decomposition theorems in radar polarimetry. *Geoscience and Remote Sensing, IEEE Transactions on*, 34(2):498–518, 1996.

[36] S.R. Cloude and E. Pottier. An entropy based classification scheme for land applications of polarimetric SAR. *Geoscience and Remote Sensing, IEEE Transactions on*, 35(1):68–78, 1997.

[37] K. Conradsen, A.A. Nielsen, J. Schou, and H. Skriver. A test statistic in the complex Wishart distribution and its application to change detection in polarimetric SAR data. *Geoscience and Remote Sensing, IEEE Transactions on*, 41(1):4–19, 2003. ISSN 0196-2892. doi: 10.1109/TGRS.2002.808066.

[38] J.W. Cooley and J.W. Tukey. An algorithm for the machine calculation of complex Fourier series. *Mathematics of computation*, 19(90):297–301, 1965.

[39] T.H. Cormen, C.E. Leiserson, R.L. Rivest, and C. Stein. *Introduction to algorithms*. The MIT press, 2001.

[40] J.C. Curlander and R.N. McDonough. *Synthetic aperture radar: systems and signal processing*. Wiley New York, 1991.

[41] C.-A. Deledalle, L. Denis, and F. Tupin. Iterative Weighted Maximum Likelihood Denoising With Probabilistic Patch-Based Weights. *IEEE Transactions on Image Processing*, 18(12):2661–2672, 2009. doi: 10.1109/TIP.2009.2029593.

[42] C.-A. Deledalle, F. Tupin, and L. Denis. Polarimetric SAR estimation based on non-local means. In *Proc. IEEE Int. Geoscience and Remote Sensing Symp. (IGARSS)*, pages 2515–2518, 2010. doi: 10.1109/IGARSS.2010.5653936.

[43] Centre d'Etudes Bourguignonnes and Dijon. *Annales de Bourgogne: revue historique*, volume 33. Centre d'études bourguignonnes, 1961.

[44] J.L. Doob, L.S. Ornstein, G.E. Uhlenbeck, S.O. Rice, M. Kac, and S. Chandrasekhar. *Selected papers on noise and stochastic processes*. Dover Publications, 1954.

[45] P. Drineas, A. Frieze, R. Kannan, S. Vempala, and V. Vinay. Clustering large graphs via the singular value decomposition. *Machine learning*, 56(1-3):9–33, 2004.

[46] M. Dyer, A. Frieze, and R. Kannan. A Random Polynomial-time Algorithm for Approximating the Volume of Convex Bodies. *J. ACM*, 38(1):1–17, January 1991. ISSN 0004-5411. doi: 10.1145/102782.102783.

[47] E. Eisemann and F. Durand. Flash photography enhancement via intrinsic relighting. In *ACM Transactions on Graphics (TOG)*, volume 23, pages 673–678. ACM, 2004.

[48] C. Elachi. Spaceborne radar remote sensing: applications and techniques. *New York, IEEE Press, 1988, 285 p.*, 1, 1988.

[49] C. Elachi and J.J. van Zyl. *Introduction To The Physics and Techniques of Remote Sensing*. Wiley Series in Remote Sensing and Image Processing. John Wiley & Sons, 2006. ISBN 9780471783381.

[50] S. Even. *Graph algorithms*. Cambridge University Press, 2011.

[51] Edward W. Forgy. Cluster analysis of multivariate data: efficiency versus interpretability of classifications. *Biometrics*, 21:768–769, 1965.

[52] G. Franceschetti and R. Lanari. *Synthetic aperture radar processing*. CRC, 1999.

[53] A. Freeman. SAR calibration: an overview. *Geoscience and Remote Sensing, IEEE Transactions on*, 30(6):1107 –1121, nov 1992. ISSN 0196-2892. doi: 10.1109/36.193786.

[54] A. Freeman and S.L. Durden. A three-component scattering model for polarimetric SAR data. *Geoscience and Remote Sensing, IEEE Transactions on*, 36(3):963–973, 1998.

[55] C.C. Freitas, A.C. Frery, and A.H. Correia. The polarimetric $\mathcal{G}$ distribution for SAR data analysis. *Environmetrics*, 16(1):13–31, 2005.

[56] H.H. Goldstine and J. Von Neumann. *Planning and coding of problems for an electronic computing instrument*. Institute for Advanced Study, 1948.

[57] D. Gonzalez-Asensio. Análisis de técnicas basadas en el crecimiento de regiones aplicadas a datos SAR multidimensionales. Master's thesis, Technical University of Catalonia (UPC), Barcelona, 2008.

[58] J.W. Goodman. Some fundamental properties of speckle. *JOSA*, 66(11):1145–1150, 1976.

[59] J.W. Goodman. *Statistical optics*. New York, Wiley-Interscience, 1985, 567 p., 1985.

[60] N.R. Goodman. Statistical analysis based on a certain multivariate complex Gaussian distribution (an introduction). *The Annals of Mathematical Statistics*, 34(1):152–177, 1963.

[61] R. Gordon and R.M. Rangayyan. Feature enhancement of film mammograms using fixed and adaptive neighborhoods. *Applied Optics*, 23(4):560–564, 1984.

[62] F.E. Grubbs. Procedures for detecting outlying observations in samples. *Technometrics*, 11(1):1–21, 1969.

[63] F. Harary. *Graph Theory*. Addison-Wesley, Reading, MA, 1969.

[64] V.J. Hodge and J. Austin. A survey of outlier detection methodologies. *Artificial Intelligence Review*, 22(2):85–126, 2004.

[65] J.R. Huynen. Measurement of the target scattering matrix. *Proceedings of the IEEE*, 53(8): 936–946, 1965.

[66] I.R. Joughin, D.P. Winebrenner, and D.B. Percival. Probability density functions for multilook polarimetric signatures. *Geoscience and Remote Sensing, IEEE Transactions on*, 32 (3):562–574, 1994. doi: 10.1109/36.297975.

[67] T. Kanungo, D.M. Mount, N.S. Netanyahu, C.D. Piatko, R. Silverman, and A.Y. Wu. A local search approximation algorithm for k-means clustering. In *Proceedings of the eighteenth annual symposium on Computational geometry*, pages 10–18. ACM, 2002.

[68] P.R. Kersten, J.S. Lee, and T. L. Ainsworth. Unsupervised classification of polarimetric synthetic aperture Radar images using fuzzy clustering and EM clustering. *IEEE Transactions on Geoscience and Remote Sensing*, 43(3):519–527, 2005. doi: 10.1109/TGRS.2004.842108.

[69] E.M. Knox and R.T. Ng. Algorithms for mining distancebased outliers in large datasets. In *Proceedings of the International Conference on Very Large Data Bases*, pages 392–403. Citeseer, 1998.

[70] A. Kostinski and W-M Boerner. On the polarimetric contrast optimization. *Antennas and Propagation, IEEE Transactions on*, 35(8):988–991, Aug 1987. doi: 10.1109/TAP.1987.1144209.

[71] H. Krim, P. Forster, and J.G. Proakis. Operator approach to performance analysis of root-MUSIC and root-min-norm. *Signal Processing, IEEE Transactions on*, 40(7):1687–1696, 1992.

[72] E. Krogager. New decomposition of the radar target scattering matrix. *Electronics Letters*, 26(18):1525–1527, 1990.

[73] J.S. Lee. Speckle analysis and smoothing of synthetic aperture radar images. *Computer graphics and image processing*, 17(1):24–32, 1981.

[74] J.S. Lee. Refined filtering of image noise using local statistics. *Computer graphics and image processing*, 15(4):380–389, 1981. doi: 10.1016/S0146-664X(81)80018-4.

[75] J.S. Lee. Digital image smoothing and the sigma filter. *Computer Vision, Graphics, and Image Processing*, 24(2):255–269, 1983.

[76] J.S. Lee and E. Pottier. *Polarimetric radar imaging: from basics to applications*. CRC Press, 2009.

[77] J.S. Lee, K.W. Hoppel, S.A. Mango, and A.R. Miller. Intensity and phase statistics of multi-look polarimetric and interferometric SAR imagery. *Geoscience and Remote Sensing, IEEE Transactions on*, 32(5):1017–1028, 1994. doi: 10.1109/36.312890.

[78] J.S. Lee, D.L. Schuler, R. H. Lang, and K.J. Ranson. K-distribution for multi-look processed polarimetric SAR imagery. In *Geoscience and Remote Sensing Symposium, 1994. IGARSS '94. Surface and Atmospheric Remote Sensing: Technologies, Data Analysis and Interpretation., International*, volume 4, pages 2179–2181 vol.4, Aug 1994. doi: 10.1109/IGARSS.1994.399685.

[79] J.S. Lee, K.P. Papathanassiou, T.L. Ainsworth, M.R. Grunes, and A. Reigber. A new technique for noise filtering of SAR interferometric phase images. *Geoscience and Remote Sensing, IEEE Transactions on*, 36(5):1456–1465, 1998.

[80] J.S. Lee, M. R. Grunes, and G. de Grandi. Polarimetric SAR speckle filtering and its implication for classification. *IEEE Transactions on Geoscience and Remote Sensing*, 37(5):2363–2373, 1999. doi: 10.1109/36.789635.

[81] J.S. Lee, M.R. Grunes, T.L. Ainsworth, Li-Jen Du, D.L. Schuler, and S.R. Cloude. Unsupervised classification using polarimetric decomposition and the complex Wishart classifier. *Geoscience and Remote Sensing, IEEE Transactions on*, 37(5):2249–2258, 1999.

[82] J.S. Lee, T.L. Ainsworth, J.P. Kelly, and C. López-Martínez. Evaluation and bias removal of multilook effect on Entropy/Alpha/Anisotropy in Polarimetric SAR decomposition. *Geoscience and Remote Sensing, IEEE Transactions on*, 46(10):3039–3052, 2008.

[83] A.M. Leroy and P.J. Rousseeuw. Robust regression and outlier detection. *J. Wiley&Sons, New York*, 1987.

[84] F.K. Li and R.M. Goldstein. Studies of multibaseline spaceborne interferometric synthetic aperture radars. *Geoscience and Remote Sensing, IEEE Transactions on*, 28(1):88–97, 1990.

[85] S.Z. Li and S. Singh. *Markov random field modeling in image analysis*, volume 3. Springer, 2009.

[86] S. Lloyd. Least squares quantization in PCM. *Information Theory, IEEE Transactions on*, 28(2):129–137, Mar 1982. doi: 10.1109/TIT.1982.1056489.

[87] A. Lopes, R. Touzi, and E. Nezry. Adaptive speckle filters and scene heterogeneity. *Geoscience and Remote Sensing, IEEE Transactions on*, 28(6):992–1000, 1990.

[88] C. López-Martínez. *Multidimensional Speckle Noise, Modelling and Filtering Related to SAR Data*. PhD thesis, Technical University of Catalonia (UPC), Barcelona, June 2003.

[89] C. López-Martínez and X. Fàbregas. Polarimetric SAR speckle noise model. *Geoscience and Remote Sensing, IEEE Transactions on*, 41(10):2232–2242, 2003.

[90] C. López-Martínez, E. Pottier, and S.R. Cloude. Statistical Assessment of Eigenvector-Based Target Decomposition Theorems in Radar Polarimetry. *IEEE Transactions on Geoscience and Remote Sensing*, 43(9):2058–2074, 2005. doi: 10.1109/TGRS.2005.853934.

[91] C. López-Martínez, A. Alonso-González, and X. Fàbregas. Perturbation Analysis of Eigenvector-Based Target Decomposition Theorems in Radar Polarimetry. *Geoscience and Remote Sensing, IEEE Transactions on*, 52(4):2081–2095, April 2014. doi: 10.1109/TGRS.2013.2257802.

[92] J. MacQueen. Some methods for classification and analysis of multivariate observations. In *Proceedings of the fifth Berkeley symposium on mathematical statistics and probability*, volume 1, page 14. California, USA, 1967.

[93] S.N. Madsen. Analysis and Applications Related to Synthetic Aperture Radar Data. *Ph.D. Thesis, Technical University of Denmark*, 1986.

[94] A. Maleki, M. Narayan, and R.G. Baraniuk. Suboptimality of nonlocal means for images with sharp edges. *Applied and Computational Harmonic Analysis*, 33(3):370 – 387, 2012. ISSN 1063-5203. doi: 10.1016/j.acha.2012.02.003.

[95] W.H. McCrea and F.J.W. Whipple. Random paths in two and three dimensions. In *Proc. Roy. Soc. Edinburgh*, volume 60, pages 281–298, 1940.

[96] M. Mitzenmacher and E. Upfal. *Probability and computing: Randomized algorithms and probabilistic analysis.* Cambridge University Press, 2005.

[97] R.J. Muirhead. *Aspects of Multivariate Statistical Theory.* Wiley, New York, 1982.

[98] A.D.C. Nascimento, R.J. Cintra, and A.C. Frery. Hypothesis Testing in Speckled Data With Stochastic Distances. *Geoscience and Remote Sensing, IEEE Transactions on*, 48(1): 373–385, Jan 2010. ISSN 0196-2892. doi: 10.1109/TGRS.2009.2025498.

[99] L. M. Novak and M.C. Burl. Optimal speckle reduction in polarimetric SAR imagery. *IEEE Transactions on Aerospace and Electronic Systems*, 26(2):293–305, 1990. doi: 10.1109/7.53442.

[100] A. Nuttall. High-order covariance functions for complex Gaussian processes (Corresp.). *Information Theory, IRE Transactions on*, 8(3):255–256, 1962.

[101] J.A. Ogilvy and H.M. Merklinger. Theory of wave scattering from random rough surfaces. *The Journal of the Acoustical Society of America*, 90:3382, 1991.

[102] C. Oliver and S. Quegan. *Understanding synthetic aperture radar images.* SciTech Publishing, 2004.

[103] F.D. Ortín, D.A. García, and J.R. Martos. *Campos electromagnéticos*, volume 70. Edicions UPC, 1998.

[104] A. Papoulis, S.U. Pillai, and S. Unnikrishna. *Probability, random variables, and stochastic processes*, volume 196. McGraw-hill New York, 1965.

[105] S. Ramaswamy, R. Rastogi, and K. Shim. Efficient algorithms for mining outliers from large data sets. In *ACM SIGMOD Record*, volume 29, pages 427–438. ACM, 2000.

[106] I. Reed. On a moment theorem for complex Gaussian processes. *Information Theory, IRE Transactions on*, 8(3):194–195, 1962.

[107] A. Rosenqvist, M. Imhoff, A. Milne, and C. Dobson. Remote sensing and the Kyoto protocol: a review of available and future technology for monitoring treaty compliance. In *Workshop Report, Ann Arbor, MI, USA*, pages 20–22, 1999.

[108] I. Saarinen. Color image segmentation by a watershed algorithm and region adjacency graph processing. In *Image Processing, 1994. Proceedings. ICIP-94., IEEE International Conference*, volume 3, pages 1021–1025 vol.3, 1994. doi: 10.1109/ICIP.1994.413690.

[109] P. Salembier and L. Garrido. Binary Partition Tree as an Efficient Representation for Image Processing, Segmentation, and Information Retrieval. *IEEE Transactions on Image Processing*, 9(4):561–576, 2000. doi: 10.1109/83.841934.

[110] P. Salembier and M.H.F. Wilkinson. Connected operators. *Signal Processing Magazine, IEEE*, 26(6):136–157, 2009. ISSN 1053-5888. doi: 10.1109/MSP.2009.934154.

[111] C. W. Sherwin, J. P. Ruina, and R. D. Rawcliffe. Some Early Developments in Synthetic Aperture Radar Systems. *Military Electronics, IRE Transactions on*, MIL-6(2):111–115, April 1962. ISSN 0096-2511. doi: 10.1109/IRET-MIL.1962.5008415.

[112] M.I. Skolnik. *Introduction to radar systems*. McGraw-Hill (New York), 1980.

[113] R.R. Sokal and C.D. Michener. A statistical method for evaluating systematic relationships. 1958.

[114] H. Steinhaus. Sur la division des corp materiels en parties. *Bull. Acad. Polon. Sci*, 1: 801–804, 1956.

[115] M. Tello-Alonso. *Post-processing methods for ocean monitoring in SAR images*. PhD thesis, Technical University of Catalonia (UPC), Barcelona, February 2013.

[116] C. Tomasi and R. Manduchi. Bilateral filtering for gray and color images. In *Proc. Sixth Int Computer Vision Conf*, pages 839–846, 1998. doi: 10.1109/ICCV.1998.710815.

[117] R.J.A. Tough, D. Blacknell, and S. Quegan. A statistical description of polarimetric and interferometric synthetic aperture radar data. *Proceedings of the Royal Society of London. Series A: Mathematical and Physical Sciences*, 449(1937):567–589, 1995.

[118] R. Touzi. Target scattering decomposition of one-look and multi-look SAR data using a new coherent scattering model: The TSVM. In *Geoscience and Remote Sensing Symposium, 2004. IGARSS'04. Proceedings. 2004 IEEE International*, volume 4, pages 2491–2494. IEEE, 2004.

[119] R. Touzi, A. Lopes, J. Bruniquel, and P.W. Vachon. Coherence estimation for SAR imagery. *Geoscience and Remote Sensing, IEEE Transactions on*, 37(1):135–149, 1999.

[120] R. Touzi, W.M. Boerner, J.S. Lee, and E. Lueneburg. A review of polarimetry in the context of synthetic aperture radar: concepts and information extraction. *Canadian Journal of Remote Sensing*, 30(3):380–407, 2004.

[121] L. Tsang, J. A. Kong, and R. T. Shin. *Theory of microwave remote sensing*. Wiley (New York), 1985.

[122] G.L. Turin. An introduction to digital matched filters. *Proceedings of the IEEE*, 64(7): 1092–1112, 1976.

[123] F. T. Ulaby and C. Elachi. *Radar polarimetry for geoscience applications*. Norwood, MA, Artech House, Inc., 1990.

[124] F.T. Ulaby, R.K. Moore, and A.K. Fung. *Microwave remote sensing: Active and passive. Volume 2 - Radar remote sensing and surface scattering and emission theory*. Reading, MA, Addison-Wesley Publishing Co., 1982.

[125] G. Vasile, E. Trouve, J.S. Lee, and V. Buzuloiu. Intensity-driven adaptive-neighborhood technique for polarimetric and interferometric SAR parameters estimation. *IEEE Transactions on Geoscience and Remote Sensing*, 44(6):1609–1621, 2006. doi: 10.1109/TGRS.2005.864142.

[126] G. Vasile, J. P Ovarlez, F. Pascal, C. Tison, L. Bombrun, M. Gay, and E. Trouve. Normalized Coherency Matrix Estimation Under the SIRV Model. Alpine Glacier PolSAR Data Analysis. In *Geoscience and Remote Sensing Symposium, 2008. IGARSS 2008. IEEE International*, volume 1, pages I–74–I–77, 2008.

[127] G. Vasile, J. Ovarlez, F. Pascal, and C. Tison. Coherency Matrix Estimation of Heterogeneous Clutter in High-Resolution Polarimetric SAR Images. *Geoscience and Remote Sensing, IEEE Transactions on*, 48(4):1809–1826, 2010.

[128] J.H. Ward. Hierarchical grouping to optimize an objective function. *Journal of the American statistical association*, 58(301):236–244, 1963.

[129] J.H. Wilkinson. *The algebraic eigenvalue problem*. Oxford Univ Press, 1965.